UNIVERSITÀ
DEGLI STUDI
DI BRESCIA

DOTTORATO DI RICERCA IN INGEGNERIA MECCANICA E INDUSTRIALE

ING-IND/13 MECCANICA APPLICATA ALLE MACCHINE

XXXV CICLO

STUDY AND DEVELOPMENT OF MECHATRONIC DEVICES AND MACHINE LEARNING SCHEMES FOR INDUSTRIAL APPLICATIONS

FRANCO LUIS TAGLIANI

PROF. FRANCESCO AGGOGERI, Università degli Studi di Brescia

PROF. NICOLA PELLEGRINI, Università degli Studi di Brescia

ING. ANGELO MERLO, Centro Studi Industriali Ce.S.I.

Ringraziamenti

Mi è doveroso dedicare questo spazio del mio elaborato alle persone che hanno contribuito, con il loro instancabile supporto, alla realizzazione dello stesso.

Ringrazio i professori Francesco Aggogeri, Rodolfo Faglia, Nicola Pellegrini e l'ingegnere Angelo Merlo per l'opportunità e il sostegno fornitomi in questi tre anni di dottorato.

Vorrei ringraziare a tutti coloro che mi sono stati vicini: la mia famiglia italiana, la mia famiglia argentina, e i miei amici. Senza di voi non sarei riuscito ad arrivare dove mi trovo oggi, GRAZIE.

Infine, ringrazio di cuore i miei genitori, i miei nonni e mia sorella che mi hanno supportato e sono stati sempre al mio fianco, permettendomi di portare a termine questo progetto. Avete saputo accompagnarmi e darmi dei consigli nei momenti in cui ne avevo più bisogno, GRAZIE.

Contents

Sommario

Obiettivo del presente progetto di dottorato è lo studio e sviluppo di sistemi meccatronici e di modelli machine learning per macchine operatrici e celle robotizzate al fine di incrementarne le prestazioni operative e gestionali.

Le pressanti esigenze del mercato hanno imposto lavorazioni con livelli di accuratezza sempre più elevati, tempi di risposta e di produzione ridotti a costi contenuti. Le aziende manifatturiere richiedono quindi dispositivi innovativi da integrare nelle macchine convenzionali, riconfigurandole e fornendo loro le capacità richieste dal mercato, impiegando dati ed informazioni. In questo contesto nasce il progetto di dottorato, focalizzato su applicazioni di lavorazioni meccaniche come la fresatura, che includono sistemi complessi quali, ad esempio, macchine a 5 assi e robot industriali, il cui utilizzo varia a seconda dell'impiego. Oltre alle specifiche problematiche delle lavorazioni, si deve anche considerare l'interazione macchina-robot per permettere un'efficiente capacità e gestione dell'intero impianto. La complessità di questo scenario può evidenziare sia specifiche problematiche inerenti alle lavorazioni (e.g. vibrazioni, posizionamento del pezzo, interazione pezzo-utensile) sia inefficienze più generali che riguardano l'impianto produttivo (e.g. asservimento delle macchine con robot, consumo energetico). Vista la vastità della tematica, il progetto si è concentrato su specifiche problematiche sia a livello macchina che a livello di impianto e si è suddiviso in due parti:

- la sezione 1 ha lo scopo di presentare lo studio e lo sviluppo di due specifici dispositivi meccatronici, integrabili in macchine operatrici, che puntano principalmente alla compensazione di vibrazioni indotte dal processo di lavorazione. I dispositivi sono stati progettati per essere integrati in macchine convenzionali, incrementando le loro capacità per soddisfare i requisiti, sempre più stringenti, delle lavorazioni meccaniche di alta precisione.
- la sezione 2 si focalizza invece sull'integrazione di robot per l'asservimento di macchine utensili in celle robotizzate, impiegando modelli di machine learning per definire le traiettorie ed i punti di raggiungibilità del robot, al fine di migliorarne l'accuratezza del posizionamento del pezzo in diverse condizioni. Lo scopo è di identificare modelli data-driven, più efficaci nel rispondere ad eventuali cambiamenti delle condizioni operative-ambientali rispetto a modelli convenzionali, basati sulla cinematica inversa del robot.

I dispositivi meccatronici proposti sono in grado di controllare attivamente e smorzare le vibrazioni indotte dal processo di lavorazione (ad esempio originate dal processo, da motori elettrici, eccentricità, squilibrio di organi rotanti, errori di forma e usura degli ingranaggi) e si basano sull'impiego di attuatori piezoelettrici, opportunamente pilotati per compensare gli spostamenti di disturbo rilevati.

Il primo dispositivo è un sistema compatto di massa inferiore a 6 kg che si interpone tra l'end-effector e la struttura di una macchina operatrice ed è costituito da

due attuatori piezoelettrici, i quali guidano delle masse sospese, lungo un moto rettilineo (in direzione X o Y) tramite delle speciali flexures per una corsa complessiva di 28.0 μm, in funzione del segnale retroazionato al controllore. Il sistema opera sul piano ortogonale all'asse di rotazione del mandrino e ha due gradi di libertà. Il dispositivo è stato sviluppato, modellizzato e validato sia in simulazione che sperimentalmente per il controllo attivo delle vibrazioni nel range 80 Hz - 300 Hz. In particolare, il controllore proporzionale (P) / proporzionale-derivativo (PD) si è dimostrato la scelta più valida per le applicazioni industriali considerate e il banco prova utilizzato, ideato durante il lavoro di questa tesi. Durante le prove sperimentali, si sono ottenuti risultati di contenimento delle vibrazioni pari al 10-94% del disturbo nel range di frequenza 100 Hz - 200 Hz.

Il secondo sistema meccatronico ha invece lo scopo di garantire il corretto posizionamento del pezzo attraverso un supporto la cui posizione è definita da tre attuatori piezoelettrici di alto voltaggio, che permettono il movimento relativo della tavola portapezzo. In questo caso, il progetto di tesi si è focalizzato sul sistema di controllo del dispositivo e la simulazione dei disturbi non lineari, isteresi e creep. Per soddisfare le richieste, è stato implementato un controllore PID con uno schema di bumpless-switching, studiando le due configurazioni applicabili: il posizionamento del pezzo da lavorare in cui non ci sono disturbi dinamici, e la fase di lavorazione, in cui questi disturbi sono generati dal processo di lavorazione. La validazione in simulazione ha ottenuto risultati promettenti nell'intervallo di frequenza 100 Hz – 1,000 Hz, con riduzioni pari al 25-56% del disturbo.

La tesi ha inoltre affrontato problematiche relative all'interazione robot-macchina, come ad esempio l'accuratezza del robot nel posizionare il pezzo in macchina. Si è studiato un modello di machine learning per ottenere la cinematica inversa dei robot industriali partendo da un set di misure sperimentali e dalla cinematica diretta. Questo approccio permette di velocizzare il calcolo durante l'ottimizzazione di traiettorie, principalmente per i giunti iniziali che richiedono più energia per la movimentazione. Il metodo presentato divide il sistema complesso (robot industriale) in un insieme di singoli sistemi dipendenti e si basa su di uno schema di rete neurale per la creazione del modello cinematico inverso. Il modello considera sia la posizione finale del tool center point del robot sia le informazioni dei singoli giunti, riducendo la deviazione rispetto alla posizione di riferimento da raggiungere e la complessità di calcolo. La validazione è stata effettuata su due robot industriali, sia in simulazione che sperimentalmente.

In conclusione, la presente tesi vuole proporre soluzioni meccatroniche e di machine learning per incrementare le prestazioni di macchine e sistemi robotizzati convenzionali. I sistemi studiati possono essere integrati in celle robotizzate, focalizzandosi sia su problematiche specifiche delle lavorazioni in macchine operatrici sia su problematiche a livello di impianto robot-macchina. Le ricerche hanno riguardato un'approfondita valutazione dello stato dell'arte, la definizione dei modelli teorici, la progettazione funzionale e l'identificazione delle criticità del design dei prototipi, la realizzazione delle simulazioni e delle prove sperimentali e l'analisi dei risultati.

Abstract

The aim of this Ph.D. project is the study and development of mechatronic systems and machine learning models for machine tools and robotic applications to improve their performances.

The industrial demands have imposed an ever-increasing accuracy and efficiency requirement whilst constraining the cost. Hence, to satisfy these conditions the manufacturing companies need to develop innovative devices to be mounted upon the conventional machining centres, increasing their capabilities. In this context, this project focuses on machining processes (e.g. milling) that include complex systems such as 5-axes machine tool and, typically, industrial robots, employed for various applications. Beside the issues related to the machining process itself, the interaction between the machining centre and the robot must be considered for the complete industrial plant's improvement. This scenario´s complexity depicts both specific machining problematics (e.g. vibrations, workpiece positioning, tool-workpiece interaction) and more general issues related to the complete plant, such as machine tending with an industrial robot and energy consumption. Regarding the immensity of this area, this project focuses on specific issues related to both the machining centre and the plant, and is divided in two parts:

- Section 1 aims to present the study and development of two mechatronic devices, that can be integrated into the machining centre, for the active vibration control of disturbances during the machining process. These devices have been studied to be mounted on a conventional machining centre to increase their performance and satisfy the present industrial requirements (e.g. ultra-high precision machining).
- Section 2 focuses on the robot machine tending within the robotic cell. Employing machine learning schemes for the trajectory definition and robot reachability to improve the corresponding positioning accuracy. The objective is to define data-driven models, more accurate to handle variations in the operative-environmental conditions with respect to conventional models, based on the robot´s inverse kinematics.

The proposed mechatronic devices are able to actively contain the machining process vibrations, which might have a number of sources such as the cutting process itself, the eccentricity of the system, the electric driving system, unbalanced rotation elements, form errors and wear of the gears, among others. Furthermore, the actuation systems studied during this project are based on piezoelectric stack actuators, driven to compensate the measured vibrations.

The first device is a compact system, with a mass lower than 6 kg, that has been ideated to be mounted between the end-effector and the machining centre structure. It has two piezoelectric stack actuators that are employed to move the two corresponding, carefully shaped, masses along a straight path (for X or Y direction) through a set of flexures. The maximum achievable displacement is of 28.0 μm and is defined by the

control system based on the feedback signal. The system has two degrees of freedom and its workspace is defined within the orthogonal plane to the rotation spindle axis. The device has been developed, modelled, and validated in both simulation and experimentally for active vibration control within the range 80 Hz – 300 Hz. Particularly, the proportional (P) / proportional derivative (PD) controller has demonstrated to be the best choice in terms of the industrial application considered and the developed test bench. During the experimental campaign the system showed promising results obtaining containments of 10-94% for the disturbances within the frequency range evaluated, 100 Hz – 200 Hz.

The second device aims to accurately position the workpiece by moving the platform with three parallel high-voltage piezoelectric actuators, located between the workpiece-platform and the base. Regarding this device, this thesis focused on the control system synthesis and the simulation of nonlinear phenomenon, such as hysteresis and creep. To satisfy the requirements, a proportional-integral-derivative (PID) controller has been implemented with a bumpless-switching scheme. Thereafter, two different set of parameters were defined and validated for the identified phases: workpiece positioning without dynamic disturbances; and the machining phase where the process itself produces the vibrations. The assessment of the device has been carried out in simulation with promising results in the interval of interest, 100 Hz – 1,000 Hz, with disturbances containment of 25-56%.

Furthermore, this thesis has also focused on issues related to the robot-machining centre interaction, as for example the workpiece positioning accuracy by the robot. A machine learning model was evaluated to depict the inverse kinematics of industrial robots from a set of experimental measurements and the forward kinematics. This approach permits to reduce the computational time during the trajectory optimization and focuses on the first joints, as they required the higher energy for the robot motion. The present method divides the complex system, the industrial robot, into a set of more simple interdependent elements related to the individual joints and pursues to provide a model based on the artificial neural networks for each one. The interaction between the models produces the complete inverse kinematic model for the evaluated robot. Such model considers both the final tool centre point position and the individual joints information, reducing the deviation from the wanted position and the computational burden. The method validation has been carried out with two industrial robots, in a simulated environment and with an experimental campaign.

In conclusion, this thesis aims to provide a set of solutions, based on mechatronic devices and machine learning schemes, to improve the conventional machining centre and the robotic systems performances. The studied systems can be integrated within a robotic cell, focusing on issues related to the specific machining process and to the interaction between robot-machining centre. This research required a thorough study of the state-of-the-art, the formulation of theoretical models, the functional design development, the identification of the critical aspects in the prototype designs, the simulation and experimental campaigns, and the analysis of the obtained results.

Introduction

In this section the general introduction for this thesis is presented. Afterwards, the object of study is depicted, and the problem statement described. Finally, the thesis outline, format, and aim are explained.

1.1 Industrial Problem Statement

Nowadays the machining scheme environment has become a complex multi-device system composed of, among other secondary elements, a machining centre responsible of the actual process, and an industrial robot employed to interact and cooperate with the actual machining process. The consequent system's model requires a separation between the different components to ease their treatment and enable the issues identification and characterization. Thereby, the system is divided in two parts: (i) the machining centre, and (ii) the robotic system and its interaction with the former.

The initial component for the case study corresponds to the machining centre, more specifically ultra-precision machining and micro-milling [1]. Micro-milling cutters have relatively poor stiffness, therefore are very sensitive to cutting forces which are significantly different from those in macro milling in terms of size, morphology, and other factors. In fact, the cutting forces are usually small with amplitudes lower than 6 N [1–3]. In a similar manner, in terms of vibrations monitoring, the small size of the tool employed generates displacements of a few microns [3], among which chatter requires further consideration due to its regenerative effect as for macro-milling; indeed, machine learning applications for milling monitoring has been an important research topic during the last decade [4–8]. Despite the numerous differences, since micro-milling is based on conventional milling it does not entangle the machining process and is considered the most suitable for mass production [9]. Nonetheless, several issues related to the micro-milling process must be accounted for to assess the process performance and evaluate possible improvements. The problematics, as for macro-milling, can be summarized in tool runout, tool deflection, vibration, and chatter [3]. These disturbances are tendentially defined with periodic variations, and in some cases with unstable behaviour as for uncontrolled chatter which, if neglected, have several consequences in the quality of the final product with consequent surface roughness. These consequences increment the final cost of the produced part, as they require extra machining to limit and eliminate remaining imprecisions. Furthermore, the production cost is increased in terms of employed tool as the wear is tendentially incremented. Finally, the energy consumption of the machine is incremented due to the influence of vibration issues and tool wear\breakage.

The second part of the complex system corresponds to the inclusion of robotic systems and their interaction with the machining centre, typically related to machine tending and handling operations. Despite their current implications in direct robotic machining, which employs the robotic system as substitute of the machining centre, their

lower stiffness and further requirement of add-on devices to perform at the levels of the machining centre, for the considered application, remains a limitation for their implementation [10]. However, their inclusion within the machining environment has presented several advantages in terms of production volume, reduction in workpiece errors due to incorrect initial positioning, flexibility with machining tool changes, and wear evaluation, among others. The motion of the given robot can be controlled directly from the CNC unit. The productivity and accuracy of the operation relies on the programming, path planning, motion strategy, and dynamic optimization. Indeed, for this case study two problems are considered: *positioning* errors, related on occasions to *calibration* errors, and an increment in the *power requirements*. These have consequences upon the production and the corresponding cost as, for example, errors in robot final position could result in breakages for handling processes and interruption of the machining process. In a similar manner, wrong placement of the workpiece produces machining errors and might require further processing, increasing the production cost and tool wear. Considering instead the reduction of the power requirements in a robotic cell, it might require for example path optimization, which for analytical approaches would result in high computational burden.

In summary, the continuous increment in the demands for higher product volumes and quality while reducing the associated cost entangle the current production system. The inclusion of industrial robots has allowed to overcome some limitations, however, despite the benefits of its application, further improvements must be evaluated and considered to solve issues directly related to the machining scheme. In fact, to overcome these limitations, mechatronic devices [11–15] are mostly recommended along with machine learning schemes for identification and modelling [7,16–19]. In this scenario, this research focuses on two main issues related to the milling multi-device system, the vibrations produced during the micro-milling phase and the correct workpiece positioning. These complications are addressed with the inclusion and presentation of two different mechatronic devices and a machine learning scheme, as depicted in Figure 1. Whilst the devices are defined and validated to directly address both issues within the machine centre, with two different actuation points: at the spindle – tool holder system and at the workpiece; the machine learning model is presented as a novel methodology to simulate the inverse kinematics of a robotic system, and hence permits to deal with the positioning issues produced by the interaction between the robot and the machining centre. Furthermore, the given methodology can be employed to develop feedforward or model-based controllers for robotic milling.

1.2 Thesis Outline

The following thesis work has been distributed into two consequent sections as depicted in Figure 1:

- **Section I:** presents the research treatment of the vibration issues in machining, more specifically in milling machines. Along this section two different mechatronic devices are introduced, both of which have been studied to counteract the effect of unwanted vibrations during machining: a spindle-mounted device and an active

workpiece holder. Whilst the former is constrained to the vibrations limitations, the latter has a secondary goal, the correct location of the workpiece to avoid any miss-positioning errors during machining.

- **Section II:** presents the evaluation of a machine learning approach to define the inverse kinematic scheme of a standard industrial robot based on the D-H parameters and optimization schemes. The main goal is to improve the computational speed during trajectory planning and following whilst reducing the positioning errors for the robotic structure. These errors generate several issues during their interaction with machining centres.

Each section is divided into 5 chapters. *Chapter 1* introduces the industrial issues related to the studied case, the repercussion on the production of the machining system, and presents a literature review of studies/devices related to the present research. Finally, the main contributions for the given section are depicted. *Chapter 2* presents the object of study, the boundaries and limitations, and pursues a brief description of its working principle. *Chapter 3* defines the modelling principle employed for the case study evaluated; whilst in Section I it contains the electromechanical nonlinear modelling of the mechatronic devices for active vibration control, in Section II the machine learning scheme is defined. *Chapter 4* introduces the simulations employed to validate and assess the considered system and, finally, *Chapter 5* presents the experimental campaign.

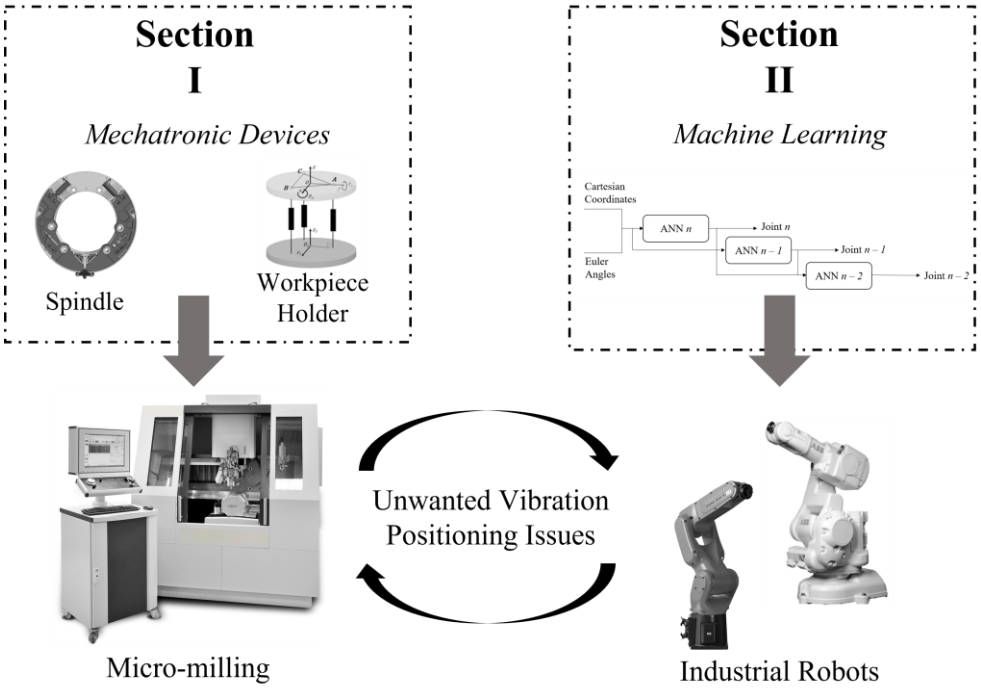

Figure 1. Machining paradigm considered.

1.3 Aim of the Thesis

The objective of this thesis research is to address the machining issues derived from industrial applications, mainly ultraprecision (micro-milling) machining and robotics integration. This work focuses on unwanted vibration control during the interaction between tool and workpiece; this will be accomplished with two different

industrial appealing mechatronic devices: a novel spindle two-axes device and a three degrees-of-motion workpiece holder. Both devices employ piezoelectric actuation for which a complete nonlinear electromechanical standard modelling scheme is implemented. Furthermore, the presence of robotic systems in the industrial environment requires consideration, in fact, the modelling and calibration problematics are addressed with a novel machine learning methodology based on their interaction with the machining centre. The three elements, both devices and the robotic machine learning model, are centred and developed based on the improvement analysis upon machining industrial requirements highlighting the potential future applications and developments to further improve the technology for these operations.

The key contributions of this thesis are summarized as follows:

1. Concept design, simulation, prototype construction, and experimental validation of a spindle active control vibration device based on piezoelectric actuation.
2. Model and regulator development, and validation, for a workpiece holder device based on piezoelectric actuation employed for positioning and vibration control.
3. Novel machine learning model methodology for inverse kinematic definition in robotic applications.

SECTION I

Mechatronic Devices for Active Vibration Containment and Workpiece Positioning

Chapter 1

Introduction

In this Chapter the problem statement for the milling centre is introduced, the main vibration sources are defined, and the consequences of the uncontrolled disturbance are depicted. Furthermore, the main solutions proposed in industry are presented, from passive process solutions to devices developed for both passive and active applications. Finally, the contributions of this thesis work to the field are described.

1.1 Problem Statement

The globalization era, within which the industrial environment is currently on, presents several requirements and necessary conditions to provide higher production and quality, whilst reducing costs. This approach has been of core importance in recent years, with a series of industrial enhancement and improvements studied to provide solutions for the production constraints [12]. However, these demands entail a set of issues related to the machining environment, which in the simplest consideration increases the relative motion between tool and workpiece, resulting in issues with the final product quality.

These vibrations can be classified in three main kinds [20–22]: (i) free vibrations, (ii) forced vibrations, and (iii) self-excited vibrations. The first type is related to pulsating excitation arising from inertial forces, or incorrect tool path that leads to a collision between tool and workpiece. Differently, forced vibrations are periodical disturbances due to imbalances between gears or bearings/spindle, intermittent cutting, or external harmonic excitations, among others. Finally, self-excited vibrations are generated by the interaction between tool and workpiece during machining; these extract energy from the system and grow during the cutting process if unattended, resulting in system's instability. Whilst for free and forced vibrations the source can be identified, and their effect handled and contained, self-excited vibrations are a more complex disturbance due to their multi-source nature. In fact, these vibrations are known as chatter and can be classified in: primary, the cutting process itself, and secondary, regenerative chatter. Despite regenerative chatter being the main research topic for vibration containment in machining, several other chatter sources can be defined, such as: frictional chatter, thermo-mechanical chatter, and mode coupling chatter.

Whatever the source, the vibration disturbance directly affects the cutting process as the cutting tool and the corresponding workpiece are intermittently out of contact [23,24]. Thereafter, several negative effects are encountered when vibrations are neglected, among which:

- Issues related to surface quality, with an increased roughness which could require further machining, incrementing the product cost.
- Limited material removal rate (MRR), incrementing the required production time and, hence, the final product cost.
- Excessive noise.
- Excessive and disproportionate tool wear, which could result in early changes incrementing the production cost and limiting the number of final pieces.

Considering the wide range of machining operations, milling is one of the most common methods due to its high productivity, high flexibility, and its capability of complex composite parts machining [21,25,26]. However, regarding the control implications, other processes such as turning, keep the tool stationary while the workpiece is rotated, this approach allows to implement a simpler device installing an actuator near the cutting point. Differently, during milling the tool rotates while the workpiece is still, and hence the fixed actuators upon the spindle – tool holder – tool system are more difficult to locate. Furthermore, milling is a multi-point process and thus the instantaneous cutting direction rotates during machining.

1.2 Literature Review

Vibration containment can be divided into three major groups: process solutions (mainly for regenerative chatter issues), solutions based on passive devices, and active devices for vibration control. The latter might be divided based on the actuation system or the sensory scheme. Nevertheless, the goal of this project is to evaluate active appealing devices based on piezoelectric actuation, as will be introduced. Passive approaches instead, which include both passive devices and process solutions, aim to improve the machine design, vary the machining process, or use add-on equipment to absorb the extra energy due to unwanted vibrations.

1.2.1 Passive Solutions

The choice of process parameters to avoid instabilities in milling process is the initial basic passive solution, which functions mainly for the so-called regenerative chatter vibrations. The idea is to choose the process parameters by evaluating what is known as Stability Lobe Diagram (SLD), which defines the curve of stability with respect to the depth of cut and the spindle speed. This graphical aid allows the user to choose the coefficients for the undertaken process, however, the accurate prediction of the SLD plays a core role in this decision. Despite the quality of the given diagram, it can only guide the parameters selection and it cannot guarantee that such conditions remain static during the machining process, which if varied could result in stability loss [26]. Furthermore, the selected parameters tend to be conservative in order to account for the expected modelling errors and, hence, result in a constrained efficiency of the machining process. Finally, it might result that machining within the stability range is impossible due to other factors such as wear of the cutting tool or limitations of the machine tool [27].

Considering the nature of the regenerative chatter, two process solutions can be found, the spindle speed variation (SSV) and the variable helix or pitch tools, whose effectiveness is dependent on the design (which requires optimization) and the process characteristics [28]. These approaches aim to tackle the chatter generation by disrupting the regenerative process. However, a critical analysis of such strategies reveals strict limitations in their general applications. In fact, SSV requires certain characteristics to be known, such as chatter frequencies and stability lobes, both of which are sensitive to slight changes in the machine set-up [24]. Additionally, a varying configuration of the machine tool during machining can guide to changes in the machine structural dynamics and as a result can lead to stability lobes becoming invalid [27]. Finally, the spindle motors are not designed to vary the spindle speed continuously [21].

An alternative passive solution is the implementation of tuned mass dampers (TMD), elements that increase the damping of the critical mode without external power through energy dissipation [29,30]. Alternatively, thin-wall milling can benefit by the inclusion of additional masses as in [31], where the authors obtained an increment of over 2 mm of the critical axial depth of cut at 6700 rpm. They need to be accurately designed, based on the modal model and, hence, their simplistic functioning is limited only to the given constrained frequency range. Furthermore, their location is of great importance to maximize its functioning due to their dependency of modal behaviour [32]. In summary, under the uncertainty and complexity of the machining process, the passive approach cannot show good performances without extra sources of energy [26], therefore, active solutions should be accounted for.

1.2.2 Active Devices

Due to the limitations encountered with passive solutions, including passive devices, the use of active vibration control is depicted as an appealing alternative solution based on several characteristics, among which: versatility, dynamic efficacy, and retrofittable to a variety of machine tools. Active approaches can be mainly divided into two solutions: devices that act directly upon the spindle-tool holder-tool system, and active workpiece holders. The latter are mainly employed for thin-walled machining for which the low-relative stiffness of the workpiece with respect to the tool compels the actuation system to be located near the machined part. The actuation systems for the active devices are mainly electromagnetic and piezoelectric.

Among the various electromagnetic applications, most of the industrial appliable devices include active magnetic bearings [33–37], employing magnetic forces to support the spindle axis in a non-contact approach. The main advantages of their use with respect to traditional ball-bearing spindles are: limited wear and friction, low maintenance cost, and long operating life; still, they reduce the system damping, which is a drawback for the spindle stability [32]. An alternative to overcome these issues was found with electromagnetic actuation, which can use a similar basic configuration as the active magnetic bearings whilst maintaining the manufacturers inner bearings upon the spindle. In fact, this new configuration provides an independent device which can be incorporated upon the spindle and control the unwanted vibrations. In [11,38] the authors proposed an

eight-stator actuator with two adjacent poles device located near the tool holder; the basic principle is that when current is applied in the coil a magnetic field is produced, which exerts an attraction force upon the rotor, and thereafter upon the tool holder – spindle system. The force amplitude in [11] is adjusted by altering the input current with a PD controller. The active damping performance presents an increment of the dynamic stiffness at the first modal frequency of 2.89 and 3.67 for the X-axis and Y-axis, respectively. An alternative control is proposed in [39], where a sliding mode approach is employed and the axial cutting depth is significantly improved under the experimental tests considered. Despite the results obtained with the given devices, an important issue related to the nature of electromagnetic actuators is due to the eddy current generation in the stator and rotator when high frequencies are considered, which decreases the applicable force [11].

Whilst electromagnetic actuators have shown their capabilities, they tend to be cumbersome devices, whereas piezoelectric materials have a reduced dimension while maintaining great qualities for active vibration control systems; due to their high-stiffness, high-resolution motion, high-amplitude force, lack of rotary parts and element interaction. It is worth mentioning that these actuators require high-cost power amplifiers, which constraints the number employed, and a set of preloading uncoupling springs to avoid transversal disturbances upon the actuator, direction upon which these actuators are fragile.

Initial approaches validated their use in workpiece holders (AWH) with a single axis piezoelectric actuator, as for the system presented in [27] employed to contain the vibrations arising during up-milling of flexible workpieces fixed to non-rigid clamping systems. The authors employed an LQG robust controller with a Kalman observer and a workpiece direct displacement feedback from a laser sensor. Furthermore, beside the low-frequency chatter control (77 Hz) the authors contained also forced vibrations due to their contribution of accuracy reduction and tool life shortening, particularly upon the second harmonic of the tooth-passing frequency. A similar flexible application was studied in [40], where the authors presented a single axis compensation system formed by a flexure hinged-based worktable with piezoelectric actuation to compensate workpiece deformation. The system uses a dynamometer table to measure the cutting force, which is employed in parallel to a rigid system force model, the difference between the two signals is used to generate the piezoelectric actuator (PEA) voltage. Such difference arises from the variations in radial depth of cut caused by workpiece deformation, hence, knowing its nominal value it is possible to compensate them in real-time obtaining the nominal depths. A further inner closed loop controller provided by the piezoelectric manufacturer based on a PI scheme was employed to linearize the PEA motion and limit the hysteresis effect.

In order to further improve the AWH capabilities, a new control concept design is introduced in [41], for which instead of the individual displacement of the workpiece, the authors proposed to employ the relative displacement between tool and workpiece, real source of vibration. A simplified approach is presented by the authors with a 2-DOF

piezo-based system to handle low-frequency chatter vibrations (~62 Hz). However, the experimental validation considered that the spindle vibrations were higher than the workpiece ones and hence neglected the latter. Indeed, by double integration the authors proposed a relative displacement constraint by handling the natural mode of the spindle structure. In other words, the active system moves the workpiece following the spindle vibrations measured with an accelerometer, obtaining a 50% increment in the achievable stable cutting depth in the conditions considered. Nevertheless, this simplistic approach encounters issues with thin-wall parts and with chatter frequencies much higher than natural modes of the spindle structure.

In fact, a better filtering approach would be to implement a filtered-x least mean squared (FxLMS) controller as in [24]; where the authors designed a FxLMS with force feedback to contain the vibrations measured during up- and down-milling for a piezo-based palletized workpiece. The system was validated with low-frequency components, for which it showed promising results, containing the mean surface roughness from 0.855 μm up to 0.502 μm for a steel workpiece and from 0.299 μm to 0.188 μm for an aluminium part. Furthermore, a tool wear measurement was performed for the steel workpiece assessing the reduction in the amount of wear when the controller was active. A further development for the FxLMS algorithm is found in Ford et al. [42] for an active workpiece holder with acceleration or force feedback. The authors implemented an Internal Modal Control (IMC) FxLMS for the adaptive controller and employed the Feintuch algorithm to determine the secondary path loop. Furthermore, the developed controller has two variations, depending on the feedback signal employed: acceleration or force. The unstable milling experiments have shown a great improvement with the piezo-based workpiece device, eliminating chatter vibrations and reducing more than 92% the modal frequencies vibration levels with the acceleration feedback. On the contrary, stable cutting processes presented better results with the force feedback, with an extra high-pass filter to avoid static forces, improving the surface finish of 21.3% roughness and 18.9% waviness in 3D measurement. However, if higher vibration frequencies are considered, on the order of kHz, the resulting requirements for the active fixturing devices would be limited by the consequent inertial forces and operability of the actuators when closed loop controllers are employed, due to their counter-act reasoning.

The active disruption of the regenerative effect obtainable in open loop through stiffness variation methods with preloaded forces in different waveforms as presented for the frequency issue in [43]; where a piezo-based active fixturing device is described and validated in simulation. The outcomes showed the open loop capabilities of these schemes by disrupting the regenerative effect with sinewaves displacements of the workpiece. The results depicted an appreciable variation over 3,000 rpm, with an enhanced response when both axes are disrupted, independently of the feed direction; furthermore, the proportion between actuated displacement and feed per tooth coefficient should always be higher than one, to maximize the SLD improvement. The simulation results have shown increments of 40% when such coefficient was equal to 1.5. Finally, the tooth frequency must be known considering the incompatibility of regenerative effect

with the given frequency and its harmonics. Nevertheless, this approach is not optimized for the machining conditions and is based on the SLD design, whose accuracy depends on the quality of the model employed. Furthermore, the lack of feedback construction implies a continuous actuation of the system, resulting hence in a reduced efficiency system and a reduced actuator's life.

A similar reasoning is carried out in [26,44] for a spindle piezo-based device. The system required an initial modelling phase to validate and optimize the variation method, while random stiffness excitation presented an increment at the peaks of the SLDs, the best mean results were obtained with the multiple harmonic stiffness excitations for which the GA was employed to optimize the Fourier coefficients. This open loop approach obtained promising results in terms of SLD expansion and, hence, increments in axial cutting depths. Nevertheless, they require an accurate modelling, the results are not point-defined, and the optimization time is excessive in terms of industrial requirements. An asymmetric stiffness open loop method is proposed in [25], where the authors employed two pairs of piezoelectric actuators in push-pull configuration to modify the axial stiffness of the spindle along the X- and Y-axes. The results showed a reduction in the unstable zone in the SLDs which varied depending on the radial depth of cut ratio and the type of milling (down-milling or up-milling) when a single axis was modified. Nevertheless, an iterative initial process based on the milling condition settings is required, for which the stiffness gain is determined based on the SLD construction and the stability at the point of spindle speed and depth of cut chosen; afterwards, during milling, a stability control based on an acceleration measurement is used to handle appearing vibration issues and re-modify the stiffness gain to regain stability. A different open loop adaptronic spindle system based on preload piezoelectric actuation is depicted in [45]. The authors presented a system with three preloaded actuators, with strain gauges to allow inner closed loop positioning schemes, disposed in a parallel kinematic configuration that is able to move the tool tip in a prismatic space along the three degrees of freedom up to 2 kHz. The aim of the paper was to handle the chatter disturbances by generating an additional lower frequency force, disrupting the regenerative process. Nevertheless, during stable machining the actuation increases the resulting milling forces. A more complex structure was introduced in [46], where the authors included 6 preloaded high voltage piezoceramic actuators in a parallel scheme to obtain a 5-DOF active system for correct spindle positioning, but no controller considerations or machining experiments were carried out. Finally, the number of actuators and their corresponding power amplifiers would result in a non-appealing solution for industrial applications mainly due to the high cost of this technology.

In summary, closed loop approaches, despite their increment in controller complexity and sensor requirement, are the most promising technologies to tackle the issues derived from machining vibrations, and hence improve the surface finishing and reduce tool wear. The authors in [15,47] proposed a system with two pairs of piezoelectric actuators in push-pull configuration with a model predictive control to contain the chatter disturbances at the spindle in milling processes. The controller required a system model descripted with a linear time invariant model that included the

chatter phenomenon, the developed structure, and the milling process models. The given scheme was obtained with: (i) a state space identification based on FRFs experiments, (ii) a milling test with a dynamometer to obtain the milling cutting coefficients, (iii) the Fourier series zero order approximation, and (iv) the Padé approximation to linearize the chatter delayed computed based on the tooth passing period. The model predictive control (MPC) weight matrices were constructed to contain only the chatter frequencies avoiding static forces whilst limiting the PEAs input voltages, obtaining an accurate and efficient actuation in the real control process. The experimental results presented a complete containment of two chatter frequencies (1,159 Hz and 1,562 Hz) with respect to the uncontrolled milling for both X- and Y-axes. A similar actuation system is employed in [48] with a nonlinear Fuzzy controller defined with expert knowledge. The controller includes a set of comb filters to filter the static components of the milling process measurements based on the spindle rotation frequency reducing the power requirement of over 97% in the experimental case (from a mean square voltage of 0.603 V^2 up to 0.014 V^2) and maximizing the chatter control effort. The regulator handles the regenerative phenomenon at the initial phase, and it quickly suppress it, hence, the control voltage is mainly determined by noises and only maintained at small amplitudes. The experimental results showed a complete containment of the chatter frequencies for a 12,000 rpm milling process (1,058 Hz, 1,118 Hz, and 1,658 Hz) while slightly varying the stable frequencies. This controller is defined based on expert knowledge and does not require an explicit complex modelling of the system. Thus, for a given system combination, the control rule can be easily designed and widely applied at different machining conditions.

Dohner et al. [49] proposed a telemetry system with stacks of electrostrictive material (PMN) embedded within the housing of the machine as actuators. The authors employed a set of strain gages at the rotating tool to measure the bending deformation through a half-bridge configuration which required translation to the stationary system. The conversion was obtained based on the angular position of the spindle, measured with an external encoder. The authors proposed an LQG robust controller to enhance the milling capabilities in terms of the maximum metal removal rate, increasing the stability of the cutting process. The results showed that the active device augmented the maximum stable depth of cut for full immersion of an order of magnitude, whilst for lower levels of immersions increments factors between 4 and 5 were obtained. The basic qualities of the piezoelectric actuators are encountered also for this PMN, however, the electrostriction is a quadratic effect, with respect to the linear piezoelectric effect. A different approach with the LQG robust controller based on the H_2 method was employed in [20,23] for a three degree of freedom, rotation around X- and Y-axes and translation along Z-axis, mechatronic module based on piezoelectric stack actuators disposed in a Stewart platform scheme. Each actuator module included a set of flexures and a strain gauge sensor disk to obtain the PEA displacement measurement. Furthermore, the disturbance feedback measurement near the tool tip was obtained with a tri-axial accelerometer positioned on the developed platform. The proposed device actuators were modified to improve the frequency range of the application (100 Hz to 900 Hz) in [50],

where the authors implemented a feedback-feedforward adaptive controller based on the harmonic steady-state concept, reducing the vibration peaks during the experimental campaign of 26.2% (850 Hz) up to 43.7% (3 20Hz); furthermore, the surface roughness was reduced from 0.8 μm in the uncontrolled case up to 0.11 μm with the active device. An alternative robust controller is presented in [14] where the authors employed a μ-synthesis controller for a smart toolholder with two pairs of piezoelectric stack actuators in push-pull configuration and a pair of displacement sensors. The paper presents an LTI model obtained through ZOA and Padé, based on which the robust controller is implemented accounting for the specific milling parameters and the parameters perturbation for both milling and modal model. These considerations allow to modify adaptively the SLD for the given milling condition. In fact, the whole milling process is stabilized accounting for the uncertainty in the system parameters and the peak control sensitivity is constrained. Both, end milling and flank milling experimental tests, were carried out assessing the chatter vibration control capabilities (1,333 Hz and 1,341 Hz), obtaining a root mean square acceleration reduction from 20.1% up to 39.9%. However, due to the higher order the μ-synthesis controller responds slower with respect to the H_∞, an important issue considering the high-frequency behaviour of the vibrations components. To tackle this problem, an H_∞ robust controller is proposed in [51,52] for the chatter mitigation through a set of piezoelectric actuators located at the bearing outer ring on a custom toolholder obtaining a 65.7% reduction of the acceleration RMS. The corresponding almost disturbance decoupling problem with measurement feedback and internal stability (ADDPMS), employs an accelerometer at the front bearing support as feedback sensor considering that tool-tip displacement cannot be measured directly and, hence, the milling process model is not explicitly considered. This robust controller has an advantage on system stabilization, robustness and feasibility as it is model based. Finally, with respect to the standard H_∞ controller, the control parameter is adjusted actively during milling and even severe chatter can be suppressed if the actuator range is wide enough.

In a similar manner, Monnin et al. [53,54] presented a robust controller (H_2) for the developed active structural control spindle unit, which included two pairs of piezoelectric stack actuators working in push-pull configuration, acting on the front bearing, and two orthogonally disposed accelerometers. The authors presented two different control structures based on the aforementioned robust controller, a disturbance rejection and a stabilization scheme. While the robust scheme required a single tuning phase, dependent on the system model but not the machining conditions, the latter was defined for a predefined process characteristic. The global controller increased the lowest experimental critical depth of cut (DOC) by 55% with a maximum stability increase of 73% at 2,300 rpm, however, a reduction in the stability at other speeds as 2,100 rpm and 2,800 rpm were observed. Moreover, the local stabilization scheme showed an augmented stability for the given process conditions up to 91%. In summary, whilst the robust controller reduced the main resonance peak increasing the global SLD, no explicit stability was assured, whilst the stabilization scheme managed to improve the machining conditions for the chosen process. A different approach to model-based control systems

is presented in [55]. The authors proposed an active noise equalizer (ANE) controller with an online Fourier transform scheme to differentiate the chatter frequencies from the displacement harmonic to the spindle rotation frequency. After a filtering phase, the controller coefficient is tuned to attenuate or cancel completely the remaining components based on the actuators' capabilities. The authors employed a set of capacitive sensors and piezoelectric actuators. The experimental campaign presented showed a containment of the 5,000 rpm chatter frequency (1,438 Hz) to about 40%. Even though the accurate results with respect to LMS scheme are presented, there is a cue dependency of the controller from the delay dimension and the accuracy in the frequency recognition, which might even result in the controller failure.

Although these applications obtained promising results in vibration control there still is a differentiation between the devices depending on the vibration of interest, resulting in two sets of mechatronic structures, the methods that aim to control the vibration of the spindle-tool system or the workpiece system. In this scenario, the device presented in [15,47,48] was employed by Li et al. [56] with an MPC scheme based on a wholesome model (ZOA and Padé approximations) that accounted for the spindle-tool-workpiece (STW) system with a resultant material removal rate (MRR) enhancement of 200% and 120% for the two experimental milling campaigns. The proposed method focused on flexible parts milling and the consequent interaction within the STW structure. Two different controllers were implemented by varying the feedback signal: (i) direct displacement measurement from the tool shank; (ii) difference between the direct workpiece displacement point and the tool tip displacement, derived with a Kalman filter from the tool shank measurement. The proposed controllers required the discretization and modelling of the workpiece, as the model used in the MPC varied with the measurement point employed for its derivation. Furthermore, if the cutting process produces a small amount of material removal, then the model for the given point can be kept constant; on the contrary, if it modifies the modal characteristics of the workpiece then the model should be revised through finite element analysis methods.

Along with piezoelectric actuation, promising research has been carried out for what are known as proof-mass or inertial actuators. The main idea is to employ a driven actuator to produce motion into a suspended mass, connected with a set of springs to the actuator, to absorb energy and contain vibrations. The main studies considered small devices which have to be rigorously located near the eigenmodes of the structure and, hence, limit the damping of the resonance point. This approach allows to overcome several issues related to actuators' safety under external disturbances as the given scheme lies parallel to the force path; in other words, the static stiffness of the original structure is maintained, and the actuator does not have to support the cutting forces directly [57]. To the author's knowledge the main applications found in terms of inertial devices for active chatter control in machining processes employ electromagnetic actuation [57–60]; limited by the maximum movable mass, which should not be greater than 10% of the structure, and the maximum displacement should be limited to avoid excessive device dimensions. These systems show accurate results for vibration control in various applications as in [61], where the authors presented an inertial actuator mounted on the

industrial robot in order to contain chatter vibrations in thin-wall machining, increasing the critical limiting depth of cut by a factor of 2.6 with respect to the system in absence of the proof-mass actuator.

1.3 Contributions

Although the literature presents various mechatronic devices for active vibration control in machining, for which significant results have been achieved for particular vibrations such as chatter. Further studies are necessary to improve the industrial appeal of these applications, with particular focus on device compactness, lightness, and high force generation, whilst maintaining reliability. These aspects are considered for the devices evaluated during this thesis work: an active workpiece holder (AWH) and a device for active vibration control (AVC) upon the spindle.

The main contribution for the AWH device is to extend and validate the compact fixture system that controls in real-time three preloaded piezo-actuated modules that act on the vertical axis at different table points, resulting in a 3-DoF (degrees of freedom) structure. This progresses the design developed in [62] by implementing a dynamic regulator to allow disturbance rejection capabilities in thin-plate precise machining with a gain-scheduling approach. The proposed method employs a bumpless PID switching controller to estimate the parameter uncertainty and enable the external disturbance containment in an extended broad-band frequency range.

Differently, the active vibration spindle device proposed in this thesis work is based on the European Patent **EP 3 587 030 A1** with the title: *"Device for Actively Controlling Vibrations in a Machine Tool"*. During this research the novel system concept has been further studied, designed, modelled, controlled, and validated both in simulation and experimentally with two purposed-constructed test benches. Different controllers have been evaluated during the simulation phase: active resonator absorber scheme, cascade controller based on PID schemes, and an industrial appealing system based on a P/PD scheme for which the experimental campaign obtained promising results.

Chapter 2

Active Mechatronic Devices

This chapter presents the mechatronic devices studied. Two different systems are evaluated: an active vibration control system for the spindle – tool holder – tool structure, and an active workpiece holder for both positioning and active vibration control. These devices employ piezoelectric actuators and eddy current sensors, or accelerometers, as feedback source. The functioning principle, features, and limitations are introduced to be accounted for during the model development and system validation.

2.1 Introduction

Nowadays several mechatronic devices have been developed and employed in industry to solve a number of mechanical issues to increase the production's quality and volume. Among these different issues, the vibration and modelling elements are of core importance for any type of machining or device development. Thereafter, this research is based on three main different mechatronic devices-to-be or currently existing in industry.

The first device, a platform to contain vibration disturbances due to machining acting directly on the spindle, was in a conceptual phase design. A prototype of the device was developed, and the corresponding electronics were defined. Furthermore, a test bench was ideated and constructed in order to test such prototype. The controller chosen for this application was a P/PD and the experimental tests were carried out under low-power drivers to evaluate their effect on the final results with respect to the ideal situation in the simulated environment. Moreover, the device modelling was developed in MATLAB environment in order to develop and test a number of control schemes.

The second device corresponds to an actuated workpiece holder (AWH) which was already prototyped, but for whom no dynamical considerations have been carried. Hence, this work aimed to study the benefits in dynamic control for this device when a given machining process was carried out, obtaining promising results in terms of isolation and vibration control. The controller chosen for this approach was an industrial PID.

2.2 Piezo-Actuated Platform for Spindle AVC

This is the main device studied and developed during this thesis. The aim was to obtain a scalable compact device capable of high forces and high reliability for surface finishing improvement based on vibration containment. In fact, differently from the previous device, this platform is positioned on the spindle-tool holder structure and will

have an effect on the tool-tip instead of varying the workpiece position. Such platform is based on the European Patent **EP 3 587 030 A1** with the title: *"Device for Actively Controlling Vibrations in a Machine Tool"*.

Several devices have been developed for this kind of applications with a direct actuator application as in [14,44,48,49,51–54,63] where there is an ongoing research on how to deal with transversal disturbances and heat generation due to the interaction between actuator and rotation element (bearing, spindle, or tool holder). This kind of devices show less appeal in terms of compactness but manage to exert direct forces upon the element of interest. Among the typical sensor applications: positioning sensors, as the eddy current, or accelerometers are the most used. Further developments have been pursued in terms of compactness by modifying the corresponding spindle, with both supports or adaptronic systems [45,46,64].

The final approach is to define external devices or platforms which are easily located upon the spindle without modifying the actual machining centre structure or their corresponding natural behaviours (resonance frequency and modal behaviour) as in [20,23,50,63,65]. This structure represents the device presented in this section. The idea was to deploy a platform device containing an inertial actuator where the actuation is obtained through two orthogonally disposed piezoelectric stack actuators as represented in Figure 2.

(a) **(b)**

Figure 2. Spindle Device: (a) CAD Design, (b) Uncovered Prototype

2.2.1 Working Principle

The core idea is to employ a pair of PEAs (PST 150/10/40 VS15) to create a displacement of a given mass contained by a set of flexures, spring elements, which counteract the PEA force. The final force produced by the system corresponds to the inertial component due to the mass motion. Henceforth, a critical aspect of this platform is the definition of the mass, as it will directly determine the maximum obtainable force.

Furthermore, the piezoelectric actuators should provide enough force to create the required motion and allow the wanted displacement. In fact, the actuated mass and the PEA are rigidly connected in order to avoid issues due to the separation between mass and piezoelectric element for this kind of inertial actuation, as presented in Figure 3. This is one of the reasons why the flexure system was designed, to avoid an over elongation of the piezoelectric actuator.

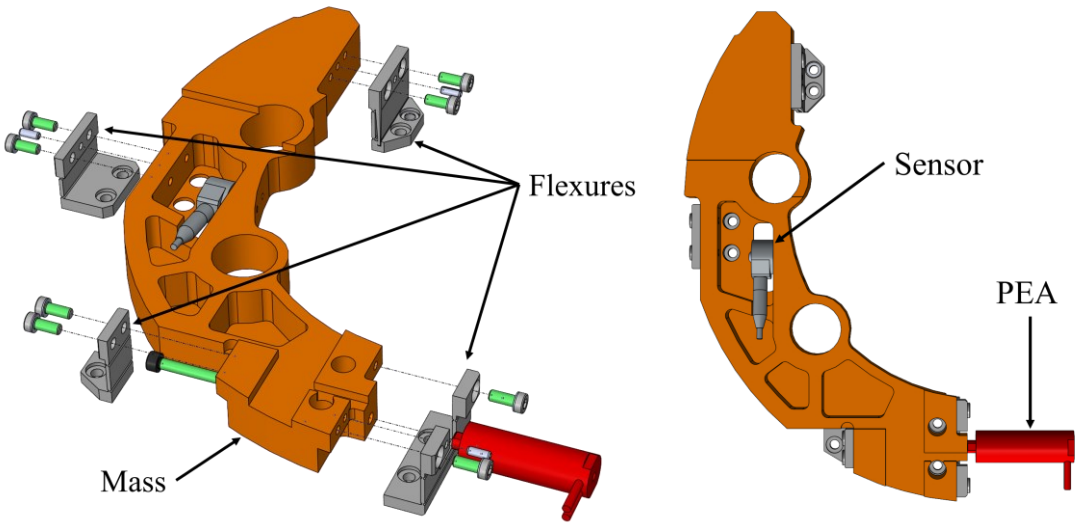

Figure 3. Spindle Device Actuation: (a) Exploded Vision, (b) CAD Design

Based on the application and the controller employed, two different sensors can be used. If the system is employed as an Active Resonator Absorber (ARA), then the internal accelerometer fixed on the moving mass, near its centre of mass, can be used as feedback sensor. This containment scheme is based on the limitation of a given disturbance through an antinode behaviour; in fact, the resonance of the system is modified through the actuator to counteract the external disturbance. Thereafter, the acceleration measurement of the moving mass is sufficient for this application, with the benefit of avoiding the requirement of any external sensors. Differently, traditional controllers as the industrial well-known PID or more sophisticated applications as FxLMS, based on the filter theory, or H_∞, a robust controller, in most of the cases require the usage of additional sensors for the feedback signal to the controller, an acceleration or a displacement measurement.

2.2.2 Features

The application is based on piezoelectric stack actuators which determine the great speed in their displacement variations, nonetheless, require expensive power amplifiers in order to function correctly. However, these actuators are more reliable and create fewer mechanical issues due to the absence of moving parts with respect to traditional electromagnetic actuators. Moreover, the absence of electromagnetic disturbances from these smart actuators are a cue aspect. Despite these improvements, the stack actuators are less stiff and much more fragile under transversal disturbances and motions which is an issue for this kind of mechanical applications and requires further study for direct applications as the mentioned above. In fact, the development of the flexure system allows not only to obtain a spring element to protect the actuator in the axial direction displacement limitation but, also, they provide high stiffness in the transversal direction; reducing the disturbances along such direction upon the PEA.

Furthermore, when the PEA is given a positive voltage in input it will elongate creating a corresponding displacement of the final tip which is used to move the mass. Still, the opposite behaviour functions differently, as in order to return to the initial position the PEA voltage is decreased (or cancelled completely to obtain the initial state) and hence the reactiveness of the actuator is different from the pushing phase. In order to improve the mechanical reactiveness, the flexures behave as linear springs and push backwards the mass aiding the contraction of the PEA.

As stated before, the moving mass is one of the main parameters for the system, considering that the inertial actuation is proportional to it. Depending on the application where the device is employed, the maximum force should be estimated or measured, and the corresponding mass chosen. In Figure 4, the force-frequency curve is depicted for a 1 µm displacement with a varying mass: 1, 2, and 5 kg. Nevertheless, the mass choice should not modify the natural resonance of the machining structure upon which the device is, nor should exceed the maximum force of the PEA actuator.

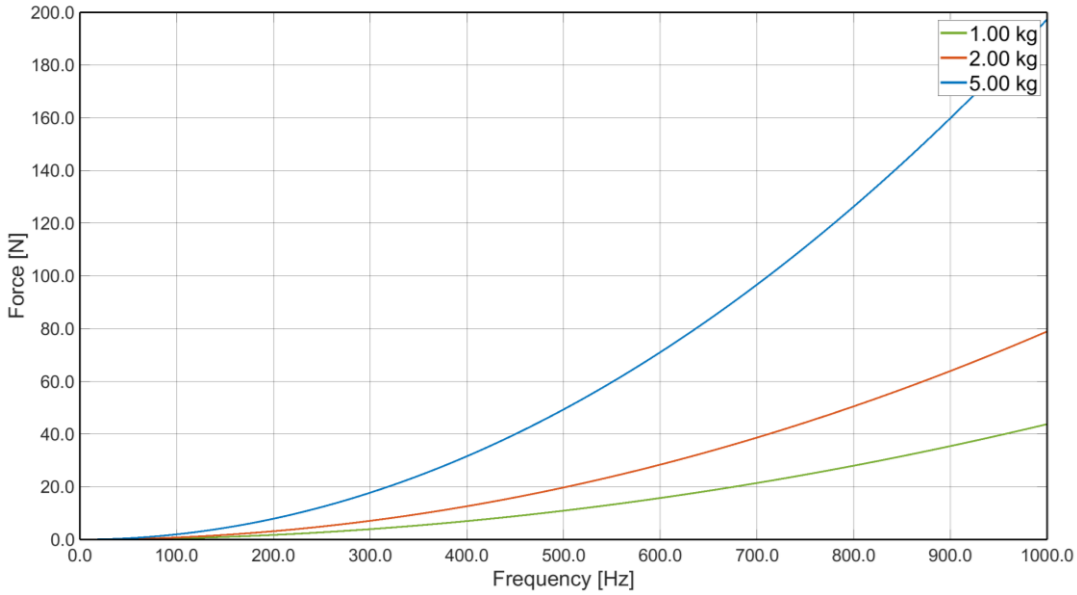

Figure 4. Maximum inertial force for a 1 µm displacement with mass variation.

In order to install this device in a given machine an adapter flange has been developed to match the holes of both the platform and a standard machining structure. This device is presented in Figure 5a along with a CAD representation of its disposition on a machining centre, Figure 5b.

(a) **(b)**

Figure 5. Device Connection to Spindle Housing: (a) Real Flange Adapter, (b) Simulated mounting

2.2.3 Applications and Boundaries

The spindle device is not limited by the dimension of the workpiece and hence can be employed for every type of machining; still, due to the limited force generation with respect to other applications the main aim was to use it for micro-machining. For this type of machining the forces are contained, and the displacement of interest for surface finishing and correct production gains major importance.

The frequency range of interest lies between 80 Hz and 300 Hz, but the interval under study depends on the power electronics combination with the PEAs and the moving mass. Furthermore, there could be a requirement of an external sensor positioned on the spindle depending on the control law chosen. For example, for low-powered applications where the power amplifier does not reach the wanted frequencies, the low-pass filter behaviour limits the applicability of the active resonator absorber reasoning and hence results in an obliged extra sensor. Nonetheless, if this was not the case, the controller allows the complete independency from the machine upon which the device is mounted, consenting this mechatronic device to become an actual plug-in system.

Further applications will aim to deploy the artificial intelligence capabilities of the device based on the acceleration measurements of the platform internal sensors to predict wear or failure events [7]. A different application for such sensors could be their use to develop an observer for the position of the mass which is related to the actual elongation of the piezoelectric actuator and therefore obtain an indirect feedback measurement for hysteresis and over-elongations considerations.

2.3 Piezo-Actuated Workpiece Holder

During machining applications an important aspect is to handle the workpiece displacement variations under the external disturbance while correctly positioning it on the Z-axis. Several devices have been introduced in literature to handle this kind of issue [24,41,66–70], nevertheless, the challenge is still to obtain an industrial appeal for such compact fixture systems. The idea of the AWH device derives from the Stewart platform [71–74], but instead of six degrees of freedom it only has three (rotations around X- and Y-axes and translation along Z), actuated with a set of piezoelectric modules. The

resulting scheme can be studied as an actuation block between two plates, the fixed bottom base and the moving platform, as observed in Figure 6.

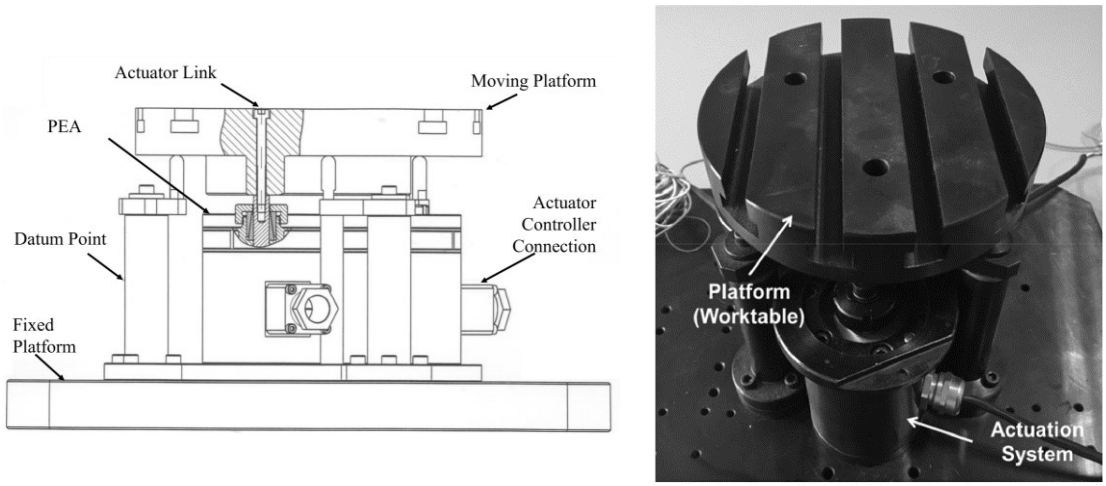

(a) **(b)**

Figure 6. AWH Device: (a) Parts Definition, (b) Prototype

This system is capable of high forces generation by employing piezoelectric stack actuators, nonetheless, it suffers from an important amount of coupling due to the mechanical connection to the workpiece plate with the three actuators.

2.3.1 Working Principle

The working principle is based on the simultaneous activation of three piezoelectric stack actuators (PST 1000/25/40 VS35) positioned parallel to the Z-axis, fixed rigidly to the moving platform, and at equal angular distance from each other ($\pi/3 = 120°$) upon a circumference with a 54 mm radius, as depicted in Figure 7. Each PEA has a maximum stroke capability of 40 µm, an axial stiffness of 450 N/µm, and a blocking force of 25 kN.

Each actuator has an independent Eddy positioning sensor with a 0-10 kHz bandwidth. This distribution allows to conceptually structure the Multiple-Input-Multiple-Output (MIMO) system as 3 Single-Input-Single-Output (SISO) with internal disturbances due to the coupling effect between the lines.

In order to produce a vertical displacement, or keep the moving platform still without any orientation, the three actuators must be powered with equal voltages as presented in Figure 7a. Furthermore, to create a rotation around the X-axis, at least one between the A or B actuators should be powered, as shown in Figure 7b. Finally, in order to obtain a rotation around the Y-axis, actuators A and B should be moved in the same sense, whilst actuator C should be actuated accordingly. Otherwise, actuator C could be actuated alone, as presented in Figure 7c.

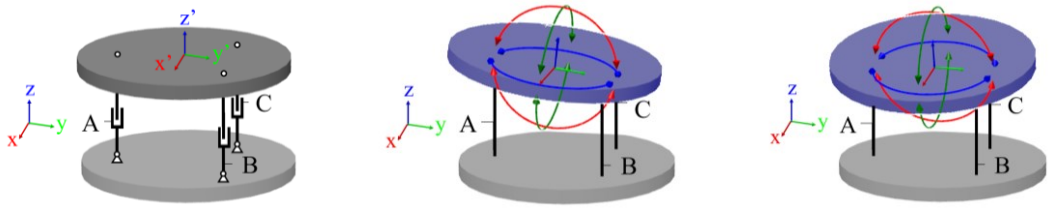

Figure 7. AWH: (a) Z-axis Vertical Actuation, (b) Rotation Around X-axis, (c) Rotation Around Y-Axis.

A PID controller with back-calculation and bumpless switching is defined in order to handle two main different situations: a set-point following phase where the machining centre is not yet activated and, hence, no external disturbance due to the machining process is present; and a disturbance rejection phase where the system has positioned the workpiece in the wanted configuration and is ready to start the machining process. Extra consideration to the coupling effect was carried out, nonetheless, there was no requirements of decoupling schemes as the internal disturbances were contained within a reduced displacement interval with respect to the external disturbances.

2.3.2 Features

The AWH device benefits from the use of PEAs, considering their great force capabilities along with their high-precision displacements, and its stiffness behaviour under the passive configuration. Despite such considerations, the PEA has a limited stroke with respect to other electric actuation schemes. In addition to this issue, the chosen PEA can exert forces over 20 kN but requires expensive electronics to be actuated with optimal performance.

Furthermore, by varying the circumference radius upon which the actuators are positioned, the system shows high scalability, nevertheless, there is a limitation due to the small angles approximation employed for the control development and modelling phase for the minimum radius. In fact, the system presented in Figure 6b is at its minimum disposition.

Moreover, the individual positioning sensors permit to consider the MIMO system as three SISO systems, with a certain amount of coupling internal disturbances. These ease the controller synthesis phase and improves the final results. Finally, it allows to handle the known nonlinearities of the actuators, hysteresis and creep among others, as their displacements are obtained directly.

2.3.3 Applications and Boundaries

The AWH device can be used for several types of machining, as milling and grinding operations, and it has been especially developed for thin-wall applications. However, the moving platform dimension determines the maximum workpiece size, resulting in a clear limitation of this system application. Nevertheless, due to the high-force capabilities of the actuator the system can handle a number of disturbances in a broadband frequency with various amplitudes.

Even though the maximum displacement is limited by the nature of the employed actuators, the resulting workspace capabilities of the system are: Z-axis translation of ±20 μm, rotation around X-axis of ±427.67 μrad, and rotation around Y-axis of ±493.83 μrad.

Further developments are required to measure and handle the vibrations arriving from the table structure upon which the fixed base of the mechanism is positioned. In fact, in order to allow for both active vibration control and external vibration isolation, the system should be able to obtain the relative displacement of the moving platform with respect to the pavement, but an extra sensor would be required. Nonetheless, the main source of disturbance for the frequency range of interest (100 Hz – 1,000 Hz) arises from the machining mechanism, and not from external sources.

Chapter 3

Mechatronic System Modelling

This chapter presents the modelling schemes for each device. Considering the importance of the piezoelectric actuators, which are employed as force sources for both devices, an initial part is included of their linear and non-linear description, with a particular focus on complete stage and hysteresis modelling. Finally, the presented stage nonlinear models are deployed for the spindle device and the active workpiece holder with the derivation of the electromechanical model and design approach.

3.1 Piezoelectric Stages Modelling

Both devices studied in this thesis work were develop based on the piezoelectric stack actuator, hence, an introduction to the, linear and nonlinear, modelling and considerations for such elements is of great importance to comprehend the complete device functioning.

These actuators are sources of great force with small displacements and lack of moving parts, which is an important characteristic. In the following section the linear model of the piezoelectric actuator will be introduced to obtain the equation that links the input voltage to the force produced. Nevertheless, the PEA deformation is necessary in order to evaluate the maximum displacement capabilities. Furthermore, this type of actuators can be modelled as an actuated spring, whose deformation/stiffness is dependent on the input voltage. Hence, the applicable force of the actuator depends directly on its deformation.

Finally, in the electrical environment due to the piezoelectric selection to improve the actuator properties, the hysteresis phenomenon is observed between the voltage and the corresponding current. In fact, voltage-driven actuators will present this nonlinearity whilst charge-driven systems will, up to a certain extent, lack of it. Moreover, no hysteresis is exhibited when the leads are open, and hence no current is present, verifying the assumption that hysteresis in piezoelectric actuators is produced in the voltage-charge connection (input voltage to resulting charge) [75–77] .Nonetheless, the voltage amplifiers are the most common power source for piezo actuation and, therefore, the following modelling and equation will consider this as chosen power supply system.

3.1.1 Linear Model

Despite being non-linear by nature, whenever the input voltage or mechanical disturbance are contained the behaviour of the PEA can be approximated by the constitutive equations in the IEEE piezoelectric standard [78]. This linear assumption is

limited by the predefined electromechanical requirements, nevertheless, it is still employed in control synthesis and device validation in the literature [13,20,23,79–81]. In fact, if the piezoelectric displacement is directly measured the nonlinearities can be considered as disturbances and hence, these equations can be used.

As presented before, the PEAs are considered smart actuators due to their electromechanical characteristics: when a piezoelectric actuator is mechanically strained an electric charge is produced, and this is known as direct effect. Conversely, the inverse effect is when an electrical charge is applied the system generates a deformation. Therefore, the strain and stress of the piezoelectric material is related to the corresponding electric charge of the system, and this can be described by the following constitutive equations [78]:

$$\begin{aligned} S_i &= d_{ki}E_k + s_{ij}^{E}T_j \\ D_m &= \epsilon_{mk}^{T}E_k + d_{ki}T_j \end{aligned} \quad \textbf{1}$$

where S is the mechanical strain, D is the electric displacement, E is the electric field, T is the mechanical stress, d is the piezoelectric constant, s^E is the elastic compliance at constant field E, and ϵ^T corresponds to the permittivity at constant stress T. Furthermore, the subindexes i,j = 1:6, and m,k = 1:3 refer to different directions within the Cartesian coordinate system with respect to the polarization direction (poling direction), as depicted in Figure 8.

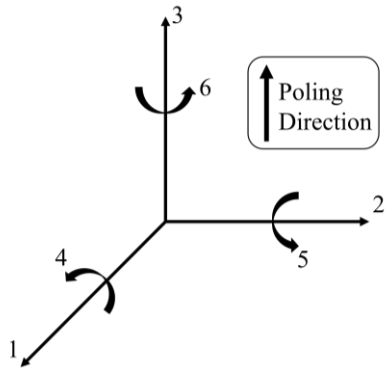

Figure 8. Cartesian coordinate system for PEA.

Considering the PEAs employed in this study, stack actuators, a further simplification can be executed. Typically, this kind of actuators are assumed to have a single execution direction, which corresponds to the poling direction. Thereafter, Equation 1 is approximated considering the poling direction 3, obtaining the following:

$$\begin{aligned} S_3 &= d_{33}E_3 + s_{33}^{E}T_3 \\ D_3 &= \epsilon_{33}^{T}E_3 + d_{33}T_3 \end{aligned} \quad \textbf{2}$$

Assuming each layer has a thickness h, a cross-sectional area A, and the electrical potential between the two faces of each layer is dV, the following equations are obtained:

$$S_3 = \frac{\Delta h}{h}, E_3 = \frac{dV}{h}, T_3 = -\frac{F}{A} \quad \textbf{3}$$

Furthermore, the displacement of each layer, Δh, can be formulated in terms of voltage and force as:

$$\Delta h = -\frac{h\, s_{33}^E\, F}{A} + d_{33} dV \quad \textbf{4}$$

Regarding a PEA with n layers, the resulting final displacement, ΔL, can be computed as:

$$\Delta L = n\Delta h = -\frac{(n\, h) s_{33}^E F}{A} + d_{33}(n\, dV) = -\frac{F}{K_m} + d_{33} V \quad \textbf{5}$$

Hence, the piezoelectric actuator can be studied as a spring whose elongation is determined by the input voltage and the corresponding force. Its stiffness is determined with two components, a mechanical one denoted as K_m and obtained as $\frac{\boldsymbol{A}}{(\boldsymbol{n}\cdot\boldsymbol{h})\cdot \boldsymbol{s_{33}^E}}$, and an electrical one (d_{33}). In fact, in order to obtain the voltage-force function, Equation 5 is rewritten as:

$$F_{PEA} = -K_m \Delta L + K_m d_{33} V \quad \textbf{6}$$

Finally, the PEA charge (Q_{PEA}) can be obtained in a similar manner based on its capacitance value (C_{PEA}) as:

$$Q_{PEA} = -d_{33} F_{PEA} + C_{PEA} V \quad \textbf{7}$$

However, this set of equations fail to model the complete behaviour of piezoelectric actuators neglecting important factors; except when they are considered as external disturbances and the PEA elongation is measured directly.

3.1.2 Nonlinear Model

PEAs modelling can be further improved when nonlinearities, like creep and hysteresis, are taken into account and their compensation are still a core research topic in piezo-actuated stages and positioning.

The creep is a phenomenon that cause a drift behaviour of the output under a constant input. It is a low-frequency property that can result in loss during long-periods precision positioning. The nature of such characteristic is related to a slow realignment of the poles of the piezoelectric material when subject to a constant input voltage.

The nonlinear model typically employed to simulate this behaviour is called the logarithmic model and is expressed as:

$$y(t) = y_0[1 + \gamma \log_{10}\left(\frac{t}{t_0}\right)] \quad \textbf{8}$$

where $y(t)$ is the PEA displacement; t_0 is the time stamp at which the creep is observable; y_0 is the displacement at time t_0; and γ is a rate coefficient. These values are obtained with experimental data.

However, this low-frequency component is easily contained through closed-loop controllers as, for example, with an integrator. Furthermore, when the interest of the application relies on high-frequency signals then the creep influence can be neglected without further consideration.

Conversely, the hysteresis phenomenon observable in the piezoelectric actuators when voltage-steered is not related to a specific frequency interval. In fact, this characteristic is frequency dependent, meaning that as the driving frequency is increased the hysteresis effect changes. Another important aspect is its amplitude-dependent behaviour, as the resulting curve will vary depending on the input voltage. Finally, the hysteresis current output state exhibits a nonlocal memory behaviour, as it depends also on the previous states [82].

Modelling this nonlinear characteristic has been a core topic in research, and a number of research items can be found in the literature for this application. Nonetheless, it is important to consider the interaction between the previously mentioned nonlinearities; despite the reduction due to the increment in frequency, the creep characteristic does not disappear completely, hence, both behaviours are not mutually exclusive. Indeed, the estimation of one characteristic will be influenced, up to a certain extent, by the other and this needs consideration when the experimental data is obtained [83–85] along with residual displacement, created by remanent polarization [86].

There is no standard modelling for the actuator hysteresis, depending on the application two main groups are depicted: physics-based models and phenomenological models. While physics-based models aim to comprehend the hysteresis with complex material-specific estimations, which limits their application; the phenomenological models' goal is to reproduce a similar output characteristic of the real system with simpler expressions, without providing an explanation of the actual phenomenon. The latter has more appeal in terms of controller synthesis and simulation. Furthermore, these models can be once more divided into two different groups depending on the nature of their hysteretic estimation in: operator-based models, and differential-based models.

The operator-based models such as the Maxwell slip model [87–92], the Preisach model [93–99], and the Prandtle-Ishlinskii model [100–110] employ elementary operators based on mechanical elements or mathematical integrations to characterize the hysteresis. These types of models are rate-independent (in their classical applications), lacking any frequency dependency in their definition of the relation between input voltage and resulting displacement. Furthermore, inverse feedforward controllers are

difficult to implement for these models due to their operator-based nature. Conversely, differential-based models, such as the Bouc-Wen model [94,111–115] and the Backlash-like model [84], use nonlinear differential equations, typically first-order, to describe the hysteresis behaviour [116], easing the controller development**.** Based on these considerations, the Bouc-Wen model is selected to model the hysteresis phenomenon for the studied applications. Nevertheless, certain modifications are required to obtain a better approximation to the real behaviour as will be presented afterwards.

Bouc-Wen Model:

The Bouc-Wen (BW) model, based on the Duhem model [117,118] that was first ideated and applied for hysteresis modelling in ferromagnetic materials, has been sorely studied and applied in literature due to its simple form, reduced number of parameters, and the simpler approach for the derivation of a feedforward compensator with an inverse model [94,112,113,119–122]. The generalized BW model is a semi-physical approach formulated as:

$$\begin{aligned} v(t) &= k_1 v_{in}(t) + h(t) \\ \dot{h}(t) &= \alpha \dot{v}_{in}(t) - \beta |\dot{v}_{in}(t)||h(t)|^{n-1} h(t) - \gamma \dot{v}_{in}(t)|h(t)|^n \end{aligned} \quad \textbf{9}$$

where v is the total voltage; k_1 is a constant weight parameter to link the input voltage to the total one; v_{in} is the input voltage to the actuator; h is the hysteresis component of the real voltage; α defines the hysteresis amplitude; β and γ define the shape of the hysteresis loop; and n , approximated to 1 due to the actuator flexibility [113,120,121], controls the smoothness of the transition from elastic to plastic region, analogous to the mechanical application.

Despite the previously mentioned advantages, the generalized BW model shows a symmetrical behaviour, producing a hysteresis component which is stable around the centre point of the displacement/voltage curve. This behaviour is not representative of the real applications, as PEAs powered with higher input voltages have higher force capabilities and thus increase their resistance to deformation to the low-voltage input, resulting in a higher component in this point with respect to the previous one. Furthermore, the independent behaviour of the BW model concerning the frequency variation (rate-independent) produces an increment in the modelling error. In fact, while the input voltage amplitude variation creates different hysteresis loops, the model shows no influence from the input frequency, which is observed in real applications with PEAs.

Thus, further studies have been carried out to approach these issues considering the introduction of an asymmetrical component derived from the sign of the hysteretic voltage component [116,123,124], Equation 10, and a frequency influenced factor or rate-dependency component [125,126], Equation 11:

$$\begin{aligned} \dot{h}(t) = \alpha \dot{v}_{in}(t) - \beta \dot{v}_{in}(t)|h(t)|^n - \gamma |\dot{v}_{in}(t)||h(t)|^{n-1} h(t) \\ + \delta v_{in}(t) sign(\dot{v}_{in}) \end{aligned} \quad \textbf{10}$$

$$v(t) = \frac{k_1}{\tau} e^{-t/\tau} v_{in}(t) + h(t) \quad \textbf{11}$$

where τ is the frequency factor; and δ is the asymmetrical coefficient. Another approach considered in literature to solve the rate-dependency issue is to update in real-time the Bouc-Wen parameters with a recursive least-square online identification method [127].

The limited number of parameters present in this model formulation is an advantage as it facilitates the corresponding modelling while simplifying the corresponding simulation and feedforward cancellations. However, it is sometimes considered a limitation for the corresponding modelling capabilities along with a criticism for the first-order differential equation employed [128]. The derivation of such parameters is carried out in numerous ways among which, particularly interesting applications have been carried out by employing optimization algorithms to identify the corresponding values [124,129–133].

3.1.3 Electromechanical Model

Up to this point the PEA liner model has been presented with the obvious limitations due to the neglected inherent nonlinearities present in piezoelectric actuators: creep, hysteresis, and voltage saturation. This limitation, despite obtaining accurate approximations with closed-loop schemes is indeed a constraint for the real simulation and control synthesis. In fact, if not modelled and taken into consideration, the controller will be required to be more robust to handle the higher uncertainties of the linear model. Thereby, the corresponding modelling schemes for the nonlinearities have been introduced separately, with their advantages and disadvantages. Nonetheless, until now, no complete electromechanical model has been formulated. In this scenario, the initial approaches presented a scheme as depicted in Figure 9, where there is a double input representation due to the smart electromechanical characteristics of the piezoelectric actuators that relate the mechanical stress/strain with the electrical units [75–77]. Therefore, a variable is introduced called the *transformer ratio* (T_{em}) to relate the electrical and the mechanical models, the piezo effect.

The electromechanical model has two ports, a voltage/current port in the electrical domain, and a force/velocity in the mechanical domain. Regarding the actuator, the model is then represented with an electrical port driven in voltage source and a mechanical port with a force source representing the external mechanical load. The mechanical approximation to a lumped mass and linear stiffness and damping is an assumption obtained based on the frequency range of interaction, which is within the first resonance (typically in the order of kHz) [77].

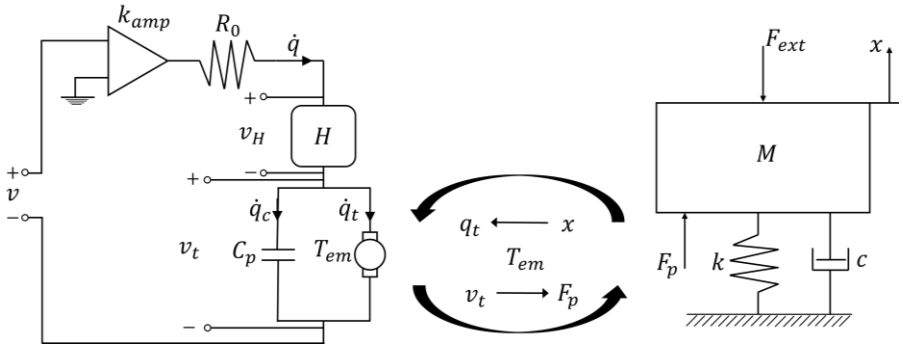

Figure 9. Electromechanical Scheme Representation for a PEA Stage.

Further developments implemented the k_{amp} and R_0 variables. The first corresponds to the power amplifier's voltage gain, whereas the latter represents an internal equivalent resistance. When this resistance is set to 0, hence neglected, the previous modelling scheme is obtained, nonetheless, the presence of this variable allows to express the electrical part as a differential equation of the charge q [82,84]. The electrical system, left part in Figure 9,can be represented by the following constitutive equations [76,77,84]:

$$v(t) \cdot k_{amp} = v_H(t) + v_t(t) + R_0 \cdot \dot{q}(t) \quad \textbf{12}$$

$$v_H(t) = H(q(t)) \quad \textbf{13}$$

$$q(t) = q_c(t) + q_t(t) \quad \textbf{14}$$

$$q_c(t) = C_p \cdot v_t(t) \quad \textbf{15}$$

$$q_t(t) = T_{em} \cdot x(t) \quad \textbf{16}$$

where $v(t)$ is the input voltage to the piezo power amplifier; $v_H(t)$ is the voltage generated by the hysteresis component; $q(t)$ is the total charge in the PEA; C_p is the piezoelectric capacitance and $q_c(t)$ is the corresponding charge stored in it; $q_t(t)$ is the charge generated by the interaction between the electrical and mechanical domain and $v_t(t)$ is the related voltage; $H(q(t))$ is the hysteresis model which can be any of the aforementioned schemes; finally, $x(t)$ corresponds to the PEA displacement.

By substituting Equations 15 and 16 in Equation 14 and solving for $v_t(t)$ the following equation is obtained:

$$v_t(t) = \frac{q(t) - T_{em} \cdot x(t)}{C_p} \quad \textbf{17}$$

The final constitutive equation is therefore obtained substituting Equation 17 and 13 in Equation 12 and rewriting the system with respect to the charge $q(t)$:

$$R_0 C_p \cdot \dot{q}(t) + q(t) - T_{em} \cdot x(t) = C_p \cdot \left[v(t) \cdot k_{amp} - H(q(t))\right] \quad \textbf{18}$$

Through the transformer ratio the electrical domain interacts with the mechanical one. The aim is to model the piezo stage completely, and hence, the corresponding

mechanical variables will be defined by both the PEA and the structure/platform within which is placed. In this scenario, the PEA will be seen as a force generator driven by the input voltage while its spring and damping behaviour will be coupled with the real mechanical system, related through the T_{em} variable. Therefore, the mechanical domain can be formulated as follows:

$$F_p(t) = T_{em} \cdot v_t(t) \quad \textbf{19}$$

$$M \cdot \ddot{x}(t) + c \cdot \dot{x}(t) + k \cdot x(t) = F_p(t) - F_{ext}(t) \quad \textbf{20}$$

where $F_p(t)$ is the force generated by the PEA; $F_{ext}(t)$ is the external/disturbance force; M, c, k are the mass, damping coefficient, and stiffness of the mechanical system; finally, $\ddot{x}(t), \dot{x}(t), x(t)$ are the acceleration, speed, and displacement of the PEA, respectively. Substituting Equation 17 in Equation 19 the formulation can be rewritten as:

$$F_p(t) = \frac{T_{em}}{C_p} \cdot q(t) - \frac{{T_{em}}^2}{C_p} \cdot x(t) \quad \textbf{21}$$

$$M \cdot \ddot{x}(t) + c \cdot \dot{x}(t) + \left(k + \frac{{T_{em}}^2}{C_p}\right) \cdot x(t) = \frac{T_{em}}{C_p} \cdot q(t) - F_{ext}(t) \quad \textbf{22}$$

The electromechanical formulation is therefore obtained in a system of equations formed by Equations 18 and 22:

$$R_0 C_p \cdot \dot{q}(t) + q(t) - T_{em} \cdot x(t) = C_p \cdot \left[v(t) \cdot k_{amp} - H(q(t))\right] \quad \textbf{23}$$

$$M \cdot \ddot{x}(t) + c \cdot \dot{x}(t) + k_{eq} \cdot x(t) = \frac{T_{em}}{C_p} \cdot q(t) - F_{ext}(t) \quad \textbf{24}$$

where $k_{eq} = \left(k + \frac{{T_{em}}^2}{C_p}\right)$ is the equivalent mechanical and electrical stiffness. When the system is voltage driven then the corresponding charge will not be directly defined, hence it will be a function of the input voltage. In fact, a usual approach is to consider the $\left[v(t) \cdot k_{amp} - H(q(t))\right]$ block as a new hysteretic system whose output *w* is the actual voltage arriving to the actuator. This reasoning permits to obtain a linear system between $w(t)$ and the final displacement $x(t)$ as the hysteresis is present in a previous step.

Moreover, it is observed that when the PEA is charge driven then the corresponding hysteresis effect is missing in Equation 24. Furthermore, when $R_0 = 0$, as stated before, the system is simplified into a single equation by employing the charge formula obtained from Equation 23 in Equation 24:

$$M \cdot \ddot{x}(t) + c \cdot \dot{x}(t) + k \cdot x(t) = T_{em}\left[v(t) \cdot k_{amp} - H(q(t))\right] - F_{ext}(t) \quad \textbf{25}$$

3.2 Spindle Device Modelling

A special structure based constrained into an adaptable platform for the spindle was presented, where a piezoelectric stack actuator is employed to create a given motion upon a mass supported by spring elements called flexures that were developed in order to allow the piezo axial displacement while containing the orthogonal disturbances upon the PEA to avoid damage. The elementary component corresponds to an inertial actuator as depicted in Figure 10a, whose force arises from the inertial component of the moving mass (M_a), Figure 10b. This kind of devices is known as active resonators absorbers (ARA), and the standard control design aims to employ the actuation element to modify the resonance frequency of the *absorber* in order to counteract the disturbance arising from the *primary* structure. By implementing two orthogonally disposed elementary actuation systems, the vibrations arriving from the primary system within the X-Y plane can be controlled.

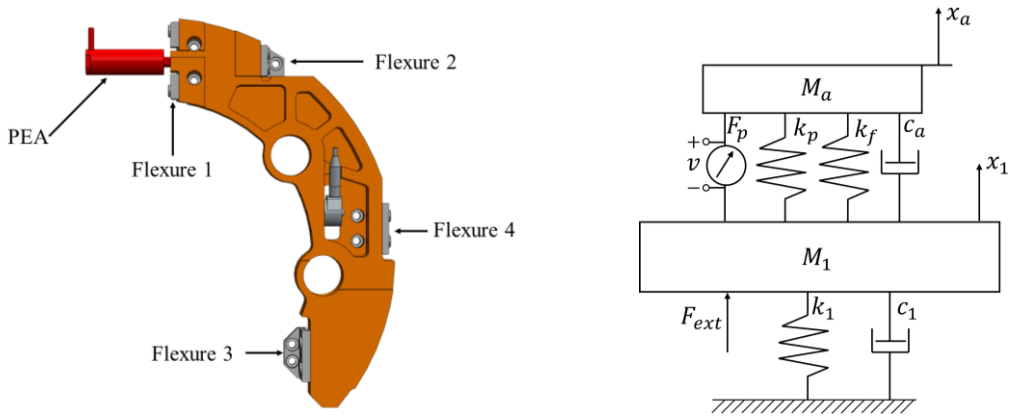

(a) **(b)**

Figure 10. Device: (a) CAD design; (b) 1-D actuation principle

The set of flexures can be modelled as a single spring, if necessary, also a coupling spring can be depicted. Hence, considering the linear approach for piezoelectric actuators to ease the formulation in the initial steps, the system component presented in Figure 10b can be expressed with the following set of equations, for a single axis:

$$M_a\,\ddot{x}_a(t) + c_a\,(\dot{x}_a(t) - \dot{x}_1(t)) + (k_p + k_f)(x_a(t) - x_1(t)) = F_p(t) \quad (26)$$

$$M_1\ddot{x}_1(t) + (c_a + c_1)\,\dot{x}_1(t) + (k_p + k_f + k_1)x_1(t) + F_p(t) = F_{ext}(t) + c_a\dot{x}_a(t) + (k_p + k_f)x_a(t) \quad (27)$$

where M_a is the absorber mass which corresponds to the sum of the inertial mass and the piezoelectric mass, the latter can be neglected being much smaller than the actuated mass; c_a is the absorber damping obtained experimentally; k_p is the PEA stiffness, this value will vary when the electromechanical model is considered by $\frac{T_{em}{}^2}{C_p}$; k_f is the flexures axial stiffness; M_1, c_1, k_1 are the mass, damping coefficient, and stiffness of the primary system under disturbance, respectively; x_a is the absorber position; x_1 is the primary system position; F_p is the PEA actuated force; and F_{ext} is the external force disturbance.

Furthermore, the difference between the primary system displacement and the absorber displacement, neglecting the possibility of detachment, corresponds to the elongation of the PEA actuator (x_{PEA}), hence the previous set of equations can be rewritten considering that:

$$x_{PEA}(t) = x_a(t) - x_1(t) \quad \textbf{28}$$

$$\ddot{x}_a(t) = \ddot{x}_1(t) + \ddot{x}_{PEA}(t) \quad \textbf{29}$$

The flexure stiffnesses are studied with a FEM test, considering the displacement at the centre of mass of the moving mass. Under an external load at the piezoelectric connection with the mass, the resulting system deformations are presented in Figure 11. Particularly, Figure 11a presents the deformation along the PEA axis, whereas Figure 11b shows the displacement with a force exerted in the orthogonal direction. The initial case presents higher displacements, as expected, with respect to the latter; this validates the flexures capabilities to decouple the orthogonal disturbances upon the piezoelectric actuator, increasing their lifespan. From the numerical computation, the mean deformation of the system under a constant force is over 10 µm for the axial load whilst the displacement is reduced up to less than 0.1 µm for the orthogonal load, with the same force amplitude.

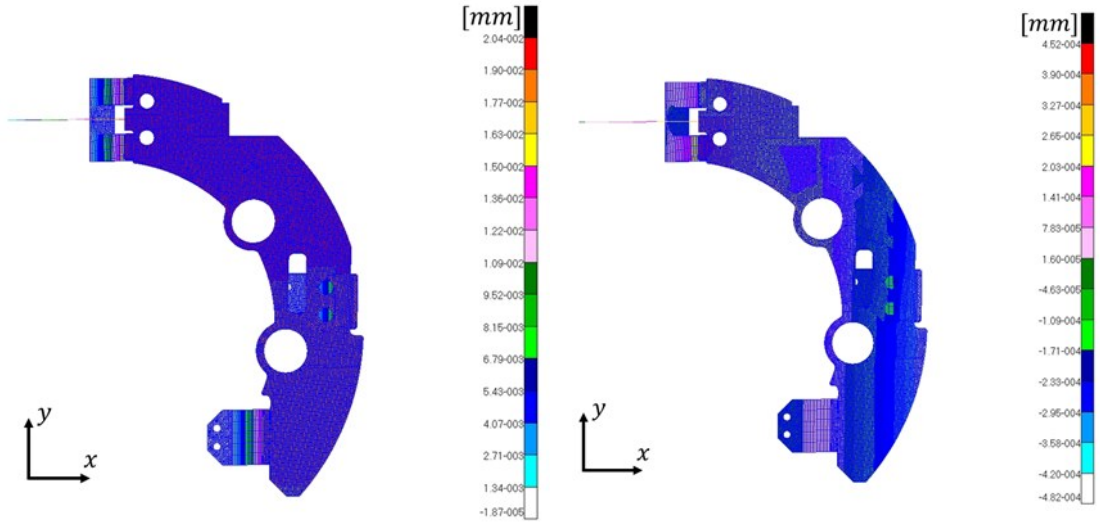

(a) **(b)**

Figure 11. FEM studies on a single axis for flexure design and evaluation:
(a) force along X-axis (parallel to PEA), (b) force along Y-axis (orthogonal to PEA).

The flexures were designed based on a two-step shape optimization. Initially, a topology optimization is carried out by employing an initial full-material flexure CAD design upon which the areas that require material reduction are depicted, as in Figure 12a. The optimization removes material by the FEM nodes, following a multi-objective task that evaluates the axial displacement, transversal displacement, and maximum load capabilities. This step produces an optimized flexure design, nonetheless, it does not produce a manufacturable piece, hence, a further shape optimization step is required.

The topology optimized flexure is therefore employed as final goal for a shape optimization based on certain free-of-choice parameters; in this scenario 5 parameters were defined, as depicted in Figure 12b, and employed to find the best flexure design in terms of construction feasibility and similarity to the topology's optimal.

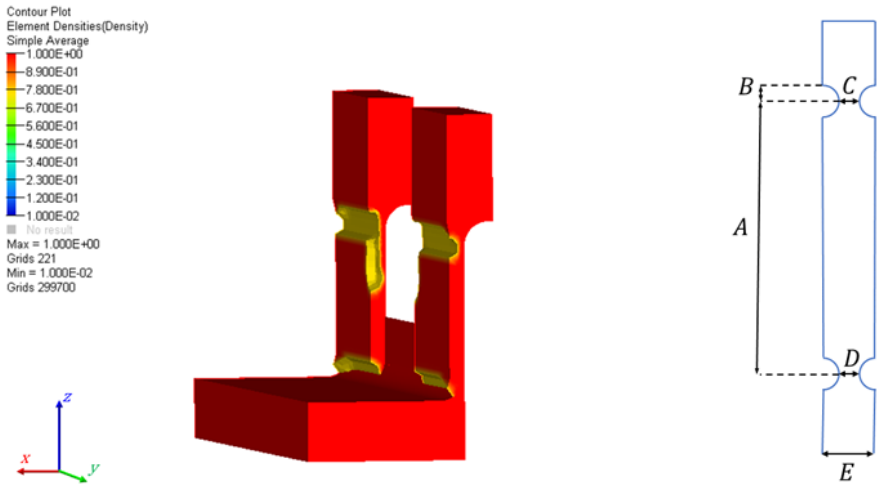

(a) **(b)**

Figure 12. Flexures design and optimization: (a) flexure 1 3-D topology optimization result, (b) parameters definiton for shape optimization.

The two-step optimization produces then the 4 flexures designs, the final parameters, presented in Table 1, are employed to manufacture these elements. The flexures are identified by a number as presented in Figure 10a, and the difference in their dimension is due to the relative location with respect to the moving mass and the PEA.

Table 1. Final flexure optimized design parameters.

Flexure	A [mm]	B [mm]	C [mm]	D [mm]	E [mm]
1	12.20	0.50	0.50	0.50	1.50
2	12.20	0.50	0.50	0.50	1.50
3	13.30	0.55	0.40	0.40	1.50
4	9.00	0.55	0.40	0.40	1.50

Regarding the moving mass design, the limitations are the maximum weight, to avoid any natural behaviour modifications of the machining structure, and the dimension limitation of the available space inside the platform. These conditions, however, must account for the request to obtain the maximum exerting force, which means, to maximize the moving mass weight. The resulting mass weights 1.109 kg, and considering the stiffness of the flexures, the maximum obtainable displacement is of 30.2 µm which corresponds to a maximum force at the minimum frequency (80 Hz) of ~4.4 N and at the maximum frequency (300 Hz) of ~61.5 N. The frequency-force diagram of the resulting system is depicted in Figure 13.

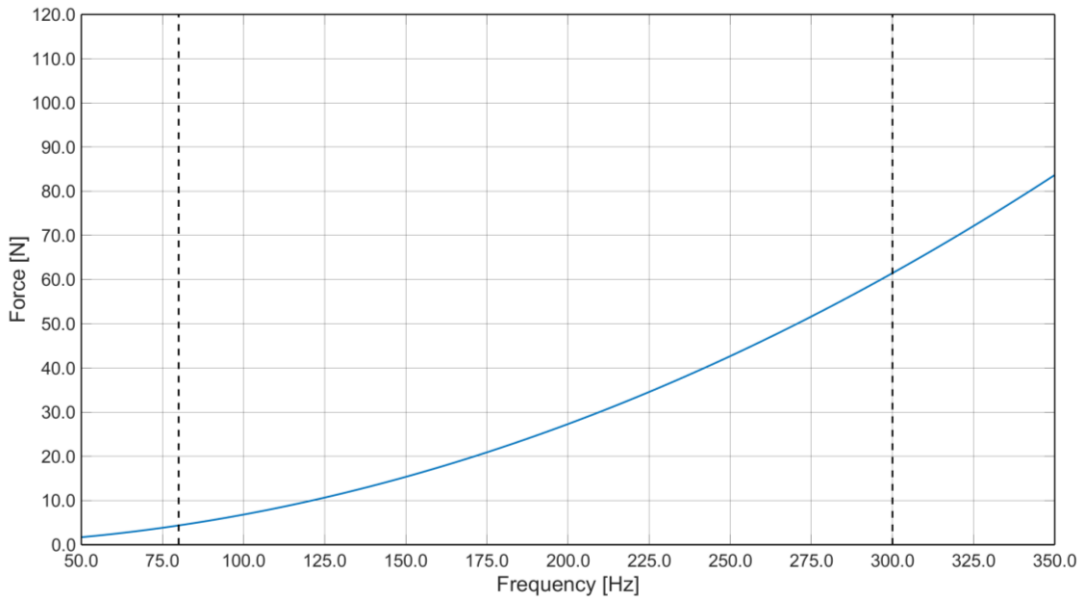

Figure 13. Maximum force by the inertial actuator.

3.3 Active Workpiece Holder Modelling

The AWH motion is generated with the three vertical PEAs connected to the moving platform and to fixed platform, as depicted in Figure 14. The connection is achieved through three axial rods with a set of flexural hinges designed to decouple the transversal motion and shear forces to avoid any damage to the actuator. The AWH mechanical device has three degrees of freedom and is capable of vertical translation (Z-axis), rotation around X-axis (ϑ_x), and rotation around Y-axis (ϑ_y).

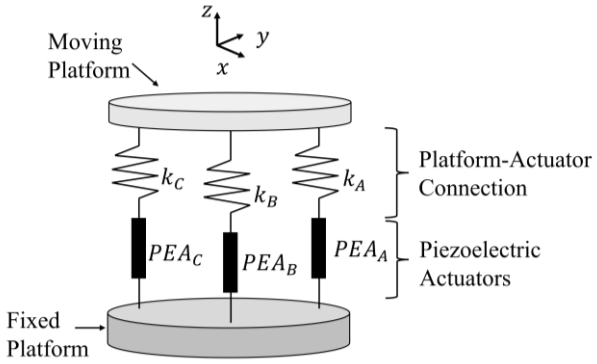

Figure 14. AWH mechanical scheme representation.

The platform description requires the definition of two different coordinate frames, a local one upon the centre of the moving platform (XYZ) and a fixed global reference system on the base ($X_1Y_1Z_1$). Both coordinate frames are aligned upon their centre along the Z-axis and are equally oriented when the moving platform is kept at its initial position, as depicted in Figure 15a.

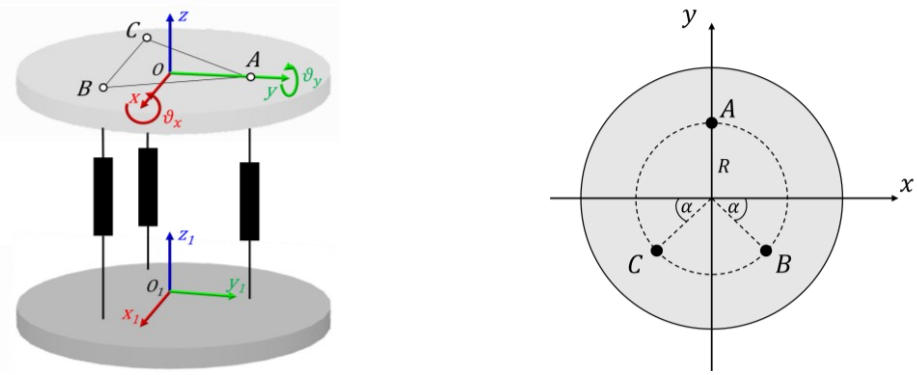

(a) **(b)**

Figure 15. AWH reference system: (a) 3-D representation; (b) actuator disposition.

The three actuators (A, B, C) are distributed at equal angular distance from each other along a circumference of radius R with centre O coincident with the origin of the moving frame (XYZ), as can be seen in Figure 15b. Moreover, PEA_A is positioned along the Y-axis and consequently will not influence the platform's rotation around it.

Two main approximations have been employed to model this structure. First, the hypothesis of small angular motion ($sin(\vartheta) \approx \vartheta$) which has an inherent translation on the vertical deformation of the axial rod. In fact, the table rotation is contained and hence the actuator motion through the rod is estimated to be along the Z-axis, neglecting any deformation. Indeed, with a maximum actuators' displacement of 40 µm, and considering a rotation around the Y-axis, the maximum angle motion of the table is obtained when PEA_B and PEA_C are driven in opposite directions. Based on Figure 15b, B and C are equally distanced from the Y-axis, $d = R \cdot cos(\alpha) = 46.76$ mm. With a 20 µm vertical displacement of point C (and -20 µm for point B) the rotation angle around the Y-axis is obtained, $sin(\varphi) = 20\ \mu m / 46.76\ mm \approx 4.28x10^{-4} \approx \varphi$. This approximation allows to obtain the transformation matrix T between the platform centre of mass displacement and the corresponding actuators' displacements. The final displacement at the actuator point will be determined based on the vertical displacement of the platform motion and its corresponding orientation variations. Considering for example PEA_B, based on the known trigonometric approximations, the vertical displacement of this actuator when a rotation around the X-axis is observed, can be formulated as:

$$z_B = -sin(\vartheta_x) \cdot R_B \quad \textbf{30}$$

$$R_B = R \cdot sin(\alpha) \quad \textbf{31}$$

where z_B is the displacement of the actuator B; and R_B is the distance of the final point with respect to the origin O (centre of mass for the moving platform). Taking into account what stated previously for the small angles' approximation, and substituting Equation 31 into Equation 30 the following equation is obtained:

$$z_B = -(R \cdot sin(\alpha)) \cdot \vartheta_x \quad \textbf{32}$$

where R is the circumference radius; and α is the angular distance of PEA_B from the X-axis. This approach provides the equations for the actuators with respect to the three degrees of motion $[z, \vartheta_x, \vartheta_y]$:

$$Z = \boldsymbol{T} \cdot S = [z_A, z_B, z_C]^T \quad \textbf{33}$$

$$S = [z, \vartheta_x, \vartheta_y]^T \quad \textbf{34}$$

$$\boldsymbol{T} = \begin{bmatrix} 1 & R & 0 \\ 1 & -R \cdot sin(\alpha) & -R \cdot cos(\alpha) \\ 1 & -R \cdot sin(\alpha) & R \cdot cos(\alpha) \end{bmatrix} = \begin{bmatrix} 1 & R & 0 \\ 1 & -R/2 & -\frac{\sqrt{3}}{2}R \\ 1 & -R/2 & \frac{\sqrt{3}}{2}R \end{bmatrix} \quad \textbf{35}$$

where Z is a vector containing the three actuators' displacements; S contains the variations of the degrees of freedom of the moving platform; and $\boldsymbol{T}$ is the transformation matrix that links both vectors. Based on Equation 35, the inverse matrix to obtain S from Z is obtained:

$$\boldsymbol{T^{-1}} = \begin{bmatrix} \frac{1}{3} & \frac{1}{3} & \frac{1}{3} \\ \frac{2}{3 \cdot R} & -\frac{1}{3 \cdot R} & -\frac{1}{3 \cdot R} \\ 0 & -\frac{\sqrt{3}}{3 \cdot R} & \frac{\sqrt{3}}{3 \cdot R} \end{bmatrix} \quad \textbf{36}$$

The mechanical modelling part is then implemented based on the Newton's laws. The generic representation is described by the following equation:

$$\boldsymbol{M}\,\ddot{S}(t) + \boldsymbol{C}\,\dot{S}(t) + \boldsymbol{K}\,S(t) = \boldsymbol{B}\,F_{PEA}(t) + F_{EXT}(t) \quad \textbf{37}$$

where $\boldsymbol{M}, \boldsymbol{C}, \boldsymbol{K}$ are the mass matrix, modal damping matrix, and the stiffness matrix, respectively; F_{PEA} is a vector containing the force exerted by the three actuators; $\boldsymbol{B}$ is the transformation matrix for the force components to centre of mass disturbances; and F_{EXT} are the external disturbances upon the workpiece moving platform.

To proceed in the modelling description, the second approximation must be introduced. It arises from the serial connection between the spring element with the PEA, the axial rod linking the movable platform with the actuator. The accurate representation for this kind of scheme is depicted in Figure 16a where the actuator, along with the preload spring, are represented with the following components: a voltage driven force generator, a spring, and a damping element. However, the idea is to simplify the scheme to ease the control synthesis; in fact, the serial connection with the complete actuator is re-designed as an extra preload spring as represented in Figure 16b.

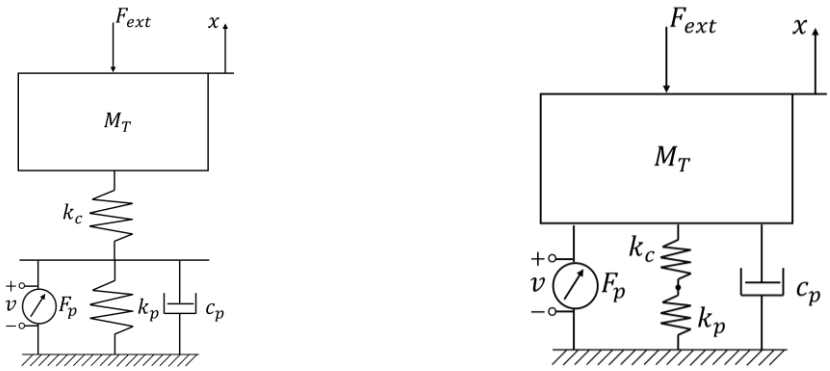

Figure 16. AWH Mechanical Approximation (a) real scheme; (b) simplified scheme.

This simplification was acceptable based on the high stiffness value of the rod which behaved as a rigid element. Furthermore, in order to validate the simplified model, a modal comparison scheme was performed by considering the three actuators influence upon the corresponding degrees of motion ($[z, \vartheta_x, \vartheta_y]$). The difference between the simplified scheme, Figure 16b, and the initial scheme, Figure 16a, is lower than 4.93 dB confirming the applicability of the second approximation, with a minimum disturbance in terms of the overall performance. Nonetheless, this was considered when the corresponding controller was synthesised by increasing its robustness. The simplified structure was modelled, and the corresponding matrices numerical values were found through FEM studies and hammer tests (for the diagonal damping matrix). The final symbolic matrices from Equation 37 are defined as:

$$\boldsymbol{M} = \begin{bmatrix} m & 0 & 0 \\ 0 & I_x & 0 \\ 0 & 0 & I_y \end{bmatrix} \tag{38}$$

$$\boldsymbol{C} = \begin{bmatrix} c_1 & 0 & 0 \\ 0 & c_2 & 0 \\ 0 & 0 & c_3 \end{bmatrix} \tag{39}$$

$$\boldsymbol{K} = \begin{bmatrix} -(k_A + k_B + k_C) & \frac{R}{2}(k_A + k_B) - k_C R & \frac{\sqrt{3}}{2}R(k_B - k_A) \\ \frac{R}{2}(k_A + k_B) - k_C R & -\left(\frac{R}{2}\right)^2 (k_A + k_B) - k_C R^2 & \frac{\sqrt{3}}{4}R^2(k_A - k_B) \\ \frac{\sqrt{3}}{2}R(k_B - k_A) & \frac{\sqrt{3}}{4}R^2(k_A - k_B) & -\frac{3}{4}R^2(k_A + k_B) \end{bmatrix} \tag{40}$$

$$\boldsymbol{B} = \begin{bmatrix} 1 & 1 & 1 \\ R & -\frac{1}{2}R & -\frac{1}{2}R \\ 0 & -\frac{\sqrt{3}}{2}R & \frac{\sqrt{3}}{2}R \end{bmatrix} \tag{41}$$

The electromechanical model was obtained afterwards based on both the linear approach presented in Equation 6, obtained based on the IEEE standard; and the nonlinear characteristic modelling based on equations 23 and 24, where the chosen hysteresis components were defined with the Bouc-Wen approach. Finally, the creep was implemented in simulation based on the Equation 8. These implementations were described based on the force generation hypothesis, hence the connection with this mechanical model is obtained through the $\boldsymbol{B}$ matrix and the $\boldsymbol{T}$ matrix. For the nonlinear electromechanical components the corresponding actuators' stiffnesses ($k_A,\ k_B,\ k_C$) are modified to include the electrical component $\frac{{T_{em}}^2}{C_p}$.

Chapter 4

Simulation and Control Synthesis

This chapter presents the simulation studies carried out for both active vibration control devices: the spindle device and the AWH. For each system an initial study of the inherent nonlinearities and main considerations are introduced. Specifically, a hysteresis description and creep effect are depicted. The controller proposed for both devices are based on industrial appliable regulators, mainly PID and its alternative schemes. However, different controller approaches are introduced and evaluated.

4.1 Introduction

The mechatronic devices introduced in the previous chapters are both based on piezoelectric actuators; hence, an initial phase of the simulations start from the schematization of these elementary devices. The dependency of these actuators on their force generation, based on their corresponding elongation, create an inner loop within the control synthesis that require consideration as it limits the achievable forces. A standard approach is to separate the mechanical nature of the piezoelectric actuators from the corresponding electrical one, producing a passive stiffness parallel with a force generator in the first part driven by the latter. The electrical model of the piezoelectric actuator is represented in Figure 17.

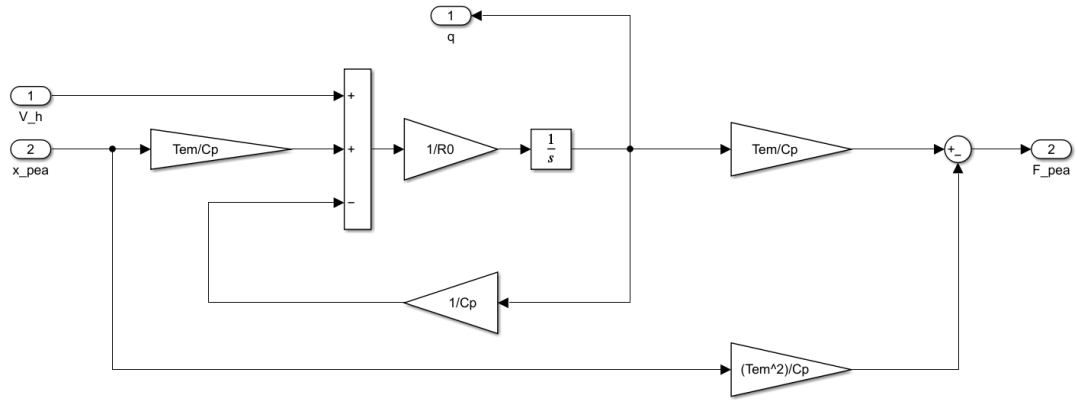

Figure 17. Piezoelectric actuator linear electrical model.

It is worth mentioning that the PEAs require to first reach half the maximum displacement to permit the maximum oscillations amplitudes whilst protecting the actuators from over-elongations/contractions. Furthermore, an important aspect of these actuators is that a positive voltage creates a corresponding elongation, in a similar

manner, a negative voltage produces a contraction of the nominal size. In addition, when the input voltage is reduced from a given elongation of the PEA, no negative voltage is given as input but rather the amplitude is decremented, producing a discharge of the PEA capacitance; the final contraction will hence depend on the speed of discharge and the external disturbance. Indeed, when the electromechanical approach chosen to model the PEA is based on the IEEE standard these properties are somehow neglected, whereas a complete treatment, as presented previously, is a more wholesome and accurate approach with respect to the real actuator. In that sense, it permits a distinction between the electrical domain and the mechanical system, which is of particular importance during the simulation. As for other actuation systems, the electrical domain tends to have faster dynamics with respect to the mechanical analogous.

Furthermore, the linear representation of the piezoelectric actuators lacks the capability to account for inherent hysteretic disturbances, hence, a hysteresis model for the PEAs is described with the Bouc-Wen structure, Figure 18 along with a creep model.

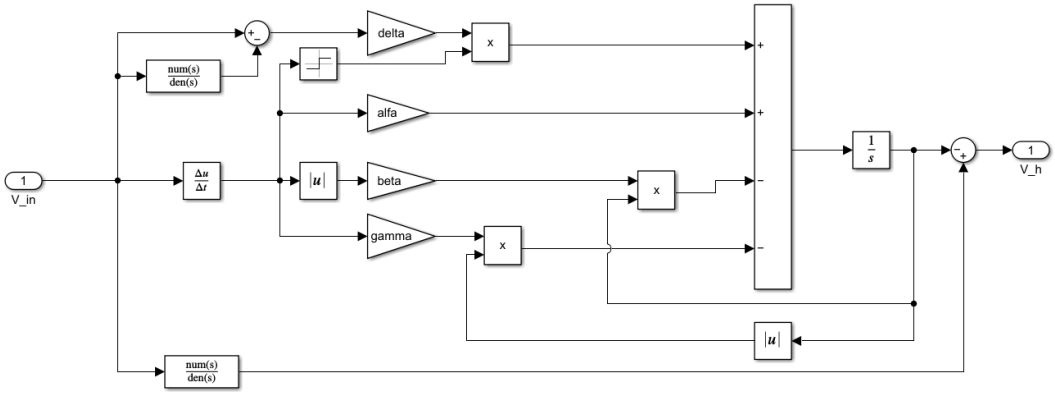

Figure 18. Piezoelectric actuator hysteresis model based on Bouc-Wen.

4.2 Spindle Active Platform for Vibration Control

The cutting force produced at the tool tip is transmitted through the spindle to the platform actuation point. A general first order model is deployed in simulation to evaluate the device capabilities to counteract the arising machining forces. Initially a linear model of the system is implemented based on the electromechanical equations, which include the coupling disturbances arising from the interaction between the elements inner connections. Indeed, to improve and validate the robustness of the controller, the native nonlinearities of the PEAs are included and simulated.

First, the active resonator absorber controller is designed based on the nature of the inertial actuator forces and the interaction between the spindle and the platform. This type of regulator requires acceleration feedback in most of their applications, nonetheless, velocity and position loops have also been evaluated and employed. Indeed, despite the possibility of including an accurate displacement feedback, this kind of applications upon the spindle has inherent difficulties in the sensor positioning, as the measurement point will not correspond to the actual tool. However, acceleration sensors can be easily installed within the platform structure and allow accurate feedbacks. Furthermore, considering that the disturbances can be described with sinewave functions,

the corresponding accelerations are amplified with a second derivative reducing the required sensor resolution; but this amplification is also observed for the noise which entails more complex filtering with respect to direct displacement measurement.

In summary, the acceleration sensors are easy to apply and are relatively low-cost. Hence, for the controllers designed in simulation the acceleration feedback is employed and the corresponding displacement is obtained through a state observer based on the linear model of the machining structure. Alternatively, a double filtered integration is implemented to depict the displacement from the acceleration measurement.

Further industrial controllers are tested as alternative applications to the active resonator, to overcome some of its issues related to the required known disturbance frequency and lack of the multi-frequency disturbance capabilities. The first application employs a cascade control with an inner loop related to the PEA displacement with a synthesised PID controller, while incorporating an external P controller to handle the disturbed vibration created upon the primary structure, the idealized spindle. Finally, a controller related to the industrial application is employed based on a PD scheme that directly limits the vibration employing displacement feedback obtained from the acceleration sensor.

The industrial controllers allow multi-frequency disturbances, which are usually present in machining. The latter presents the harmonic disturbances related to the rotation velocity of the spindle-tool system, although non-harmonic components could be found produced by the chatter characteristic. Thereby, the simulations are carried out by including both types of disturbances.

The detailed model is implemented in MATLAB (Simulink) environment as depicted in Figure 19, to validate the system functioning and the limits in its disturbance containment capabilities in terms of amplitude and frequency. The nonlinear electrical model is based on PEAs and hence is structured with their corresponding electrical definitions as depicted in Figure 17 and Figure 18.

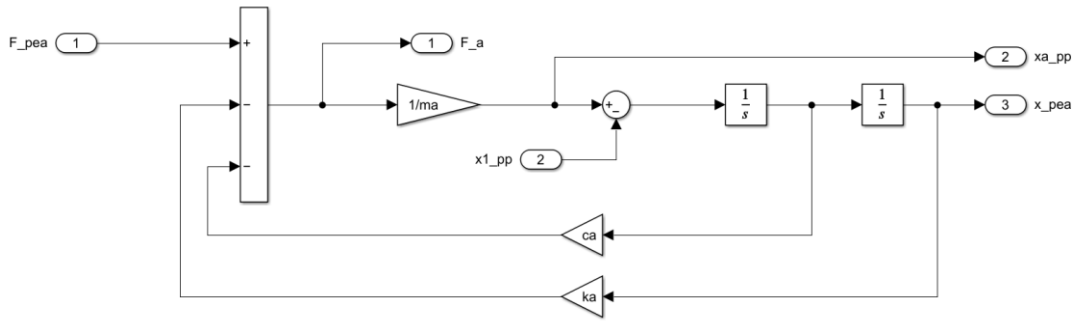

Figure 19. Simulink mechanical model employed for the device simulations.

4.2.1 Coupling Effect and Nonlinear Considerations

Piezoelectric actuators are fragile to transversal disturbances, and hence, is of particular importance to consider the inner effects of the platform when the actuation system is activated. The coupling transmission within the system structure is obtained through the FEM study of the CAD design of the platform; this certainly corresponds to an approximation taking into account that when the device is mounted on a spindle (or in a tests bench) their inherent modes will define other inner disturbances which are not evaluated in the FEM study. Nonetheless, as no direct evaluation and control of the coupling disturbance is carried out, as its influence on the final results tend to be limited, the active controller capabilities will be assessed in terms of single axis actuation. This approximation neglects the inner modes with the primary structure, which could be seen as a further disturbance within the single individual lines. Considering that the controllers proposed in this study correspond to disturbance rejection schemes, the coupling disturbances are implemented as an extra input to the system during the simulation.

Moreover, since the device is actuated through voltage control mode, the charge generated upon the PEA to produce the corresponding expansion can be expressed as a function of the input voltage ($q(t) = f(v(t))$). Hence, the hysteresis definition presented in Equation 13 can be modelled as a function of the input voltage, considering its dependency of the charge ($v_{in}(v(t)) = v(t) \cdot k_{amp} - H(f(v(t)))$. In fact, the hysteretic component becomes a preceding component to the PEA model. This characteristic is derived from the PEA's displacement measurements and were designed to assimilate the real measured behaviour of the PEAs in the experimental phase, presented in Figure 20. However, the importance of the implementation of similar components lies on the robustness considerations for the corresponding controller synthesis, hence, the aim is to produce a hysteretic component that creates a displacement variation between the expected output and the actual one.

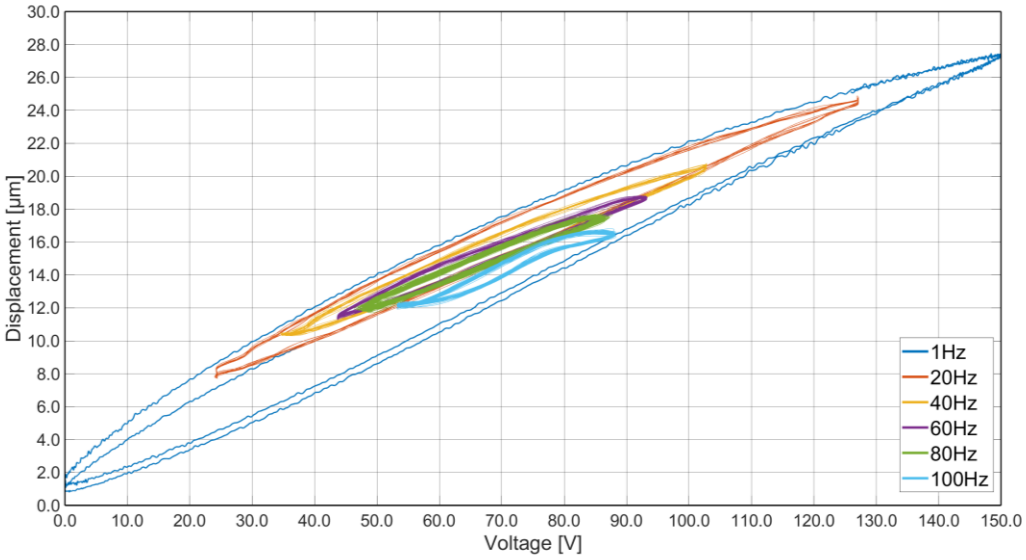

Figure 20. Measured hysteresis for multiple frequencies.

Despite the small influence of the creep effect for this application, typically found at low-frequency almost static components, its influence on the device was measured experimentally and modelled based on a set of transfer functions, as depicted in Figure 21. Indeed, the piezoelectric actuator drifted of near 1 µm in 16 s. In the figure there are three signals represented, the measured values from the experiments (*Measured*), the output from the electromechanical model presented in Equations 23 and 24 (*Electromechanical*), and the linear model based on the IEEE standard as in Equation 5 (*IEEE*).

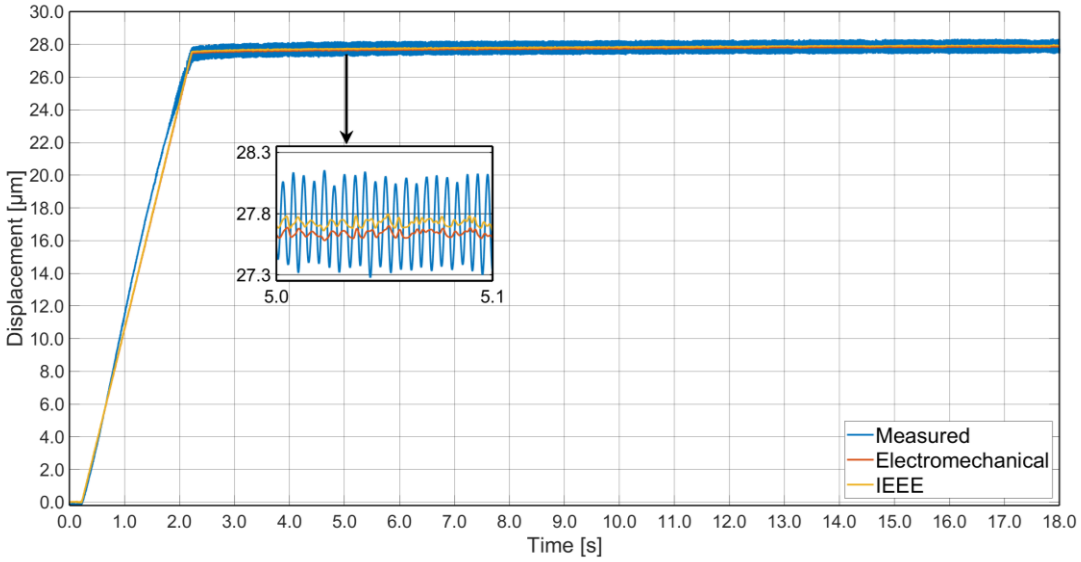

Figure 21. Creep effect, measured and modelled.

Both characteristics were measured for the complete stage and not from the independent PEA as the complete actuation system will define and influence the native individual behaviour of the actuators. Hence, the mass displacement under no external disturbance was measured near its centre of mass. These models, nonetheless, are not used to implement specific feedforward controllers to linearize the actuator but are rather determined and simulated to consider the influence of these phenomena upon the final control capabilities.

4.2.2 ARA Control

The active resonator theory, otherwise approached as delayed resonators, has been sorely studied and validated in the literature [134–140] for vibration suppression of mechanical systems. These active systems find the initial applications on the tuned mass damper passive structure, which despite the accurate results for known systems and the inherent stability without any external energy source, obtains a narrow band application centred upon the device natural frequency. Regarding such limitation, the active devices permit to modify the central frequency, reaching a wider spectrum. The applicable frequency is bounded within the stability limits and the sampling rate due to the delay definition; the latter is further treated through extensions to the initial approaches with lumped or distributed delays [134].

In this case scenario, regarding the platform, by reproposing Equation 26, the PEA generated force F_p is defined with the following equation:

$$F_p(s) = u(s) = P(s)\, X_a(s) \quad \textbf{42}$$

where $F_p(s)$ is the PEA's force in the Laplace domain; u is the control output;P is the ARA transfer function; and X_a is the absorber's mass position. Considering that for this application the feedback corresponds to the acceleration measurement, the transfer function $P(s)$ will contain the double derivative to relate the controller to the acceleration (s^2). The resulting equation, considering the ARA transfer function, can be expressed as:

$$[M_a s^2 + c_a s + k_a - P(s)]\, X_a(s) - (c_a s + k_a)\, X_1(s) = 0 \quad \textbf{43}$$

$$[M_1 s^2 + (c_1 + c_a)s + (k_1 + k_a)]X_1(s) + [P(s) - (c_a s + k_a)]X_a(s) = F_{ext}(s) \quad \textbf{44}$$

with $k_a = (k_p + k_f)$ as the absorber stiffness. Rewriting Equation 43 and replacing $X_a(s)$ in Equation 44 the following is obtained:

$$X_a(s) = \frac{A(s)}{[B(s) - P(s)]} X_1(s) \quad \textbf{45}$$

$$X_1(s) = \frac{[B(s) - P(s)]}{[B(s) - P(s)]D(s) + [P(s) - A(s)]A(s)}\, F_{ext}(s) \quad \textbf{46}$$

where $A(s) = (c_a s + k_a)$; $B(s) = (M_a s^2 + c_a s + k_a)$; and $D(s) = (M_1 s^2 + (c_1 + c_a)s + (k_1 + k_a))$. Therefore, $P(s)$ is defined to obtain $B(s) - P(s) = 0$ which results in a couple of poles in $s_{1,2} = \pm\omega j$, the transmission between the external force to resulting vibration of the primary system at the given frequency ω is thereafter null based on the numerator in Equation 46, with the requirement of stability imposed by the denominator.

The controller synthesis ($P(s)$) has been a core aspect in research for this kind of devices. The initial approaches employed directly implemented delays which increased the system complexity and resulted in several issues for the practical implementation. New approaches tend to employ industrial PI controllers, which have shown worse results, or varying delay approaches: lumped or distributed [134,135,137]. This study was centred on the *extended distributed delay* introduced in [134], defined with the following equations:

$$u(t) = g\, \frac{1}{\tau} \int_0^{\tau} \ddot{x}_a\,(t - \rho)\, d\rho - h\, \ddot{x}_a(t) \quad \textbf{47}$$

$$h = \frac{k_a}{\omega^2} - M_a \quad \textbf{48}$$

$$\tau = \frac{\pi}{\omega} \quad (49)$$

$$g = \frac{c_a \pi}{2\omega} \quad (50)$$

where $u(t)$ is the control output force and ω is the disturbance frequency. The extended approach implements the h coefficient which serves to adjust with the controller the absorber's mass from M_a to $M_a + h$ and hence modify its resonance to $\widehat{\Omega} = \sqrt{\frac{k_a}{M_a+h}}$.

As stated in [134], this control logic functions near the frequency resonance of the absorber (Ω), with a corresponding containment window for the disturbance frequency (ω). This depends on the damping factor of the absorber, which for this application was below 0.1, increasing the span of frequency functioning. Furthermore, the controller board determines a limit in the maximum sampling time of $1\text{x}10^{-4}$ s, which results in an upper constraint for the frequency range of functioning for the lumped approach [134,141,142]. Indeed, the final frequency interval for the case study in the ideal application, where no hysteresis was introduced and the amplifier electronic limitation was implemented as a low-pass filter with a frequency band of 5 kHz (higher than the value encountered for real applications), was of [500 Hz, 1,300 Hz].

Test 1 implements a 3.0 µm amplitude sinewave upon the primary system at 500 Hz. The controller parameters were obtained based on Equation 47-50, and a low-pass filter was included to account for the amplifier limitations. The PEA model is linear without any considerations of the creep nor of the hysteresis. In Figure 22, three different representations are presented: the output displacement plot, the PEA displacement, and the control output voltage after the power amplifier (voltage input to the PEA). The control dashboard limitation was neglected to ease the initial treatment and the results considerations (minimum sampling time of $1.0\text{x}10^{-4}$ s), nonetheless, this constraint has a major effect when $\tau < 1.0\text{x}10^{-4}$ s which is not this case. However, a decrement in the containment capability is expected due to the delay approximation of the sampling time imposed. In Figure 22a, it is observed that the open loop (OL) output is contained from the initial 3.0 µm amplitude up to 1.2 µm with the closed loop (CL) configuration, resulting in a 60% containment. The PEA input voltage is presented in Figure 22c while its displacement is shown in Figure 22b, both figures demonstrate that the physical limitation of the PEA, in terms of voltage (0 V – 150 V) and displacement (0 µm – 40 µm) are both satisfied.

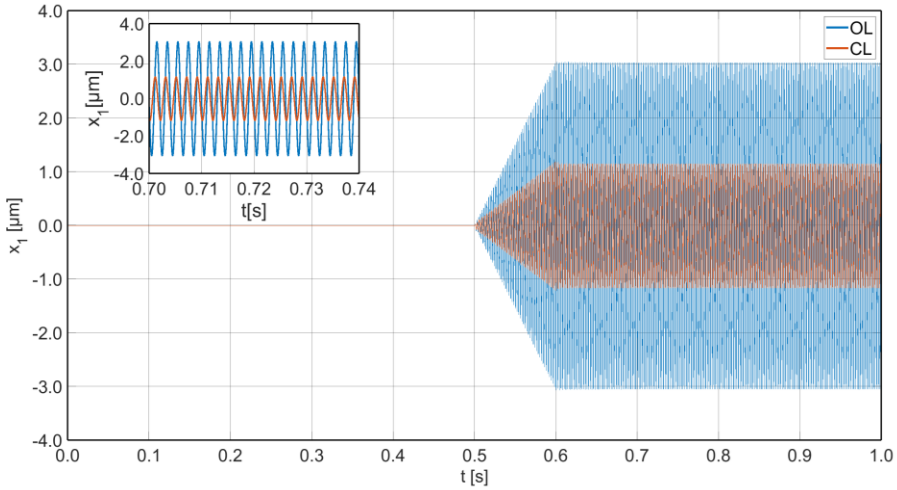

(a)

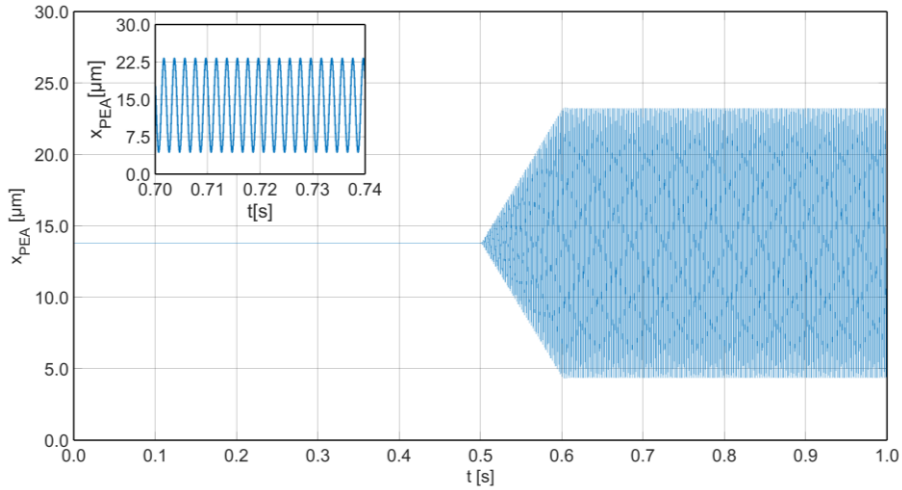

(b)

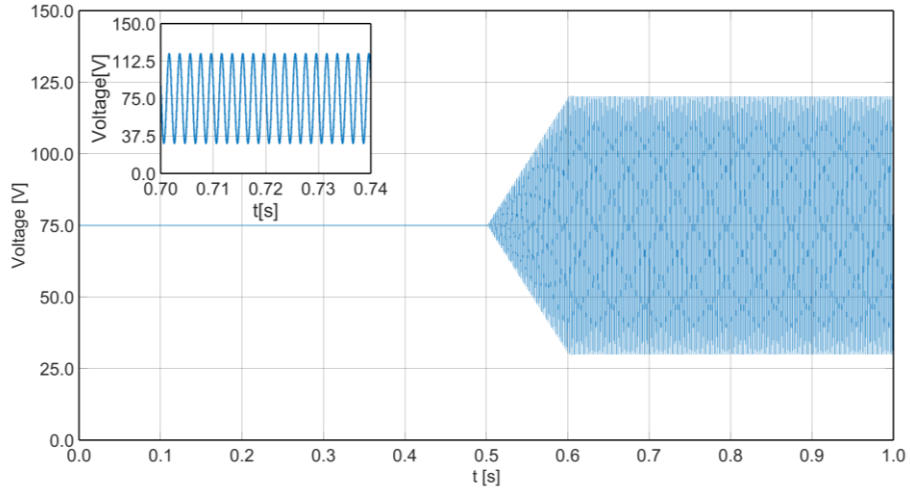

(c)

Figure 22. Test 1: 500 Hz. (a) primary displacement, open loop (OL) and closed loop (CL); (b) PEA displacement; (c) PEA voltage.

Test 2 increases the frequency of the application to 1,300 Hz, with an amplitude of 2.8 µm, and the same configuration as in Test 1 is employed. Figure 23a presents an OL output of 2.8 µm which is contained up to 1.3 µm with the CL configuration, a 54% containment. Furthermore, the PEA input voltage is presented in Figure 23c while its displacement is shown in Figure 23b, both figures demonstrate that the physical limitation of the PEA, in terms of voltage and displacement are both satisfied. Due to the vicinity of the disturbance frequency with the absorber resonance the resulting control output is more contained with respect to Test 1.

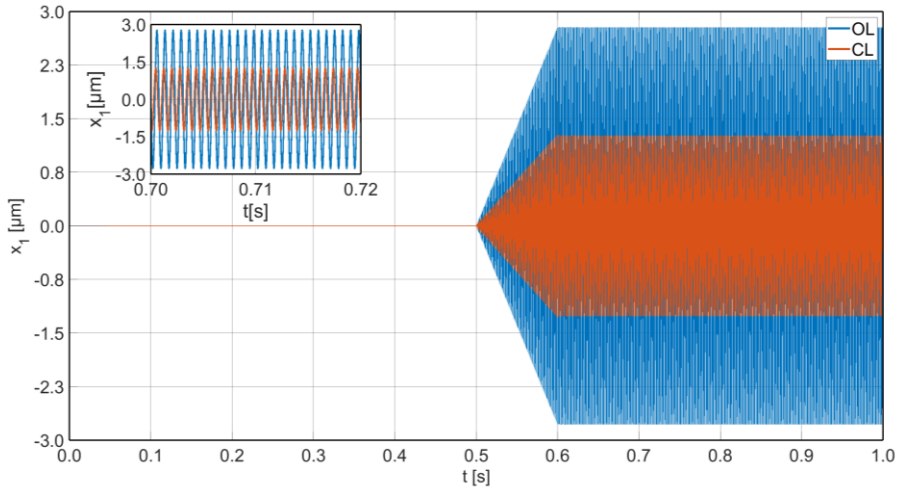

(a)

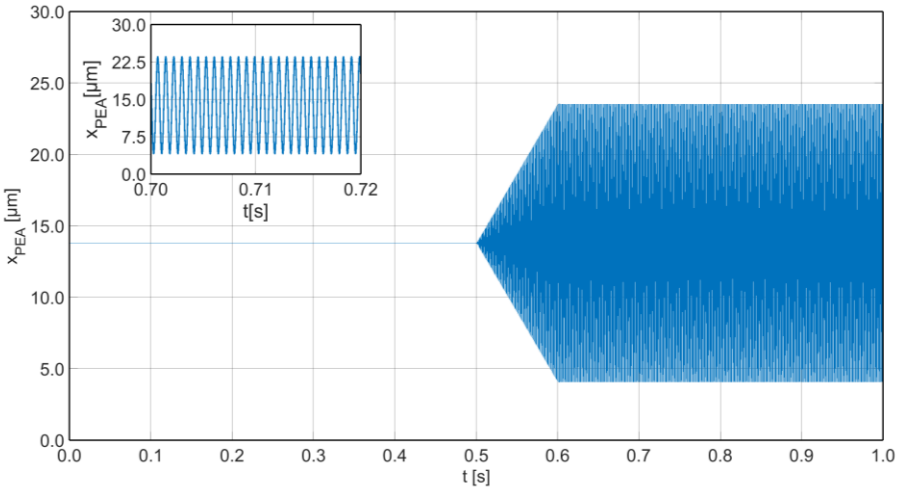

(b)

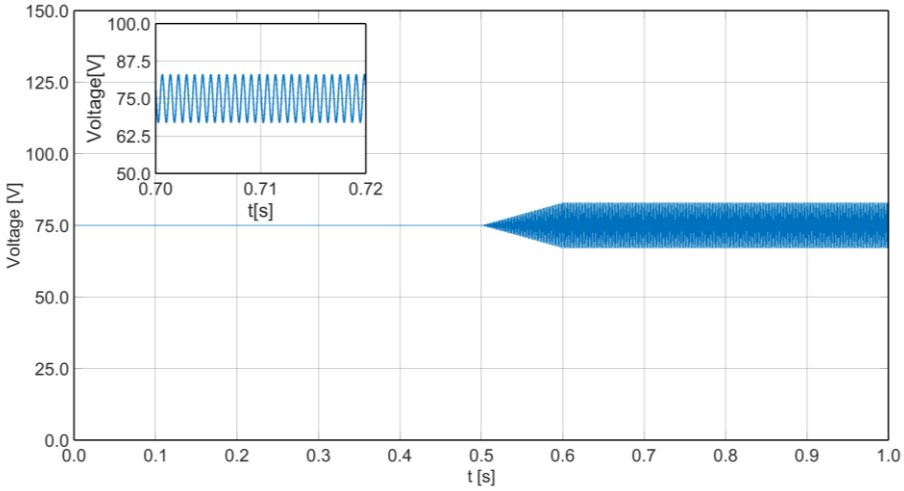

(c)

Figure 23. Test 2: 1,300Hz. (a) primary displacement, open loop (OL) and closed loop (CL); (b) PEA displacement; (c) PEA voltage.

Despite the good results obtained in Tests 1 and 2 there are several considerations that require particular attention. First, the frequency interval for which this system would be applicable is over the range of interest. Second, despite the advantage of the control action definition being independent of the primary vibrating structure, as nor $B(s)$ or $P(s)$ contain other parameters than the absorber characteristics; the complexity of multi-frequency systems might arise several issues for this controller robustness, which depends directly on a good esteem of the frequency ω. In fact, despite the possibility to implement optimization schemes based on the hypothesis that the real frequency is near the expected one [140], these must be within a certain distance. A first step of frequency recognition can also be employed, nonetheless, the possibility of unwanted vibration appearances away from the main vibration frequency or its harmonics in machining determines a problematic element for this controller employment.

To demonstrate the lack of robustness from the frequency recognition, a new Test is carried out, Test 3. The controller is tuned to handle a disturbance at 500 Hz, as for Test 1, but the real disturbance is implemented at 550 Hz (+10% difference). The results are depicted in Figure 24a-c; differently from the good results obtained in Figure 22a, the output displacement for the closed loop is amplified with respect to the open loop from 1.8 µm to 2.4 µm as shown in Figure 24a. The amplitude difference from Test 1 is due to the high values of the PEA displacement during this robustness tests which showed over-elongation and breakage for the amplitude in Test 1, hence its reduction.

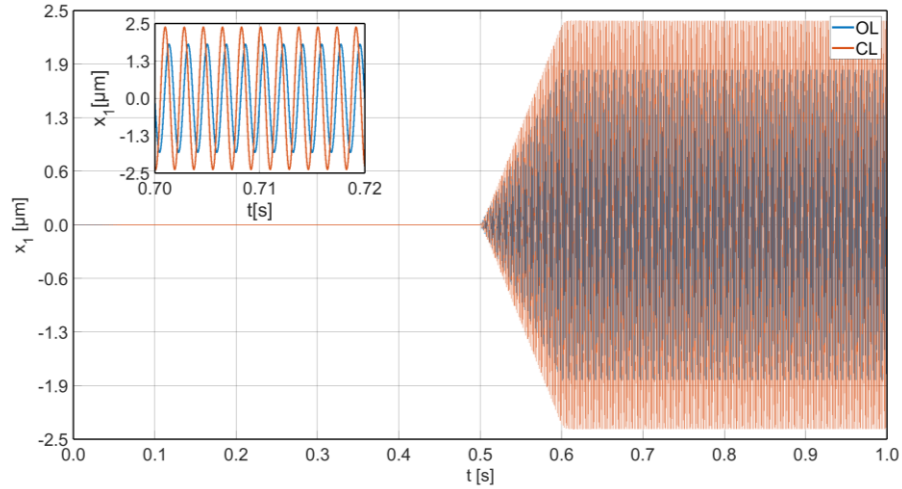

(a)

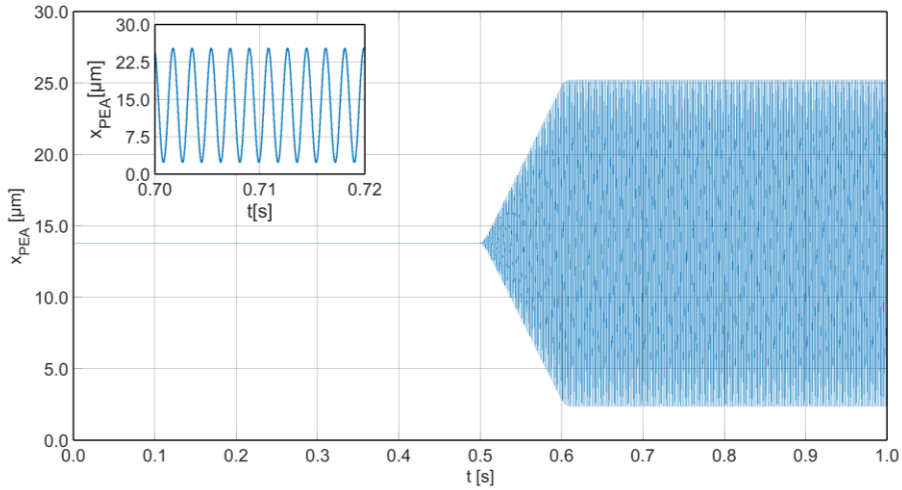

(b)

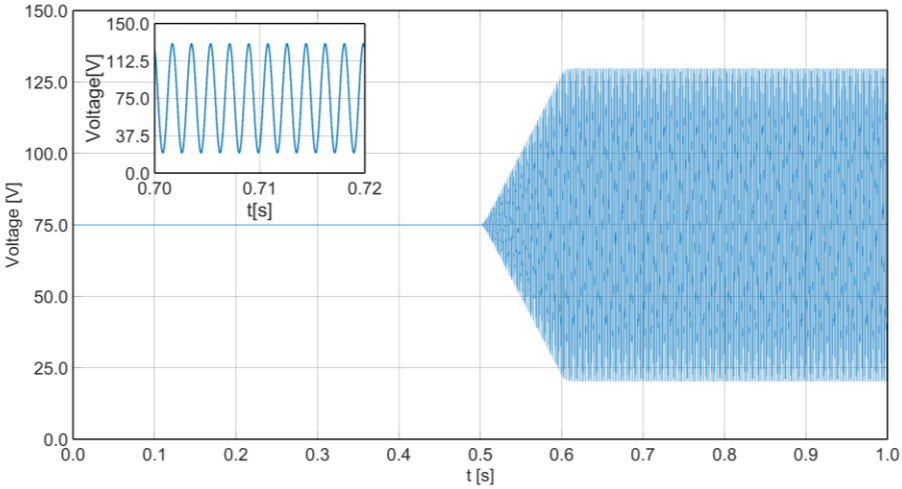

(c)

Figure 24. Test 3: 550 Hz with wrong frequency identification (500 Hz). (a) primary displacement, open loop (OL) and closed loop (CL), (b) PEA displacement, (c) PEA voltage.

In summary, the practical implementation of such controller would require high-cost electronics, a finesse disturbance frequency recognition method, and a hysteresis control to limit its effects in the resulting sinewave, among other improvements. Furthermore, the single-frequency disturbance imposes an important constraint for its application in the industrial case study. Hence, in the following subsections two industrial appealing controllers will be presented, which require a modelling/tuning initial phase but are independent of any forward optimization steps.

4.2.3 Cascade Control

Considering the limitations encountered with the ARA regulator, a cascade scheme is implemented. This controller aims to handle the piezoelectric position in the inner loop and the primary system vibration with the external loop. In fact, the first is a position loop whilst the second is a force loop (actuator output). Regarding the PEA displacement, the incapability of a direct measurement requires the implementation of an indirect path based on the inner mass accelerometers signals. A state observer is implemented based on the linear model of the device, which employs both the inner acceleration signal and the acceleration measurement of the spindle structure. The importance of a displacement measurement arises from the actuator force nature, as the resulting force is inertial when the displacement of the piezoelectric actuator is near its maximum and minimum displacements the nature of the force might create a push-pull behaviour which could damage the actuator. The state observer tends to underestimate the corresponding PEA displacement which increases the robustness of the inner controller and contains the possible damage to the actuators, but it will limit the maximum achievable displacement. Furthermore, a hysteresis loop is implemented to test the robustness of the controller with a nonlinear disturbance. Finally, the passive influence of the absorber utterly reduces the disturbed displacement, therefore, the control validation is carried out considering three different outputs: (i) the primary system without the device; (ii) the primary system with a passive device scheme; and (iii) the primary system with an active device scheme. The disturbance frequency range is defined from 80 Hz up to 300 Hz. The initial tests consider a single frequency single axis system, followed up with multi-frequency tests.

In absence of a primary system the device single-axis equation is derived based on the electromechanical model of the PEA actuator. Indeed, the acceleration of the primary body and its corresponding influence in the PEA displacement is viewed as a disturbance modelling. The corresponding transfer function from input voltage to PEA displacement is represented by the following equation:

$$\frac{X_{PEA}(s)}{V(s)} = \frac{T_{em}}{\left[\left(C_p R_0 m_a\right)s^3 + \left(m_a + C_p R_0 c_a\right)s^2 + \left(R_0 {T_{em}}^2 + c_a + C_p R_0 k_a\right)s + k_a\right]} \quad \textbf{51}$$

The numerical values are substituted within the equation and the resulting transfer function presents a couple of complex conjugate poles and a real pole, as depicted in Figure 25. Regarding the frequency interval of interest, the complete structure behaves as a single real pole system, and hence the controller tuning can be performed based on this approximation. The inner controller is synthesised based on a PI structure with a back-calculation scheme for saturation handling. Moreover, a filter is deployed to avoid any high-frequency unreal activation. The controller *Kp* is defined based on the control margins, phase (58.7°) and gain (12.6 dB), *Tt* is determined by the standard tuning for PI controllers (0.9 *Ti*), and *Ti* is set to cancel the approximated process pole.

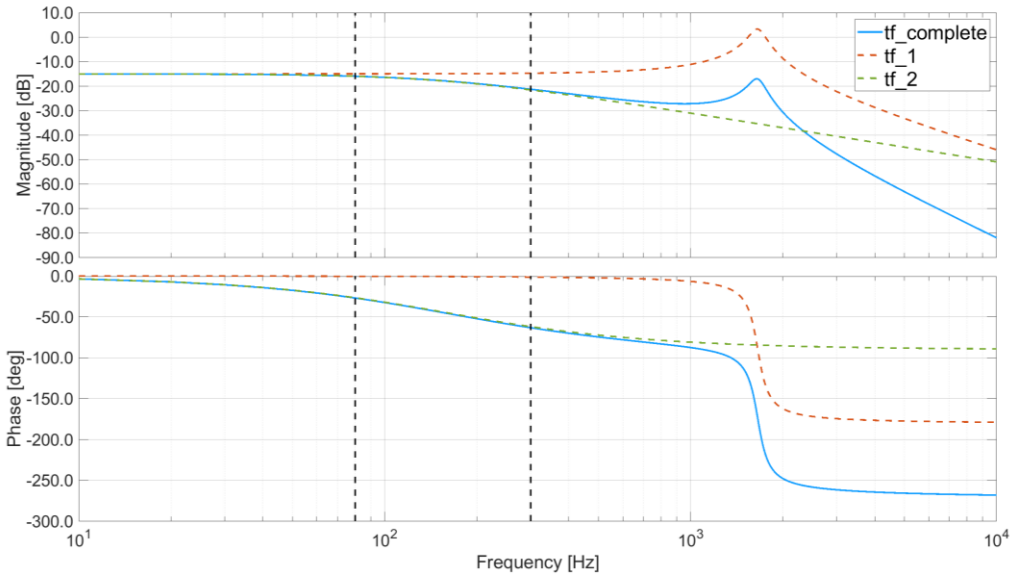

Figure 25. Bode diagram for the direct actuated device: (tf_complete) complete system model, (tf_1) single real pole, (tf_2) complex conjugate poles.

The external *Kp* cannot produce an unstable behaviour due to the inner loop actuated limitation. Without an inner controller the voltage limitation of the PEA prevents the amplification of the structure, along with the absence of resonance peaks within the frequency interval of interest.

The initial tests carried out are employed to evaluate the minimum and maximum frequencies of interest, 80 Hz and 300 Hz respectively. In Figure 26a-b the results obtained for an 80 Hz disturbance upon the primary structure are depicted, the *Active* corresponds to the controlled device, while the *Passive* and *Primary* correspond to the passive scheme and the results without the device, respectively.

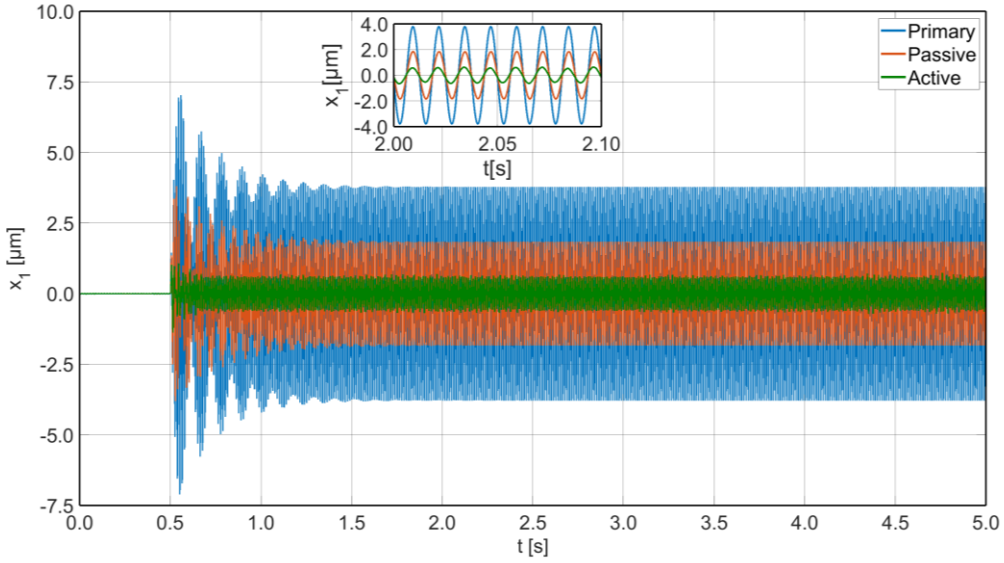

(a)

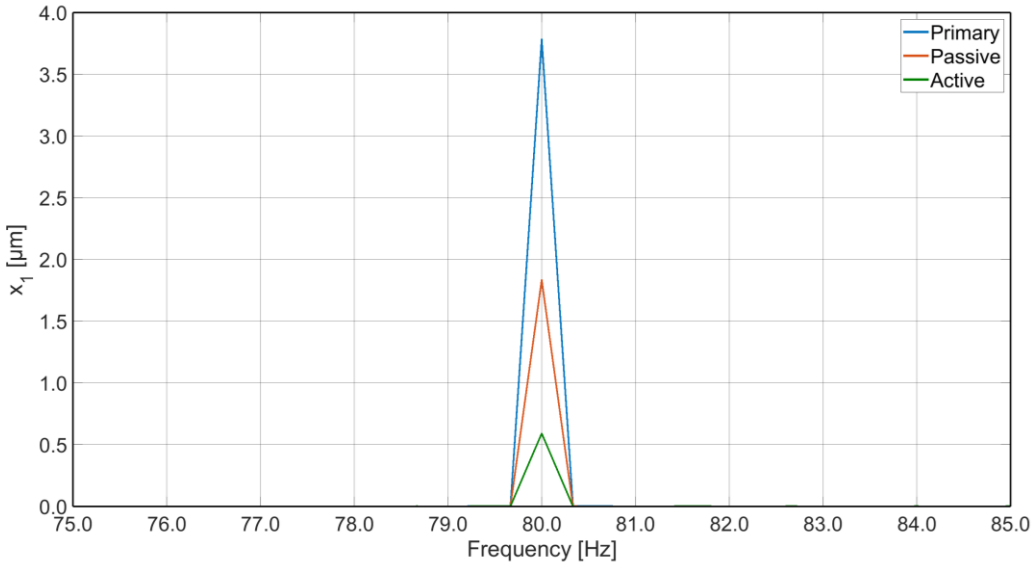

(b)

Figure 26. Test 1: Primary (blue), Passive (red), and Active (green). (a) Time Plot, (b) Frequency Plot.

Test 1 shows a disturbance in terms of primary displacement of ±3.8 µm amplitude at 80.0 Hz, this value is contracted up to ±1.8 µm with the device structure and without any active component. Finally, the actuation permits to further improve the primary structure displacement up to ±0.6 µm, as depicted in Figure 26b. These results are computed after the initial system dynamics end, however, it is important to notice that in this interval (from 0.5 s to 2.0 s) the high amplitude dynamics of the system, and even for the passive structure, is contained with the active controller deployed, as presented in Figure 26a.

Furthermore, the hysteretic component of the piezoelectric actuator has an influence upon the obtainable containment, as shown in Figure 27a where the

piezoelectric displacement is presented. Nonetheless, for the 80 Hz disturbance the hysteresis component is smaller with respect to higher frequencies. The results obtained without the hysteretic model showed a primary displacement of ±0.5 µm, as presented in Figure 27b. The remaining displacement is highly influenced by the accuracy of the feedback measurement and position conversion, obtained with an observer for the PEA and a double filtered integration for the primary displacement, with a simulated noise injection on both feedbacks.

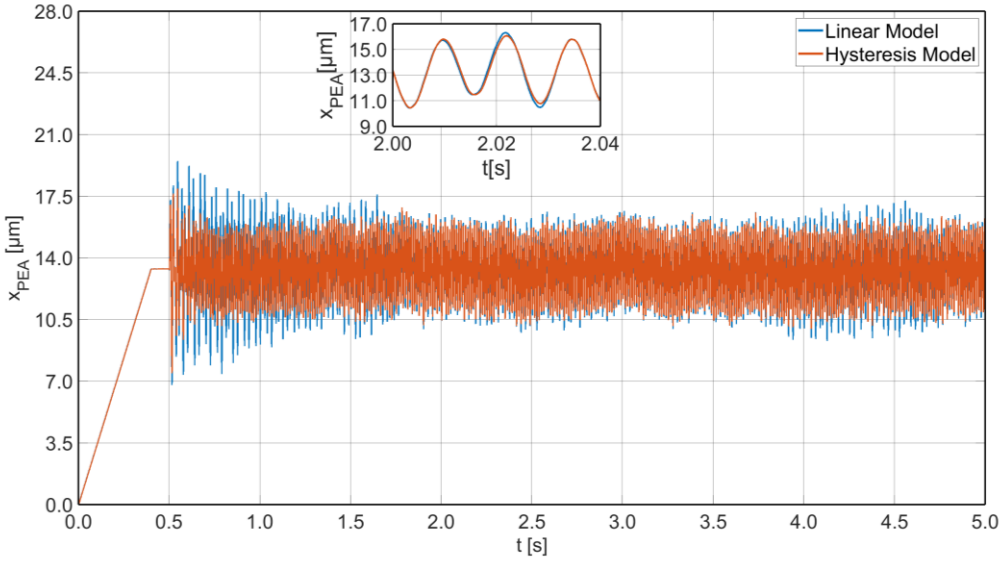

(a)

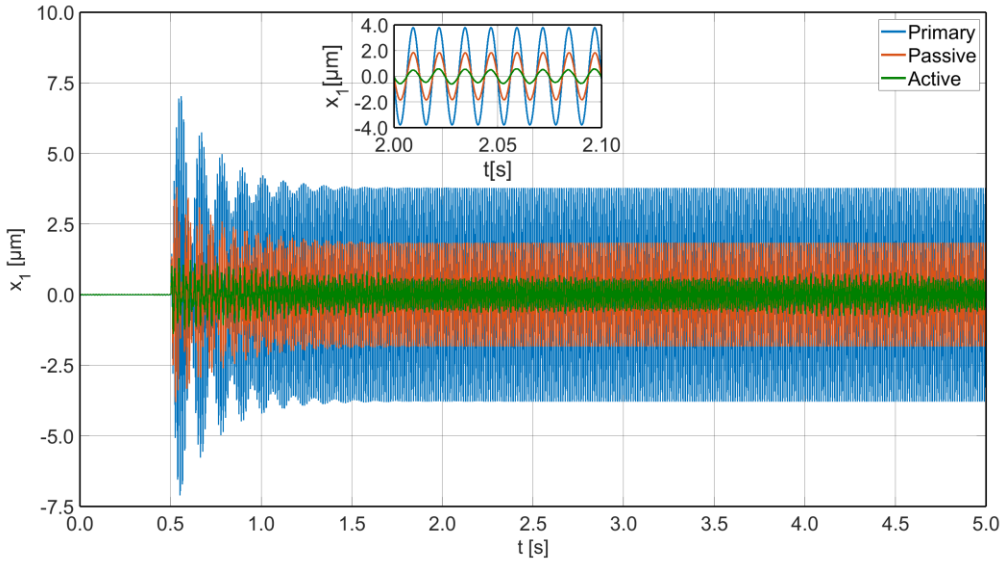

(b)

Figure 27. Test 1: (a) PEA displacement for the Linear Model (blue) and with Hysteresis (red) , (b) Primary displacement results without hysteresis.

A higher hysteretic component is observed for Test 2, with a 300Hz disturbance, as the PEA is subject to frequency-dependent hysteresis. The difference between PEA's displacement produced with and without hysteresis is presented in Figure 28. Indeed, the

limitation in the PEA's displacement reduces the maximum applicable force of the proposed device, and hence, obtains a worse result in terms of disturbance containment.

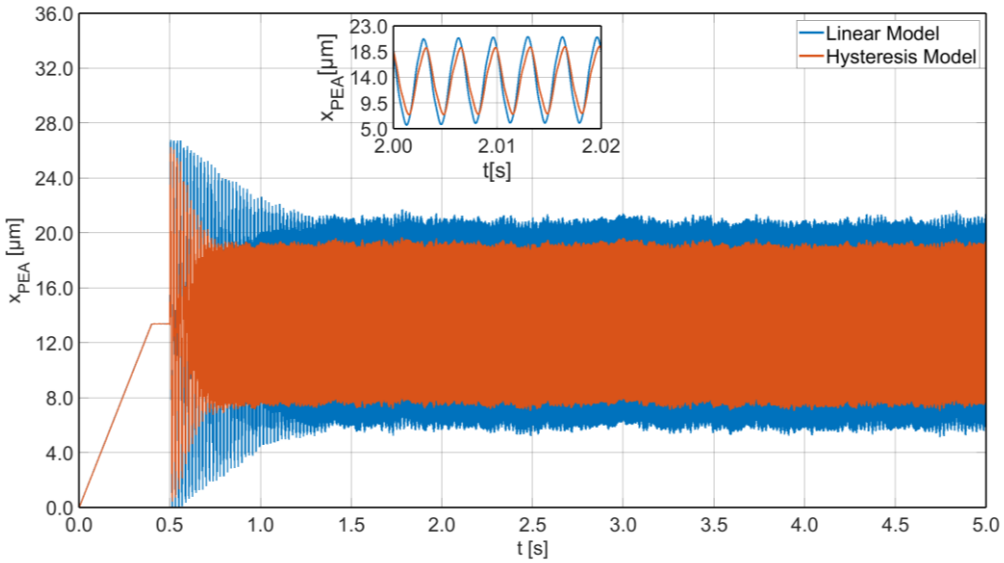

Figure 28. Test 2: PEA displacement with (blue) and without (red) hysteresis.

The primary displacement for Test 2 is presented in Figure 29a-b where the active representation includes the hysteretic component. The voltage limit and the actuator's displacement containment reduce the difference between the passive and the active application, nevertheless, the latter achieves a further 10% reduction with respect to the passive application. The active approach obtains a final displacement of ±2.2 µm amplitude, with almost a 30% amplitude containment from the primary structure without the device (~±3.0 µm). Furthermore, an important containment for the transient phase is observed in Figure 29a.

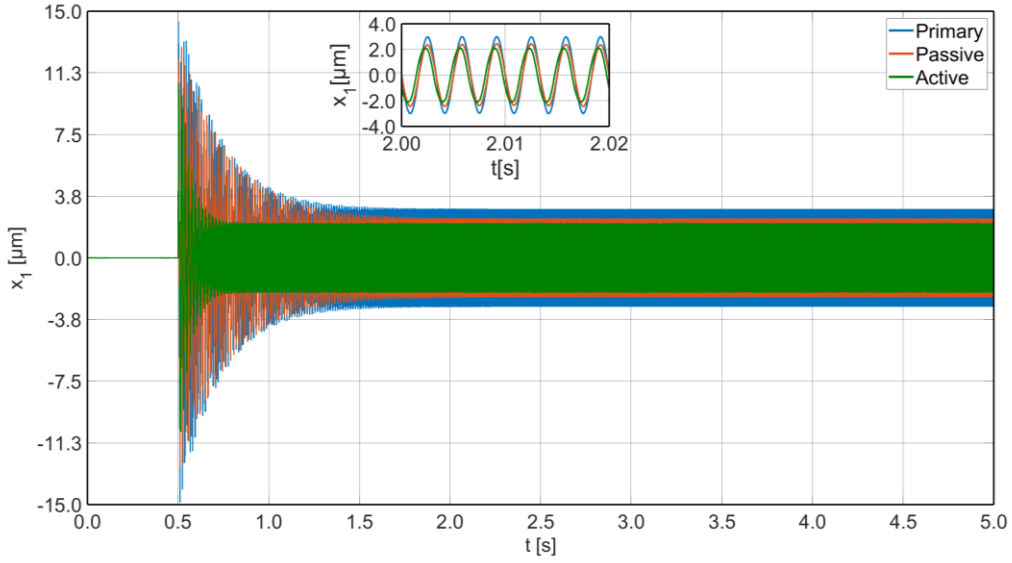

(a)

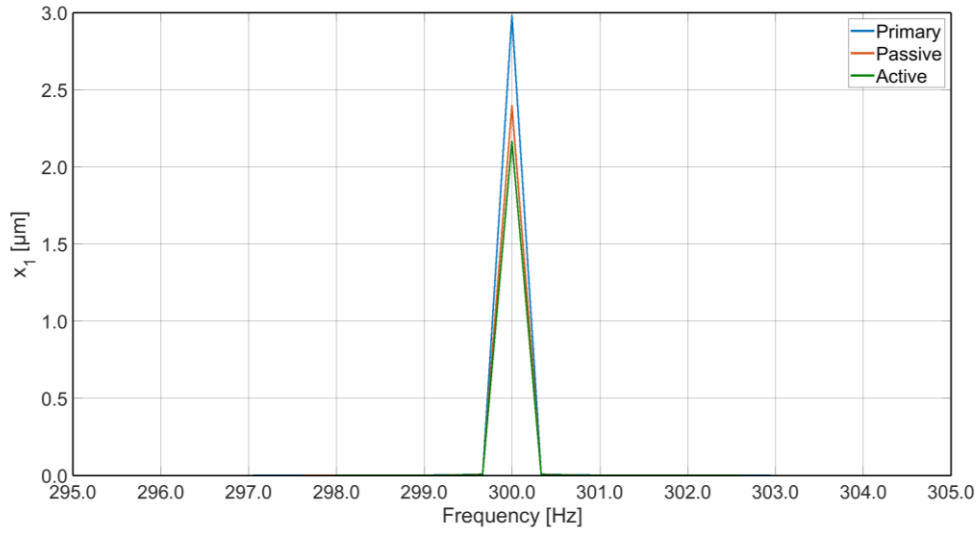

(b)

Figure 29. Test 2: Primary (blue), Passive (red), and Active (green). (a) Time Plot, (b) Frequency Plot.

Similar results are obtained for a 200 Hz disturbance, Test 3, where the active system showed a final displacement of ±4.9 µm, improving the passive results of 15% (±5.8 µm) and of 33% for the primary structure result (±7.3 µm), as shown in Figure 30b. As for the previous single frequency tests, the transient phase, which might create issues with the contact between tool and workpiece is reduced in both amplitude and time lapse, as observed in Figure 30a.

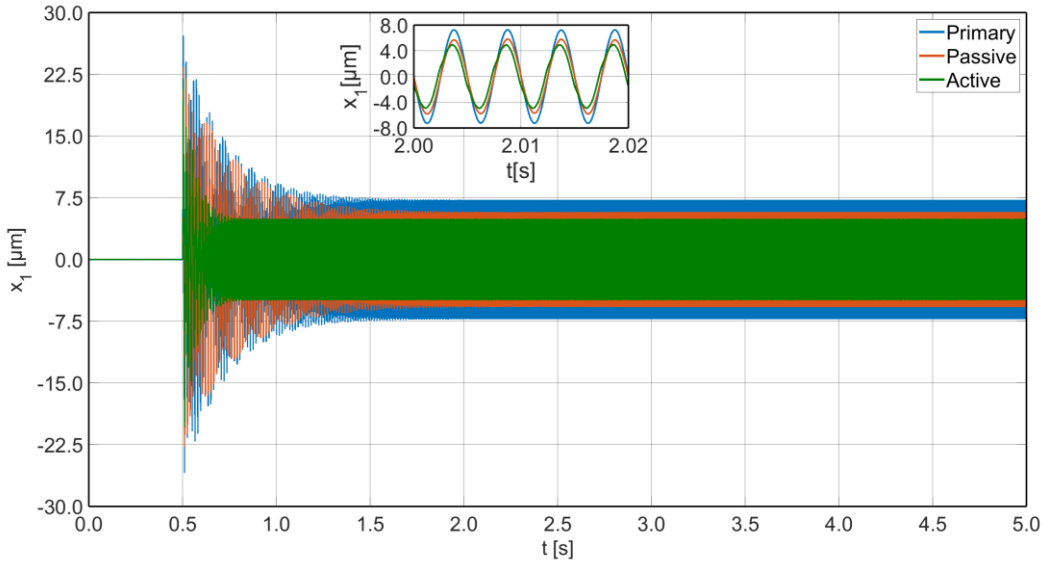

(a)

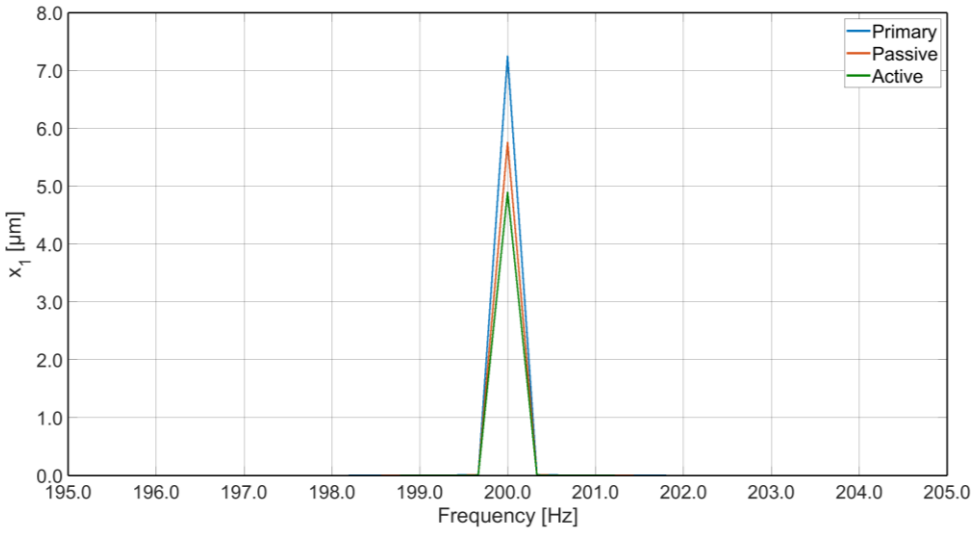

(b)

Figure 30. Test 3: Primary (blue), Passive (red), and Active (green). (a) Time Plot, (b) Frequency Plot.

Differently from the single-frequency limit of the active resonator scheme presented before, this controller allows, through a known industrial applicable controller, to counteract multi-frequency disturbances. Hence, even though the single frequency tests permit to validate the deployed control scheme, to further demonstrate its capabilities, four different multifrequency tests are presented. Regarding the limits of the frequency interval and the harmonic disturbances in a real machining case, and to ease the treatment and comparison between the different tests, the amplitude at each frequency was selected accordingly to obtain a ±2.5 µm displacement at the primary structure without the device. As for the single-frequency tests, the hysteresis component is used, and its effect increases with the increment of the frequency component limiting the resulting containment capabilities.

The initial multi-frequency test, Test 4, considers the minimum and maximum applicable frequency, in fact, the disturbance force has two components: 80 Hz and 300 Hz. The primary structure displacement is presented in Figure 31, where the active scheme contains the ±2.5 µm peaks to ±0.5 µm and ±1.8 µm for the 80 Hz and the 300 Hz components, respectively. The passive scheme shows worse results with an amplitude of ±1.2 µm (+140%) for the 80 Hz component and ±2.0 µm (+11%) for the 300 Hz one.

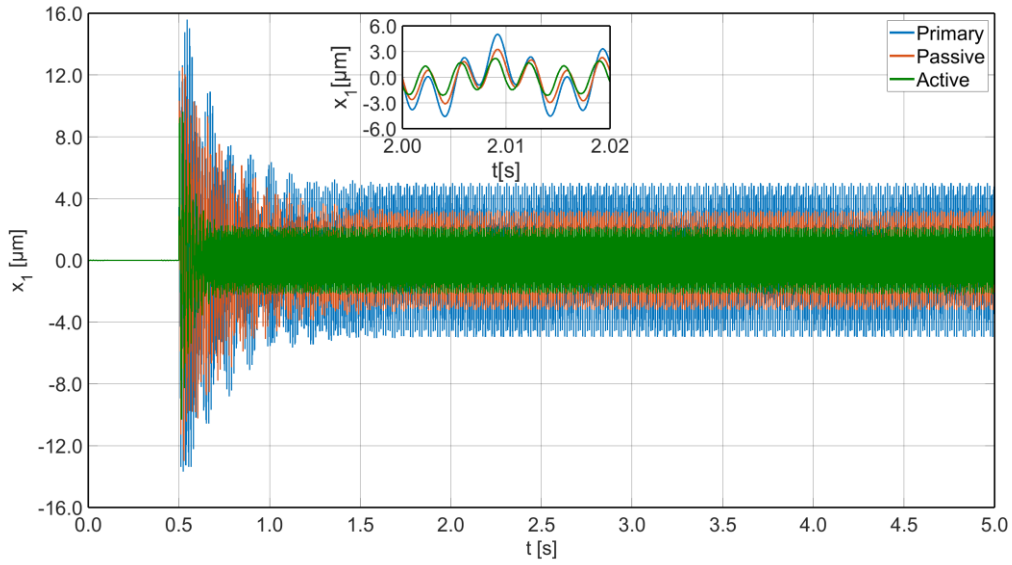

(a)

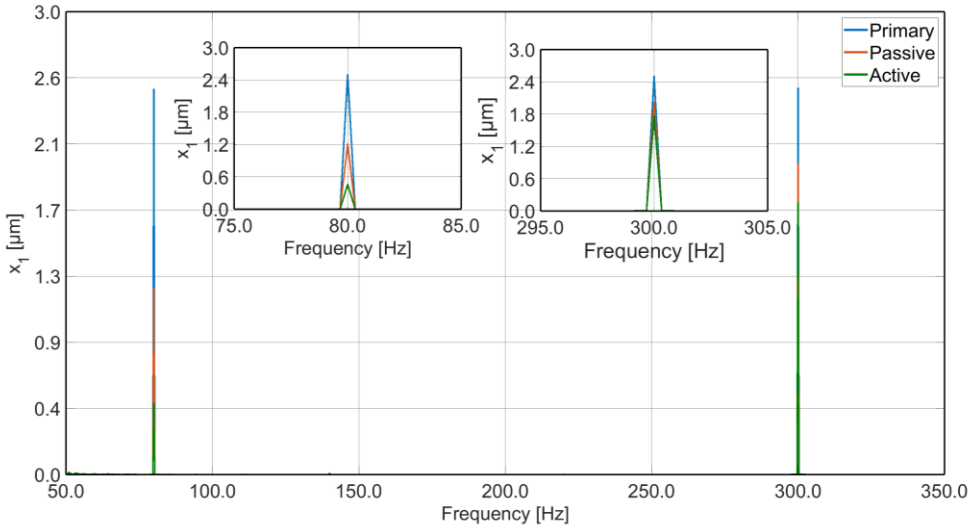

(b)

Figure 31. Test 4: Primary (blue), Passive (red), and Active (green). (a) Time Plot, (b) Frequency Plot.

Test 5, depicted in Figure 32, presents the response of the primary structure under two harmonics, 80 Hz and 160 Hz, similar to the expected forced disturbance of the machining process. In this scenario, the primary structure with the passive scheme contained the two peaks from ±2.5 µm up to ±1.2 µm for the first harmonic and to ±2.0 µm for the second, a containment of 52% and 20%, respectively. These results were further improved by the active controller, achieving a contraction of 84% (±0.4 µm) for the 80 Hz peak and of 52% (±1.2 µm) for the 160 Hz, assessing the controller capabilities under harmonic disturbances.

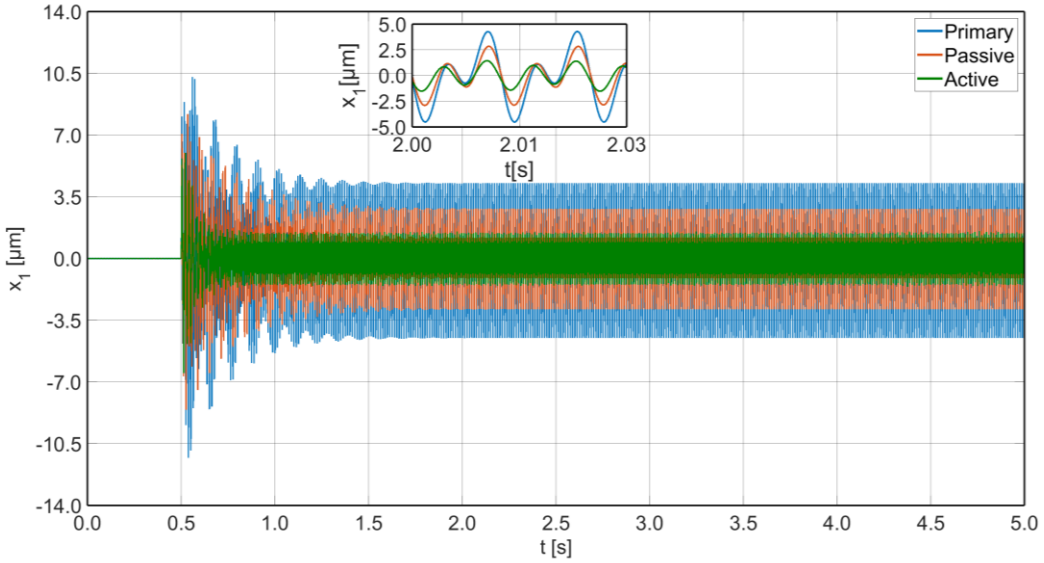

(a)

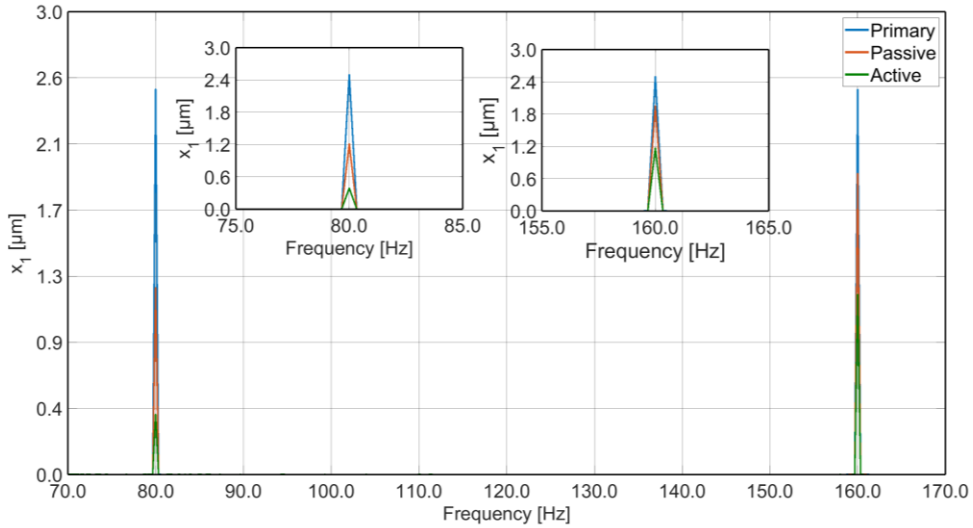

(b)

Figure 32. Test 5: Primary (blue), Passive (red), and Active (green). (a) Time Plot, (b) Frequency Plot.

Finally, Test 6 implements a disturbance with the following components: 150 Hz and its consequent harmonic at 300 Hz, as presented in Figure 33. Regarding the primary structure displacement, the active system obtained a 48% containment of the 150 Hz peak, ±1.3 µm, and a 28% for the 300 Hz peak, ±1.8 µm. The passive approach obtained worse results, with a final displacement of ±1.9 µm and ±2.0 µm for the 150 Hz and its harmonic, respectively.

Tests 4-6 assess the control capabilities to handle multi-frequency disturbances for uncorrelated and harmonic signals, achieving a contraction of the primary structure displacement from 28% to 80% in the frequency interval of interest, 80 Hz to 300 Hz.

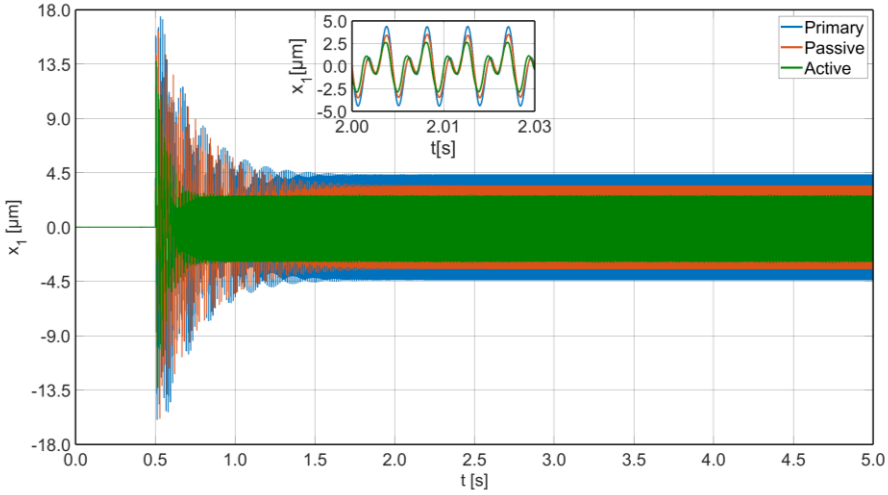

(a)

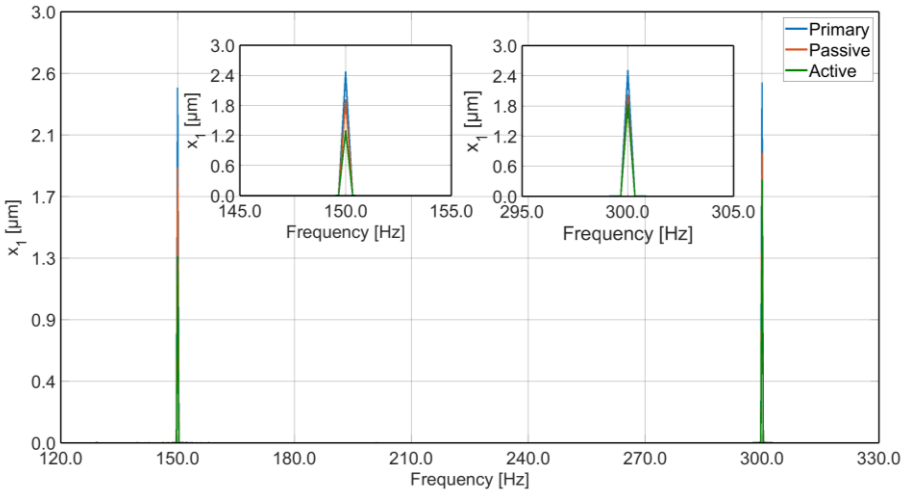

(b)

Figure 33. Test 6: Primary (blue), Passive (red), and Active (green). (a) Time Plot, (b) Frequency Plot.

The difference between the percentages is produced by the power limitation of the piezoelectric actuator and the hysteresis behaviour. As the frequency components increase the hysteresis has a greater influence in the final active achievable displacement. In fact, Test 6 shows a high contraction between the achievable displacement of the PEA for the linear case without hysteresis with respect to the hysteretic model, as presented in Figure 34. The compelling effect of the hysteresis limitation for the PEA displacement directly determines the amount of force the system can produce; being composed of inertial actuators the device's output force is determined by the achievable elongation and contraction of the PEA. In fact, for the linear approach, and considering a mass of 1 kg, the resultant force difference for a 1 µm amplitude is of 3.55 N, a 10% contraction for the total applicable force considering the maximum PEA displacement.

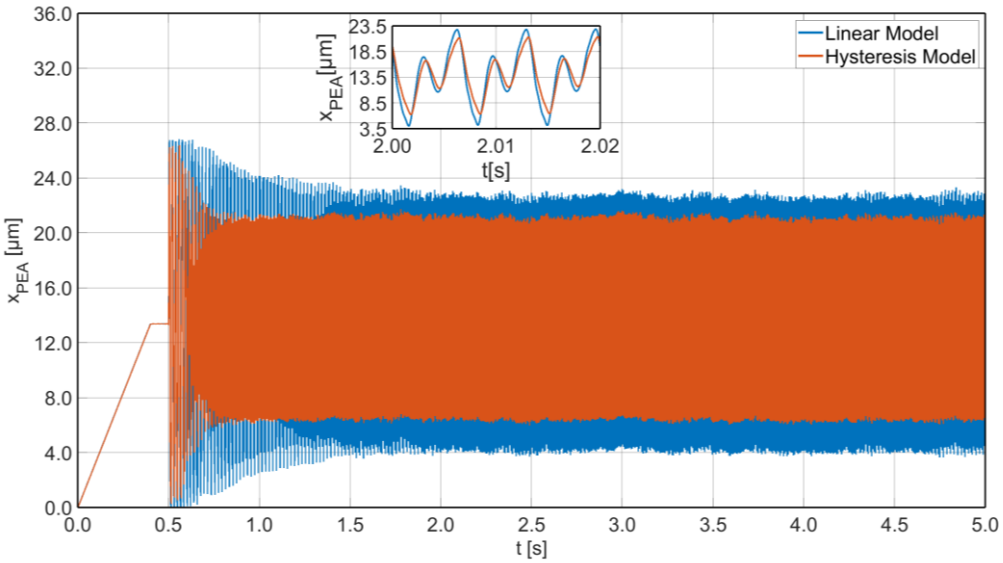

Figure 34. Test 6: PEA displacement with (blue) and without (red) hysteresis.

The controller showed promising results for the application of interest within the frequency interval of interest, overcoming the faults encountered with the active resonator approach. However, the inner loop, despite increasing the robustness and protection of the actuator, might create a containment of the final force based on the saturation of the actuator with respect to the observed displacement obtained from the hysteretic system. A more industrially appliable controller is therefore studied, for which a simpler controller is deployed by removing the inner displacement controller of the piezoelectric actuator and handling the complete structure as a force source system.

4.2.4 Industrial Rejection Scheme Controller

Differently from the cascade control, this new structure relays on a single loop scheme with a proportional controller which employs as feedback the position of the primary structure, obtained through signal treatment from the acceleration with a band-pass filter defined based on the frequency interval requested by the application.

This controller is easier to implement and modify with respect to the previous application, nonetheless, lacks the capability of obtaining an indirect measurement of the actuator's displacement and its consequent control. The corresponding modelling scheme for the system without nonlinearities, such as saturation or hysteresis, is represented in Figure 35. The controlled scheme presents worse results than those in the Bode diagram for the active scheme as the hysteresis, saturation, and feedback obtention will influence the obtainable containment. Based on simulation studies and hysteresis evaluation it is expected an uncertainty of +2 dB for the active response.

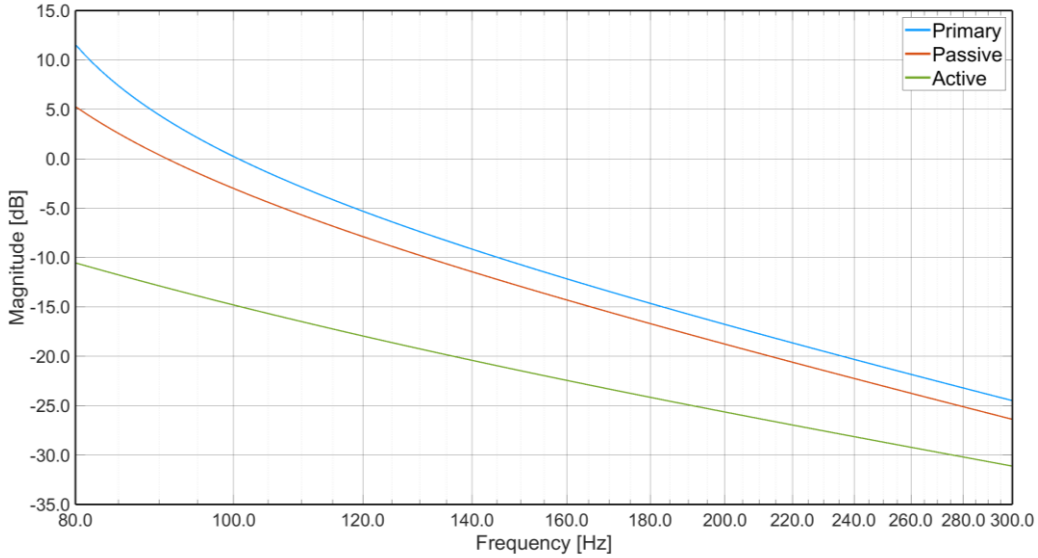

Figure 35. Bode diagram from external force [N] to primary displacement [μm] for: Primary (blue), Passive (red), and Active (green).

To assess the synthesised structure the Tests 1-6 are repeated with this new scheme. The results obtained for the passive scheme are presented in the following figures along with the active device and the free structure; nonetheless, with respect to the cascade control, this approach modified only the active scheme. Test 1, with an 80 Hz disturbance produced a final displacement of ±0.3 μm from the initial ±3.8 μm obtained without the device, as presented in Figure 36. The results were obtained with the hysteretic model, and they overachieve the cascade control ones. The difference between both schemes is due to the increment in the external loop gain and the reduced robustness for the inner loop control employed for the actuator's displacement.

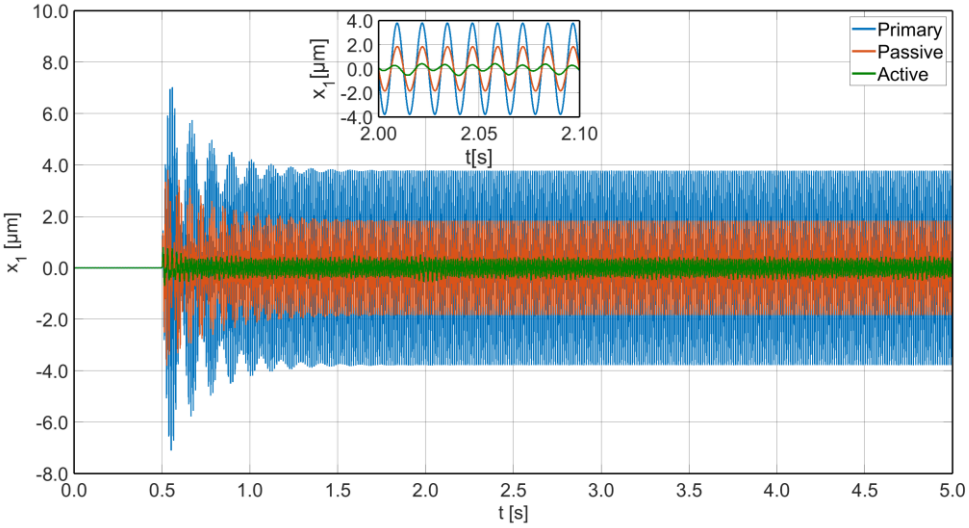

Figure 36. Test 1 time plot: Primary (blue), Passive (red), and Active (green).

Test 2 with a 300 Hz disturbance, depicted in Figure 37, shows a 37% reduction with respect to the free primary structure, with a final displacement of ±1.9 µm. As before, the results obtained present a further containment with respect to the cascade scheme.

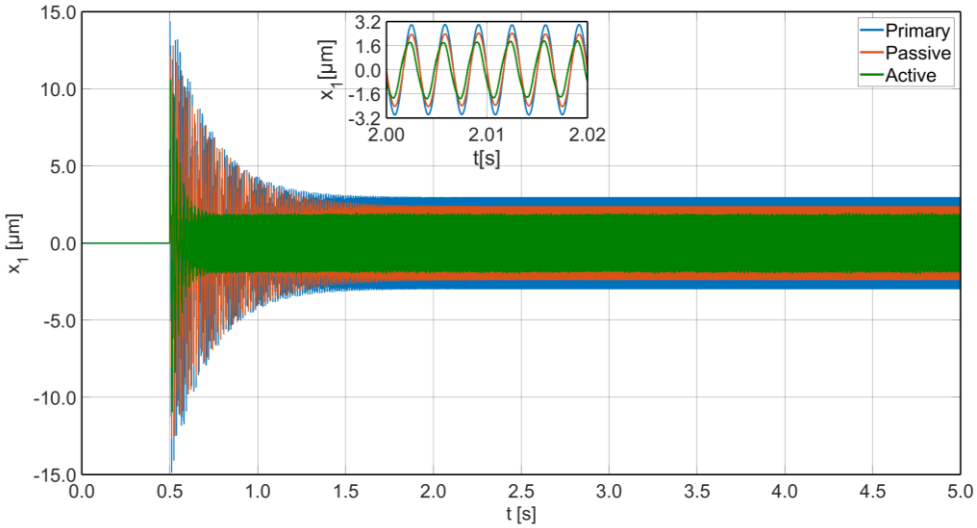

Figure 37. Test 2 time plot: Primary (blue), Passive (red), and Active (green).

The final single-frequency test, Test 3, corresponds to a 200 Hz disturbance, presented in Figure 38. The active approach managed to contain the initial ±7.3 µm up to ±4.7 µm, a 35% contraction. This test exerted a higher force and, hence, produced a higher displacement which reduced the control capabilities due to the saturation of the control action; obtaining a worse percentual result with respect to Test 2.

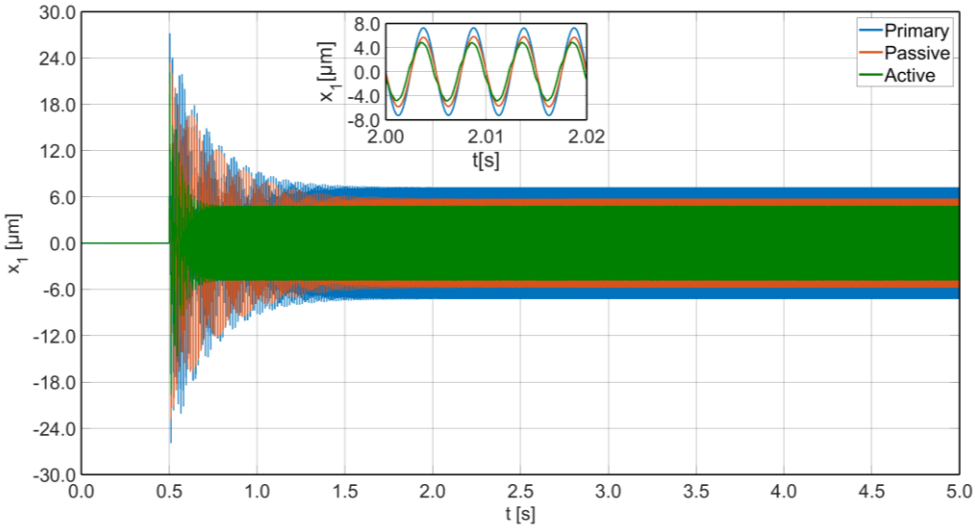

Figure 38. Test 3 time plot: Primary (blue), Passive (red), and Active (green).

The first multi-frequency test, Test 4, employs a disturbance with two frequency components: 80 Hz and 300 Hz; for both peaks the amplitude of the corresponding sinewave was kept at ±2.5 µm, as for Tests 5 and 6. The results obtained with the proposed controller are presented in Figure 39; the active approach achieved the following amplitudes for the two peaks: ±0.3 µm for the 80 Hz component and ±1.5 µm for the 300 Hz component.

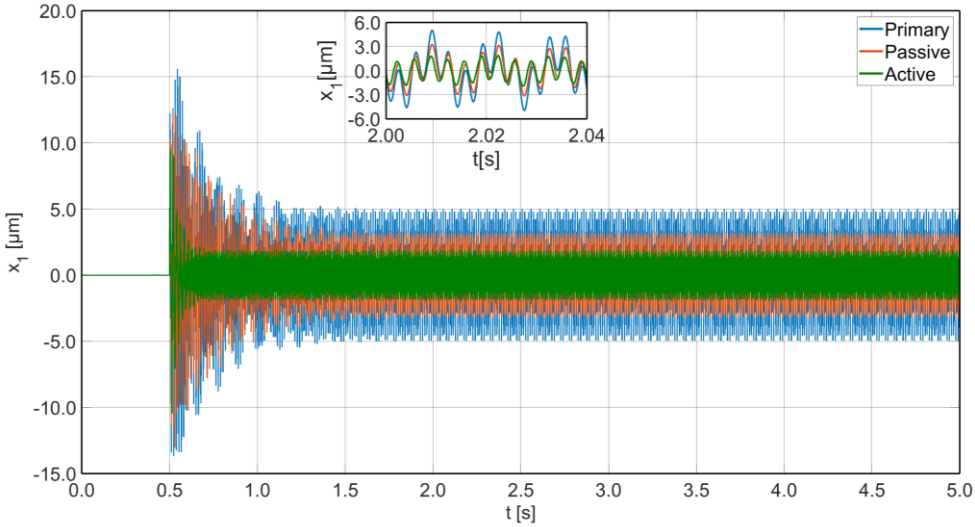

Figure 39. Test 4 time plot: Primary (blue), Passive (red), and Active (green).

Test 5, depicted in Figure 40, presents a disturbance with two harmonics at 80 Hz and at 160 Hz. The amplitude of each peak remains the same as for Test 4. The contraction of the final displacement under the external disturbance shows a ~90% containment for the 80 Hz peak (±0.2 µm) and a ~63% for the second harmonic (±0.9 µm).

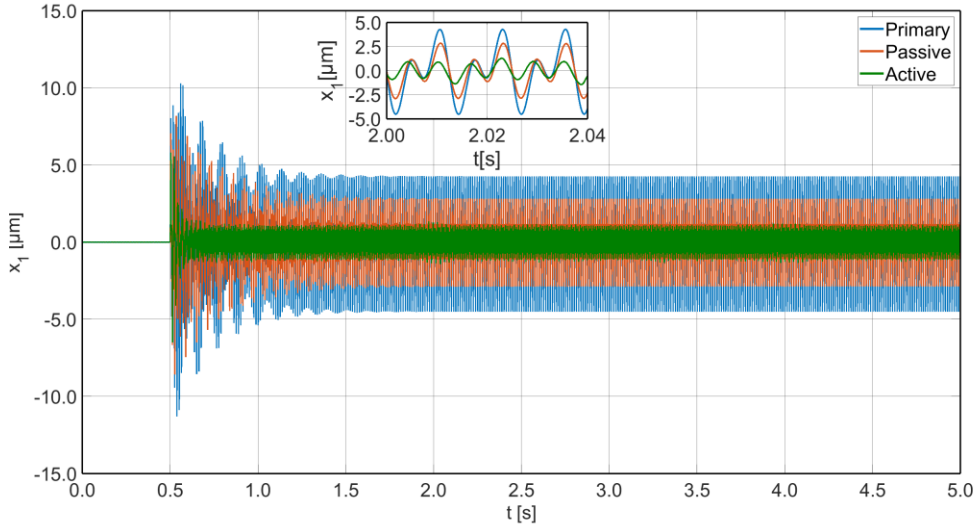

Figure 40. Test 5 time plot: Primary (blue), Passive (red), and Active (green).

Finally, Test 6 results, depicted in Figure 41, presents another two-harmonic disturbance with a 150 Hz component and a 300 Hz component. This test, as stated for the cascade control scheme, has the highest hysteretic influence due to the higher frequency components, hence the reduction in the final performance. Nonetheless, the active device reduced the amplitude of both peaks, with a final peak of ±1.2 µm for the 150 Hz component, and of ±1.6 µm for the 300 Hz one. Indeed, the controller obtains a 52% contraction for the first peak and a 36% contraction for the second one.

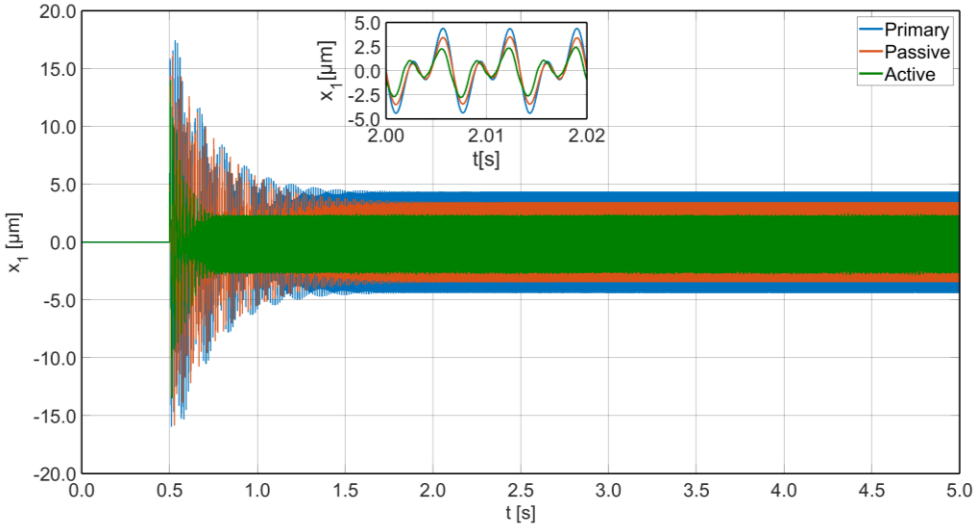

Figure 41. Test 6 time plot: Primary (blue), Passive (red), and Active (green).

The PEA displacement for the last test is presented in Figure 42, considering the saturation of the control action for the exerted disturbance. The constrained displacement with respect to the [0 µm, 28 µm] span is due to the hysteresis effect. Furthermore, the amplitude variations at steady state are generated by the position feedback and the accelerometer noise employed to obtain this measurement.

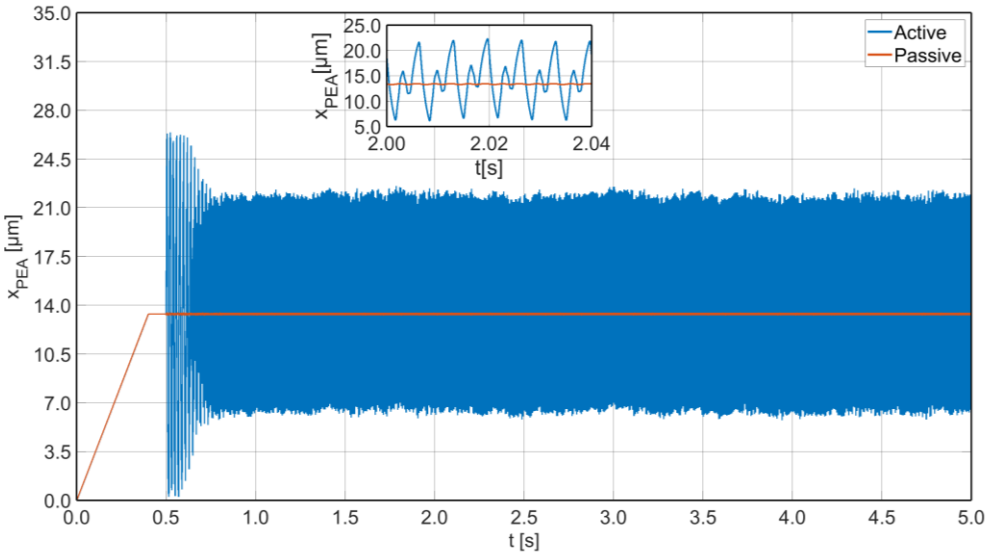

Figure 42. Test 6: PEA displacement for the passive scheme (Passive) and the active scheme (Active).

The performance obtained for the deployed controller assess its capabilities and robustness in terms of external force amplitude control. Furthermore, despite the absence of a direct control and limitation of the PEA displacement, the results obtained during the different tests, and the corresponding hysteretic behaviour, showed that the necessity of an inner loop was not justified.

Finally, the active approach reduced the displacement disturbances within the frequency interval of interest (80 Hz – 300 Hz) of more than 30% in the worst-case scenario, assessing the active device capabilities.

4.3 Active Workpiece Holder Control

High-precision machining requires significant contribution to limit the inherent disturbances and reduce the vibrational issues. The active workpiece holder device is a parallel kinematic machine with three vertical PEAs that are used to position the workpiece holder and contain the process disturbances. The motion equations were introduced previously along with the corresponding approximations and considerations.

The controller is implemented for the MIMO (Multiple-Input-Multiple-Output) system, employing the collocated measured position signal as feedback input for each axis. The controller has two main configurations, internally linked through a bumpless switching scheme to avoid sudden loads on the voltage input to the PEAs. The first scheme corresponds to a set-point following tuned controller based on a PID, with both a derivative and set-point weight and an integrator anti-wind up. The controller allows multi-frequency disturbances containment, usually present in machining, with harmonic disturbances, related to the rotation velocity of the spindle-tool system, and non-harmonic components, such as chatter. Both disturbances characteristics are employed to validate the system capabilities in the simulated environment.

The detailed AWH model is implemented in MATLAB (Simulink) environment, the corresponding scheme for the piezoelectric actuator and the hysteretic component are shown in Figure 17 and Figure 18. The mechanical structure that links the three actuators is implemented in a MIMO state-space scheme to account for coupling disturbances and multiple-disturbances. Such system is defined with a force input and an actuator displacement as output, for each line. The containment performance, taking into consideration the positioning capability of this device, is compared to the open loop scheme obtained without voltage input to the controller.

As before, the PEA actuator is first required to reach half its maximum displacement to permit the maximum oscillations amplitudes whilst protecting the PEA from over-elongations/contractions.

4.3.1 Coupling Effect and Nonlinear Considerations

The coupling effects of the platform is modelled through the developed state-space model. The bode diagram for the corresponding transfer function is presented in Figure 43. Despite creating a non-negligible disturbance between the actuators, no specific decoupling scheme is implemented to avoid any mis-modelling disturbances

which would need a further increment in the robustness requirement for the synthesised controller.

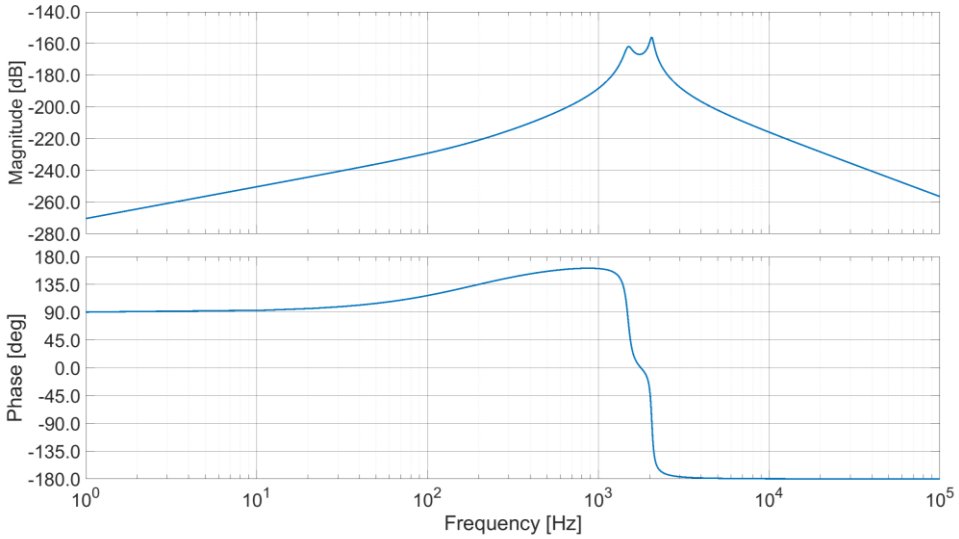

Figure 43. AWH coupling bode diagram: magnitude (top) and phase (bottom)

As the main task of this device is to correctly position the workpiece, the controller will have to both position the workpiece and handle the external disturbances. Hence, for this case scenario is particularly important to take into account the influence of the PEA inherent nonlinearities: creep and hysteresis.

Conversely to other applications where the hysteretic behaviour requires complex and accurate models of the real system to develop feedforward components to linearize the PEA motion, the goal of this research is to evaluate the controller capabilities under this kind of disturbances. Hence, a standard parametrization was implemented to simulate these characteristics and define the controller robustness. Both the creep and hysteresis models outputs can be observed in Figure 44, where the hysteresis was implemented based on the Bouc-Wen modified scheme. A frequency related component was designed to simulate the hysteresis loop dependency upon the frequency variation, and the non-symmetric component was also included.

The consequent plot produced by the hysteresis component lacks the creep influence to permit the individual study and consideration of both characteristics. The hysteresis obtained, shown in Figure 44, depicts a containment of the maximum displacement due to the reduction in the voltage produced. The voltage axis is obtained based on the expected voltage, as stated before the modelled characteristic is simulated as a voltage inherent modification before the PEA structure. This association produces the limited displacement and a simil-rotation behaviour of the produced voltage-displacement curve.

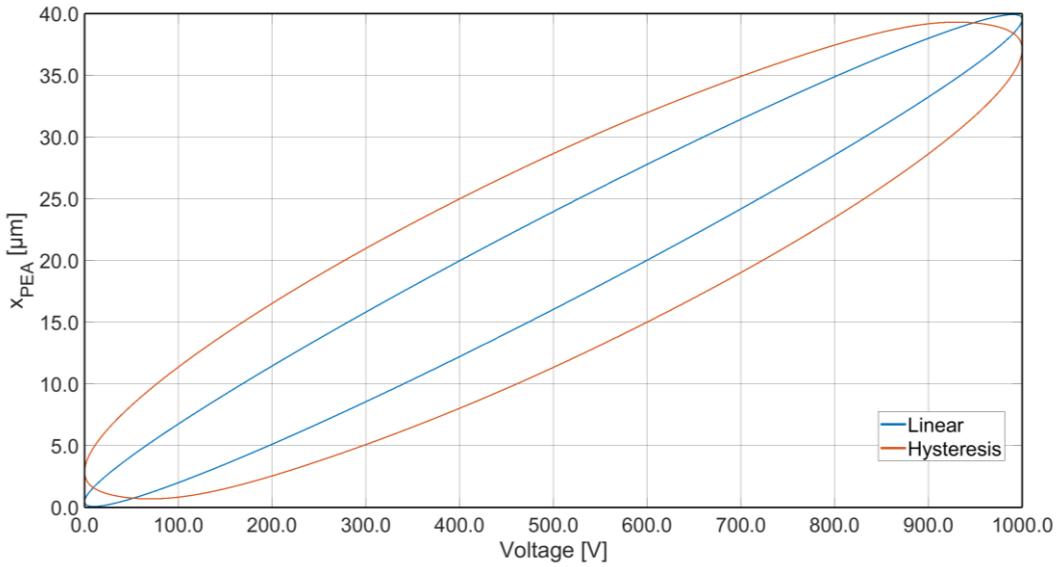

Figure 44. AWH nonlinear hysteresis curve for a 500 V at 200 Hz input voltage.

The hysteretic component is hence modelled as a major disturbance in the obtainable maximum displacement of the PEA, constraining the corresponding device performance. Both nonlinear disturbances will be included in the following simulation and are taken into account to synthesise the corresponding controller for the MIMO device.

4.3.2 Bumpless Switching PID Controller

The proposed controller for this application is based on the PID industrial controller and is defined in its standard ISA form as follows:

$$u_{PID} = K_p \left((bSP - Y) + \frac{T_d s}{1 + \frac{T_d s}{N}} (cSP - Y) + \frac{1}{T_i s} (SP - Y) \right) \quad \textbf{52}$$

where SP is the set point signal, Y is the measured output, K_p is the proportional gain, T_i is the integral time constant, T_d is the derivative time constant, b is the set point weight, and c is the derivative weight. Moreover, a back-calculation scheme is provided introducing an add-on parameter, the tracking time constant (T_t), that is obtained as $T_t = \sqrt{T_i \cdot T_d}$. This factor supports the saturation avoidance by regulating the integral action.

Two different sets of parameters are defined to comply with the two process phases: (1) tracking trajectory to reach the required configuration, and (2) disturbance rejection phase during which the machining process is executed and hence the controller must maintain the initial set-point. Considering the usual approach for other applications, a step input is employed to assess the controller's tracking performance; in fact, the main goal is to avoid an overshoot and contain oscillations. These requirements along with the absence of motion during the machining process, allows to obtain the initial tracking controller.

Afterwards, the disturbance rejection scheme is tuned, which conversely will avoid step-like as reference input or disturbance; however, an integrator is employed to maintain the set point. To evaluate the effectiveness of the synthesised controller, a series of single-frequency and multi-frequency disturbances are employed in simulation accounting for harmonic forces and not, similar to what is expected from a machining process. Furthermore, the disturbances won't start suddenly at its maximum amplitude but will pursue a dynamic increment to simulate the tool initial interaction with the workpiece. Considering the limitations due to the inherent hysteresis and creep characteristics, along with the expensive electronics, the frequency interval of interest is defined from 100 Hz to 1,000 Hz.

In summary, during the initial positioning phase the platform is affected by limited disturbances, with static or low-frequency contributions as the interaction between tool and workpiece is still null. Once the cutting tool reaches the workpiece higher disturbances appear, whose frequency content depends on the vibration's source. Hence, the two controllers require a bumpless-switching scheme to avoid a controller disturbance during the control switch. The aforementioned considerations were taken into account for the parameters' tuning. The initial tracking phase pursues high stability margins (phase margin higher than 75°) with a low-frequency bandwidth to produce a first-order response within the frequency of interest; the consequent parameters obtained produced the closed loop presented in Figure 45, where the magnitude is obtained with micrometre displacement.

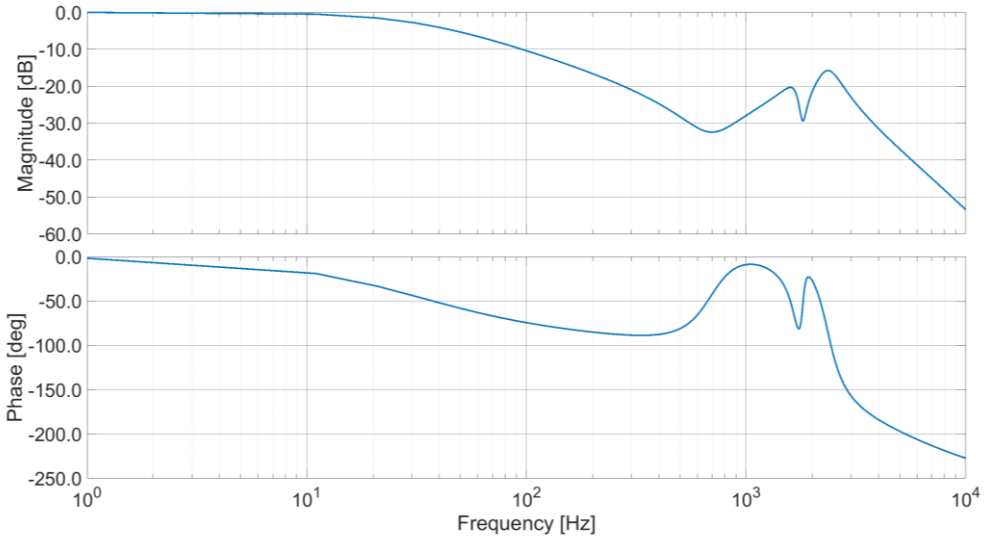

Figure 45. AWH closed loop bode diagram for tracking phase.

Conversely, the disturbance rejection phase's parameters are defined to maximize the containment in the frequency interval of interest. Due to the inner disturbance produced by the simulated hysteretic component the final performance is lower than expected. The initial approach has been to neglect any considerations upon the hysteresis model whilst tuning the parameters, however, issues related to the inherent constraint depicted the major influence of this disturbance in the stability of the final controlled

system. In fact, a low-pass approximation is employed to define the PID parameters for this phase; including this hysteretic basic information allows to improve the results whilst retaining a higher robustness. The PID rejection scheme is used to produce the closed loop model presented in Figure 46a; where the transfer function represents the influence of the input force disturbance to the corresponding displacement produced in micrometres.

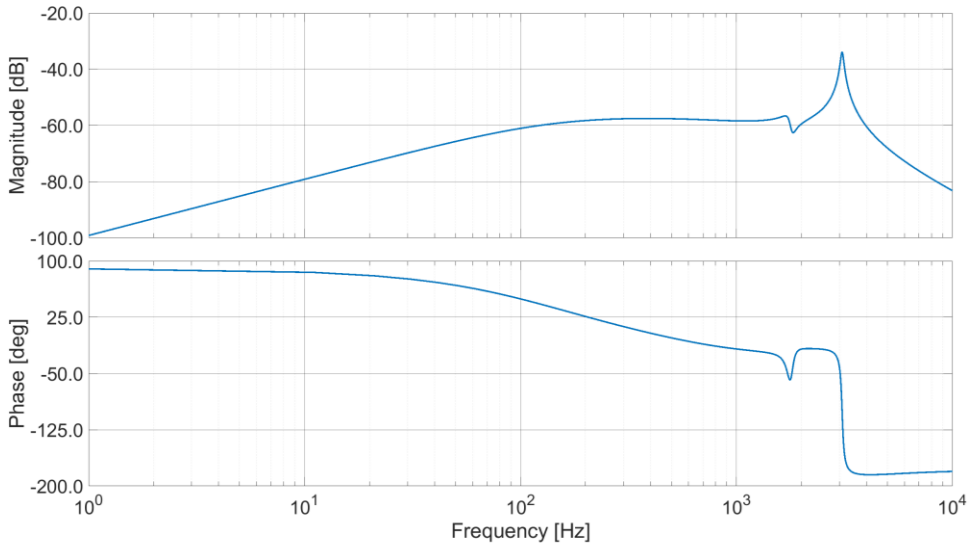

(a)

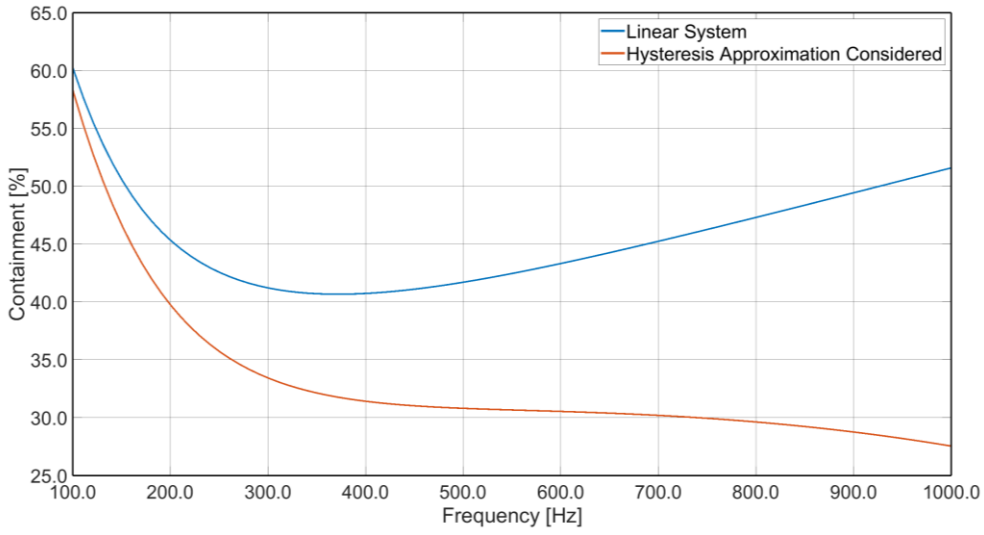

(b)

Figure 46. AWH closed loop disturbance rejection: (a) bode diagram; (b) percentual containment within the range of interest.

The overall performance in terms of percentual containment is presented in Figure 46b. The minimum containment without hysteresis considerations, blue curve, is obtained between 300 Hz and 400 Hz, with a containment of almost 40% of the final displacement; conversely, the maximum containment is obtained at the extremes of the frequency interval: 60% at 100 Hz, and 51% at 1,000 Hz. These promising results do not

consider the hysteresis disturbance, which reduces the controller performance, therefore, by assimilating the nonlinear hysteresis to a basic element (a low-pass filter) a higher fidelity of the result is obtained as represented with the red curve in Figure 46b. In this scenario, the containment is reduced, particularly for higher frequencies, obtaining thus a minimum containment at 1,000 Hz of 28% and a maximum at 100 Hz of 58%. Despite including an approximation of the hysteresis disturbance, the curve does not consider the effects of the complementary nonlinearities of such behaviour. In fact, the results obtained during the simulated tests show a lower performance for the containments, with a minimum value of ~25%.

To evaluate the effectiveness of the proposed controller, a series of experiments were conducted in a simulation environment. The initial experiments assess the positioning capabilities of the tracking controller with step inputs: a vertical positioning (z) test; a rotation around the X-axis (ϑ_x); and a rotation around the Z-axis (ϑ_y). The three tests take into a certain position and orientation the platform, and after 0.5 s return to the initial zero position; during this period there is no controller switching as no external disturbances are applied.

The pure vertical motion is obtained with an equal input for all three PEAs, in this case of 20 µm. The simultaneous input allows to maintain the orientation of the platform during the transient motion; furthermore, the equivalent displacement keeps the orientation at its home position, which has null rotation. The test, shown in Figure 50, assess the step-tracking performance of the set-point following controller, without any overshoot nor influence of the nonlinearities, particularly from the creep effect. The settling time for z-displacement, with a 2% threshold, is 0.016 s.

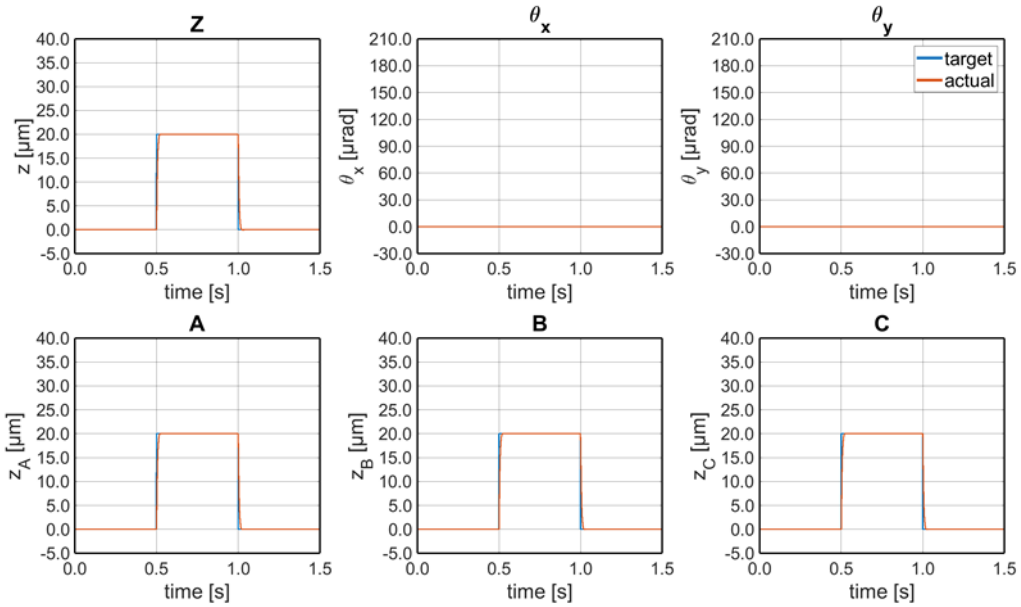

Figure 47. Vertical motion with null orientation test.

To proceed with the tracking performance assessment the following test, presented in Figure 48, shows a rotation around the X-axis with a constant z-displacement of the centre of mass at 20 µm. Considering the disposition of the actuators, to produce

the wanted orientation the PEA in position A is elongated up to 30 µm while the remaining actuators are positioned at 15 µm, resulting in a 185.2 µrad rotation around the X-axis. The controller positioned the workpiece holder with a settling time, with a 2% threshold, of 0.018 s. Furthermore, no appreciable overshoot is observed.

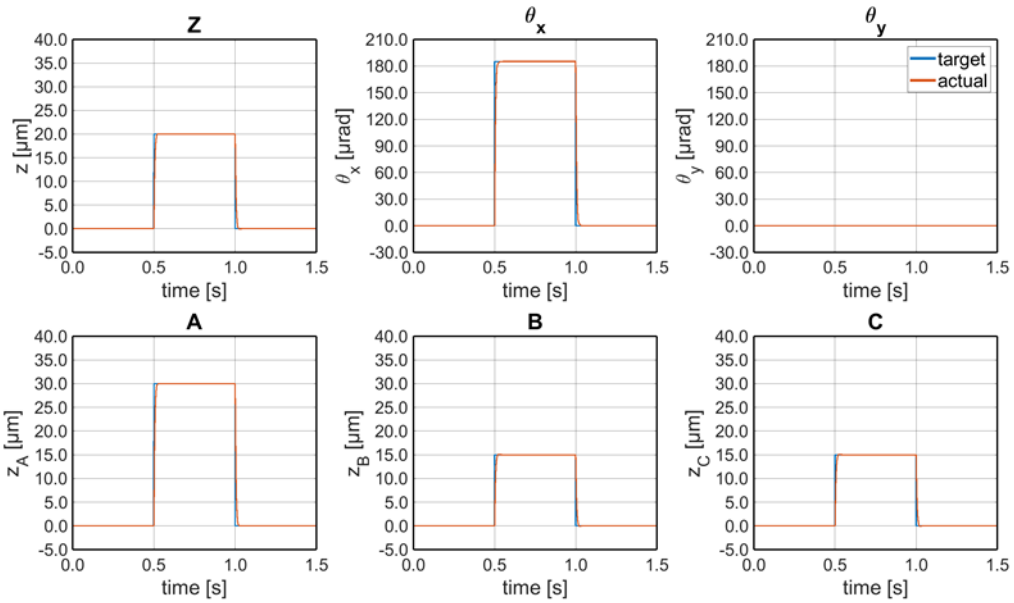

Figure 48. Vertical motion with rotation around X-axis test.

Finally, the last motion is a rotation around the Y-axis as presented in Figure 49, while maintaining the z-position at 20 µm. The corresponding motion is a 107 µrad rotation, obtained with the following PEAs configurations: 20 µm, 15 µm, and 25 µm for A, B, and C, respectively. The positive rotation value is due to the higher displacement imposed to actuator C with respect to PEA B. As for the previous tests, no significant overshoot is observed and the test shows a 2% settling time of 0.018 s.

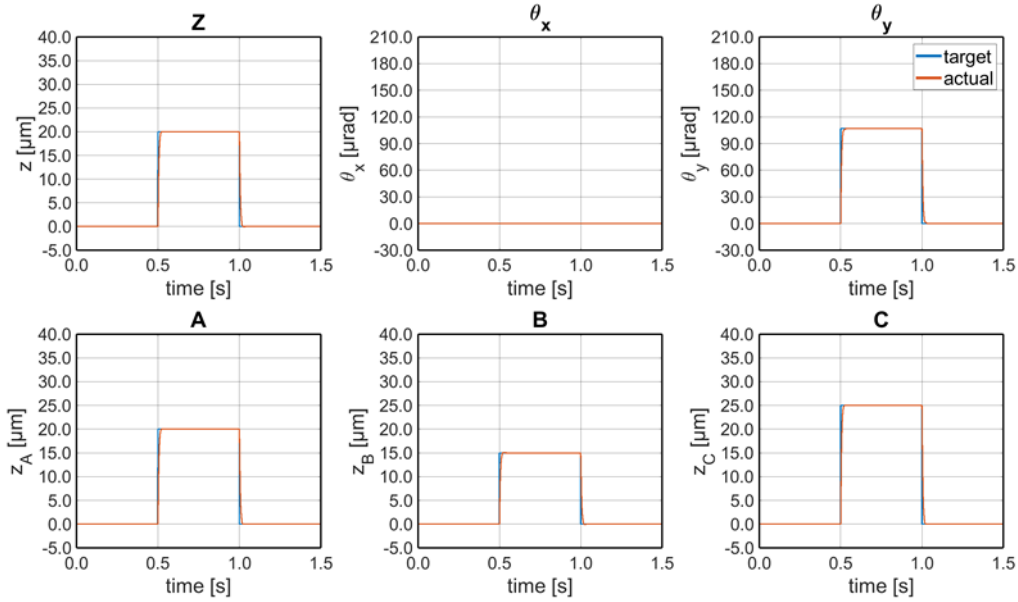

Figure 49. Vertical motion with rotation around Y-axis test.

The results obtained assess the set-point following capabilities of the synthesised controller. Due to the coupling effect and the high-amplitude steps as all the input signals are in the vicinity of half the maximum displacement of the PEAs, the presence of a small, less than 0.5 μm, overshoot during the Y-axis rotation is observed. Nevertheless, step-signals are to be avoided in the real application to avoid PEAs breakage due to high inertial loads. Indeed, considering the lack of any time requirement for the initial positioning phase, ramp signals should be employed.

To further validate the proposed controller, a set of simulated tests is proposed by including single-frequency and multi-frequency disturbances for the three degrees of motion ($[z, \vartheta_x, \vartheta_y]$). For each test an initial phase of platform positioning is implemented along with a final phase to return to base; the initial platform position is chosen as half the maximum PEA displacement, and hence corresponds to a vertical motion along the Z-axis. This set-point following phases are carried out with step input signals to provide coherent reasoning with respect to the tracking validation phase. Differently from the previous tests, for these cases the presence of bumpless switching between the two controllers is a necessary design to avoid unwanted inner disturbances due to differences between the parameters' values of both synthesised regulators. The switching between controllers is executed at 0.9 s and at 4.1 s for all the tests. The implemented tests are listed in Table 1, for each test a minimum frequency disturbance (100 Hz), maximum frequency (1,000 Hz), and harmonic disturbances (500 Hz + 1,000 Hz) are defined. Finally, a multi-disturbance test is presented to assess the control capabilities for disturbances arising to all three degrees of motion.

Table 2. Disturbance tests information.

Name	Test	Disturbance Amplitude [kN]			Disturbance Frequency [Hz]
		A	B	C	
z-disturbance	1	3.0	3.0	3.0	100.0
	2	3.0	3.0	3.0	1,000.0
	3	3.0	3.0	3.0	500.0
					1,000.0
ϑ_x-disturbance	4	3.0	-1.5	-1.5	100.0
	5	3.0	-1.5	-1.5	1,000.0
	6	3.0	-1.5	-1.5	500.0
					1,000.0
ϑ_y-disturbance	7	0.0	-3.0	3.0	100.0
	8	0.0	-3.0	3.0	1,000.0
	9	0.0	-3.0	3.0	500.0
					1,000.0
Multi-Disturbance	10	3.0	-3.0	-1.5	500.0
		0.0	-1.5	3.0	700.0

Tests 1 to 3 correspond to disturbances along the Z-axis, hence equal forces were applied for all three actuators. The first simulation is carried out with a 100 Hz frequency,

and the results are depicted in Figure 50, where both the open loop (OL) and closed loop (CL) final displacements are presented. The perturbation along the Z-axis generated a displacement for the OL case of 6.66 µm which was contained of 56.5% with the deployed controller, obtaining a final displacement of 2.90 µm. The same values were obtained at actuators' line due to the mechanical dependency between the PEAs and the corresponding z-coordinate. The disturbance containment capability of the controller is constrained at higher frequencies due to the inherent nonlinearities of the PEA, as shown in Figure 46, hence a conservative difference is expected between the OL and CL results for the 1,000 Hz disturbance, Test 2. In this case, presented in Figure 51, the OL displacement is of 6.53 µm whilst it is contained of 24.5% with the CL, producing a final displacement of 4.93 µm.

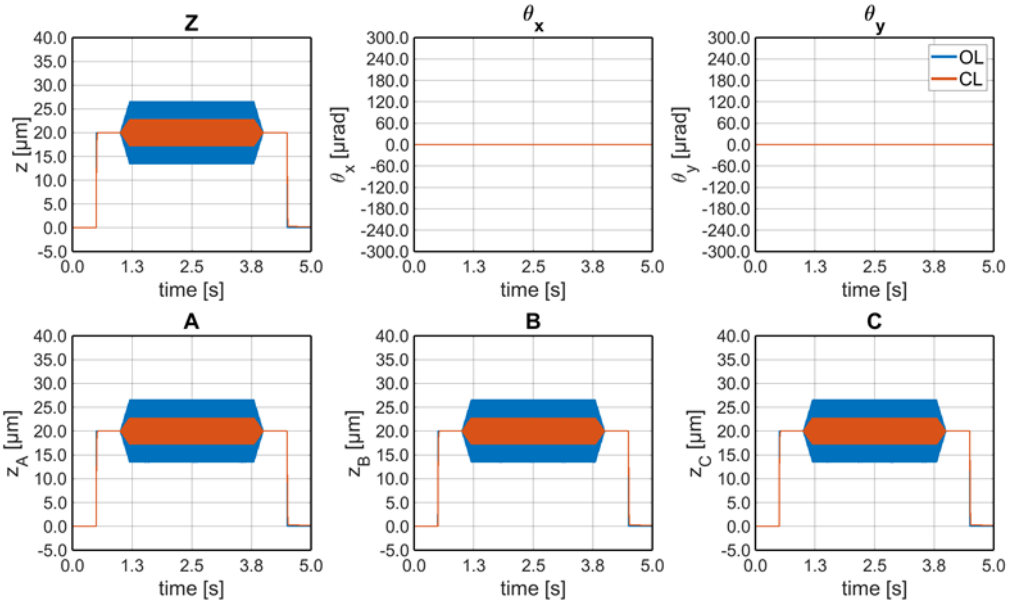

Figure 50. Test 1: 100 Hz results for z-disturbance.

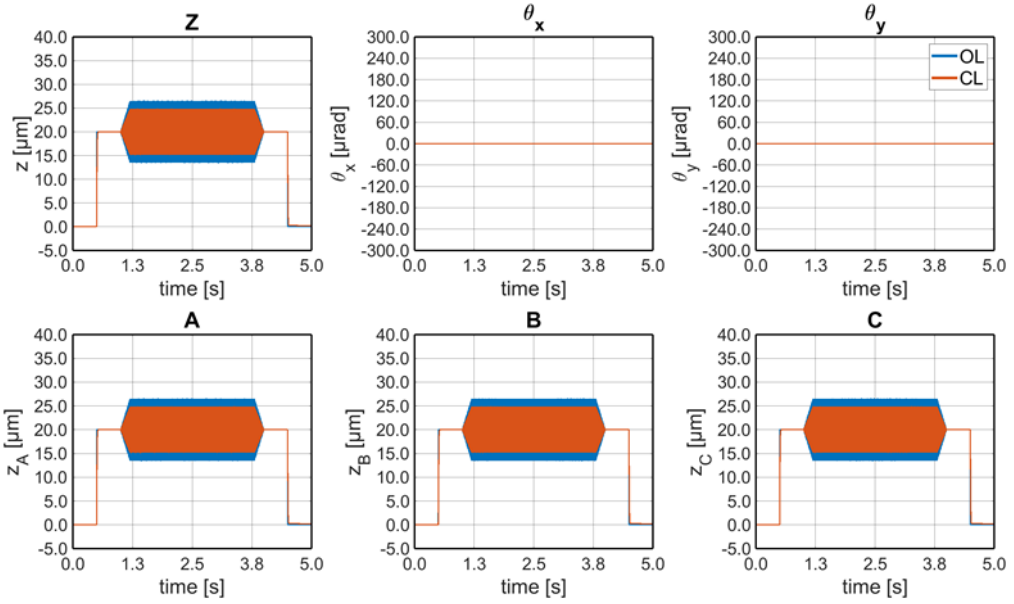

Figure 51. Test 2: 1,000 Hz result for z-disturbance.

Finally, Test 3, depicted in Figure 52, is the last z-disturbed simulated experiment; differently from the previous tests, a multi-frequency harmonic disturbance force is employed with a 500 Hz and a 1,000 Hz component. The CL contains the initial 6.54 µm and 6.53 µm to 4.57 µm and 4.90 µm for the lower frequency and higher frequency, respectively; with a percentual containment of 30.1% for the 500 Hz component and of 25.0% for the 1,000 Hz one.

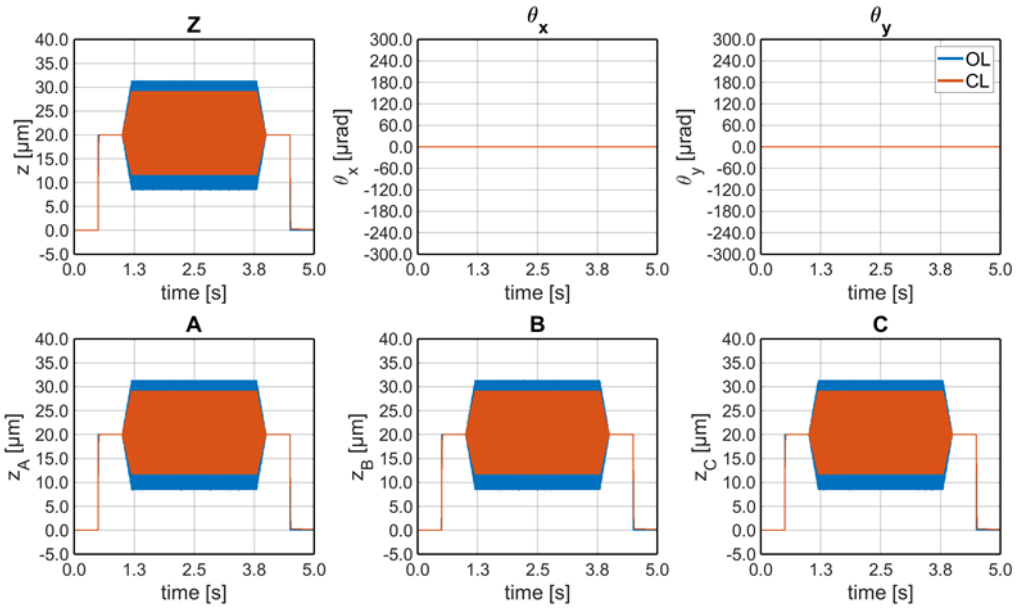

Figure 52. Test 3: Multi-frequency result for z-disturbance.

The following tests, Test 4 to 6, change the disturbance type, in these cases the perturbed direction corresponds to the rotation around the X-axis, hence ϑ_x. In order to maximize the capability of the control action a z-positioning is first required and thus the 20 µm value for the Z-axis. The perturbation is produced by applying counterphase forces to point A with respect to points B and C, for which the phase is identical. This mechanical design produces equal disturbances to B and C.

The initial simulation employs a disturbance at 100 Hz, for which the three PEAs axes and the three degrees of motion displacements are presented in Figure 53. The OL rotation around the X-axis is equal to 123.56 µrad, which is contained with the CL scheme up to 54.72 µm, a 55.7% containment. Nonetheless, the controller action should be also presented in terms of PEAs displacement error considering that the control action aims to contain them; in fact, point A shows a displacement of 6.67 µm for the OL scheme, which is further contained with the CL scheme of 56.5% resulting in a 2.90 µm displacement. The remaining PEAs, B and C, present a lower displacement disturbance as the perturbation force has smaller amplitude; indeed, the OL displacement for these is of 3.34 µm, contained afterwards with the disturbance controller resulting in a 1.53 µm final displacement (CL) with a 54.2% containment.

Similarly, Test 5, presents a 1,000 Hz perturbation around the x-axis. As stated, the results obtained are expected to be constrained due to the inherent nonlinearities of the PEA actuator. Henceforth, the higher frequency test presented in Figure 54 shows an

OL displacement amplitude for the direction of motion of 145.50 µrad, which in terms of PEAs displacements correspond to: 7.86 µm for A, 3.93 µm for B, and 3.93 µm for C. These perturbed displacements are contained with the CL scheme, obtaining a rotation of 108.98 µrad, 25.1% containment, for ϑ_x; a displacement along A of 5.82 µm, 26.0% containment, and a displacement for B and C of 3.00 µm, with a 23.7% containment.

Both Test 4 and 5 show no displacement variation for the Z-axis nor rotation around the Y-axis. Nonetheless, the multi-frequency test, Test 6, presented in Figure 55, shows a perturbed z-variation under 0.5 µm, which is produced by harmonic perturbation addition.

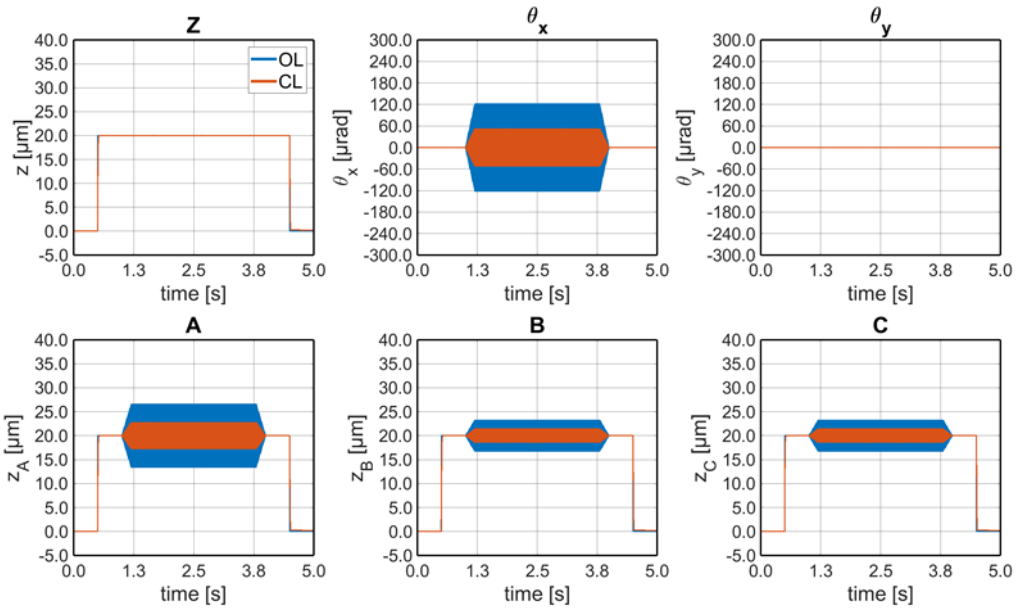

Figure 53. Test 4: 100 Hz results for ϑ_x-disturbance.

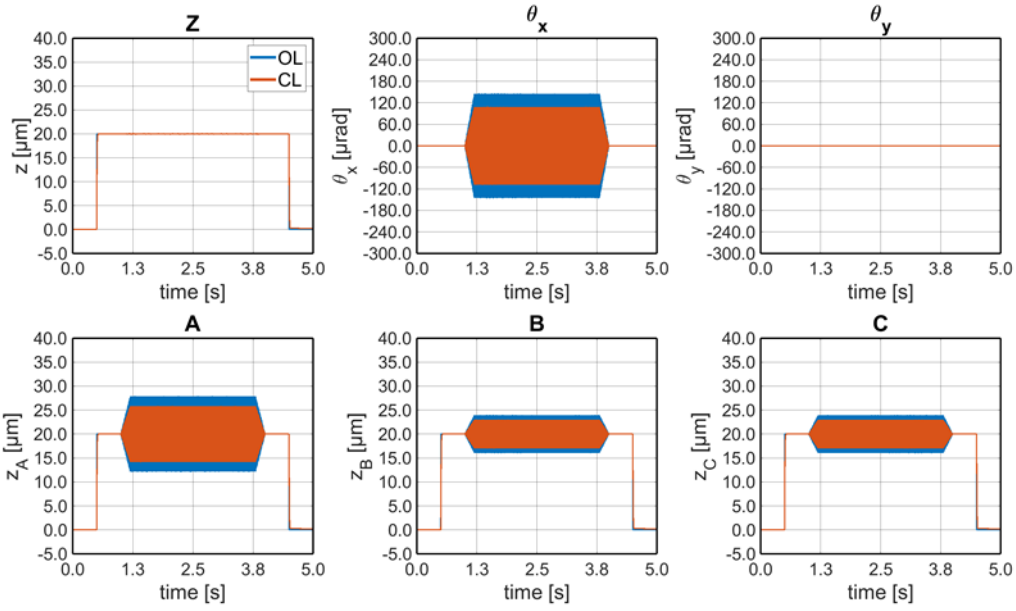

Figure 54. Test 5: 1,000 Hz results for ϑ_x-disturbance.

Finally, Test 6 presents a harmonic disturbance with a 500 Hz and 1,000 Hz components around the X-axis. The CL contains the axis of motion ϑ_x of 30.3% for the first peak and of 25.5% for the higher frequency component, with a reduction of the OL values from 126.89 µrad and 145.50 µrad to 88.46 µrad and 108.36 µrad, respectively. The result in terms of PEA motion shows a containment for PEA A of 31.0% for the 500 Hz component reducing the initial 6.85 µm up to 4.73 µm, and of 26.5% for the 1,000 Hz component, from 7.86 µm to 5.78 µm. PEA B and C instead, show a containment of 28.9% for the 500 Hz peak, with a reduction from 3.42 µm to 2.43 µm with respect to the OL, and of 23.7% for the higher frequency component, with a final displacement of 3.00 µm from the 3.93 µm of the OL.

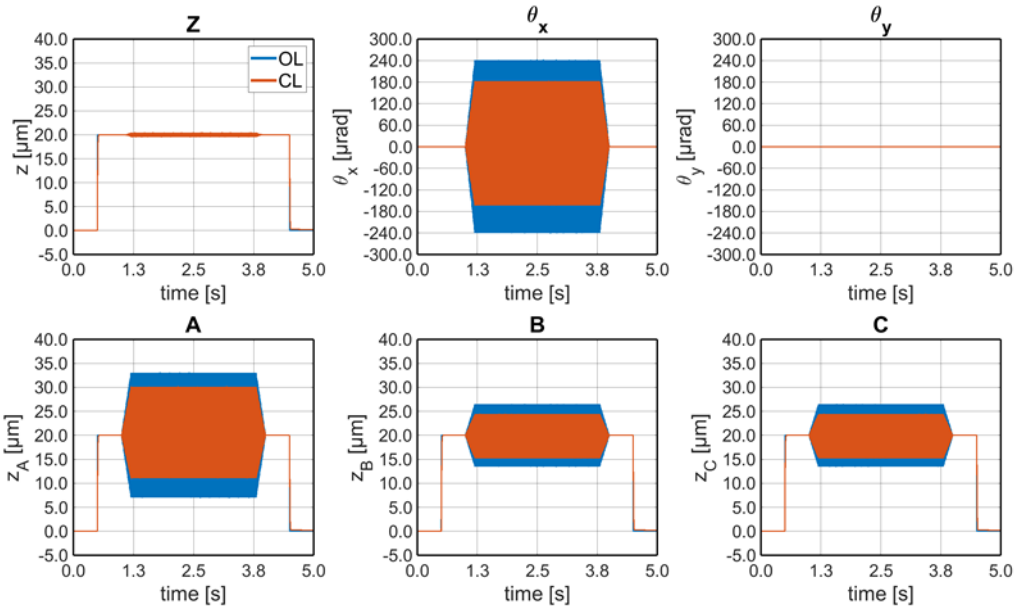

Figure 55. Test 6: Multi-frequency results for ϑ_x-disturbance.

The degree of motion to assess is the rotation around the Y-axis (ϑ_y), similar to the alternative rotation around the X-axis discussed before, the system is taken into a predefined position (20 µm) and the PEAs are disturbed to produce the wanted perturbation. In fact, to produce a rotation around the Y-axis, actuator A is kept still at the predefined position whereas B and C are actuated in counterphase between each other. The initial test, Test 7 presented in Figure 56, shows an OL perturbed rotation of 142.68 µrad, which corresponds to a motion of actuators B and C of 6.67 µm. These disturbances are contained of 56.5% for the CL scheme with a final rotation of 62.08 µrad and a displacement of 2.90 µm. The percentage containment is equal for the perturbed directions due to the nature of the disturbed axis of motion.

Test 8 presents a 1,000 Hz disturbance around the Y-axis, with an OL rotation of 168.00 µrad as shown in Figure 57; the perturbed motion generates a displacement of actuators B and C of 7.86 µm. The CL scheme contains 26.1% of these motions, with a final rotation of 124.21 µrad, and a motion of B and C of 5.81 µm. Similar to Tests 2 and 5, the containment capability of the synthesised controller are limited for higher frequencies with respect to lower components, as in Test 7.

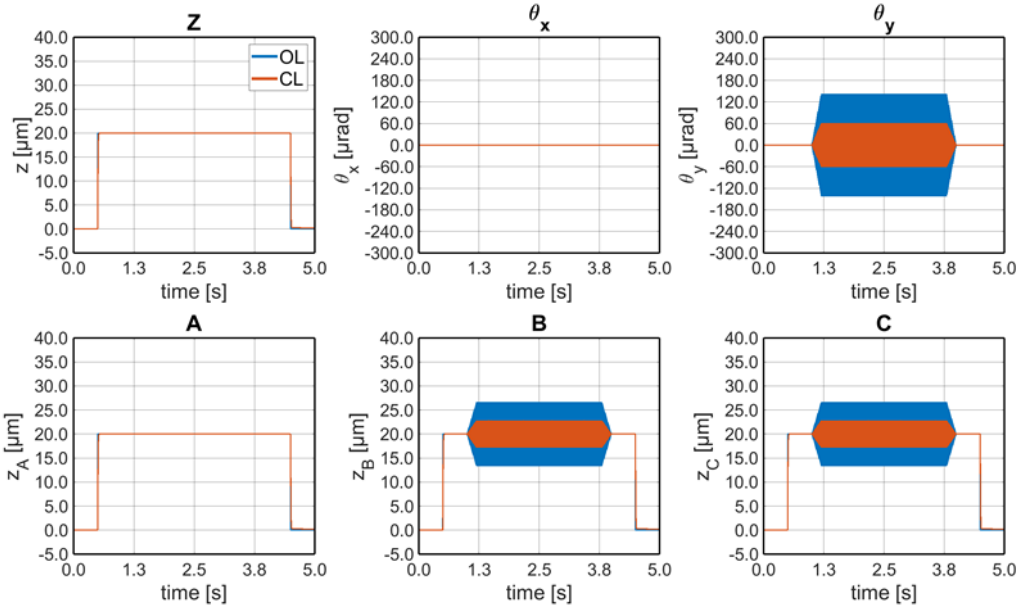

Figure 56. Test 7: 100 Hz results for ϑ_y-disturbance.

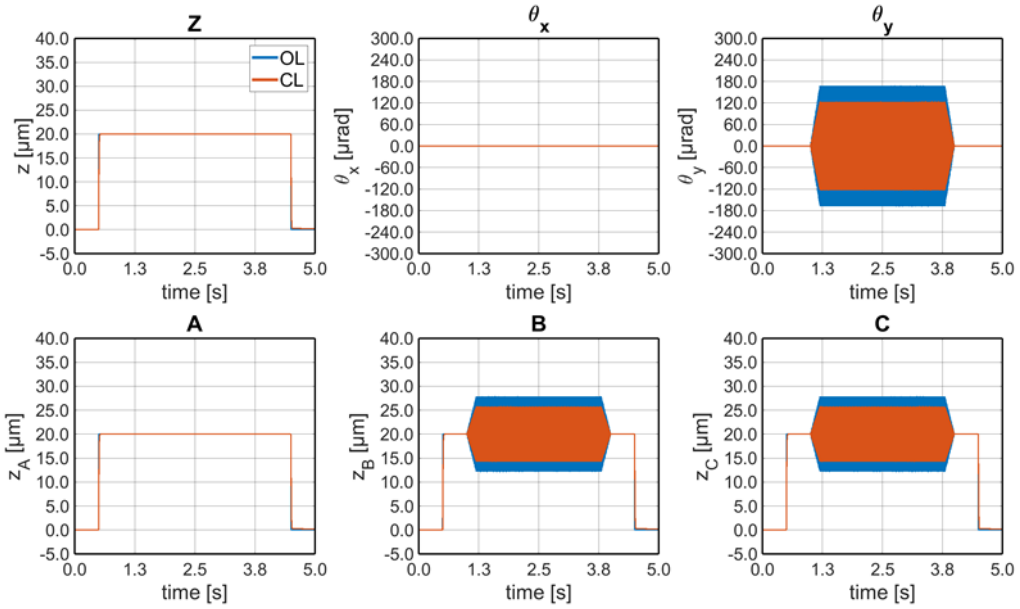

Figure 57. Test 8: 1,000 Hz results for ϑ_y-disturbance.

Similar to Test 3 and 6, Test 9 presents a harmonic disturbance with two frequency components: 500 Hz and 1,000 Hz. The results presented in Figure 58 show a rotation for the lower frequency component of 146.52 µrad and of 168.00 µrad for the higher one. In terms of PEAs displacements instead, it produces a perturbed motion of 6.85 µm at 500 Hz and of 7.86 µm at 1,000 Hz. The proposed controller contains the unwanted motion of 30.8% for the lower frequency component and of 26.1% for the higher one, with a final rotation of 101.42 µrad and 124.14 µrad respectively. The CL PEAs displacement instead shows a final motion of 4.74 µm for the 500 Hz peak and of 5.81 µm for the 1,000 Hz.

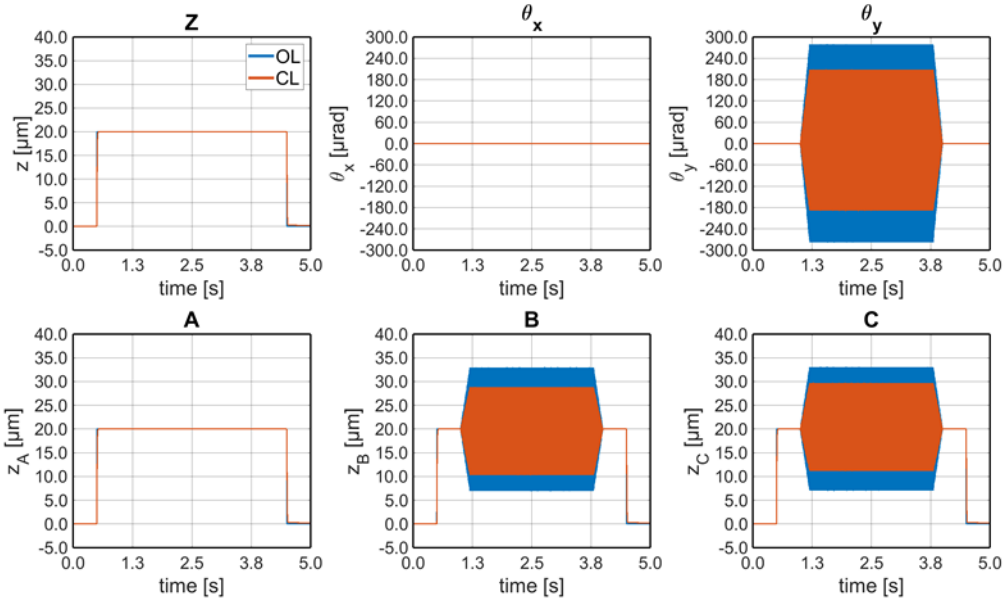

Figure 58. Test 9: Multi-frequency results for ϑ_y-disturbance.

Finally, the last test corresponds to a multi-axes disturbance where the three degrees of motion are perturbed at two different non-harmonic frequencies: 500 Hz and 700 Hz. The results of Test 10 are depicted in Figure 59 for both the OL and CL schemes. The synthesised controller contains the corresponding motion disturbances from a minimum of 27.0% for the ϑ_y-disturbance at 500 Hz up to 31.2% for the z-disturbance at 500 Hz. The corresponding PEAs displacement is contained from 6.90 µm, 6.80 µm, and 3.37 µm at 500 Hz to 4.94 µm, 4.85 µm, and 2.35 µm for A, B, and C, respectively. The 700 Hz disturbance instead presents an OL PEA's displacement of 0.37 µm, 3.24 µm, and 6.79 µm which are contained with the CL up to 0.20 µm, 2.35 µm, and 4.91 µm, for A, B, and C, respectively.

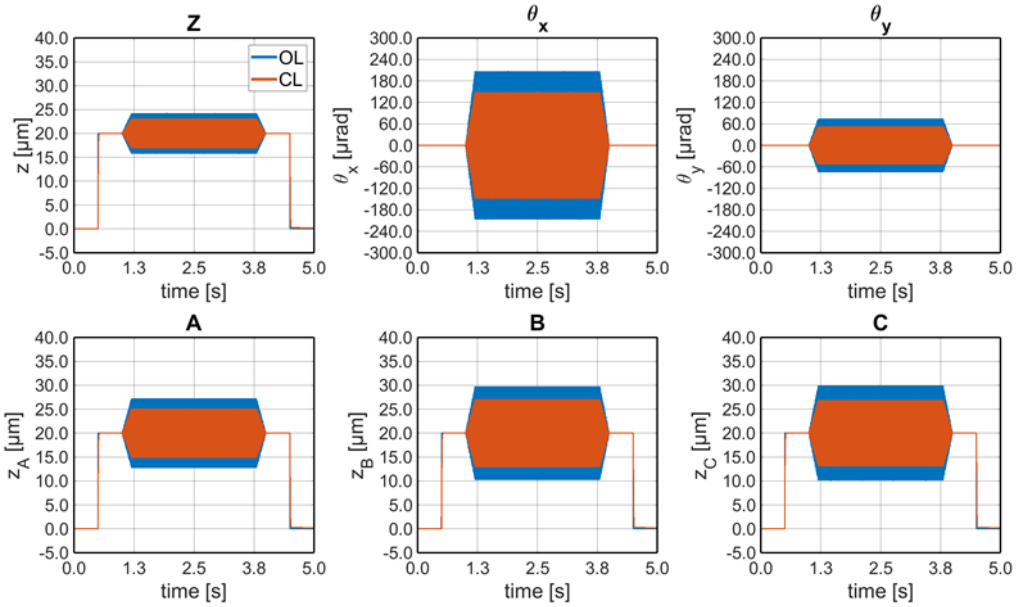

Figure 59. Test 10: Multi-perturbation along the three degrees of motion.

Based on the simulated scenarios, the synthesised bumpless switching controller is assessed, in both the initial and final tracking phase, and the intermediate disturbance rejection task. Under the inherent nonlinearities of the PEAs the proposed controller managed to contain the external disturbances of a minimum of ~24%. The results obtained with the presented tests for both the axis of motion ($[z, \vartheta_x, \vartheta_y]$) and the PEAs displacement axes ([A, B, C]), validate the deployed controller in the frequency interval of interest: 100 Hz to 1,000 Hz. The corresponding numerical values are listed in Table 3 for the axes of motion and in Table 4 for the individual actuators; for each test the open loop (OL) error, the closed loop (CL) error, and the percentual containment (%) are presented.

Table 3. Results obtained for the axes of motion.

T	F [Hz]	z [µm]			ϑ_x [µrad]			ϑ_y [µrad]		
-	-	OL	CL	%	OL	CL	%	OL	CL	%
1	100.0	6.66	2.90	56.5	-	-	-	-	-	-
2	1000.0	6.53	4.93	24.5	-	-	-	-	-	-
3	500.0	6.54	4.57	30.1	-	-	-	-	-	-
	1000.0	6.53	4.90	25.0	-	-	-	-	-	-
4	100.0	-	-	-	123.56	54.72	55.7	-	-	-
5	1000.0	-	-	-	145.50	108.98	25.1	-	-	-
6	500.0	-	-	-	126.89	88.46	30.3	-	-	-
	1000.0	-	-	-	145.50	108.36	25.5	-	-	-
7	100.0	-	-	-	-	-	-	142.68	62.08	56.5
8	1000.0	-	-	-	-	-	-	168.00	124.21	26.1
9	500.0	-	-	-	-	-	-	146.52	101.42	30.8
	1000.0	-	-	-	-	-	-	168.00	124.14	26.1
10	500.0	1.09	0.75	31.2	148.04	105.48	28.7	36.63	26.75	27.0
	700.0	3.24	2.36	27.2	65.76	47.25	28.1	37.97	27.45	27.7

Table 4. Results obtained for the individual PEAs.

T	F [Hz]	A [µm]			B [µm]			C [µm]		
-	-	OL	CL	%	OL	CL	%	OL	CL	%
1	100.0	6.66	2.90	56.5	6.66	2.90	56.5	6.66	2.90	56.5
2	1000.0	6.53	4.93	24.5	6.53	4.93	24.5	6.53	4.93	24.5
3	500.0	6.54	4.57	30.1	6.54	4.57	30.1	6.54	4.57	30.1
	1000.0	6.53	4.90	25.0	6.53	4.90	25.0	6.53	4.90	25.0
4	100.0	6.67	2.90	56.5	3.34	1.53	54.2	3.34	1.53	54.2
5	1000.0	7.86	5.82	26.0	3.93	3.00	23.7	3.93	3.00	23.7
6	500.0	6.85	4.73	31.0	3.42	2.43	28.9	3.42	2.43	28.9
	1000.0	7.86	5.78	26.5	3.93	3.00	23.7	3.93	3.00	23.7
7	100.0	-	-	-	6.67	2.90	56.5	6.67	2.90	56.5
8	1000.0	-	-	-	7.86	5.81	26.1	7.86	5.81	26.1
9	500.0	-	-	-	6.85	4.74	30.8	6.85	4.74	30.8
	1000.0	-	-	-	7.86	5.81	26.1	7.86	5.81	26.1
10	500.0	6.90	4.94	28.4	6.80	4.85	28.7	3.37	2.35	30.3
	700.0	0.37	0.20	45.9	3.24	2.35	27.5	6.79	4.91	27.7

Chapter 5

Experimental Tests

This chapter introduces the experimental campaign for the spindle active vibration control device. First, the electronic devices and scheme are introduced. Then, the piezoelectric actuator motion limitation due to the power amplifier and the flexures, springs, elements is described. Finally, the experimental campaign is depicted in two parts, an initial low-frequency to assess and validate the device functioning and a higher-frequency test bench to evaluate disturbances within the range of interest.

5.1 Introduction

The spindle active device has been prototyped for the compelling experimental campaign. The test bench development has two main stages, an initial low-frequency validation phase, out of the device real frequency boundaries, introduced to avoid the piezoelectric power amplifier low-pass behaviour with the available electronics; and a second stage with higher frequencies, for which several disturbance sources were encountered, such as hysteresis and the amplifier filter behaviour. Both phases required the inclusion of a flange adapter to link the primary structure to the device. This flange, presented in Figure 60, has been ideated to permit the addition of the studied device on standard spindle housings.

Figure 60. Device flange adapter.

The test benches required an initial structural study for the main resonance frequencies identification. The corresponding models were created based on a first-order scheme and their parameters were computed through a set of pulley tests. In fact, a pulley system was constructed, with which a known mass was used to obtain a static perturbation. The produced displacements were measured and, hence, the stiffness along the studied axis derived. This approach permitted to define the frequency intervals to perturb the primary structure whilst maximizing the obtainable displacement. Finally, the coupling characteristics were also derived to account them during the system assessment.

Based on the results obtained during the pulley tests, the initial low-frequency interval was defined within 14 Hz and 20 Hz. This limited interval was evaluated to assess the synthesised controller. Moreover, the test bench showed high coupling disturbances due to the primary structure, hence the controller was also validated for this typology of perturbations. Afterwards, the second system permitted to assess the controller capabilities in an interval from 95 Hz to 140 Hz. Differently from the low-frequency scheme, in this new structure the proportional controller (P) included a derivation part (PD) and, hence, the two variations were evaluated and compared. This structure showed limited coupling disturbances that were therefore neglected during the control validation.

As stated before, the spindle device exerts forces in two orthogonal directions. For each axis an inertial structure containing a moving mass, a set of flexures, and a piezoelectric actuator is employed. Furthermore, each mass has an accelerometer at its centre of mass to measure the produced motion; in fact, during the simulation phase, the acceleration was employed to derive the PEA displacement for the cascade control. Nonetheless, the simulation campaign showed higher robustness and containment capabilities for the industrial rejection scheme and, hence, the inner acceleration was neglected. However, despite the lack of information provided for the synthesised controller, the accelerometers can be used to accumulate data for machine learning schemes, for example for tool wear or breakage, for the machining centre within which the device is installed.

5.2 Electronics

The experimental scheme consisted of the mechatronic device, with two inertial actuation systems that used the piezoelectric stack PST 150/10/40 VS15 as actuator. Each axis had an eddy current displacement sensor, a KAMAN KD-2440 with a 5C probe; this is a high-precision, high-bandwidth sensor with compact electronics and negligible hysteresis on ferrous targets. Moreover, the external disturbances were generated with a PST 1000/16/40 VS25. Finally, the dSPACE 1104 controller board was chosen to link all the devices for the real-time closed loop control.

The electronic loops were driven with a host pc running both dSPACE and MATLAB/Simulink RTI environments, the driving analog voltages (±10V) of the board were amplified to feed the corresponding input to the PEAs with a consequent offset. During the closed-loop mode, the measured displacement with the eddy current sensor was acquired through the ADC port and the output voltage was computed correspondingly for the synthesised controller. Furthermore, a graphical interface has been produced in dSPACE environment to assess the signals of interest and interact with the device. Figure 61 presents the electronic schematic diagram representative of the aforementioned elements and connections.

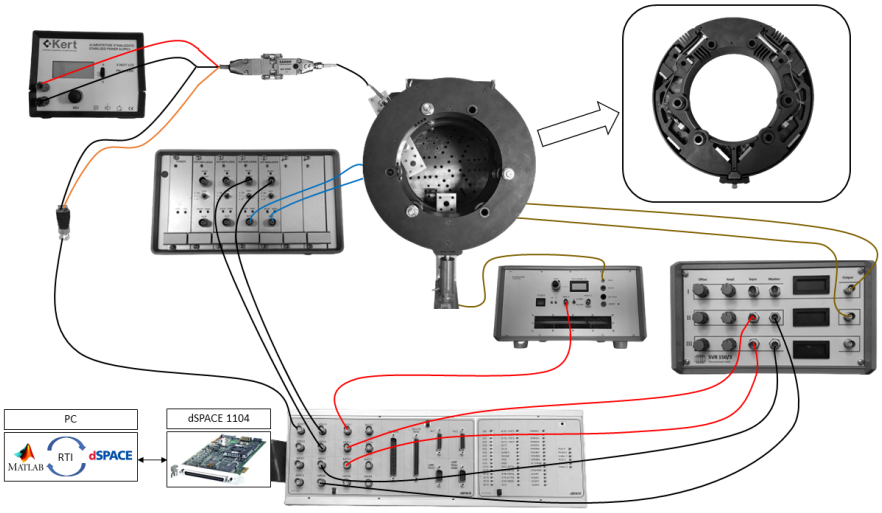

Figure 61. Electronic scheme for the experimental tests.

5.2.1 Controller Board

The RTI controller board and connector panel dSPACE 1104 were employed to perform the experimental tests. Considering future applications, and the controller performances and limitations during the simulation phase, the sampling frequency was set to 10 kHz. The method chosen for the data acquisition was the iterative sampling data saving, which collects a given number of samples and saves it afterwards in MATLAB format, easing the treatment of data collecting and study. Nevertheless, this approach required time to save the data and to restart the acquisition producing 1 s blocks between acquisition sets; indeed, even though the RTI system is still running, the data is not saved. The main characteristics of both the controller board and the connector panel are depicted in Table 5.

Table 5. Datasheet summary for dSPACE 1104.

Characteristic	Value
Processor	MPC8240 64-bit processor with PPC 603e core
CPU Clock	250 MHz
Cache Memory	2x16 KB
Global Memory	32 MB SDRAM
Flash Memory	8 MB
ADC	4 channels | ±10 V range | 12-bit
DAC	8 channels | ±10 V range | 16-bit

The controller board and connector panel have certain limitations in terms of performance, which requires explicit treatment and consideration for their use. The implemented electronic scheme presented in Figure 61 used the 4 12-bit sample-hold parallel ADC channels with ±10 V input range, resulting in a ±4.9 mV quantization error which cannot be neglected. Furthermore, the input conversion time required 800 ns but for the studied applications, due to the limited time lapse with respect to the sampling time, it can be neglected. In a similar way, the DAC channels employed had a 16-bit

resolution and an output range of ±10 V, with a quantization error of ±0.3 mV. Like the ADC ports, the maximum settling time of 10 μs can be neglected.

5.2.2 Feedback Sensor

The displacement feedback during the simulation case studies was derived from acceleration measurement from the primary structure; this choice was defined regarding the availability of accelerometers and their simple installation, accurate measurement, and working capabilities in machining environment. However, as the idea of the experimental campaign was to assess the device containment capabilities with an industrial controller, a direct displacement acquisition was performed to avoid disturbances arising from the displacement derivation. In fact, as stated before, an eddy current displacement sensor KAMAN KD-2440 with a 5CM probe was employed.

The sensor has a resolution of 0.3 μm with a bandwidth of 10 kHz. Its measuring range depends on the gain choice which is determined based on the corresponding knob rotation located in the signal conditioning and electronic module. The sensor's output relies on the power options and the type of measured material, as depicted in Figure 62a-b. The power required by the sensor corresponds to a continuous feeding voltage between 12 V and 24 V, which also determines the maximum output voltage from the sensor as can be observed in Figure 62a. Regarding these conditions, the experimental campaign performed employed a Kert KAT4VD stabilized power supply for the eddy current sensor.

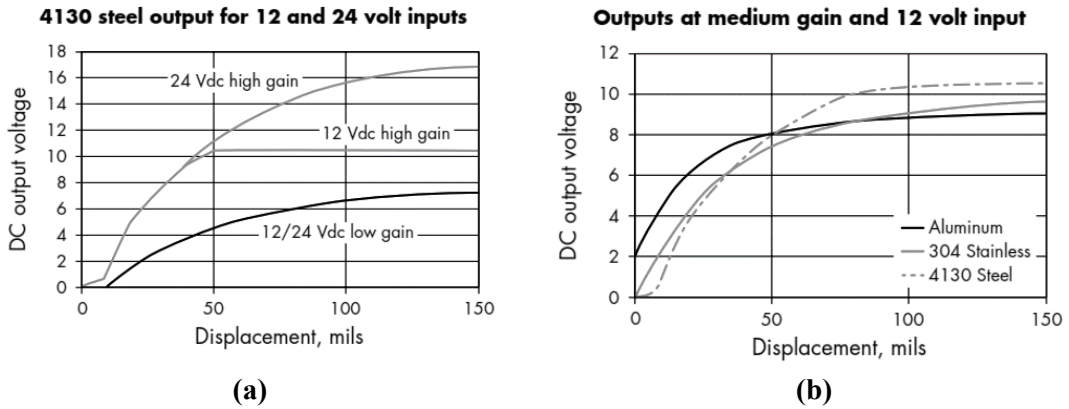

Figure 62. Gain curve dependency on: (a) Input Voltage; (b) Measured Material.

5.2.3 Disturbance Actuator

The perturbations upon the primary structure were generated with a piezoelectric stack actuator, a PIEZOMECHANIK PST 1000/16/40 VS25. This high-voltage PEA can exert a maximum force of 12,000 N whilst maintaining an open loop sensitivity at 10 mV of approximately 0.05 nm. Furthermore, the actuator has a maximum stroke of 40 μm, a capacitance of 360 nF, and a stiffness of 200 N/μm. The input voltage might vary from -200 V up to 1,000 V; however, regarding the studied application, this interval remained within the positive voltage range from 0 V to 1,000 V, which in terms of actuator motion corresponds to the solely elongation without contraction.

This actuator requires a power amplifier to convert the ±10 V control output up to the voltage range of interest. For this application the power amplifier employed was the dynamic amplifier LE500-200. It has an output range from 0 V to 500 V which limits the maximum elongation of the driven actuator as depicted in Figure 63, where the obtained Force/Displacement curve is presented. Differently from the 1,000 V curve, the limited voltage results in a blocking force of 4,000 N and a maximum displacement of 20 µm.

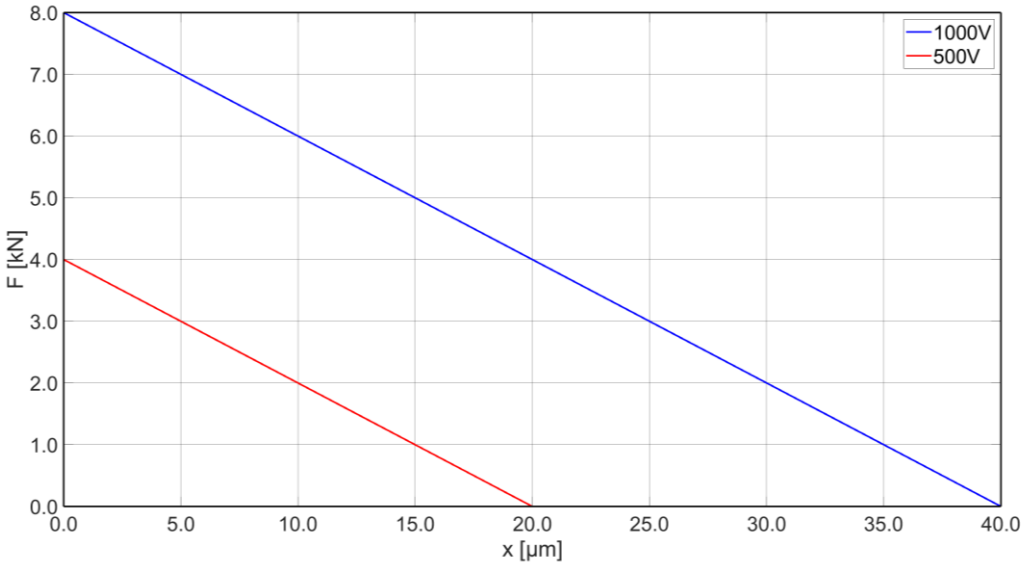

Figure 63. Force-Displacement plot for the PEA and amplifier employed.

Furthermore, the LE500-200 current characteristics are as follows: a current peak value of 2 A and an average current of 700 mA. The low capacitance of the PEA and the high-power availability of the chosen amplifier permitted to achieve a high-frequency range as verified in Figure 64a-b, where the peak and mean activations requirements are derived considering the PEA as a capacitance.

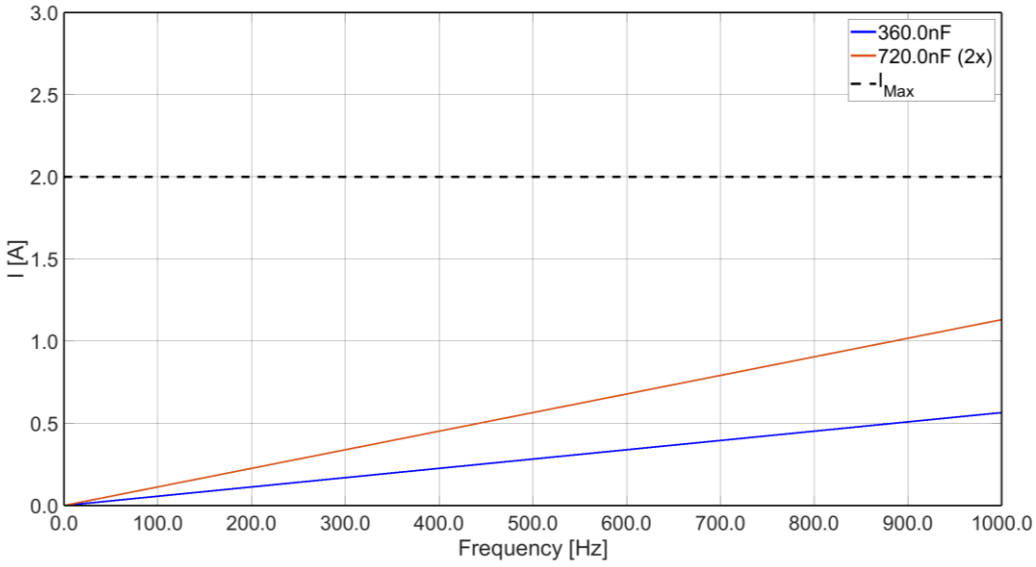

(a)

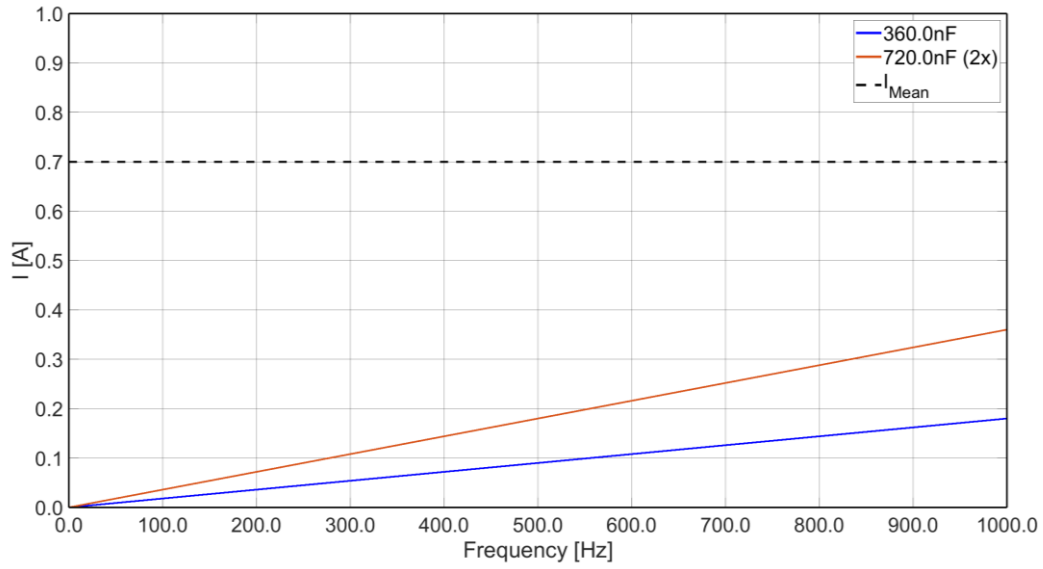

(b)

Figure 64. PST 1000/16/40 VS25 with LE500/2000: (a) maxium current-displacement frequency; (b) mean current-displacement frequency.

5.2.4 Internal Actuator

For the inner motion actuator, the PIEZOMECHANIK PST 150/10/40 VS15 was selected; a piezoelectric stack actuator with a maximum force generation of 3,500 N, a prestress force of 400 N and an open loop sensitivity at 1 mV of approximately 0.05 nm. The PEA has a capacitance of 7.2 µF, a stiffness of 60 N/µm, and a maximum stroke of 40 µm for the voltage span of -30 V to 150 V; however, the interest for this application remains in the corresponding elongation of the actuator and, hence, on the positive voltage range, from 0 V to 150 V.

The power amplifier employed for the PEA was the SVR150/3. It is driven by an input signal of ±10 V, its output voltage range is equal to the PEA interval, -30 V to +150 V, and can provide a 60 mA current peak. The initial step corresponds to the amplifier evaluation in terms of achievable motion and the explicit treatment of the consequent constraints. This treatment is depicted in Figure 65, where the peak activation was evaluated to determine the power amplifier driving capabilities based on the similarity between the PEA actuator and a capacitor.

The results obtained for this combination produced a low-pass behaviour in the corresponding PEA actuation. In fact, from 10 Hz frequency and above the feeding voltage from the amplifier was contained and it reduced the PEA's achievable displacement, with a variation dependent on the frequency considered. Indeed, two curves are depicted in Figure 65 corresponding to the unloaded application, datasheet capacitance value, and a loaded consideration which accounts for the increment of the relative capacitance during the active motion under load. This new capacitance value is approximated based on practical case scenarios, implementing a capacitance equal to the double of the ideal datasheet value.

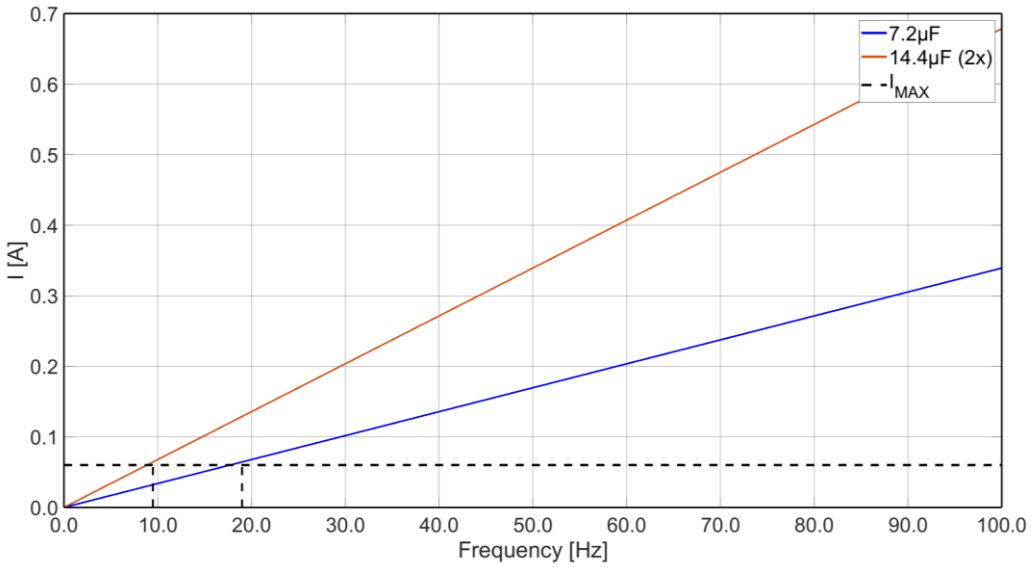

Figure 65. PST 150/10/40 VS15 with SVR150/3 maxium current-displacement frequency.

Furthermore, the Force/Displacement curve is evaluated to determine the achievable motion and blocking force. Figure 66 depicts a blocking force of 2,300 N and a maximum displacement of 40 µm for the unloaded case scenario. The final maximum displacement is contained due to the flexure system within the platform that behaves as a set of stiff elements. The stiffness value of the flexures was first estimated based on the FEM study of the internal structure of the platform, and the result was a value of 19.45 N/µm. Finally, the maximum displacement was measured experimentally with a micrometre obtaining a maximum displacement of 28.0 µm, corresponding to a flexure stiffness of 25.72 N/µm.

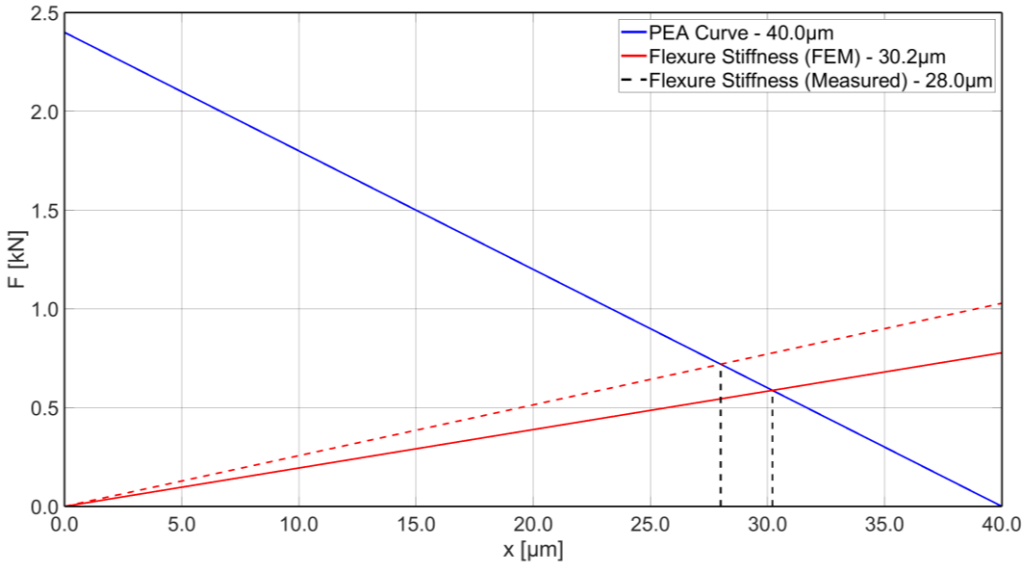

Figure 66. Force-displacement curve: (blue) PEA; (red) PEA + flexure stiffness estimation; (dashed red) PEA + flexure real.

5.3 Amplifier Model and Considerations

The combination of the PST150/10/40 VS15 actuator with the SVR150 amplifier created a containment of the driving voltage due to the amplifier power limits. Henceforth, by connecting the BNC monitor output from the SVR150 to the ADC on the dSPACE board the relative containment from expected and actual voltage was obtained. The amplifier behaviour was observed under load; therefore, the internal PEA was connected to the output connector of the SVR150, and several actuation sinewaves were applied. As expected from the power considerations, the amplifier output behaved as a low-pass filter for the expected signal which was hence approximated through the minimum square error; the obtained model is depicted in Figure 67.

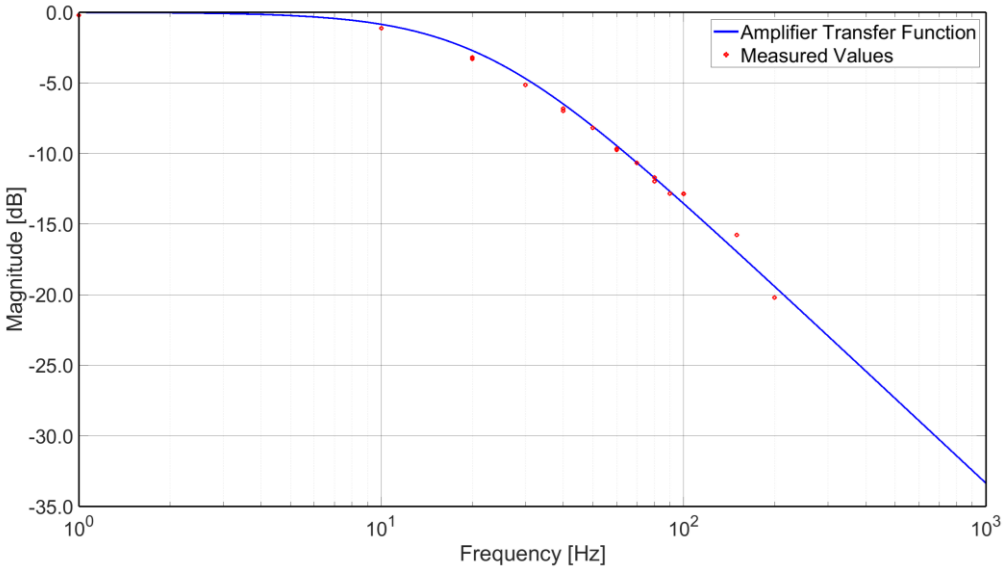

Figure 67. Amplifier behavior model.

This low-pass filter behaviour determines the maximum displacement of the actuator which means a corresponding limitation on the maximum obtainable force of the complete mechanism. In fact, the actuated force is obtained from the inertial force of the actuated mass, dependent on the acceleration exerted by the PEA. The acceleration of the mass is obtained as the second derivative of the position, whereby as the displacement is a sinewave movement, the acceleration will correspond to the amplitude multiplied by the square of the movement frequency. Therefore, by measuring the mass displacement and taking into consideration the previous model, the force (displacement)-frequency graph in Figure 68 is obtained.

The limitations encountered from the coupling effect between the available power electronics and the actuators defined a constrained frequency interval of motion for the experimental campaign. In fact, a maximum frequency in the vicinity of 120 Hz was considered for the experimental validation due to the limited amplitude of the obtainable motion and, hence, the consequent inertial forces.

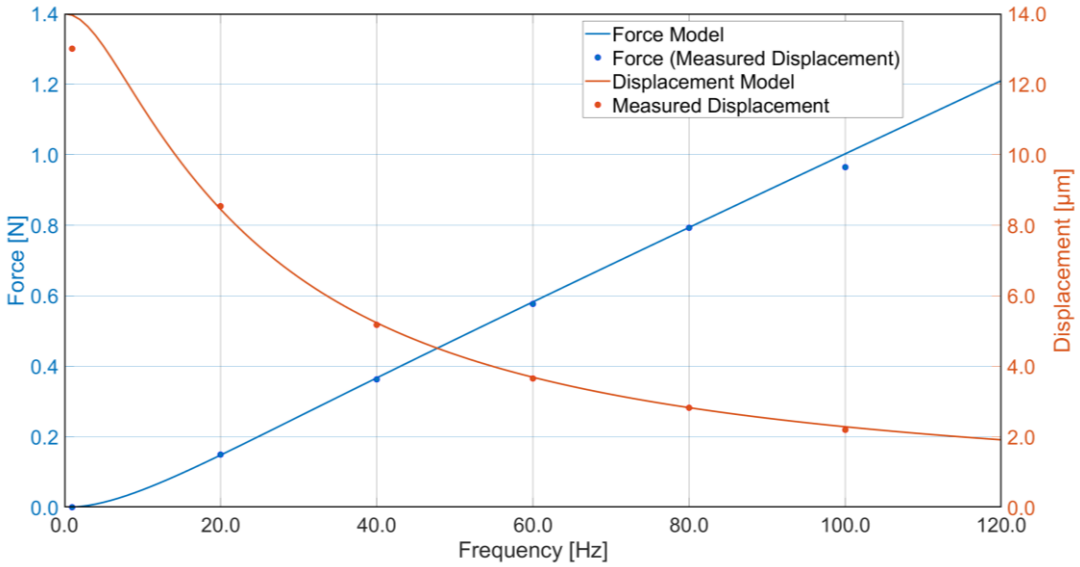

Figure 68. Force/Displacement with respect to the actuated frequency.

5.4 Test Bench: Low-Frequency Validation

The initial approach based on a low-frequency capability assessment to evaluate the controller capabilities while protecting the actuators as presented in Figure 69. The experimental test bench was constructed upon a steel base, connected to the latter with a set of steel brackets.

Figure 69. Test Bench: initial approach.

The proposed structure was first tested with the pulley system, obtaining the following stiffnesses: 0.22 N/µm for the X-axis and 0.17 N/µm for the Y-axis. In fact, the expected resonances were in the vicinity of 18 Hz for the X-axis and 16 Hz for the Y-axis. In order to validate these measurements, the external actuator was employed, positioned at 45° with respect to both X- and Y-axis. Afterwards, the coupling effect was also considered by evaluating the disturbances acquired during coupling motion without external disturbances. The containment of both perturbations was carried out with a

proportional controller for which the gain (*Kp*) parameter was tuned based on the simulated results and a fine-tuning iterative phase, to improve the performances by accounting the low-power amplifier characteristics.

5.4.1 X-Axis Experimental Tests

From the pulley measurements the resonance value was found to be near 18.00 Hz, however, a set of experimental tests showed that the actual resonance was at 15.75 Hz. The difference between these values might be due to the resolution limitation of the analogue micrometre measurements among other uncertainties within the developed pulley system. The found resonance was used to assess the controller capabilities, in fact around this frequency, the proportional controller (*Kp* = 120) managed to contain disturbance displacements of over ±2 µm. The tests performed upon the X-axis for both open loop (OL) and closed loop (CL) schemes are summarized in Table 6 with the external disturbances.

Table 6. Summary of the X-axis tests under external disturbances.

Test	Frequency [Hz]	Amplitude [V]	Containment [%]	OL [µm]	CL [µm]
1	15.75	250	85.7	2.1	0.3
2	15.75	125	100.0	0.9	0.0
3	15.75	125 before	100.0	0.9	0.0
		250 after	80.0	1.5	0.3
4	15.75	250 before	80.0	1.5	0.3
		125 after	100.0	0.6	0.0
5	10.00	50	-	0.0	0.0
	15.75	150	100.0	1.2	0.0
	20.00	50	-	0.0	0.0
6	14.50	50	-	0.0	0.0
	15.50	150	0.0	0.3	0.3
	16.50	50	-	0.0	0.0

Single Amplitude and Frequency:

Test 1 and 2 perturbed the primary structure upon the experimental resonance with different amplitudes (125 V, 250 V) and the proportional controller managed to contain the displacement within the sensor resolution. In fact, the synthesised controller limited the initial ±2.1 µm up to ±0.3 µm achieving an 86% containment; similarly, Test 2 showed a lower perturbation with a final displacement of ±0.9 µm contained completely with the controller. Figure 70 presents the time plot result for Test 1, the top figure corresponds to the measured displacement, the bottom figure is the external disturbance in volts, and in the middle graph the PEA power amplifier voltage is shown, it can be observed that even at this low-frequency test the amplifier behaves as a low-pass filter containing the "Expected" output. Furthermore, the "Real" measurement corresponds to the signal acquired from the monitor output, which due to the limited voltage of this port and the equivalent resolution of the ADC port in the controller board creates a 5 V resolution.

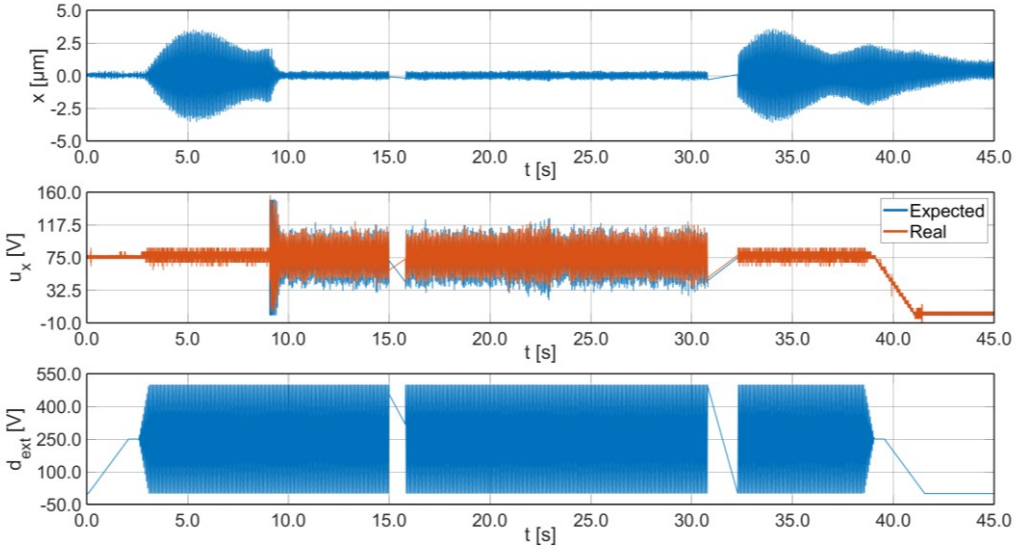

Figure 70. Time plot for Test 1 with a P controller whose voltage is shown before (Expected) and after (Real) the power amplifier.

Varying Amplitude with Single Frequency:

Differently from the previous tests, Tests 3 and 4 employed a single frequency disturbance upon the primary structure but they presented a sudden amplitude variation with the external actuator. The aim was to evaluate the controller under an instantaneous stress. In both situations the controller managed to contain the dynamic variation of the external disturbance and, hence, the consequent displacement of the primary structure. In fact, Test 3, depicted in Figure 71, shows an almost complete disturbance containment. Furthermore, the amplitude variation at 18 s presented no sudden output difference, whereas the controller action was amplified to counteract the higher disturbance.

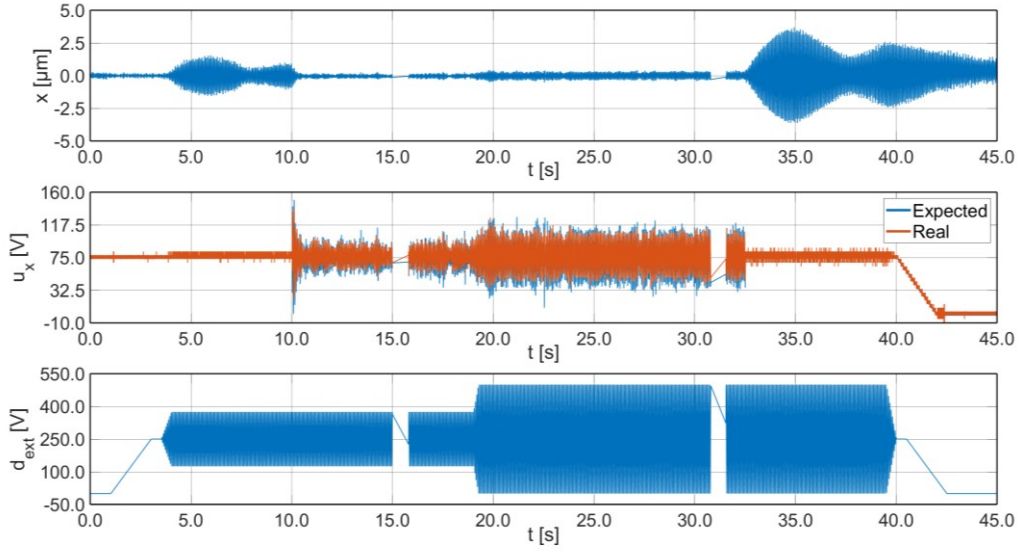

Figure 71. Time plot for Test 3 with an amplification of the disturbance.

Test 4 showed similar results to Test 3, except that in this experiment the contrary path was pursued. In fact, the perturbation was reduced after 18 s as it is easily observed in the controller output plot in Figure 72. The synthesised regulator constrained the two displacements completely considering the sensor resolution.

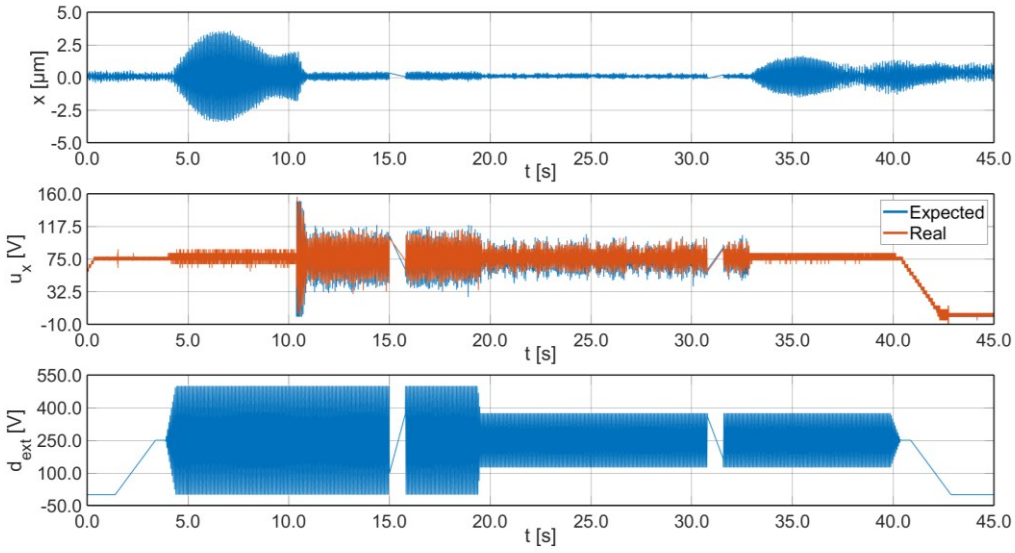

Figure 72. Time plot for Test 4 with a reduction in the disturbance amplitude.

Multifrequency Tests:

The multifrequency tests (5 and 6) showed no amplitude disturbances on the measured displacement. In fact, the narrowband within which the frequencies could be selected to test the system constrained the multi-frequency perturbation into a single peak near the resonance while the rest of the frequency components were filtered.

Coupling Considerations:

A high coupling was encountered between the X- and Y- axes during the initial tests, created by the developed structure. Hence, considering the small displacements achieved during the external disturbance phase, the coupling interaction was used to increase the observable error and further assess the control capabilities with higher displacement disturbances. In fact, the tests in Table 7 were obtained employing the Y-axis actuator as disturbance source and the X-axis one as controller. The disturbance amplitude is presented in terms of the actuator's input voltage; indeed, two inner columns show the *expected* input and the *real* value obtained from the monitor output in the PEA power amplifier.

Table 7. Summary of the X-axis tests under coupling disturbances.

Test	Frequency [Hz]	Amplitude [V]		Containment [%]	OL [µm]	CL [µm]
		Expected	Real			
1	15.75	75.0	55.6	33.9	17.7	11.7
2	15.75	60.0	45.3	41.7	10.8	6.3

3	15.75	37.5	29.2	88.2	5.1	0.6
4	15.75	18.75	15.4	85.7	2.1	0.3
5	20.00	75.0	54.7	0.0	0.6	0.6
6	15.75	30.0	22.4	92.9	4.2	0.3
	20.00	45.0	33.7	0.0	0.3	0.3
7	10.00	15.0	13.2	-	0.0	0.0
	15.75	45.0	34.3	90.5	6.3	0.6
	20.00	15.0	11.2	100.0	0.3	0.0
8	14.50	15.0	11.3	0.0	0.3	0.3
	15.50	45.0	34.4	57.1	2.1	0.9
	16.50	15.0	8.6	50.0	0.6	0.3
9	15.75	22.5	17.1	88.9	2.7	0.3
	35.00	15.0	8.6	-	0.0	0.0
	50.00	37.5	17.7	-	0.0	0.0

The first approach, Tests 1 to 4, exerted a force at the resonance frequency of the structure to study its effects on the coupling behaviour for various amplitudes. Due to a force limitation at low-frequencies and the mechanical scheme of the structure, the highest disturbances were contained but not eliminated completely, whilst under 6 µm the system managed to cancel the corresponding displacement as shown in Figure 73 where Test 3 is represented.

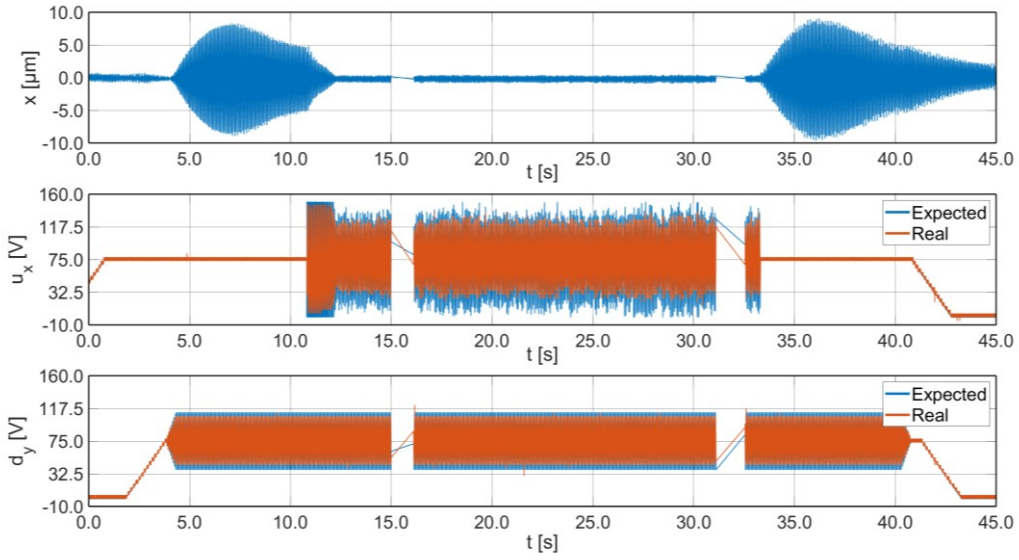

Figure 73. Time plot for Test 3 with an active controller.

It is important to remark the absence of displacement outside the resonance frequency narrow band. In this scenario, the multi-frequency tests (Tests 6 to 9) showed a single displacement peak in frequency near the resonance. Therefore, despite generating forces at different frequencies the system behaved as if a single frequency disturbance were applied. This is shown in Figure 74a, where the FFT of Test 7 is presented, being a representative subject of the multi-frequency group of tests.

Nevertheless, the time-plot, in Figure 74b, presents the multi-frequency disturbance and the corresponding multi-sinewave system. Similar results were obtained with a single frequency disturbance at 20 Hz of 75 V in Test 5 where the maximum displacement obtained was lower than 1 µm, hence no consideration was pursued.

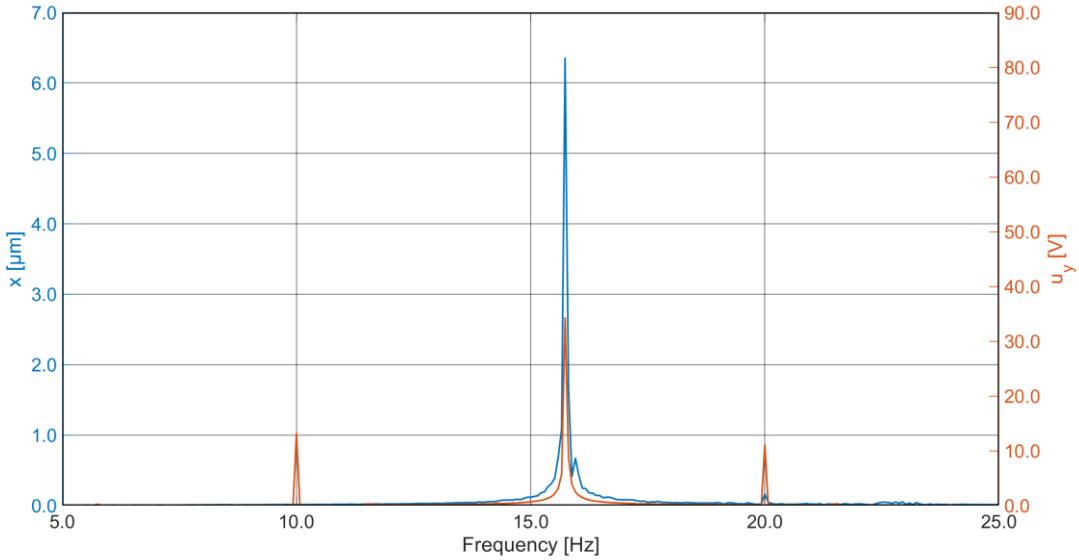

(a)

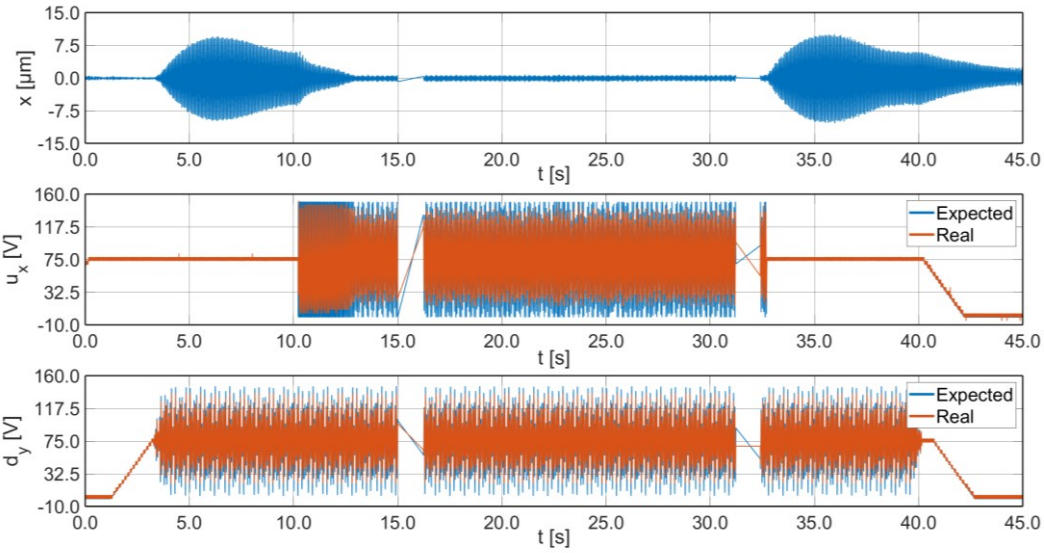

(b)

Figure 74. Test 7: (a) FFT plot without control considering the displacement measurement (left-blue) and the PEA disturbance monitor voltage (right-orange); (b) time plot with active controller.

5.4.2 Y-Axis Experimental Tests

Similar to the X-axis tests, the Y-axis presented a 15.75 Hz resonance frequency, near the expected value of 16 Hz obtained with the stiffness tests. Despite being a low-frequency system, and therefore with a reduced inertial actuation force, the external PEA

created disturbances of up to 4.3 µm that were completely contained by a proportional controller with Kp = 120.

Table 8. Summary of the Y-axis tests under external disturbances.

Test	Frequency [Hz]	Amplitude [V]	Containment [%]	OL [µm]	CL [µm]
1	15.75	250	100.0	3.9	0.0
2	15.75	125	100.0	1.5	0.0
3	15.75	125 before	100.0	2.1	0.0
		250 after	100.0	3.3	0.3
4	15.75	62.5 before	100.0	0.9	0.0
		250 after	92.9	4.2	0.3
5	15.75	200 before	100.0	2.7	0.0
		100 after	100.0	0.9	0.0
6	10.00	50	-	0.0	0.0
	15.75	150	100.0	1.8	0.0
	20.00	50	-	0.0	0.0
7	14.50	50	-	0.0	0.0
	15.50	100	100.0	0.6	0.0
	16.50	50	100.0	0.3	0.0
8	15.75	75	100.0	0.9	0.0
	35.00	50	-	0.0	0.0
	50.00	125	-	0.0	0.0

The following figures show some of the tests presented in Table 8, representing the displacement before and after the control activation, the expected and real control output voltage, and at the bottom of each figure the external disturbance.

Single Amplitude and Frequency:

Tests 1 and 2 have the same frequency of disturbance at the structure resonance but vary in amplitude: 250 V and 125 V respectively. The proportional controller showed great performances obtaining a final result under the sensor's resolution. Test 1 is presented in Figure 75, the resultant displacement without controller produced a 3.9 µm sinewave limited afterwards by the controller's activation.

Varying Amplitude with Single Frequency:

The following tests were employed to test the robustness of the controller under varying amplitude disturbances. For both incremental, Tests 3 and 4, and decremental, Test 5. Test 4 presented the highest variation with a 400% amplification; still, the proportional controller remained stable and contained the disturbance completely as shown in Figure 76. The middle plot shows the controller output before (Expected) and after (Real) the power amplifier, as it can be observed there is a containment, however, it is limited due to the low-frequency component. Similar results were obtained with the disturbance contraction in Test 5 as presented in Table 8, with a reduction to half the initial amplitude.

Multifrequency Tests:

Multiple frequencies were applied by the external actuator to test the controller capabilities. However, the structure filtered the disturbances away from the resonance frequency, near 15.75 Hz, validating the stiffness tests performed with the pulley system. Hence, the figures corresponding to these tests are not presented to avoid redundancy with the other tests. Nevertheless, the controller managed to contain the main peak and the corresponding results are presented in Table 8.

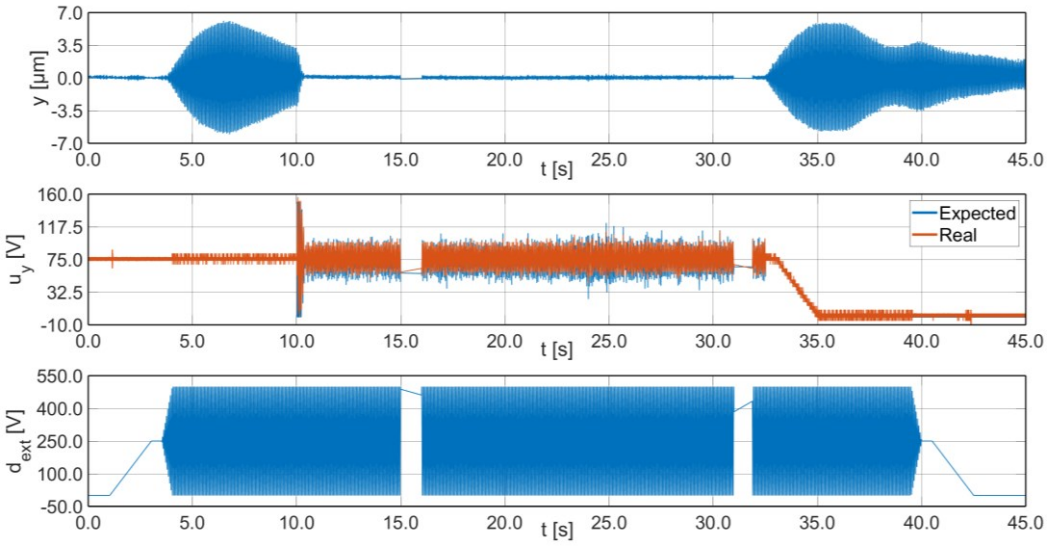

Figure 75. Time plot for Test 1: 250 V at 15.75 Hz.

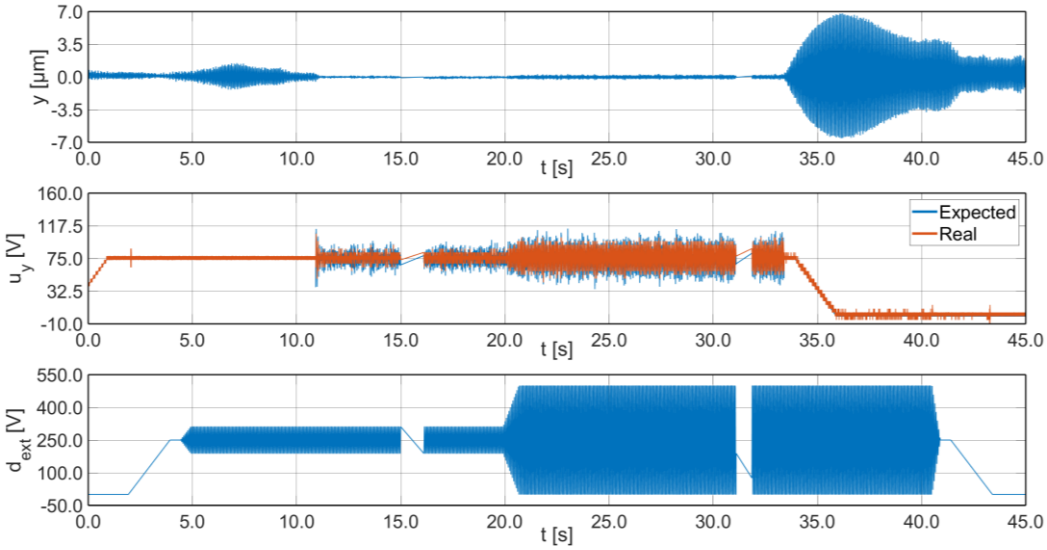

Figure 76. Time plot for Test 4: 15.75 Hz with amplitude from 62.5 V to 250.0 V.

Coupling Considerations:

Considering the measurements obtained with the coupling for the X-axis, the Y-axis presented, up to a certain extent, similar results in terms of amplification and control. Thereafter, several tests were carried out to validate the control action under internal disturbances, considering these as external to the platform. The tests performed for the coupling study upon the Y-axis are summarized in Table 9. As in Table 7, the disturbance amplitude is presented in terms of the actuator's input voltage with two inner columns presenting the *expected* input and the *real* value obtained from the monitor output in the PEA power amplifier.

Table 9. Summary of the Y-axis tests under coupling disturbances.

Test	Frequency [Hz]	Amplitude [V]		Containment [%]	OL [µm]	CL [µm]
		Expected	Real			
1	15.75	75.0	53.9	96.7	9.0	0.3
2	15.75	60.0	44.8	95.2	6.3	0.3
3	15.75	37.5	29.0	90.0	3.0	0.3
4	15.75	18.75	15.2	100.0	1.2	0.0
5	20.00	75.0	51.6	50.0	0.6	0.3
6	15.75	30.0	21.6	88.9	2.7	0.3
	20.00	45.0	32.7	100.0	0.3	0.0
7	10.00	15.0	12.9	-	0.0	0.0
	15.75	45.0	33.9	92.9	4.2	0.3
	20.00	15.0	10.8	-	0.0	0.0
8	14.50	15.0	11.3	100.0	0.3	0.0
	15.50	45.0	34.4	80.0	1.5	0.3
	16.50	15.0	9.0	100.0	0.6	0.0
9	15.75	22.5	17.4	100.0	1.8	0.0
	35.00	15.0	8.3	-	0.0	0.0
	50.00	37.5	17.0	-	0.0	0.0

Among the various coupling disturbance tests performed, the system showed high stability within the narrowband tested. Outside such band the system did not produce any displacement as can be observed for the multi-frequency tests, Tests 6 to 9, where the final displacement in the frequency domain was a single peak near the resonance. In fact, Figure 77a shows the results obtained for Test 9, where a single-peak result is observed; furthermore, the bottom plot presents the disturbance voltage power employed for this test, where a multi-sinewave is clearly present. Nonetheless, as the FFT plot depicted in Figure 77b shows, the actual disturbance contained a main single peak displacement (without control).

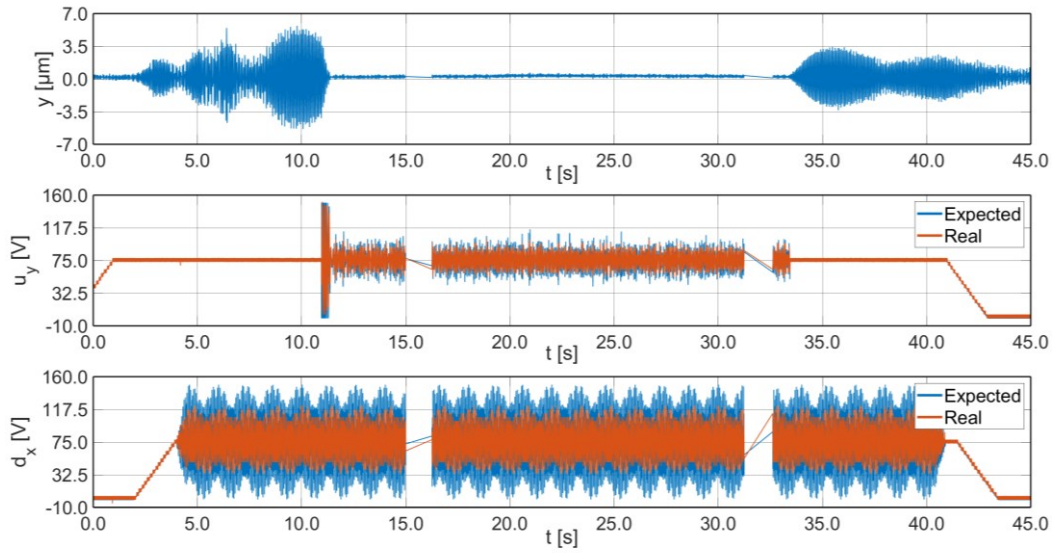

(a)

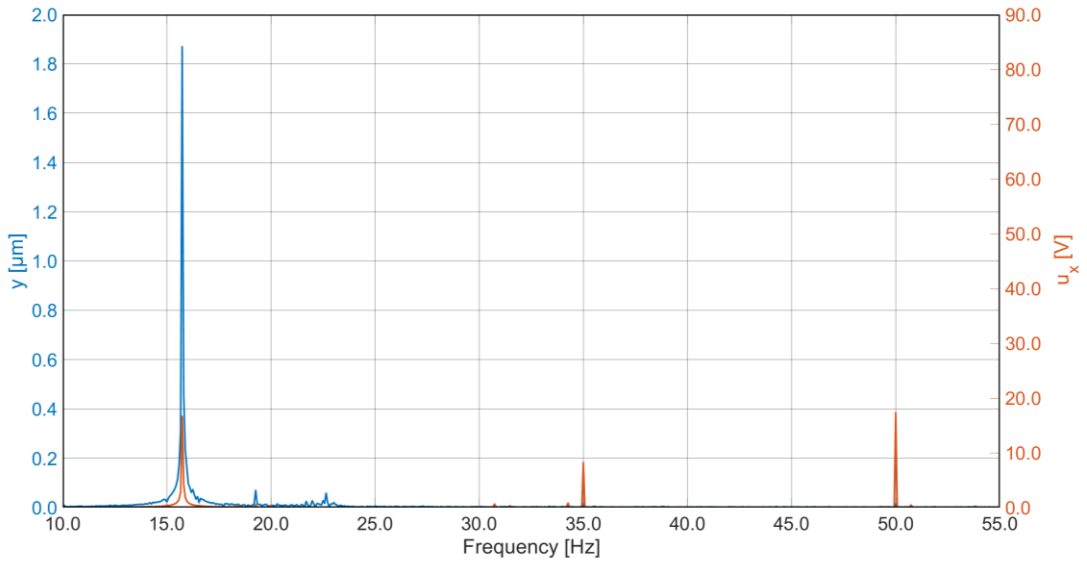

(b)

Figure 77. Test 9: (a) time plot with active controller; (b) FFT plot without control considering the displacement measurement (left-blue) and the PEA disturbance monitor voltage (right-orange).

In a similar fashion to the tests carried out for the X-axis, several single-frequency tests were executed to assess the controller capabilities at the resonance frequency. Tests 1 to 4 depicted a containment over 90% at the given resonance peak, whereas Test 5 applied a disturbance over the resonance obtaining a limited displacement which nonetheless was constrained when the controller was active. The result obtained for Test 1 is presented in Figure 78, where the displacement disturbance is clearly contained when the controller is activated from 12 s to 33 s. The reduction of the real voltage is created by the amplifier filter behaviour, nonetheless, the amplitude constraint is limited based on the low-frequency component of the disturbance.

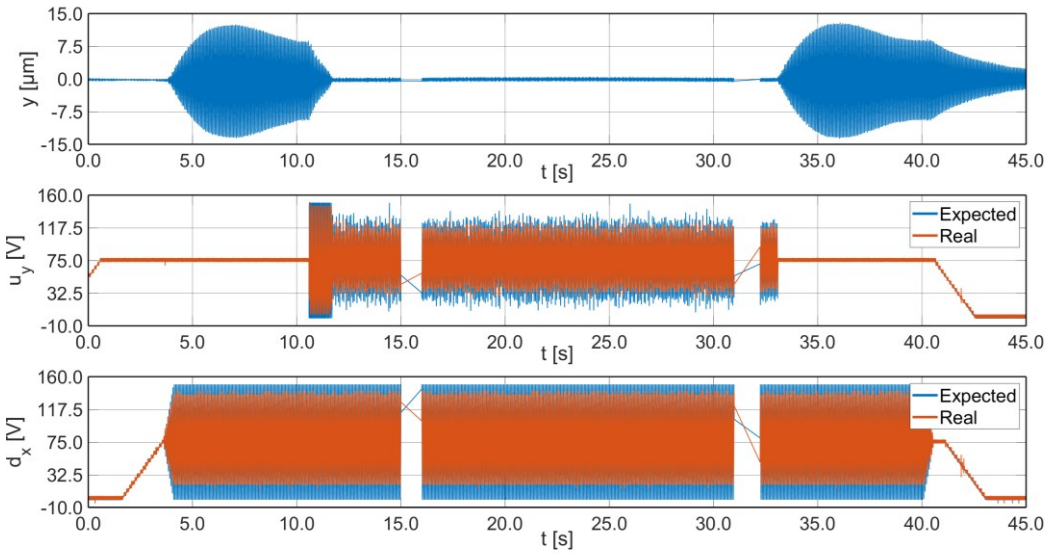

Figure 78. Time plot for the single-frequency Test 1: 75 V at 15.75 Hz disturbance.

5.5 Test Bench: High-frequency Campaign

The final structure, Figure 79, tests were executed with a single eddy current positioning sensor. In this scenario, to have a comprehensive consideration for the complete model and coupling effect, a disturbance with no control phase was implemented where each actuator was powered alone, and the corresponding displacement was measured. This approach allows to obtain the transfer functions that relate the corresponding displacement with the three possible inputs (external PEA, internal X-axis PEA, internal Y-axis PEA) in parallel. In fact, the resulting scheme produces the real displacement as the sum of the three partial displacements. However, the corresponding two-axes active control cannot be validated experimentally, but only in simulation based on the previously presented measurements.

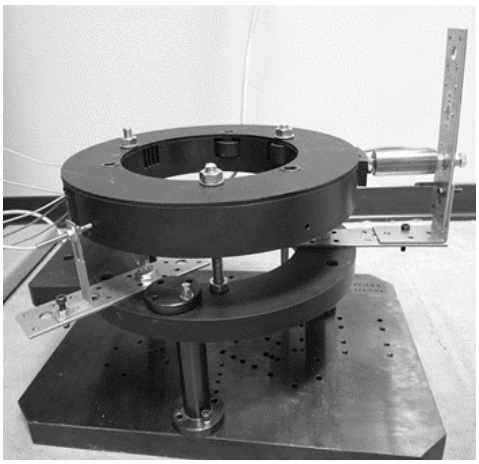

Figure 79. High-frequency Test Bench.

5.5.1 X-Axis Experimental Tests

The initial considerations were made upon the X-axis, with two different controllers: a proportional (P) controller with $Kp = 120$ gain and a proportional derivative (PD) controller with $Kp = 70$ and $Kd = 5\text{x}10^{-4}$.

The following table contains a summary of the experimental tests carried out for the X-axis, using the external PEA as the disturbance source. Each test was chosen to obtain a measurable displacement with the disturbance action and was repeated for the three variations: open loop (OL); closed loop with a proportional controller (P); and closed loop with a proportional derivative controller (PD).

Table 10. Summary of the X-axis tests under external disturbances.

Test	Frequency [Hz]	Amplitude [V]	OL [µm]	CL (P)		CL (PD)	
				[µm]	%	[µm]	%
1	100.0	125.0	3.6	2.1	41.7	1.2	66.7
2	100.0	200.0	7.2	6.9	4.2	5.7	20.8
3	110.0	100.0	17.4	10.5	39.7	13.5	22.4
4	110.0	50.0	10.2	0.9	91.2	0.6	94.1
5	120.0	50.0	1.5	0.9	40.0	0.9	40.0
6	105.0	100.0	21.0	15.9	24.3	15.0	28.6
7	105.0	50.0	8.7	2.1	75.9	1.8	79.3
8	110.0	50.0	9.6	6.6	31.3	7.8	18.8
	120.0	75.0	3.6	3.9	-8.3	3.9	-8.3
	130.0	100.0	4.5	4.5	0.0	4.5	0.0
9	110.0	50.0	9.3	5.1	45.2	6.0	35.5
	120.0	50.0	2.1	2.4	-14.3	2.4	-14.3
	130.0	50.0	2.1	2.1	0.0	2.1	0.0
10	105.0	50.0	18.3	10.3	44.3	9.9	45.9
	110.0	50.0	9.9	7.8	21.2	8.7	12.1
	115.0	50.0	3.0	2.7	10.0	2.7	10.0
11	105.0	50.0	18.3	8.1	55.7	7.2	60.7
	155.0	25.0	0.3	0.3	0.0	0.3	0.0
	205.0	25.0	0.0	0.0	-	0.0	-

Test 1 exerted a 125 V disturbance at 100 Hz with the external PEA, creating a corresponding OL displacement of ~3.6 µm. The best result was obtained with the PD controller, containing the disturbance up to 1.2 µm, whereas the P controller obtained a final displacement of 2.1 µm. Furthermore, due to the amplifier containment and the mechanical nature of the system the harmonics of the main disturbance frequency are also present in Figure 80a (200 Hz and 300 Hz) with a lower displacement.

The PD result is presented in Figure 80b, the controller is activated at 11 s and deactivated at 16 s, the missing data from 15 s to 17 s is due to the required time to save the sampling block. Furthermore, the amplifier effect is shown within the middle figure, where both the expected and the real voltages feeding for the control actuator are presented. The top figure corresponds to the displacement of the X-axis, and the figure at the bottom shows the disturbance voltage feeding the external actuator.

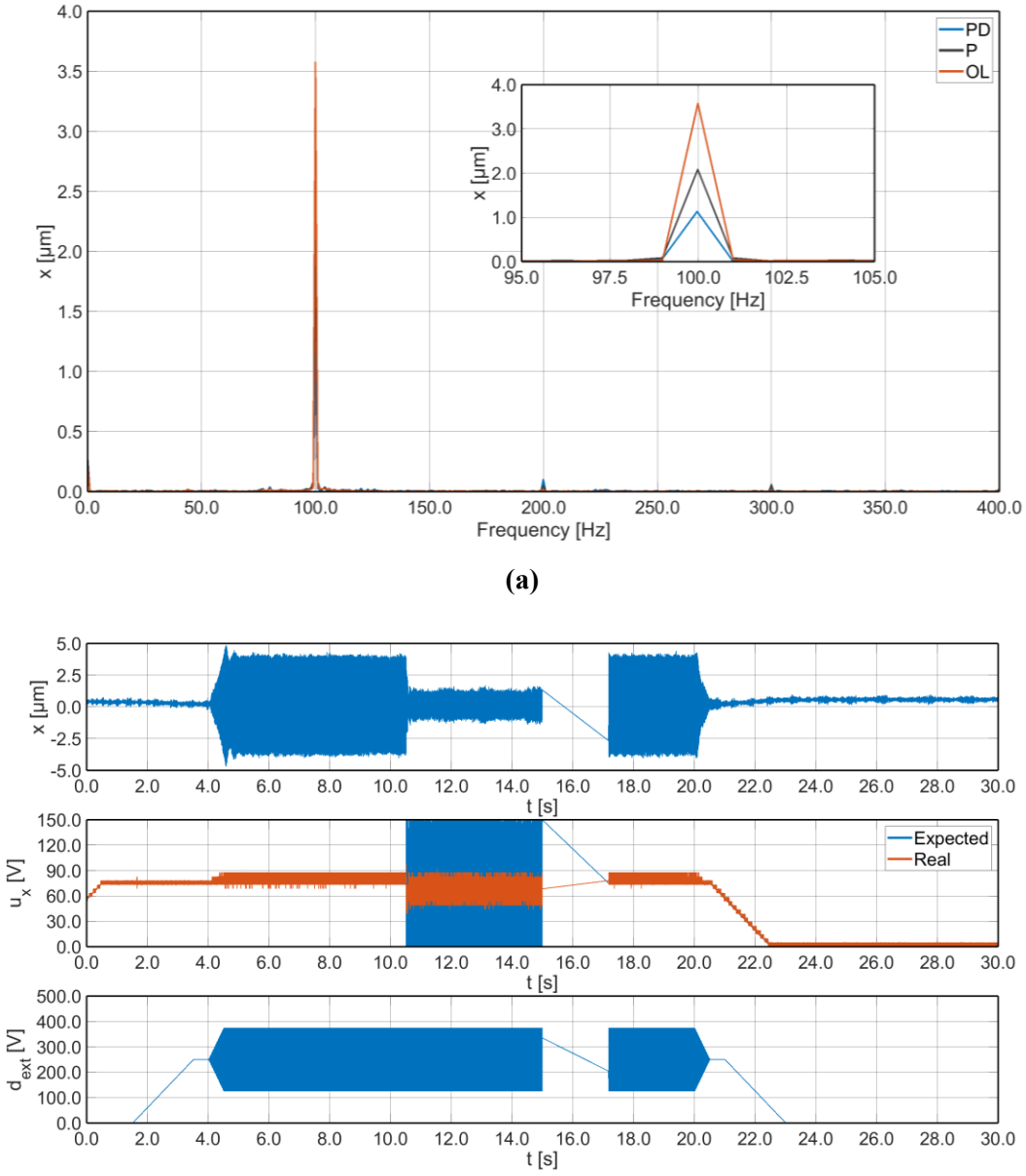

Figure 80. Test 1: (a) FFT displacements: (blue) PD controller; (black) P controller; (red) Open Loop; (b) time plot with PD controller.

Taking into consideration the containment results obtained in Test 1, the following test increased the PEA amplitude disturbance to 200 V while keeping the 100 Hz frequency, resulting in a displacement of 7.2 µm. In a similar fashion to the previous scenario, both P and PD controller were assessed obtaining a final displacement

of 6.9 µm and 5.7 µm, respectively, as shown in Figure 81a. Similarly, Figure 81b presents the displacement with the PD controller, which corresponds to the best-case scenario. The controller is turned on at 10.5 s and deactivated at 15.5 s. In this case scenario the corresponding required force produced a continuous saturation of the control action as the final force required was over the capabilities of the system, platform and electronics. Nonetheless, despite the limitation of the resulting actuator under the disturbance force, the corresponding actuator manages to still contain the final disturbed displacement of near the 21%.

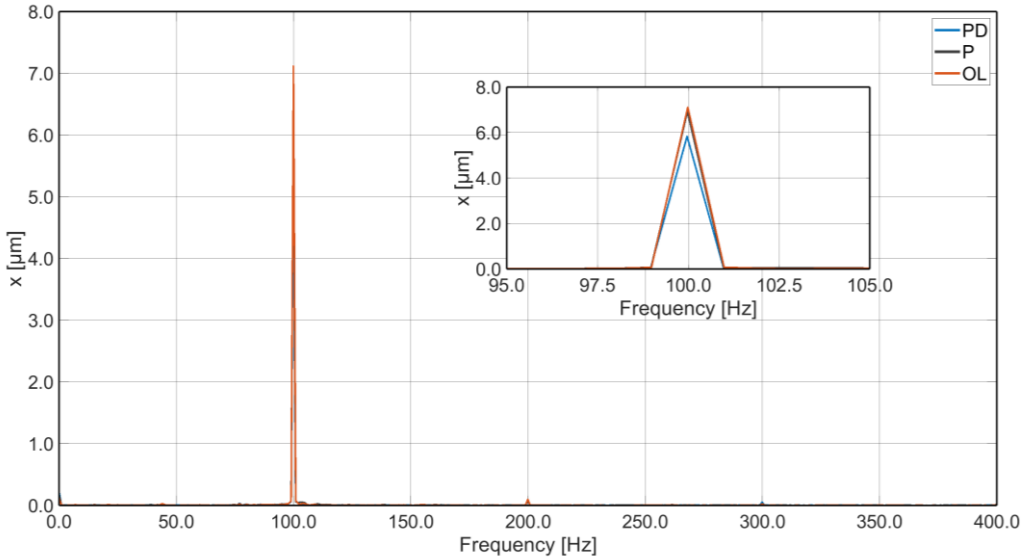

(a)

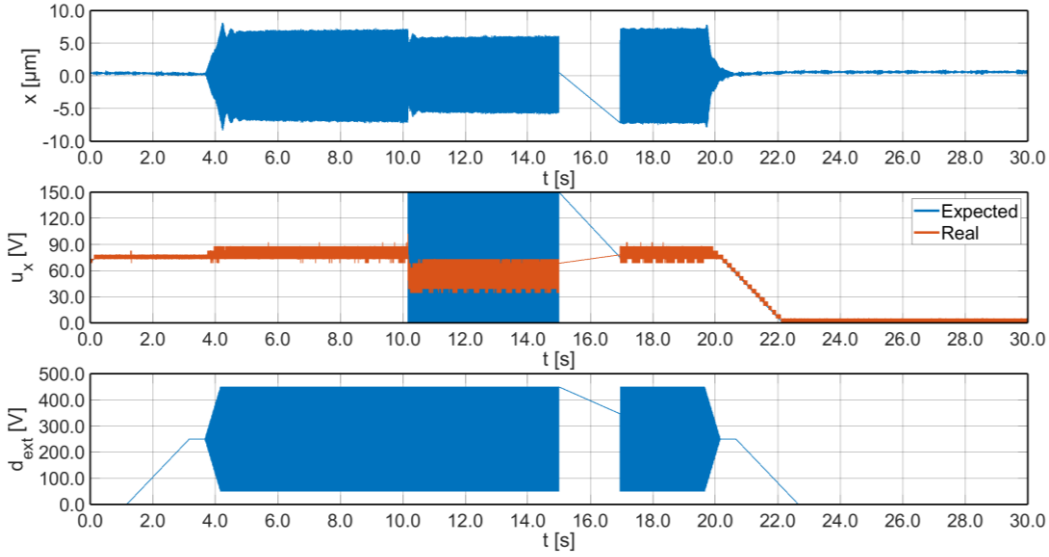

(b)

Figure 81. Test 2: (a) FFT overlap displacements representation; (b) time plot with PD controller.

The next test, Test 3, implemented a 100 Hz with 100 V amplitude disturbance with the external PEA achieving a 17.4 µm displacement. In this case scenario the proportional controller obtained the best results with a final displacement of 10.5 µm

with respect to the 13.5 µm of the proportional derivative controller. In Figure 82a, the results obtained during the corresponding simulations for the open loop (OL) and closed loop schemes: proportional (P) and proportional derivative (PD) controllers are depicted. The result obtained with the P controller in Test 3 is shown in Figure 82b. The controller is active in the interval from 11 s to 16 s and it manages to contain the disturbance displacement of almost 40%.

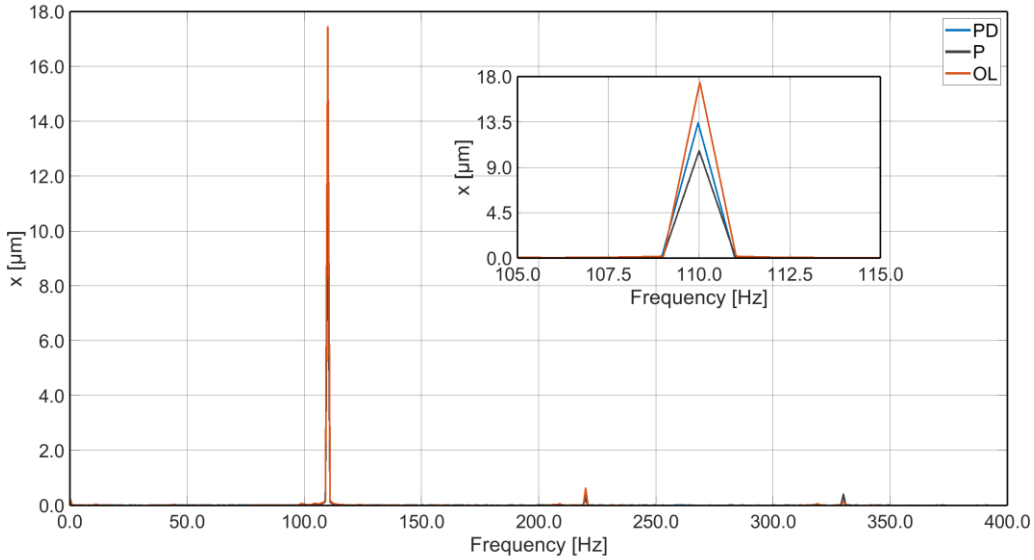

(a)

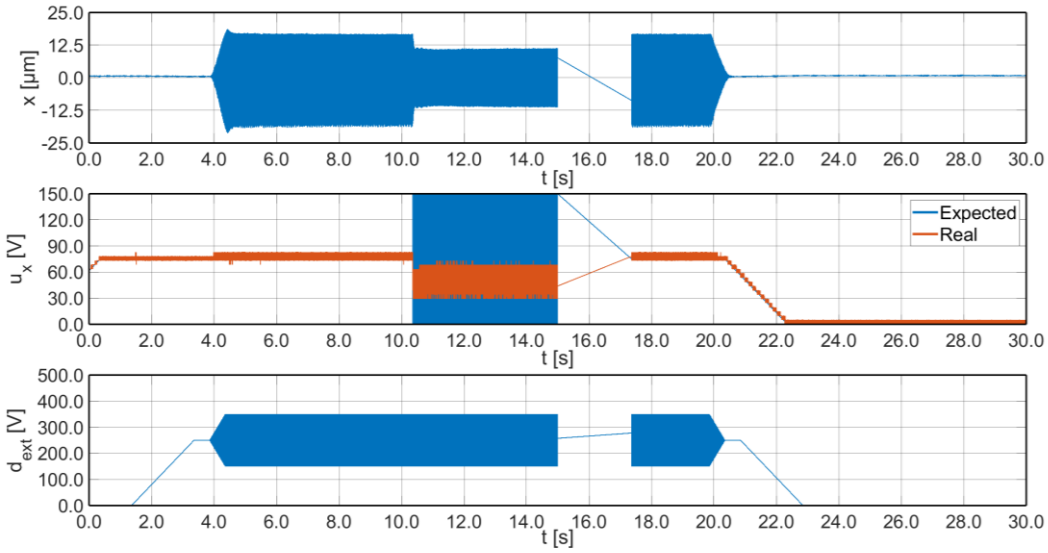

(b)

Figure 82. Test 3: (a) FFT overlap displacements representation; (b) time plot with P controller.

As before, the high displacement caused by the external disturbance is an issue for the limitation of the control action, hence, a saturation of the controller produces a reduced containment with respect to Test 4 where the frequency remains the same, but the amplitude of the disturbance is reduced by half. In fact, it presented a disturbance at 110 Hz with a 50 V amplitude, producing a displacement of 10.2 µm.

Differently from Test 3, the PD controller obtains the best results (0.6 µm) with a containment of 94.1% with respect to the 91.2% of the proportional derivative controller (0.9 µm), as depicted in Figure 83a. Nonetheless, such difference lies within the sensor resolution and hence are considered equal. The PD controller for Test 4 is presented in Figure 83b, where it can be observed how the resulting required voltage activation is not completely saturated and hence allows to an almost complete containment of the disturbed displacement with respect to the previous test.

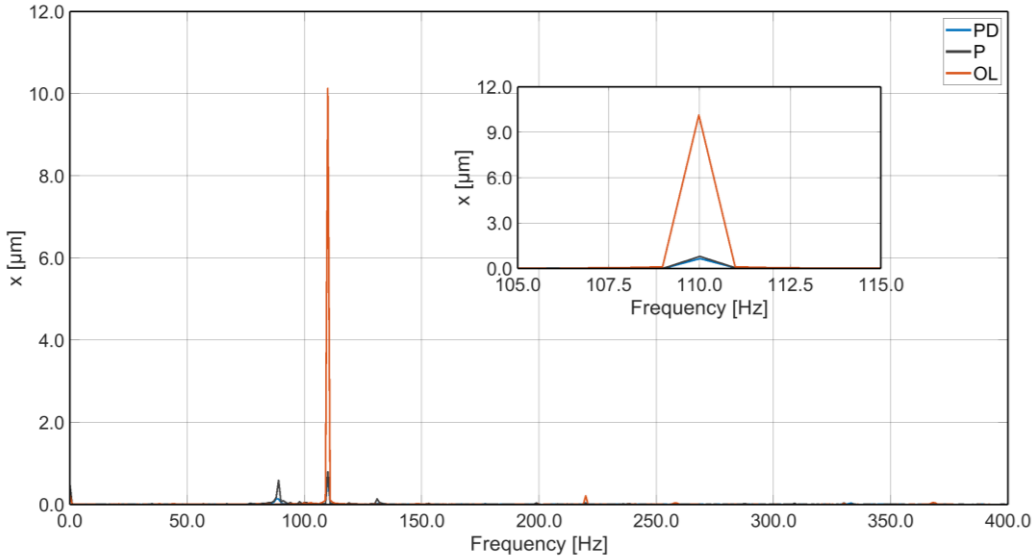

(a)

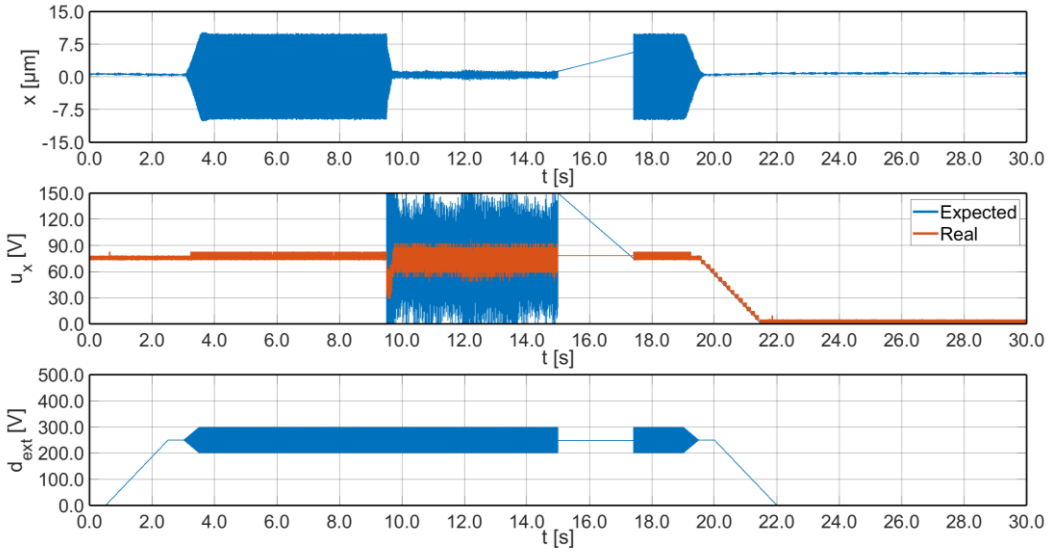

(b)

Figure 83. Test 4: (a) FFT overlap displacements representation; (b) time plot with PD controller.

Test 5 varies the disturbance frequency to 120 Hz while the amplitude is kept constant with respect to Test 4. The OL displacement is of 1.5 µm, the P and PD displacements are equal to 0.9 µm, as shown in Figure 84a.

This test shows how, despite containing near the 40% of the disturbance, the proportional controller creates a new issue at 90 Hz, where a new peak of 0.9 µm appears. Therefore, the system changes the vibration frequency instead of reducing the corresponding displacement. This is avoided in the PD controller as observed in Figure 84b.

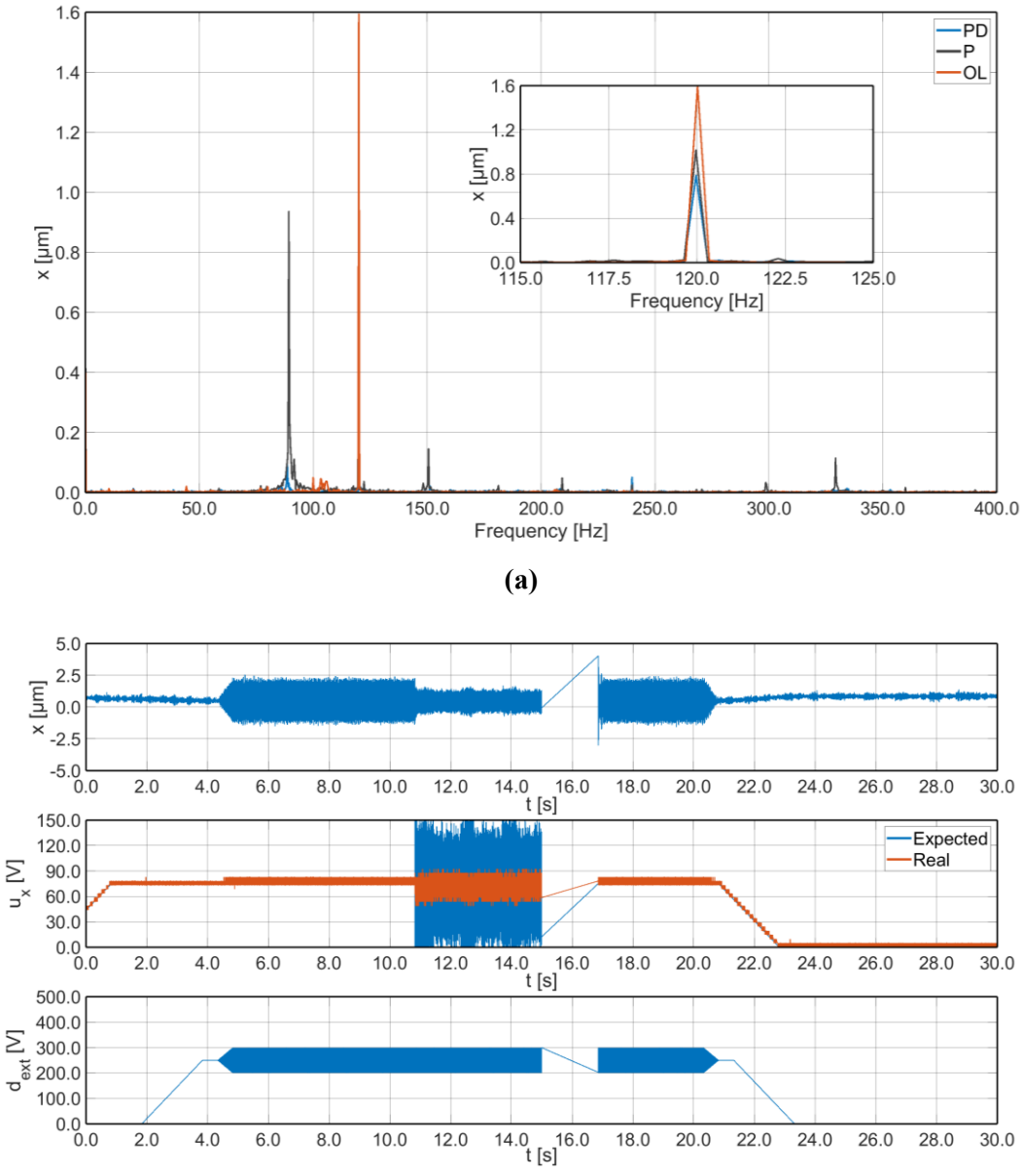

Figure 84. Test 5: (a) FFT overlap displacements representation; (b) time plot with PD controller.

In a similar manner to Test 4, the control action is less subject to the actual saturation allowing to better reduce the corresponding disturbance displacement with respect to the on/off behaviour of Test 3.

A similar behaviour is observed for Test 6, which exerts a disturbance of 100 V at 105 Hz with the external PEA producing a 21.0 µm displacement, as shown in Figure 85a. This error is contained by the PD of 28.6% (15.0 µm) and of 24.3% (15.9 µm) for the P controller. The PD result is shown in Figure 85b where, as in Test 2 and 3, the control action is saturated due to the amplitude of the disturbance which limits the corresponding platform capability to contain the final error.

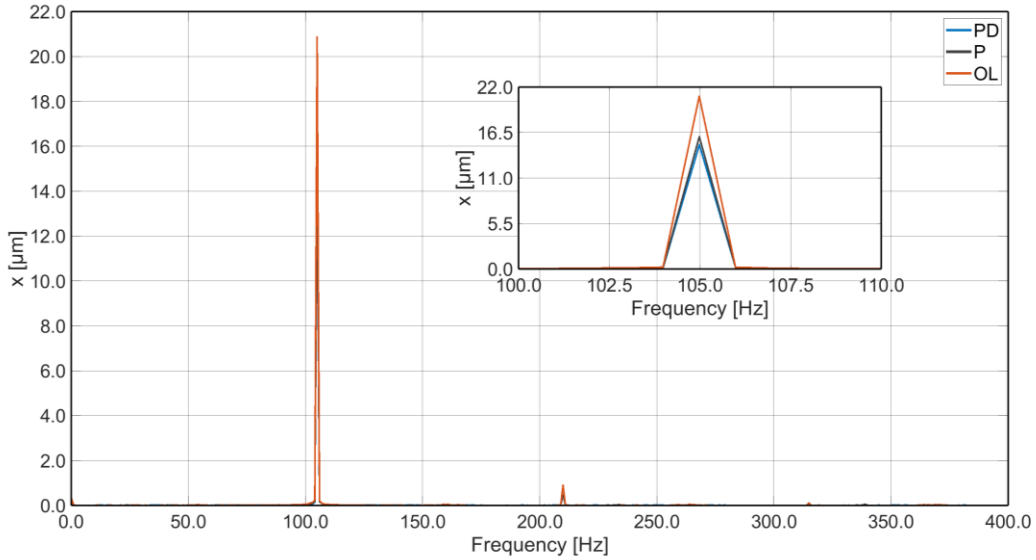

(a)

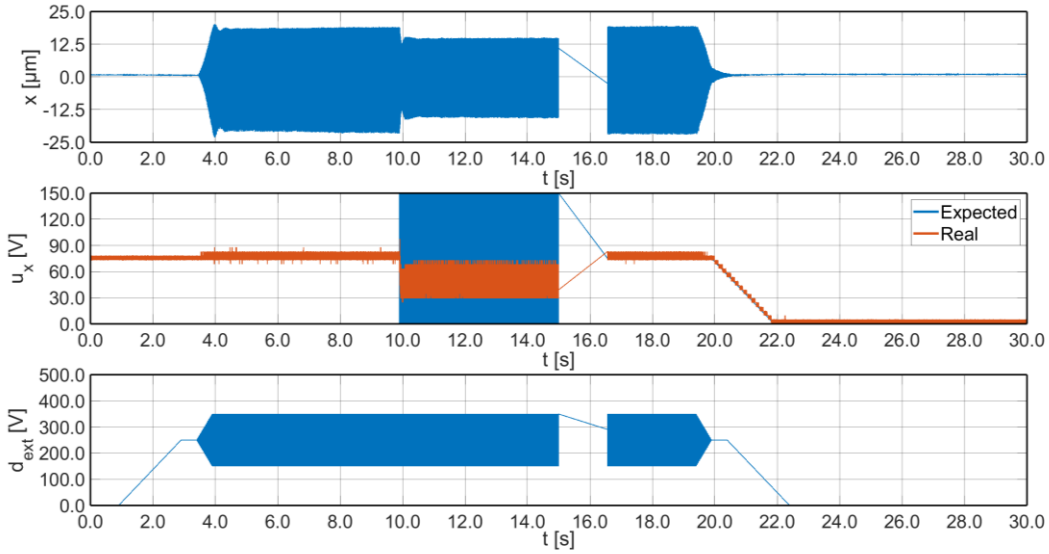

(b)

Figure 85. Test 6: (a) FFT overlap displacements representation; (b) time plot with PD controller.

The following experiment, Test 7, employed a lower amplitude for the disturbance (50 V) while keeping the frequency component, obtaining a final displacement of 8.7 µm. However, this test exerts a lower force and allows a greater effect of the control actions, obtaining a final displacement for the P and PD of 2.1 µm and 1.8 µm, respectively, as depicted in Figure 86a.

The PD controller managed to obtain the greatest containment, 79.3%, as shown in Figure 86b where the displacement, control action (Expected and Real) and Disturbance are represented for the given case study.

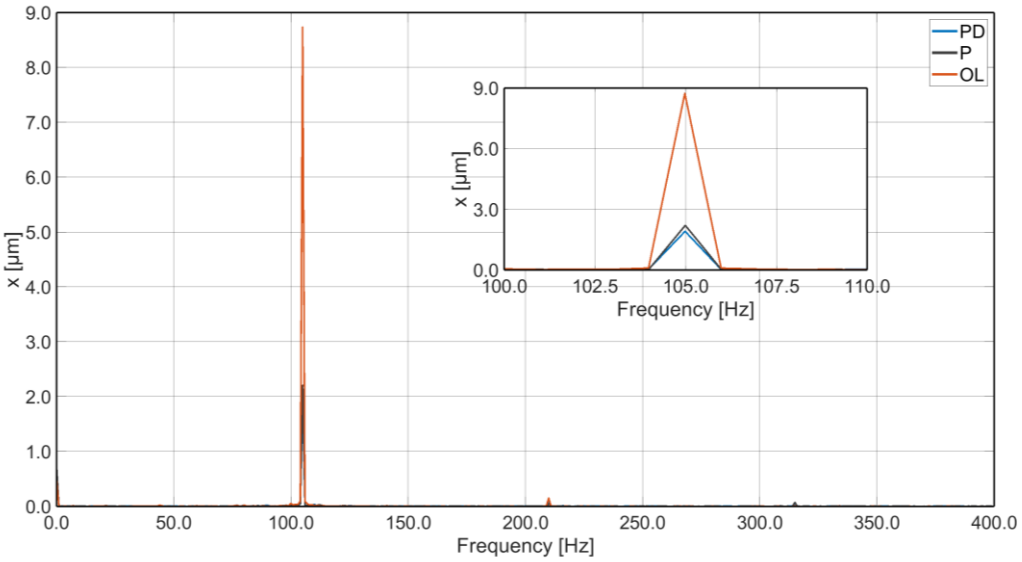

(a)

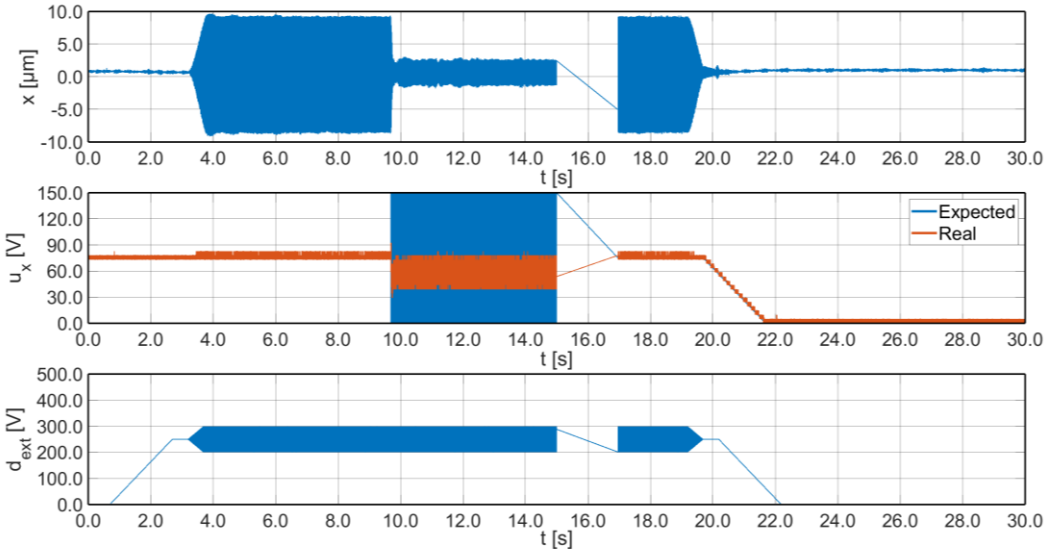

(b)

Figure 86. Test 7: (a) FFT overlap displacements representation; (b) time plot with PD controller.

The first multi-frequency experiment is Test 8, where three different frequencies within the range of interest are employed to assess the controller capabilities under multiple disturbances. In this case scenario, the disturbance can be expressed as follows:

$$D = 50 \cdot sin(110 \cdot (2\pi)t) + 75 \cdot sin(120 \cdot (2\pi)t) + 100 \cdot sin(130 \cdot (2\pi)t) \quad \textbf{53}$$

The multi-frequency disturbance proved to be an issue due to the amplifier limitation resulting in a saturation of the corresponding controller in both cases, P and PD. The highest peak (110 Hz) was contained, from 9.6 µm to 6.6 µm (P) and 7.8 µm

(PD); however, the other two elements of the disturbance were not varied by the control action as it can be observed in Figure 87a. Furthermore, as happened for the previous single tests an amplification of a non-disturbed frequency is present for both controllers at 100 Hz.

The best results, presented in Figure 87b, were obtained with the proportional controller in terms of the highest peak reduction, with a containment of over 30%. Similar to previous tests the saturation of the control action due to the low-pass filter behaviour determines the amount of achievable containment and the final frequency results.

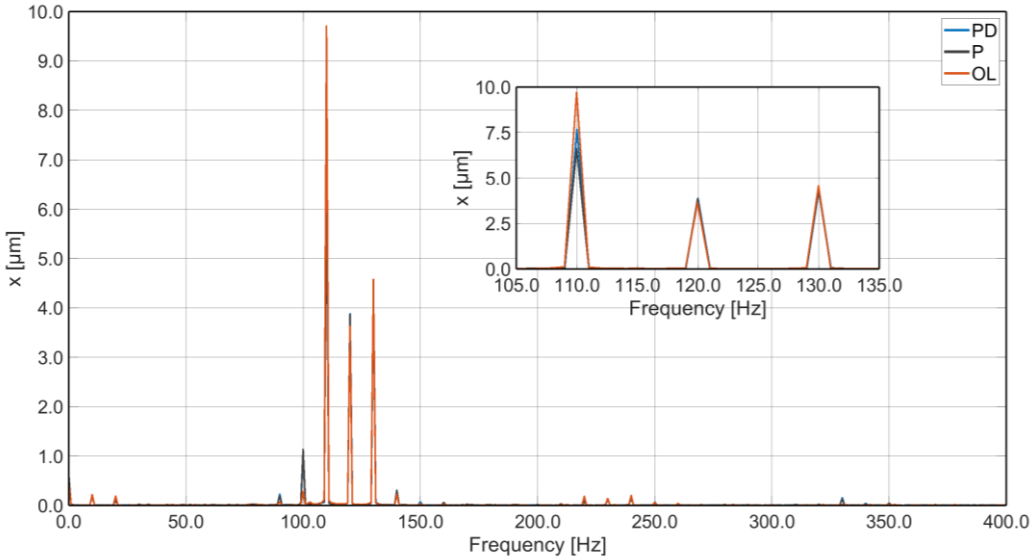

(a)

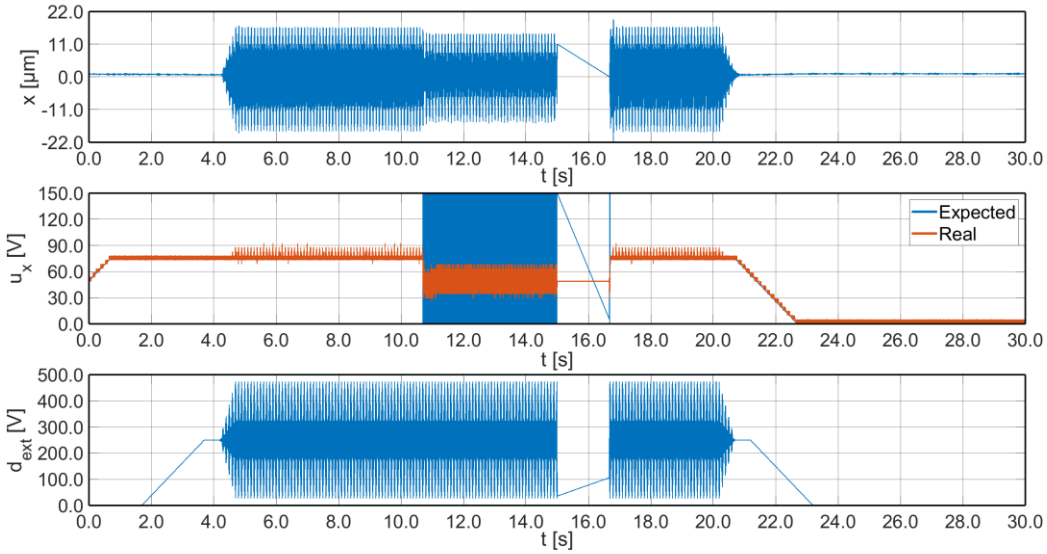

(b)

Figure 87. Test 8: (a) FFT overlap displacements representation; (b) time plot with P controller.

The next test, Test 9, reduced the amplitude of the disturbances up to 50 V for each sinewave. This new approach showed an improvement in terms of the highest peak but still the multi-frequency experiment presented the same issue as before, and two of the three peaks were left without containment. Nonetheless, the final displacement was contained from 9.3 µm for the main peak to 6.0 µm (PD controller) and 5.1 µm (P controller) as presented in Figure 88a.

As for Test 8, the maximum containment for Test 9 was obtained with the proportional controller which still created the same disturbance on the 100 Hz frequency (over 1 µm). Figure 88b presents the time plot for the corresponding test with the proportional controller.

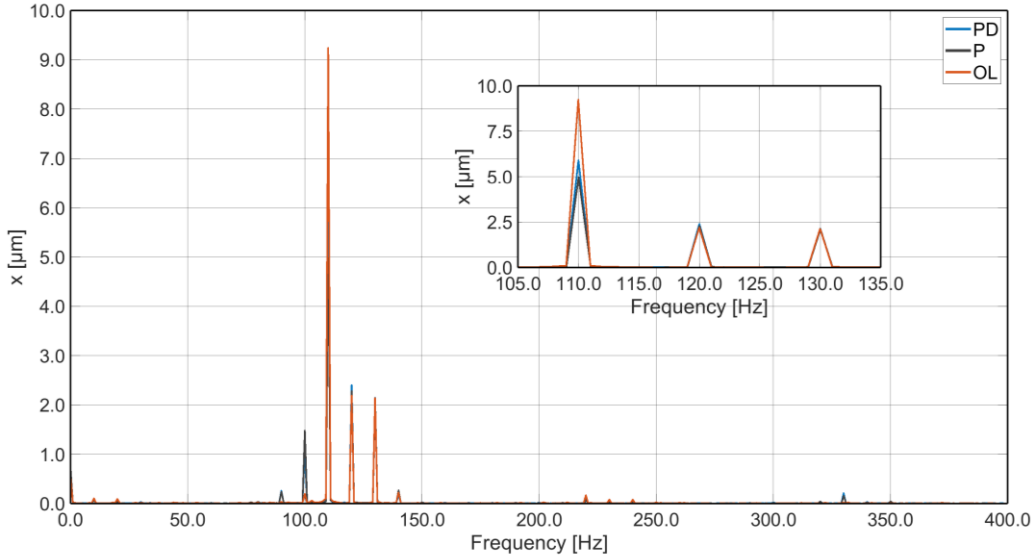

(a)

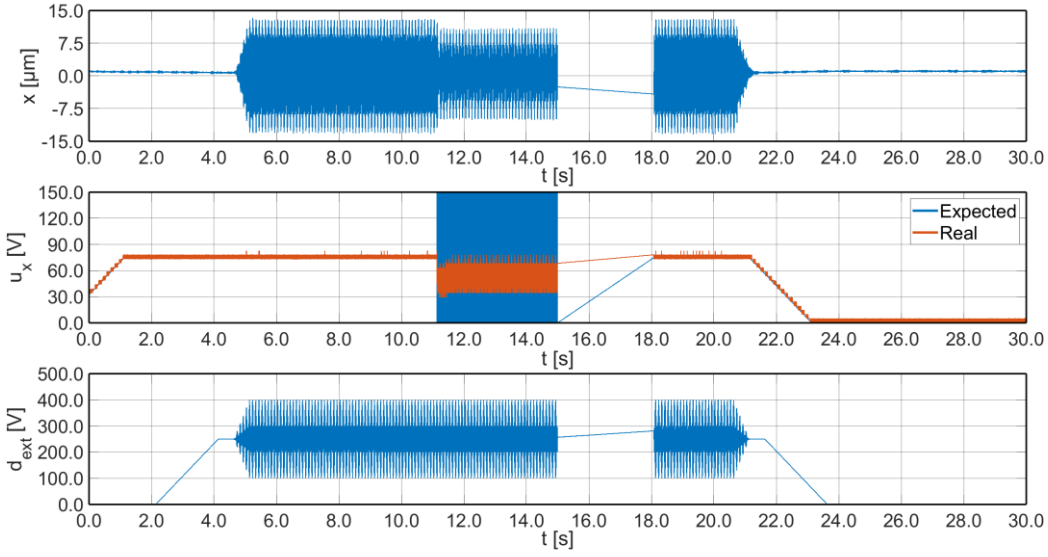

(b)

Figure 88. Test 9: (a) FFT overlap displacements representation; (b) time plot with P controller.

As before this multi-frequency experiment exerts a three-frequency disturbance with smaller distance in the frequency axis with respect to the previous tests. Differently, in this case scenario two of the three peaks were contained. The maximum peak was contained from 18.3 µm (OL) to 10.2 µm (P) and to 9.9 µm (PD). Furthermore, the second peak (9.9 µm) showed a reduction of 12% (8.7 µm) for the PD controller and of 21% (7.8 µm) for the P controller. Finally, the third peak (115 Hz) varied within the sensor resolution as presented in Figure 89a. The best result considering the sum of both peaks (28.2 µm) corresponds to the proportional controller (18.0 µm) with respect to the proportional derivative controller (18.6 µm). Nonetheless, the final error was near the sensor resolution which shows that both controllers have similar capabilities. The time plot for the PD controller experimental test is presented in Figure 89b.

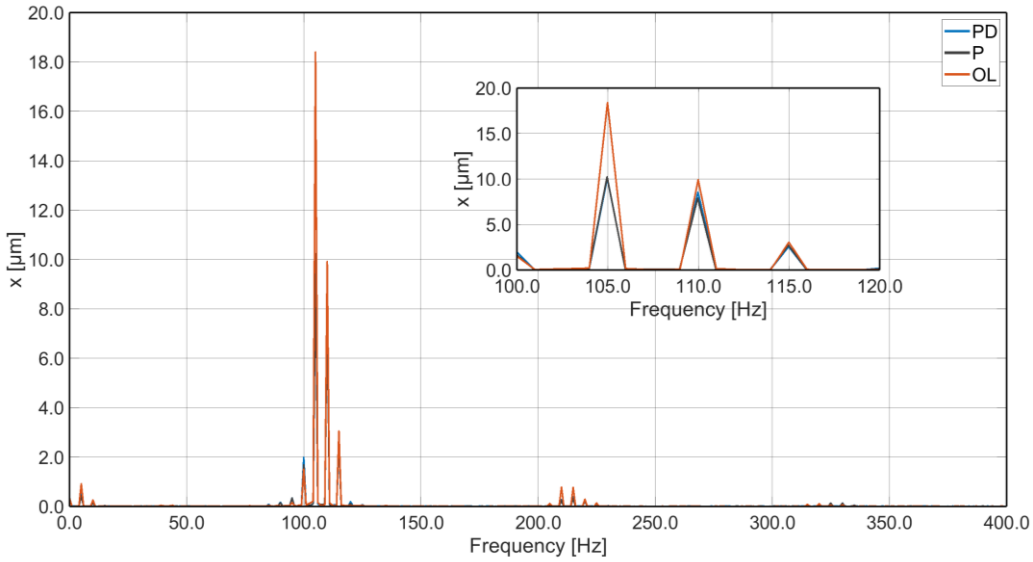

(a)

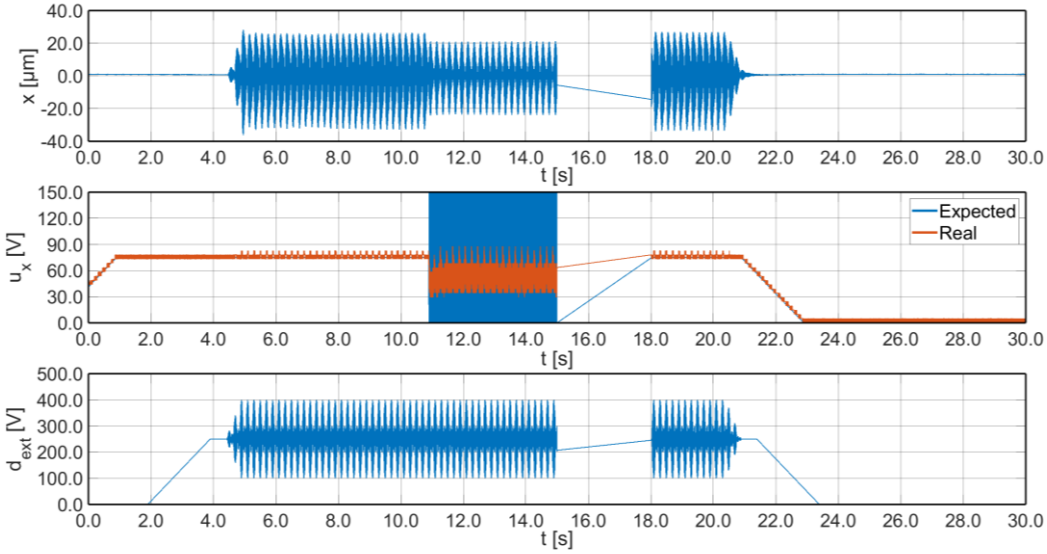

(b)

Figure 89. Test 10: (a) FFT overlap displacements representation; (b) time plot with PD controller.

The final multi-frequency test, Test 11, aimed to run a trial experiment outside the frequency range of interest to reach higher frequencies, which are at borderline of the electronics actuation capabilities. As expected, the disturbances over 150 Hz presented no visible displacements. Furthermore, the harmonics of the 105 Hz created higher disturbances with respect to the other two components.

5.5.2 Y-Axis Experimental Tests

In a similar fashion to X-axis, two controllers were tested for the Y-axis: a proportional controller with a gain Kp = 30; a proportional derivative controller with Kp = 40 and Kd = 5x10^{-4}. The experimental tests carried out for the Y-axis using the external PEA as the disturbance source are summarized in Table 11. For each test three variations were evaluated: open loop (OL); closed loop with a proportional controller (P); and closed loop with a proportional derivative controller (PD).

Table 11. Summary of the Y-axis tests under external disturbances.

Test	Frequency [Hz]	Amplitude [V]	OL [µm]	CL (P)		CL (PD)	
				[µm]	[%]	[µm]	[%]
1	110	250	10.5	3.9	62.9	5.4	48.6
2	110	200	7.8	4.8	38.5	2.7	65.4
3	130	250	15.9	10.5	34.0	12.0	24.5
4	130	200	15.6	9.3	40.4	10.8	30.8
5	130	100	9.9	3.6	63.6	4.8	51.5
6	120	250	7.2	4.8	33.3	4.2	41.7
7	120	200	4.8	3.9	18.8	2.1	56.3
8	120	100	3.6	3.0	16.7	3.0	16.7
	130	100	12.3	6.3	48.8	7.2	41.5
9	110	50	3.9	4.5	-15.4	3.9	0.0
	120	100	3.9	3.6	7.7	3.3	15.4
	130	100	12.3	7.2	41.5	7.5	39.0
10	120	100	3.6	3.0	16.7	3.0	16.7
	130	100	12.0	6.3	47.5	6.9	42.5
	150	50	2.1	1.5	28.6	1.5	28.6
11	120	75	2.7	1.8	33.3	1.8	33.3
	125	75	4.8	3.3	31.3	3.3	31.3
	130	75	9.0	4.2	53.3	4.5	50.0

Test 1 is a single frequency test with a disturbance at 110 Hz and an amplitude of 250 V, resulting in an OL displacement of 10.5 µm. Both P and PD controller were tested obtaining a final containment of 63% (3.9 µm) and 49% (5.4 µm), respectively. The FFT representations were obtained in the time interval after the control action is activated and the dynamic behaviour has ended. This simplifies the corresponding frequency plot, presented in Figure 90a, considering that the disturbance has only a single frequency component. The P controller showed the best containment, with a final amplitude of 3.9 µm and, hence, the time plot for this controller is presented in Figure 90b together with the disturbance and the corresponding displacement.

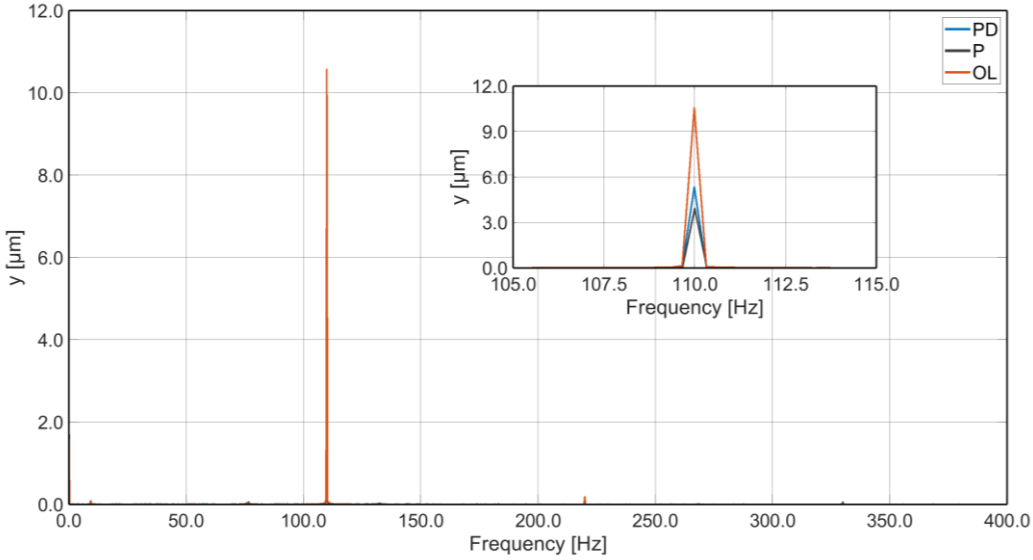

(a)

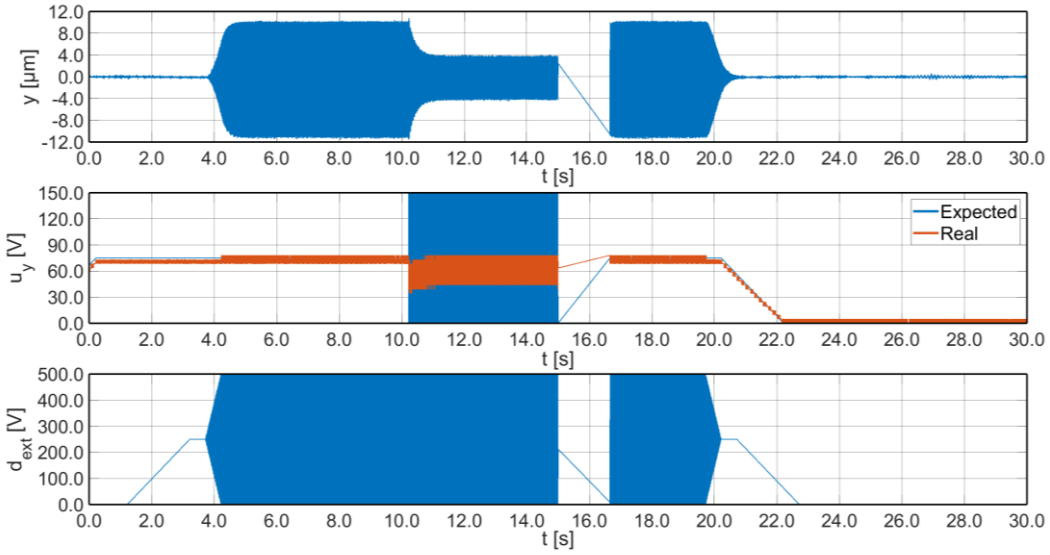

(b)

Figure 90. Test 1: (a) FFT overlap displacements representation; (b) time plot with P controller.

Test 2 exerted the disturbance at an identical frequency, nonetheless, the amplitude for this test was reduced to 200 V, obtaining a displacement of 7.8 µm. In this scenario the PD controller achieved a 65% containment (2.7 µm), a better result than the P controller, with a 39% containment (4.8 µm). Furthermore, this test presented multiple peaks which were not present in the disturbance and were created by the, saturated, control action. As can be observed in Figure 91a, the P controller creates a disturbance at 130 Hz, producing a peak of almost 5 µm; hence, despite of reducing the main disturbance, this behaviour is a limiting factor for this controller. Thereafter, the PD controller response is shown in Figure 91b where it is noted the presence of peaks elsewhere if compared with the clear response of Test 1.

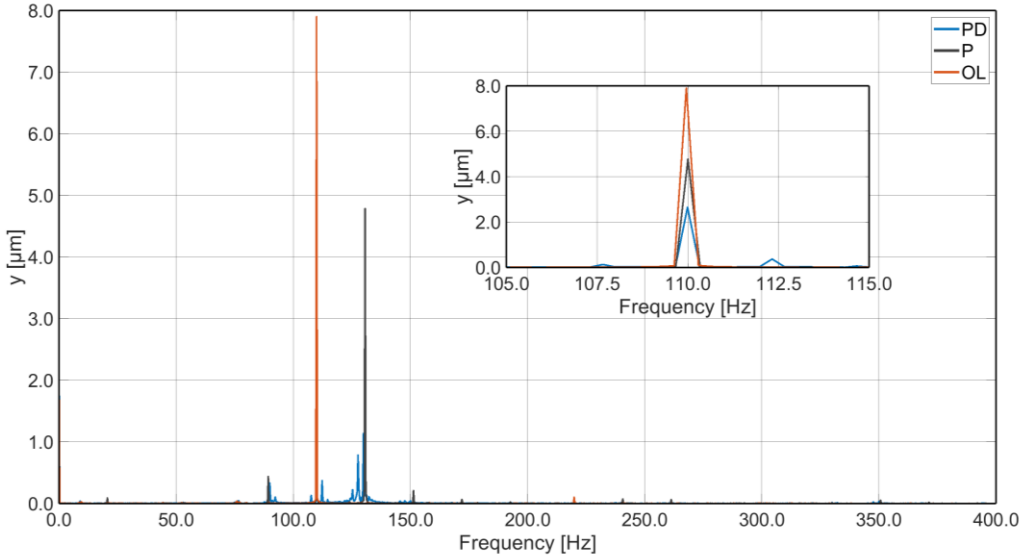

(a)

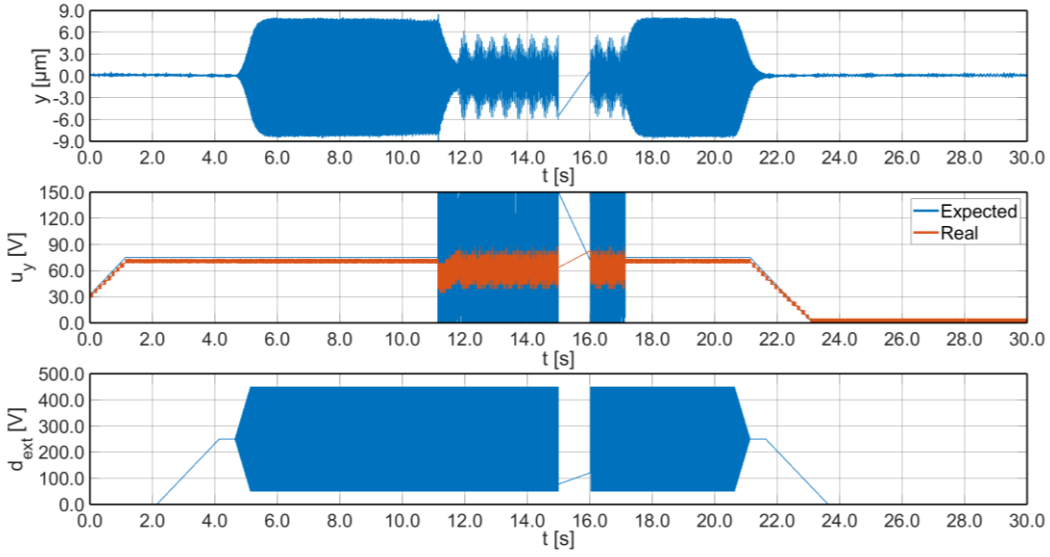

(b)

Figure 91. Test 2: (a) FFT overlap displacements representation; (b) time plot with PD controller.

The following tests (Tests 3 to 5) were executed at a 120 Hz frequency, each with a different amplitude. Test 3, depicted in Figure 92a, exerted a 250 V disturbance obtaining a displacement of 15.9 µm, contained afterward by both P (10.5 µm) and PD (12.0 µm) controllers. The second lower peak observable in the FFT figure corresponds to the first harmonic of the disturbance (260 Hz). In the evaluated case scenario, the proportional controller showed the highest containment, 34%.

Similar results were obtained in Test 4, with a 200 V disturbance amplitude (15.6 µm) and the best containment with the P controller of 40% (9.3 µm) as presented in Figure 92b.

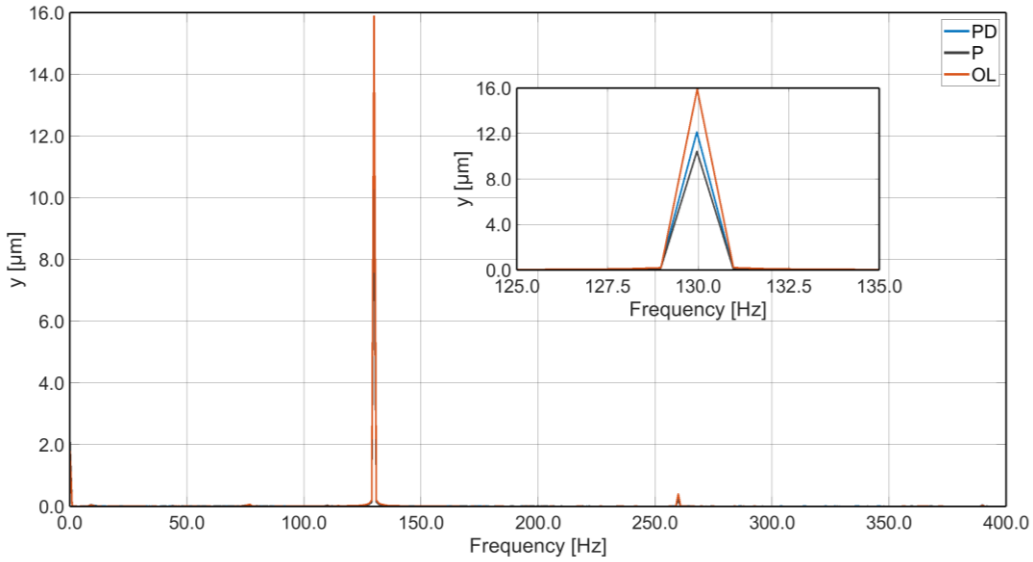

(a)

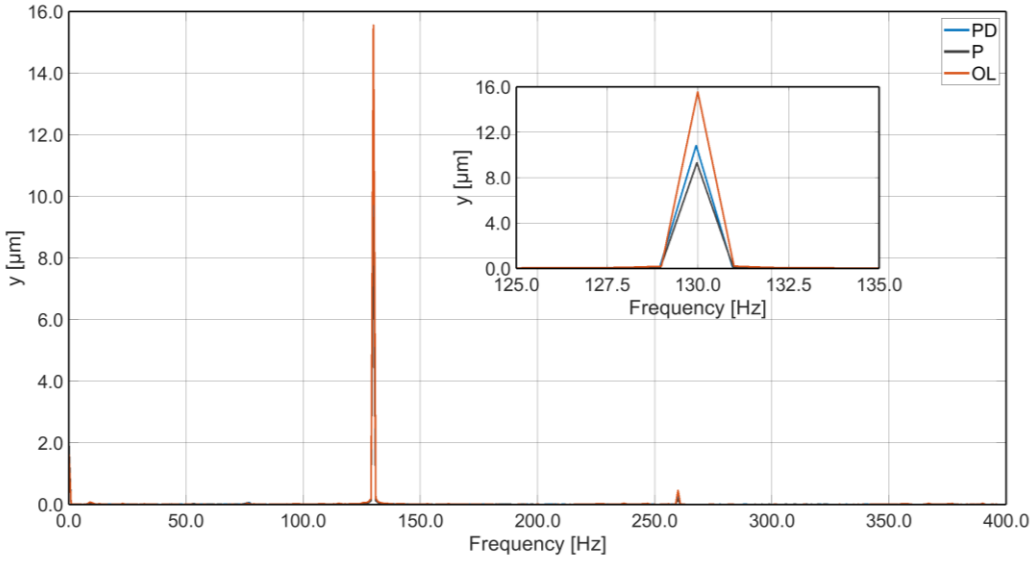

(b)

Figure 92. FFT overlap representation: (a) Test 3; (b) Test 4.

Finally, Test 5 reduces the amplitude disturbance to 100 V with a displacement of 9.9 µm. Due to the reduced required force the control actuators managed to obtain better percentual results: 64% for the P controller (3.6 µm), and 52% for the PD controller (4.8 µm). As for the previous tests, the first harmonic can be also observed in Test 5 FFT in Figure 93a, at 260 Hz.

The P controller achieved the highest containment; therefore Figure 93b presents the time plot for this controller in Test 5, similar results were obtained with Tests 3 and 4, hence this figure summarizes the time response considering for all three tests. It presents the displacement variation, the disturbance action, and the corresponding controlled output, expected and real.

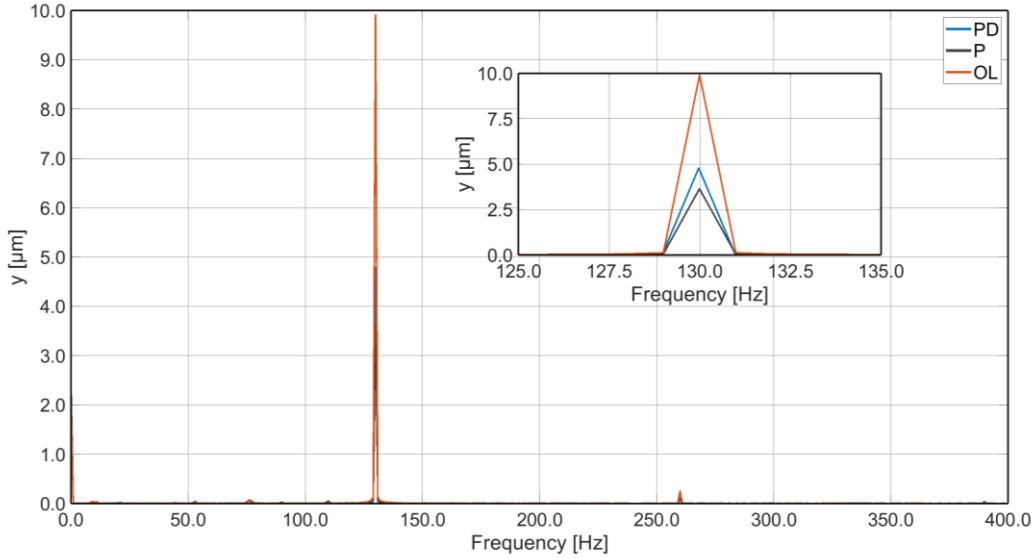

(a)

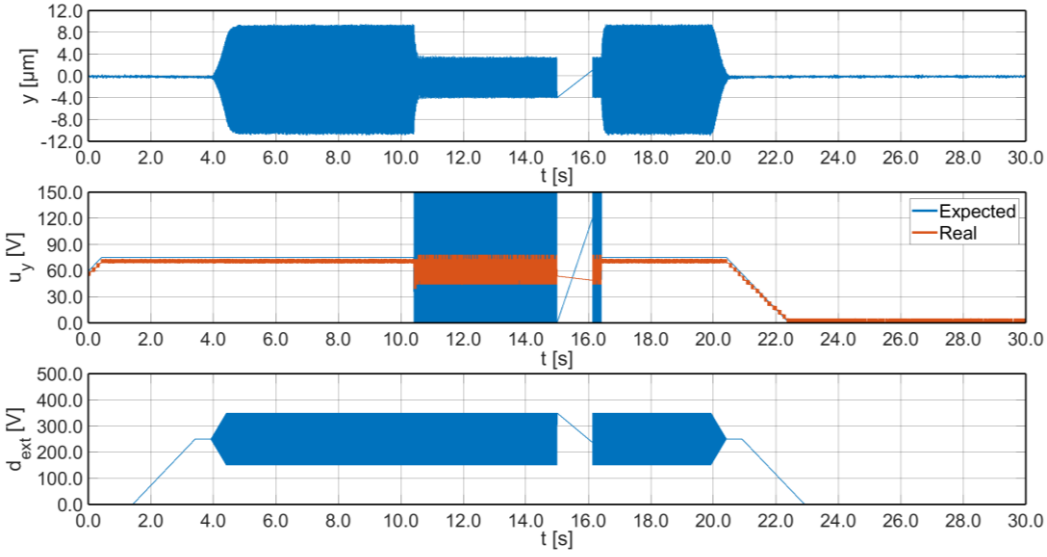

(b)

Figure 93. Test 5: (a) FFT overlap displacements representation; (b) time plot with P controller.

A 120 Hz disturbance is applied for both Test 6 and 7 with a 250 V and 200 V amplitudes, respectively. The first test produced a 7.2 µm displacement which was afterward contained by the proportional controller up to 4.8 µm and to 4.2 µm with the proportional derivative controller as represented in Figure 94a.

The PD controller obtained the highest containment (42%) while still being subjected to the saturation of the control action due to the amplifier low-pass behaviour as shown in the time plot in Figure 94b.

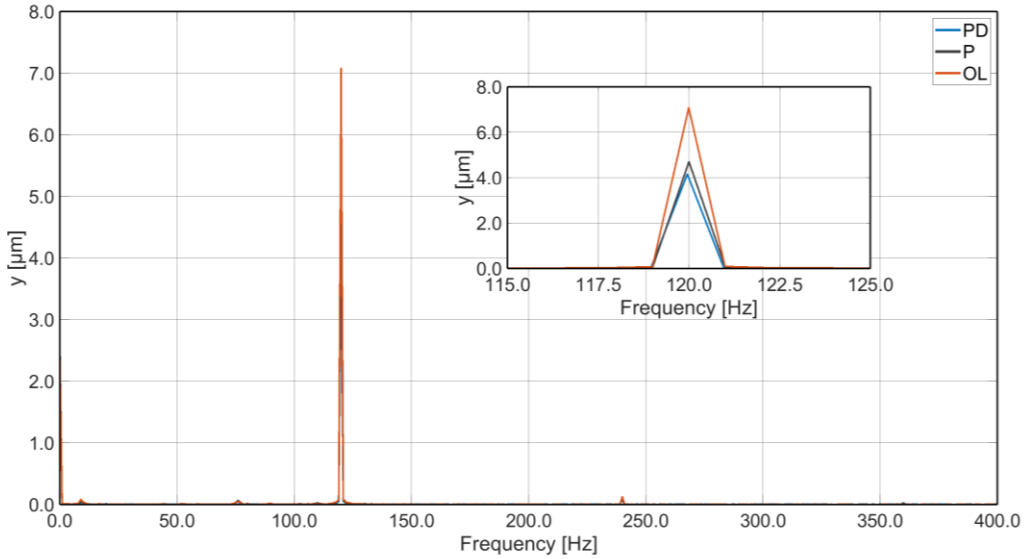

(a)

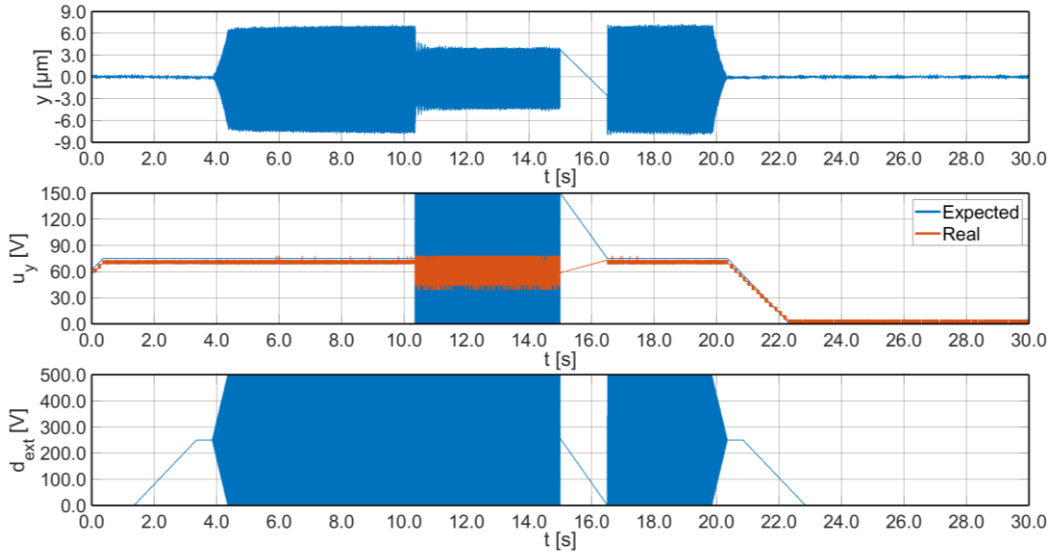

(b)

Figure 94. Test 6: (a) FFT overlap displacements representation; (b) time plot with PD controller.

Test 7 obtained an open loop displacement of 4.8 µm. The control action limited the result in both configurations P and PD, with a final motion of 3.9 µm and 2.1 µm, respectively.

Despite the containment with the P controller (19%), it produced several unwanted peaks within the frequency interval of interest, as presented in Figure 95a. In fact, the PD controller showed the best result, 56% containment, while still presenting the control action saturation as in Test 6, depicted in Figure 95b.

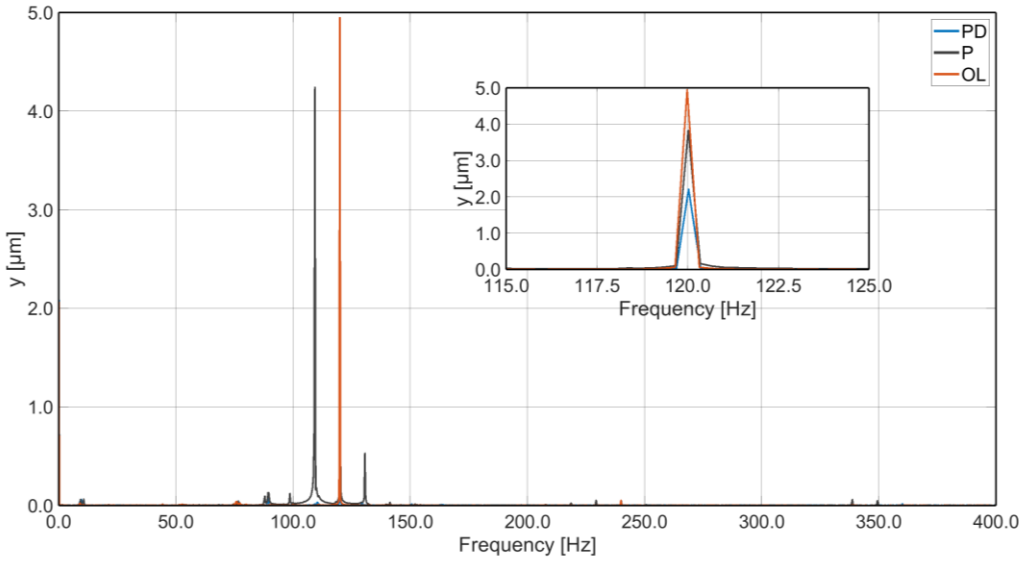

(a)

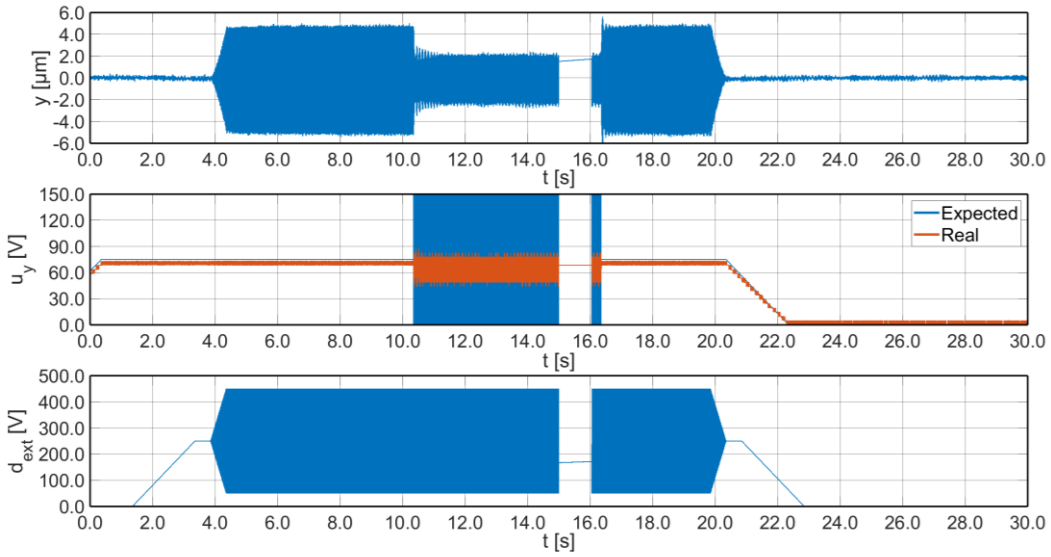

(b)

Figure 95. Test 7: (a) FFT overlap displacements representation; (b) time plot with PD controller.

Test 8 corresponds to the first multi-frequency test. It had two frequency components, 120 Hz and 130 Hz. The limited distance between these two values is caused by the limits in the system electronics which produces a narrow interval upon which the platform was tested.

The corresponding two peaks in the displacement measurements were of 3.6 µm (120 Hz) and 12.3 µm (130 Hz). Both were contained with the controllers, however, there is a clear containment for the 130 Hz peak with respect to the 120 Hz where the containment was of 0.6 µm for both controllers. Indeed, the 130 Hz peak was limited to 6.3 µm with the P controller and to 7.2 µm with the PD controller. An extra peak was created by the external actuator, which could have been due to the actuator holding structure, rather than the connection with the platform or eventually, the mechanical characteristics of the structure itself. The FFT for Test 8 is presented in Figure 96a. From these results the P controller showed the greatest containment (49%), hence its representation in the time domain is shown in Figure 96b with the disturbance and control action.

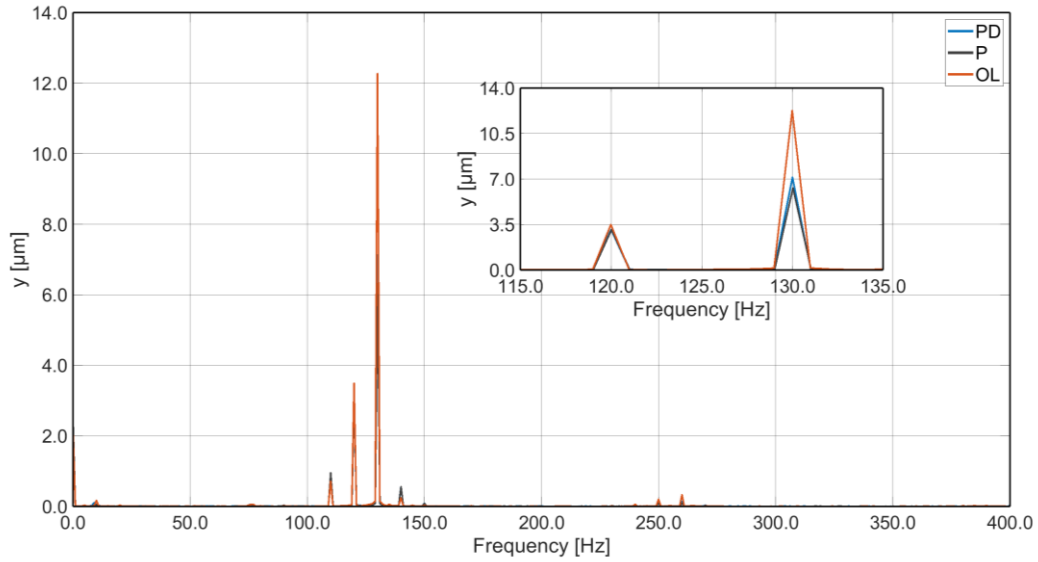

(a)

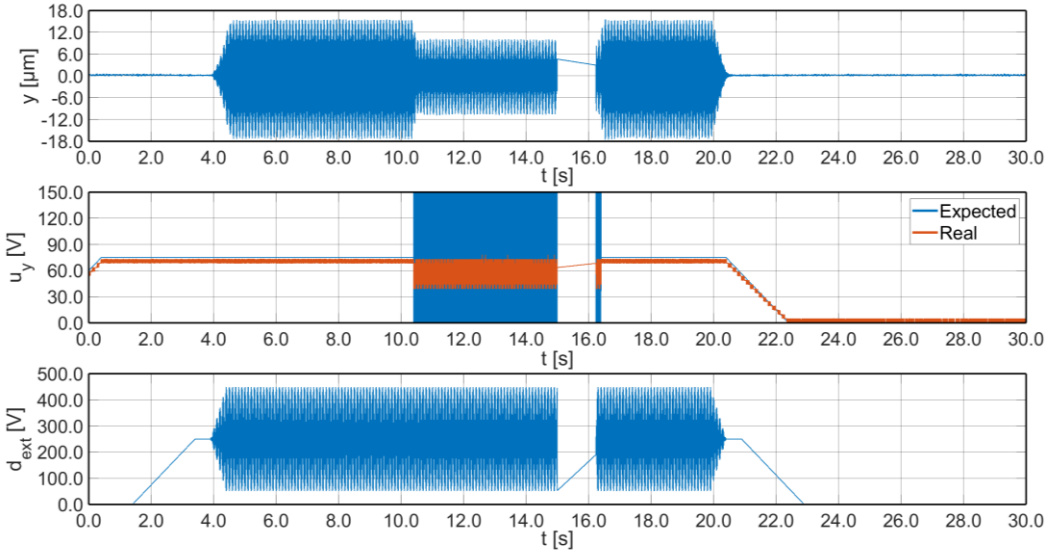

(b)

Figure 96. Test 8: (a) FFT overlap displacements representation; (b) time plot with P controller.

In a similar fashion, Test 9 presented three frequency peaks and the corresponding displacements at each frequency were: 3.9 µm at 110 Hz and 120 Hz, and 12.3 µm for the 130 Hz peaks. Despite the multi-frequency behaviour, the actual response was limited as a single 130 Hz disturbance (highest peak), and for the P controller the 110 Hz peak was incremented of 0.6 µm. Nonetheless, the main peak was contained to 7.2 µm with the P controller and to 7.5 µm with the PD controller as observed in Figure 97a. Considering the small increment caused by the P controller in the lowest frequency, the time plot in Figure 97b presents the corresponding PD control action and its effect on the displacement (top) with the above-mentioned disturbance (bottom).

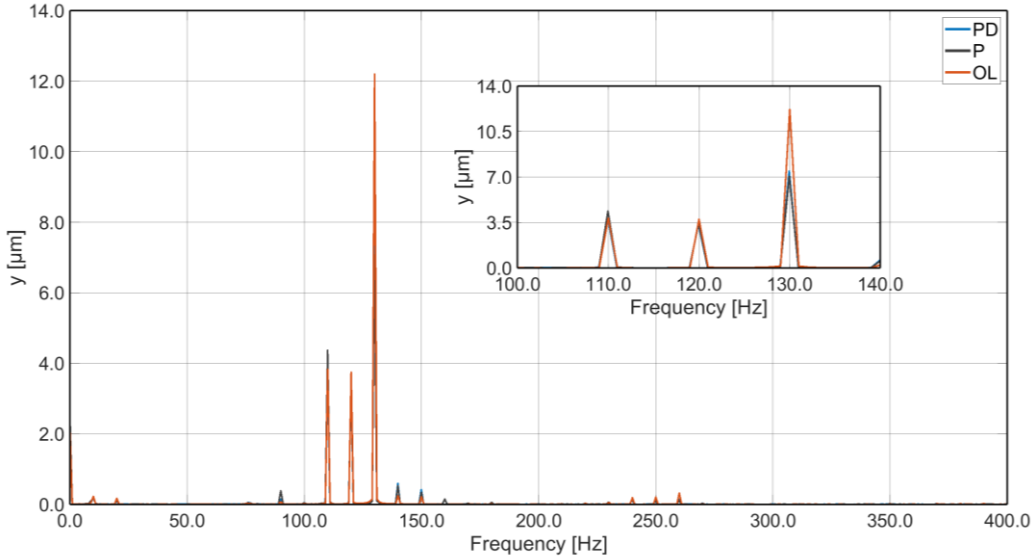

(a)

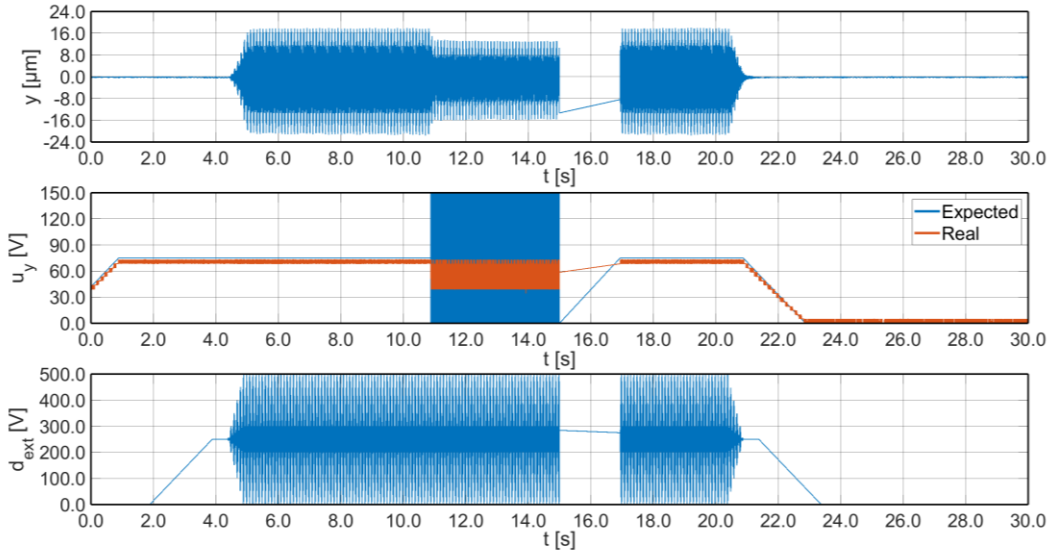

(b)

Figure 97. Test 9: (a) FFT overlap displacements representation; (b) time plot with PD controller.

Test 10 increased the frequency range to consider the borderline capabilities of the control action within the frequency interval of interest. Even though in this case there was no extra peak or amplification, a similar result to the previous test was observed as the lowest peaks remain almost the same as shown in Figure 98a with a containment of 0.6 µm for both controllers for the 120 Hz and the 150 Hz peaks. Nevertheless, the main peak was contained from the initial 12.0 µm in open loop to 6.3 µm with the proportional controller and 6.9 µm with the proportional derivative controller. This containment is depicted in Figure 98b, where the P controller displacement is presented having the highest containment.

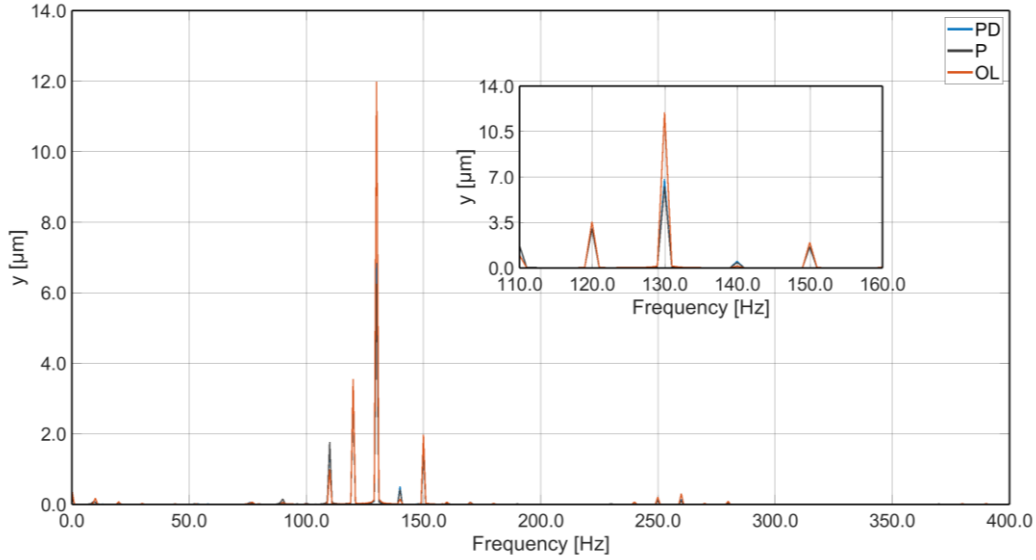

(a)

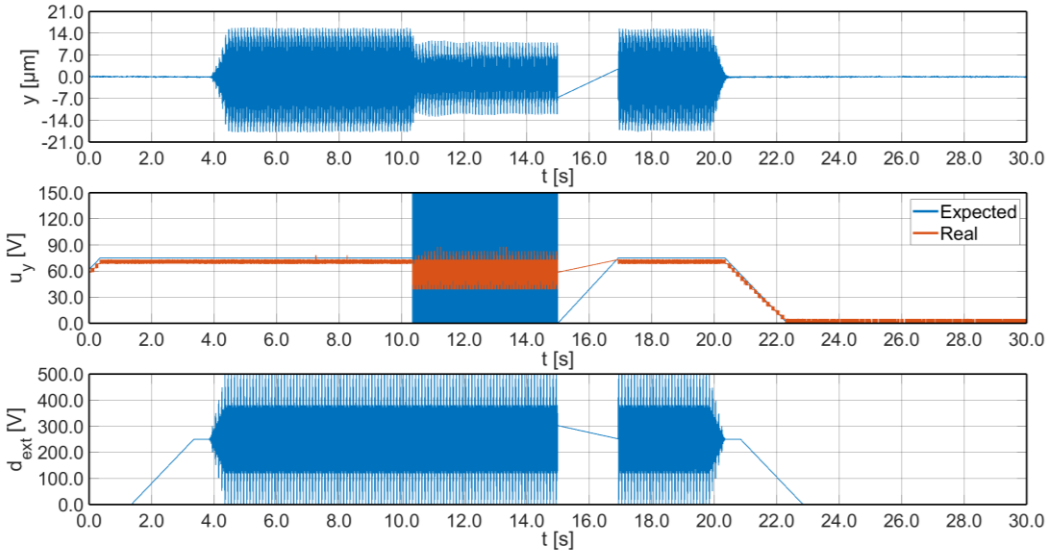

(b)

Figure 98. Test 10: (a) FFT overlap displacements representation; (b) time plot with P controller.

Finally, Test 11 showed containment for the three disturbance peaks, however the frequency interval tested was smaller than the previous tests. The final displacements at

each peak were: 2.7 µm at 120 Hz, 4.8 µm at 125 Hz, and 9.0 µm at 130 Hz. These three elements were contained with both controllers, the proportional controller results were: 1.8 µm at 120 Hz, 3.3 µm at 125 Hz, and 4.2 µm at 130 Hz; whereas the PD obtained: 1.8 µm at 120 Hz, 3.3 µm at 125 Hz, and 4.5 µm at 130 Hz. The FFT representation for Test 11 is shown in Figure 99a, the important aspect of this test was the validation of the controller's capability to deal with multiple disturbances within a small frequency interval. However, there is an appearance of an unwanted peak at 135 Hz which was excited by the external disturbance and was amplified by both controllers, nevertheless it was of small amplitude. Both controllers obtained similar results, nonetheless the P controller limited the 135 Hz amplification, as presented in Figure 99b.

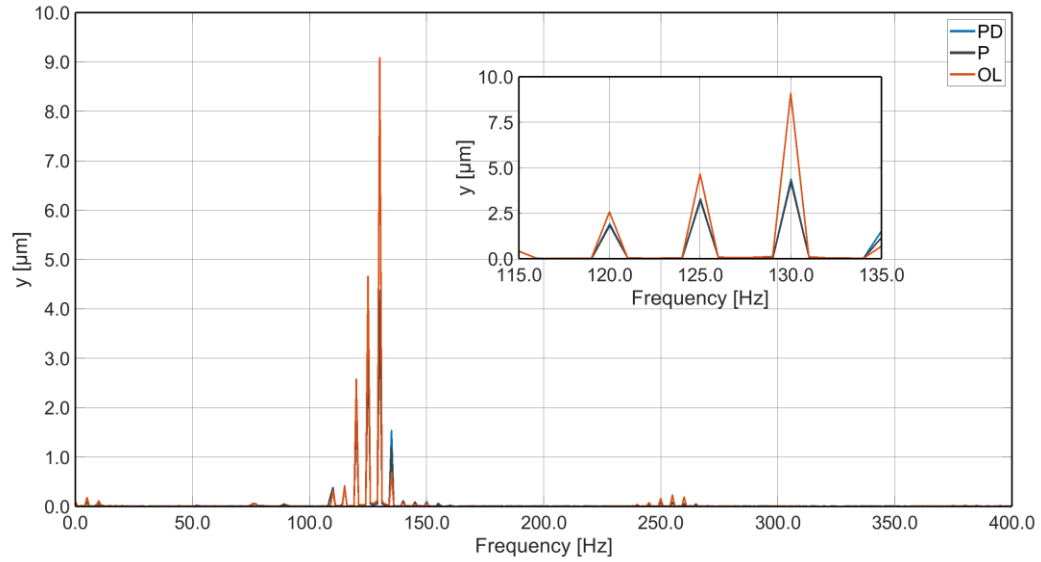

(a)

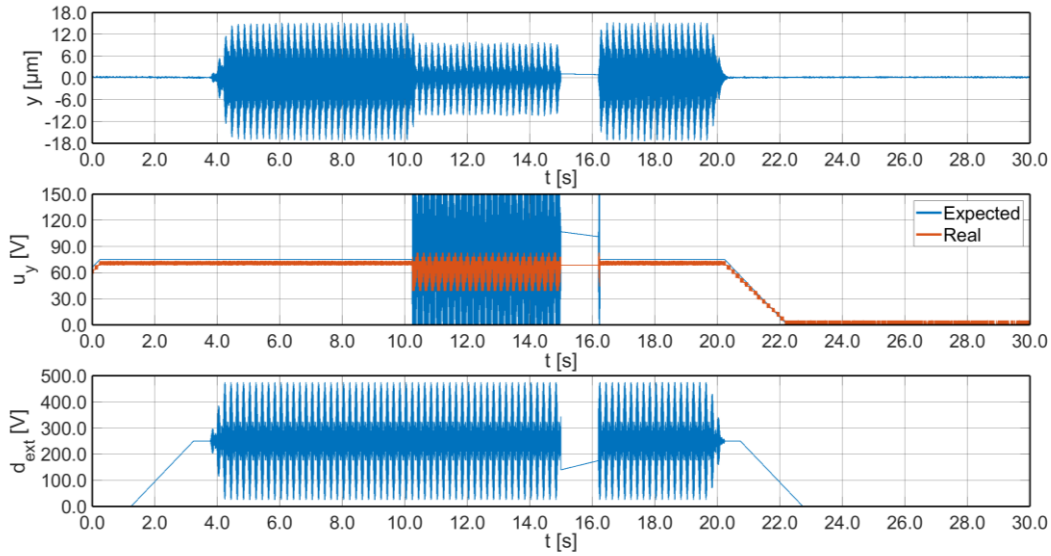

(b)

Figure 99. Test 11: (a) FFT overlap displacements representation; (b) time plot with P controller.

SECTION II

Machine Learning Scheme for Robot Inverse Kinematic Modelling

Chapter 1

Literature Review

This chapter introduces the implications of robot modelling and the main problematics encountered. In particular, the issues related to the inverse kinematic approach and the consequences of wrong calibration are elaborated. Furthermore, the state-of-the-art methods are presented, from analytical approaches to machine learning optimized schemes. Finally, the contributions of this thesis work to the field are described.

1.1 Problem Statement

The kinematic formulation plays a significant part in nowadays robotic applications, from industrial to service areas. Currently, robot configuration is based on several actuated joints that link the rigid elements in a series-wise, parallel, or hybrid approach for a general-purpose manipulation task. Multi degree-of-freedom (DOF) robots exhibit a working volume that enables the pose reaching in different configurations of the kinematic chain, except for the singularity positions. These configurations are defined based on the mapping between the base frame, located at the robot ground, and the end-effector frame, positioned at the tool-centre-point (TCP), required to define the interaction with the external environment. The robot's kinematic formulation relates the Cartesian coordinates of the end-effector accounting for the related frames and, thus, presents the coordinates with respect to the base frame, with the joints' values. Depending on the computation direction, two different sets of equations are depicted, the forward kinematics (FK) equations and the inverse kinematics (IK) equations. The former equation system is employed to compute the Cartesian coordinates of a given reference system, position and orientation, with respect to the joint configuration in a unique way; meaning that each joints' configuration corresponds to a specific Cartesian position and orientation. In other words, it is used to obtain the TCP coordinates based on the chosen actuators' values. A significant amount of research has been presented in the literature to compute this set of equations, particularly through matrix multiplication and mathematical procedures [143,144]. However, despite their simple computation, FK equations cannot be employed for correct trajectory planning or path optimization as the standard procedures require the cartesian definition of the TCP points for the pursued operation from which the joints values are defined.

Regarding the need for joints information based on the Cartesian data points, the IK equations associate the corresponding mapping between these two concepts. Unlike the FK equations, for each point within the workspace volume of the robotic manipulator exist n potential joint configurations, where n is the redundancy degree. Robots capable

of reaching a point in the cartesian space with multiple configurations are known as redundant robots since they have more degrees of freedom than required to perform the point-reaching task [145].

Simple or standard robots might allow the obtention of an algebraic solution with a closed IK equation system. However, for more complex manipulators this is hardly obtained as the DOF increases, thereby, several methods have been proposed to deal with such issue, implementing optimization schemes or constrained motions [146–148]. Indeed, there is a set of conventional techniques to solve IK problems such as algebraic, geometric, and iterative methods [143,149]. In fact, for these types of manipulators, optimization methods, such as particle swarm optimization (PSO) [150–152] or genetic algorithm (GA) [153,154], have been adopted to avoid high-order polynomials. Nevertheless, the high-computational burden, the impact of the initial setting, and the inadequate convergence are constraints that need to be regulated [155].

Recently, alternative procedures based on machine learning (ML) schemes have been proposed to compute the IK model. Despite the training time required and the scheme optimization phase which might need several attempts and validations; once the ML is trained the predictions are obtained promptly with respect to numerical and optimization schemes.

1.2 Literature Review

Among the different ML schemes proposed in literature, the artificial neural network (ANN) is one of the most important and most applied models. An ANN scheme is proposed by Duka in [156], where a 3-layers (input, hidden, output) shallow network with 100 neurons in its hidden layer is defined to model the IK of a 3-DOF planar robot employing the FK equations to produce the dataset for the corresponding training and validation of the proposed structure. The results showed a mean square error (MSE) equal to 5.4387×10^{-3} rad in the joint space. In a similar manner, Habibkhah et al. [157], employed a shallow network with 12 neurons for a planar robot, despite the constrained number of neurons, the authors included an orientation function based on the cosine function which permitted to obtain a validation of MSE equal to 3.8523×10^{-4}rad. Finally, an identical planar manipulator was used by Varedi-Koulaei et al. [158] but, instead of a shallow network, a 5-layer ANN was implemented. The authors proposed an automated optimization phase for the network parameters' tuning based on the PSO algorithm, obtaining a final validation of MSE close to 1.3×10^{-4} rad in joint space.

A higher complexity is encountered with spatial robots, as in Li et al [159] where the authors employed a shallow single hidden layer back-propagation neural network with 30 hidden neurons to model a (RS100N) 6-DOF industrial robot. The deployed network was used in a constrained workspace and validated on a rectangle trajectory. The authors stated an error lower than ±0.05°, a maximum deviation on the horizontal axis of 1.00 mm and 0.50 mm along the vertical axis. Similarly, Narayan et al. [160] proposed the ANFIS technique on a reduced workspace to predict the IK of a 4-DOF SCARA robot. The maximum observed deviation of the end-effector was 3.775×10^{-1} mm in

X-direction, $4.135x10^{-1}$ mm in Y-direction, and $2.7x10^{-3}$ mm in Z-direction. Nevertheless, these applications have limited workspace with planar or highly constrained robot motion which simplifies the corresponding inverse kinematic computation reducing the errors for the evaluated applications.

To avoid the workspace limitations, an alternative approach is presented in Shah et al [161] where the authors dealt with this problematic by dividing the spatial workspace in quadrants and producing a 5-layers ANN for each one of them to model a 5-DOF proprietary robot, the application was validated for a single quadrant obtaining a final joint error range of ±0.003 rad. The spatial complexity is considered differently in Almusawi et al [162], where the authors included an inner feedback data for the current joints' values given as extra inputs to the 10-hidden layers ANN to model the IK of a Denso VP6242 (6-DOF). The validation phase based on a spring curve trajectory has demonstrated the errors for X-, Y-, and Z-axes equal to 0.22 mm, 0.30 mm, and 0.35 mm. Despite the accurate results, the inclusion of present joint values might produce an issue in this scheme generalization based on the input trajectory requirement for the ANN. Furthermore, a Long Short-Term Memory (LSTM) method is presented by Singh et al. [163]. Authors discussed a recurrent neural network model, with two hidden layers of 10 LSTM neurons each, to perform the IK of the left arm of the Baxter 7-DOF Robot demonstrating a final MSE of the test data set lower than 0.02. A tree-based algorithm was implemented by Thomas et al. [164] to model the IK of a 6-DOF parallel manipulator. The dataset was generated by recording the end-effector pose with a camera and its corresponding joint values with ultrasonic sensors. The Random Forest (RF) algorithm obtained the best training results, with a coefficient of determination equal to 94.61% and a Root-Mean-Square Error, RMSE, of $3.59x10^{-2}$ m. Alternatively, committee schemes could represent an accurate approach as demonstrated by Köker et al. in [165]; where a neural network committee machine for a Hitachi M6100, a 6-DOF redundant robot, was proposed. The concept is based on 10 parallel shallow networks, which could be simplified to 6 as claimed by the authors, with variable hidden neurons. The committee output is chosen from the parallel networks based on the minimization of the cartesian error, obtained with the FK. The approach with respect to a global ANN approach obtained a reduction from 5.76-13.41 mm to a final error within 0.39-0.74 mm. The committee scheme showed high error reduction, nevertheless the multiple model training time and the higher amount of data required for complex applications might be an issue for their application.

To improve the model accuracy, further methodologies are the hybrid procedures based on ML models and optimization algorithms applied in cascade form. Köker et al. [166] implemented a hybrid Simulated Annealing with GA to reduce the shallow network, with 46 neurons in the hidden layer, error to 1.0 μm for a 4-DOF manipulator. Similarly, a neuro annealing approach based on Elman recurrent networks for the Stanford and PUMA 560 robotic manipulator was applied in [167] where a committee system with Elman networks was proposed as in [165], for which the final output was optimized based on a Simulated Annealing scheme; reducing the MSE from 2.10 to $7.9x10^{-6}$, in joint space. An alternative GA approach is observed in Zhou et al. [168],

where the authors applied an Extreme Learning Machine (ELM) combined with a Sequential mutation Genetic Algorithm (SGA) to reduce the model error of a 6-DOF Stanford MT-ARM robot to $2.25x10^{-2}$ mm with a standard deviation of $8.1x10^{-3}$ mm. Despite decreasing the final error, these hybrid approaches tend to highly increase the simulation time required to obtain the model results which is a critical aspect in robot motion, as in the previous application where the average computational time was increased from 0.91 ms up to 5.52 ms.

Although the literature shows promising methods and significant results in addressing ML strategies to achieve effective and robust manipulator's IK formulation, further studies are required to evaluate novel techniques for robot inverse kinematic modelling.

1.3 Contribution

From the above literature review, most of the widely used ML methods aimed at general model developments for which all the joint values were computed simultaneously, increasing the final model complexity and the computational cost. However, the deployment of a model for each single joint calculation as in [169,170] may represent a novel paradigm.

The main contribution of this section is to investigate and deploy a ML-model using a novel sequential procedure for an accurate IK formulation. At each joint, the input vector includes the previously obtained actuators' values and the present Cartesian coordinates with orientation. Moreover, the model hyperparameters are defined with the genetic algorithm optimization technique employing a cost function with accounts for multiple error performance coefficients, reducing the influence of user-inference and manual network optimization.

The dataset employed for the model training, optimization, and validation is defined with the forward kinematic (FK) equations. The artificially generated dataset reduces the required time for new robotic manipulators and permits to employ a higher number of points, limited when experimental measurements are employed. However, in order to provide an accurate FK model and avoid misleading model errors, the methodology proposed includes an initial phase of FK modelling based on D-H matrices, whose parameters are obtained automatically based on a limited set of measurements as presented in [171]. Nevertheless, an alternative path is included for which the D-H parameters can be input directly when the automatic procedure proposed does not achieve accurate results in the assessment phase for which a set of trajectories is employed to validate the obtained FK model.

Finally, the novel sequential methodology is validated in a simulated environment (IRB140) and with a real industrial robot (LR-Mate 200iC).

Chapter 2

Robotic Machine Learning Application

This chapter presents the inverse kinematic modelling methodology, based on a set of artificial neural networks tuned with genetic optimization. This machine learning application has been applied in the literature and therefore a brief introduction to the main goal is carried out. Furthermore, the working principle, applications and boundaries are depicted for the case study.

2.1 Introduction

Similar to other fields, robotics is having a constantly increasingly attention for machine learning applications, employed to solve various issues as the computation of accurate inverse kinematic/dynamic solutions in an efficient manner, motion planning, and control [163,168]. Among the different problems, determining the kinematic formulations for a given manipulator is required for any motion task [172], however, present applications based on closed-form inverse kinematics or optimization schemes usually are a cumbersome time-consuming solution. Moreover, inaccuracies due to manufacturing defects, joint friction and elasticity (difficult to model) might compromise the mathematical model performance [163]. In summary, robots are still affected by errors due to their model limitations and time-consuming applications, limiting the final performance and, therefore, the accuracy requirements for trajectories and positionings tasks might not be satisfied.

Hence, based on previous machine learning solutions, a novel approach is depicted employing a series of ANN models sequentially to model the inverse kinematic of a given robot. The main objective was to avoid the long complex process of analytical approaches [143,144] or optimization schemes [150,151,153,154]. In order to assess and validate the methodology proposed two main applications are presented with an ABB IRB 140 and a FANUC LR Mate 200iC. Whilst the first robot is modelled employing the ABB environment to produce the dataset required, the FANUC was studied in an experimental case study.

The methodology validation is carried out based on both the numerical results obtained with random points workspace and a set of trajectories in the defined workspace volume. These paths are evaluated pointwise without any dependency constraint between consequent datapoints. For each point the information of the studied joints and the Cartesian coordinates are produced.

2.2 Sequential Machine Learning Methodology

The machine learning methodology proposed in this section aims to reduce the complexity of global approach [155,158,159,162] for which all the joints are modelled with the same ML scheme; a complete black-box approach for this kind of application. The complications derived from this approach are related to the user inference capabilities, the time consumption required to train the model, and the high error with respect to the methodology proposed in this thesis.

The methodology proposed is based on the division of complex systems into simpler connected elements, which reduce the complexness of the produced model and allows a certain error reduction due to the interconnection between the modules and the increment in the provided information for the ML scheme. Furthermore, the granularity of this approach allows to evaluate the single parts and optimize certain aspects related to a given sub-element of the complex system. In summary, this application is based on the individual joint modelling based on artificial neural networks (ANN) as in [169] but instead of producing independent models, a sequential approach is included for which the individual models are interconnected, and the previously computed joints are employed as extra inputs for the following joints.

The dataset employed for the machine learning application is produced with the FK equations, obtained based on the D-H approach. Furthermore, the ANNs' hyperparameters, neurons per layer and number of hidden layers, are tuned with the genetic algorithm optimization based on a proposed cost function that accounts for the errors for both validation and training datasets.

2.2.1 Working Principle

The proposed scheme initiates by inquiring a robot structure for which a set of measurements must be carried out to provide the Denavit-Hartenberg parameters based on an automatic procedure and therefore, based on matrix multiplication, obtain the FK equations of the manipulator. Once the parameters are obtained, and hence the forward model described, an initial validation phase has been included to deal with modelling errors. This is an important task considering that the following machine learning schemes are trained based on the dataset produced with the FK model. Consequently, four trajectories within the workspace volume considered for the studied robots are defined: a circle, a spiral, an S-shape, and a rectangle. For each path the main parameters are perturbed to evaluate the influence of shorter and longer motion displacements. The FK model validation is obtained when the *mean Euclidean error* and its variation under disturbance are lower than a given threshold.

Once the FK equations are obtained the dataset is produced. It is composed of an output vector whose datapoints contain the joints' values and an input vector containing the corresponding Cartesian coordinates and orientation. For each joint a set of data-points is sampled randomly without repetition within the range of motion, producing a matrix of randomly distributed unique data points in the joint space. The Cartesian

coordinates, position and orientation, are obtained based on the FK model. The final dataset is randomly divided in three parts: train, test, and validation.

Afterwards, the dataset is sectioned by joints to train one ANN at a time, employing the previously computed models for the remaining joints. Moreover, the ANN has several hyperparameters which require tuning, in order to obtain an automatic procedure this methodology employs the Genetic Algorithm to optimize such parameters with respect to the model coefficients obtained for the training, and validation datasets through a free-of-choice weight formula. In summary, the complete model contains a set of ANNs which must be employed in a sequential scheme to obtain the complete set of joint coordinates from the Cartesian coordinates inputs.

2.2.2 Features

The developed methodology has several key features related to the dataset and model creation. First, the generalization of the methodology for any serial-type robot provided the FK is correctly modelled by the automatic procedure or manually implemented. The automatic D-H procedure employed for the FK permits to produce measured-based dataset with several datapoints, as these parameters are obtained experimentally with a reduced number of data-points. Whatever the source of the FK model, a phase of model validation is carried out with a series of perturbed spatial trajectories.

Another important feature corresponds to the method employed for the artificially generated dataset, which ease the production of large dataset and avoids the problems arising from multiple measurements. Furthermore, the uniqueness characteristic of the dataset is obtained based on the single sampling of joints' values.

Considering the machine learning scheme, the sequential approach presented previously, allows to obtain simpler ANN structures. Furthermore, the individual joint modelling permits the evaluation of the individual actuators' characteristics which constraints the effect of the black-box model. Moreover, the hyperparameter tuning of the ANNs with the GA improves the generalization and ease the model creation phase with respect to other manual applications which rely solely on expert knowledge. Finally, the sequential approach permits the parallel training of the individual joints' models reducing the final computational time, although the computational burden for the training and optimization phase are increased.

2.2.3 Applications and boundaries

This scheme permits future applications for unknown kinematics modelling on any type of actuated structure with similar serial structure. Therefore, by employing an artificial neural network with a sequential mechanism, the main parameters are obtained to ease the final modelling. Moreover, the ANN, once trained, is much faster than the continuous calculus computation or optimization procedures (dependent on the initial conditions) which is a high appeal for robotic applications.

Further developments in this area could aim to employ hybrid schemes employing the ANN, or a different machine learning scheme, to produce the initial conditions for the optimization schemes. Reducing the final time, with respect to the optimization approach, and the maximum error while increasing the robustness of the optimization scheme reducing the risk of unwanted initial conditions. Nevertheless, an important aspect to consider for these systems is that the network results are dependent of the structure, hence the robot, and cannot be applied for a different structure without increasing the final error; unless the concept of transfer learning is employed upon which, for similar robots, an already trained network is re-trained to match the specific case, reducing the required training time.

Chapter 3

Machine Learning Scheme

This chapter presents the data-driven approach based on ANN used to model the industrial robots, the iterative approach can become a standard methodology for any mechatronic device modelling. First, the process of determining the forward kinematic equations of the robot to produce the dataset is described, followed by the explanation of the novel ANN scheme, the architecture optimization, and the coefficient performances for its validation.

3.1 Methodology

The inverse kinematic function defines the joints' configuration (Q) required to reach the target frame with the Cartesian coordinates (S) of the end-effector. This study proposes a novel methodology based on a sequential scheme to iteratively model the individual joints while maintaining the rational connection between them. The flow diagram of the proposed methodology is presented in Figure 100. The approach has three macro-steps, an initial phase named "*IK boundary definition and pre-processing*" upon which the artificially generated dataset is produced based on the robot selection and the forward kinematics model. This model is created with the D-H matrix with an inner automated phase for which, after a set of experimental measurements, the parameters of the robots are computed. Alternatively, a manual approach has been defined. Before the following phase starts the FK must be validated, indeed the mean Euclidean error (MEE) computed for a set of predefined trajectories to verify the model accuracy; after which the dataset is produced.

The following step aims to define the ANN structure for the IK model with the novel *sequential* approach, "*Network Architecture Definition*", where the joints are computed sequentially from the TCP or the Base, integrating the previously modelled joint as extra input for the following one. Whilst the latter corresponds to the methodology proposed, the *Global* approach is also introduced to permit the comparison and evaluation with standard approaches. The chosen model is tuned based on the genetic algorithm (GA) optimization with a predefined tuneable cost-function. Finally, the last step concludes the novel methodology with the produced IK model validation employing the trajectories used for the FK validation

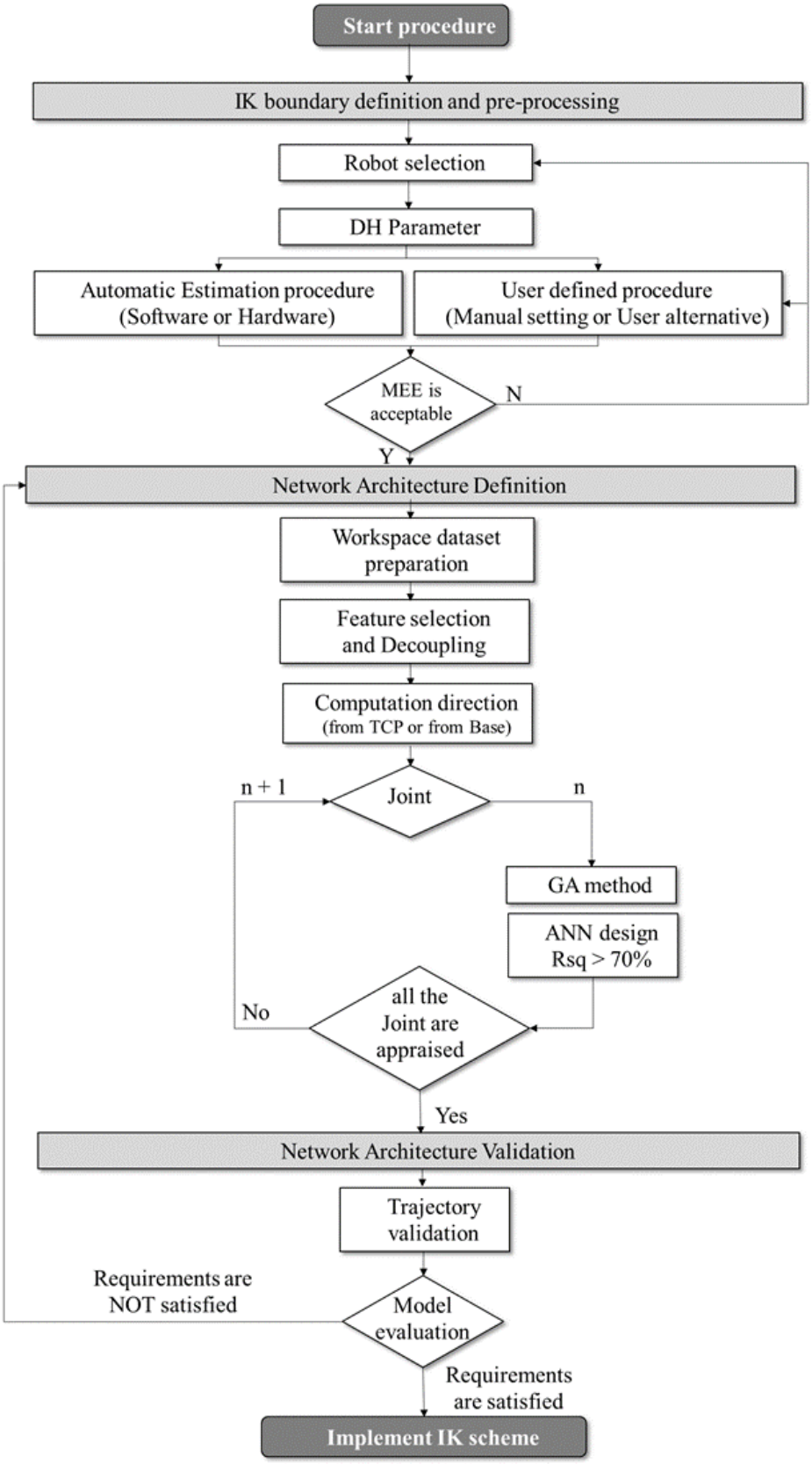

Figure 100. Flow Diagram of the IK procedure.

The following table summarizes the methodology in terms of input and output elements of the proposed IK procedure.

Table 12. Input/Output IK procedure.

IK Boundary Definition and Pre-Processing	
Input	Selet the robot
	Joint geometrical dimensions/position
	Use 70-15-15 technique to obtain the training-testing-validation datasets
Output	Estimate D-H parameters
	FK equations based on the D-H parameters and validated with the mean Euclidean error index
Network Architecture Definition	
Input	Dataset for the defined D-H parameters
	Define the number of joints
	Check algorithm constraints
	Activation functions
	Feature selection and filtering
Output	Hidden layers (HL)
	Hidden neurons (HN)
	Quantify model robustness
	Comparison between methods and datasets (training and validation)
Network Architecture Validation	
Input	Appraisal of the testing dataset
	Select optimization leverages and ranges
	ANN optimization architecture
	Select adequate deployment duration
Output	Algorithm performance
	Estimate feature prediction errors

3.2 Dataset Generation

The artificially generated dataset requires the FK modelling to provide the corresponding Cartesian coordinates from the produced joints values. As depicted in the flow diagram presented before, the FK can be obtained in two different approaches, whereas the kinematic equations or the D-H parameters are manually input to the system; or in alternative, the automatic procedure is employed to find the D-H matrix and consequently compute the FK. Considering that both approaches depend mainly on the Denavit-Hartenberg matrix, it is important to first introduce these parameters and present

the automatic methodology proposed in [171]. In the D-H algorithm, each joint is assigned with a sequential number from 1 to *n*, where 1 is the first joint located at the robot base and *n* defines the last robot's joint. This algorithm is a recurrent method which requires a certain methodology for the determination of the axes and its directions along with the parameters obtention. The first step is the axes determination, in this case the Z-axes for each joint defines the direction of motion of the given actuator, with the origin at its centre. Whereas the initial base joint is assigned with the zero-coordinate system and the X- and Y-axes related to the base reference system, the following joints must follow a set of rules. Whilst the Y-axis is found with the right-handed rule based on the frame containing the X- and Z-axes; the X-axis for the relative joint (X_i) has different computation approaches depending on the relative position of the consequent joints of the robot considered. If the Z-axis for the evaluated joint (Z_i) and the one for the previous joint (Z_{i-1}) intersect, then X_i is obtained with the cross product of Z_i *x* Z_{i-1}. If the Z-axes are instead parallel then X_i must intersect both axes, from Z_{i-1}. Once the axes have been defined the D-H parameters can be identified as follows [173]:

- **Joint angle $\boldsymbol{\theta_i}$:** rotation angle about the Z_{i-1} axis, determined from X_{i-1} to X_i. The angle corresponds to the joint value if the joint has a rotary actuator.
- **Joint distance $\boldsymbol{d_i}$:** distance along the Z_{i-1}, from the origin of the (i − 1)th frame to the intersection of the Z_{i-1} with X_i.
- **Link length $\boldsymbol{a_i}$:** distance along the X_i axis, from the intersection between the Z_i and the Z_{i-1} axis to the origin of the ith coordinate frame.
- **Link twist $\boldsymbol{\alpha_i}$:** rotation about X_i, defined from Z_{i-1} to the Z_i axis.

The D-H parameters produce a $R^{n\times 4}$ matrix containing the aforementioned parameters for each joint of interest, being *n* the number of joints of the robotic manipulator. Afterwards, the initial step corresponds to the identification of the transformation matrices, that define the relative model between consequent joints, derived from Equations 54 and 55, where *k* is the joint number for which it is being computed. The homogeneous transformation matrix A is defined, based on the D-H parameters, as follows:

$$A_k^{k-1} = R(z,\theta_k)\,T(z,d_k)T(x,a_k)R(x,\alpha_k) \tag{54}$$

$$A_k^{k-1} = \begin{bmatrix} c\theta_k & -s\theta_k \cdot c\alpha_k & s\theta_k \cdot s\alpha_k & a_k \cdot c\theta_k \\ s\theta_k & c\theta_k \cdot c\alpha_k & -c\theta_k \cdot s\alpha_k & a_k \cdot s\theta_k \\ 0 & s\alpha_k & c\alpha_k & d_k \\ 0 & 0 & 0 & 1 \end{bmatrix} \tag{55}$$

where $c\theta_k$ and $s\theta_k$ correspond to the cosine and sine functions of θ_k, $c\alpha_k$ and $s\alpha_k$ correspond to the cosine and sine functions of α_k. The matrix order multiplication produces the final transformation matrix from the end-effector to the base frame:

$$T_n^0 = \prod_{k=1}^{n} A_k^{k-1} = \begin{bmatrix} n_x & s_x & a_x & p_x \\ n_y & s_y & a_y & p_y \\ n_z & s_z & a_z & p_z \\ 0 & 0 & 0 & 1 \end{bmatrix} \tag{56}$$

where vectors *n*, *s*, and *a* define the manipulator orientation and vector *p* represents the position in Cartesian coordinates. The produced matrix corresponds to the FK equations. However, the procedure described is a time-consuming activity and requires certain expert knowledge for the manual pursue. Hence, an alternative approach is proposed based on an automatic procedure as presented in [171], despite claimed accurate results obtained for the evaluated system the authors described a remaining limitation due to the nature of the D-H notation with the non-continuity in actuators with parallel, or almost parallel consecutive joints. The proposed algorithm requires a sequence of motions iteratively for each joint from the initial position until reaching its end position, which represents the maximum and minimum permitted mechanical position, respectively.

The FK model validation is a critical point in the proposed methodology, due to the data-driven nature of the IK model. In fact, the model is afterwards used to produce the dataset for the training and testing of the ML model, hence, the FK model must be assessed to prevent misleading results. In fact, the FK validation is carried out with a set of four different trajectories, as shown in Figure 101a-d.

Furthermore, the robustness of the FK model is assessed by varying the main trajectory parameter on two different levels: contraction (low level) and expansion (high level) of 20% for the initial value. The chosen perturbation was arbitrarily defined and allows the model assessment for varying paths for which larger motions or small distances between subsequent points might represent a problematic condition. The varying parameter depends on the trajectory evaluated: (i) the radius of the Circle; (ii) the radius of the Spiral; (iii) the radius of the S-shape path; and (iv) the side length of the Rectangle.

Taking into account the workspace volume of the robotic manipulators, a performance coefficient based on the Euclidean distance in the spatial representation is chosen since it is more representative than the single-axis evaluation. Therefore, the MEE index is employed to assess the FK performances, as a measure of the mean 3D distance error. The MEE is obtained as defined in Equation 57:

$$MEE = \frac{1}{n}\sum_{i=0}^{n}\left(\sqrt{{E_{x_i}}^2 + {E_{y_i}}^2 + {E_{z_i}}^2}\right) \quad \textbf{57}$$

where $\{E_x;\ E_y\ ;\ E_z\}$ describe the error along X-, Y-, Z- axes, respectively; and n is the number of samples. This performance coefficient permits to determine if the FK model is applicable or if it should be revised; for the methodology proposed a threshold must be chosen which describes the maximum acceptable error for the application considered. If this limit is not satisfied, then the methodology proposes to repeat the automatic procedure with a greater number of points for the D-H obtention or enquires for the direct D-H manual implementation. Nevertheless, both consequent possibilities require the repetition of the model assessment.

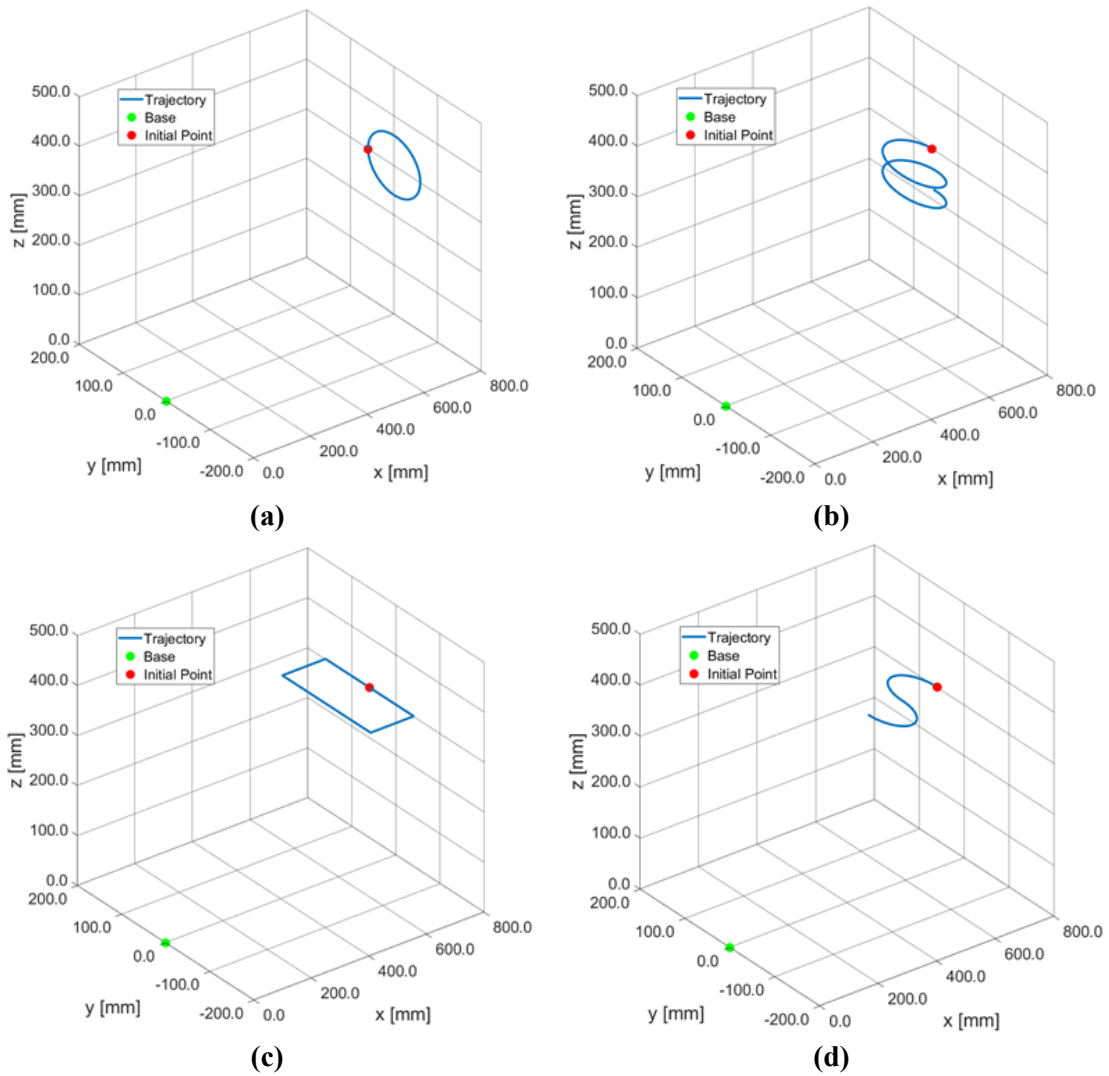

Figure 101. Implemented validation trajectories: (a) Circle, (b) Spiral, (c) Rectangle, (d) S-shape.

Once validated, the FK model is employed to produce the dataset. First the joint motion ranges are defined based on which a pseudo-random generator is employed to produce the dataset. The corresponding data is expressed with an $R^{n\times m}$ matrix, where n is the number of DOFs of the selected robot and m is the number of joint space data points (10,000 elements by default). Indeed, the pseudo-random sampling without repetition of joint datapoints within the range of motion permits to ensure the uniqueness of the dataset as each line will be unique. The corresponding joint dataset represents the output data for the ML application, therefore, to compute the input dataset the Cartesian coordinates and orientations are computed for each line with the FK model.

3.3 Model Architecture Definition

The following step in the novel methodology proposed is the "*network architecture definition*". The procedure begins with the dataset division: 70% for training, 15% for testing, and 15% for validation. This is a conventional approach for ML applications [174–176]. The feature selection process and the model fine-tuning cannot be performed based on the results of the testing dataset, as it should remain unused and unbiased data for the model assessment. Hence, the validation dataset is employed to

evaluate the model definition and the overfitting avoidance. An alternative approach to the three-part standard dataset division would be the implementation of the k-fold cross-validation to tune the model hyperparameters [172,177,178].

Afterwards, the network architecture must be defined, which requires the definition and tuning of several parameters, among which: the number of hidden layers, the number of neurons per hidden layer, and the activation function for each layer. The depth of the network determines the capability of the architecture to model non-linearities and complex structures, however, there is no direct dependency between deep models with a high number of hidden layers and improvements in the results. In fact, too many hidden layers increase the computational burden and might worsen the obtainable results. Hence, the standard approach is to define such hyperparameters based on expert knowledge and iterative approaches. To avoid such cumbersome process, the proposed methodology employs the GA optimization, which is a recognized stochastic search optimization algorithm inspired by the evolution theory, to tune the first two parameters. Nonetheless, due to the time required for the optimization and the smaller influence of the activation function in the final model performances with respect to the hidden layers definition, this parameter was tuned manually and was implemented as *tan-sigmoid* (tansig).

The consequent GA optimization requires boundaries definition for the search scheme, which are defined as follows for the proposed methodology: the number of hidden layers range is limited from 3 to 7, and the neurons per layer is defined within the range from 10 to 80, with a 5 hidden neurons resolution to reduce the computational time required. Finally, the GA method aims to minimize a cost-function, which must be defined as it determines the weight for the search process. For the proposed scheme, the GA score is determined by Equation 58, based on the training and the validation performance measurements obtained with Equations 59-61:

$$y = \alpha \cdot NRMSE_v + \beta \cdot NRMSE_{tr} + MAXE_v \cdot (1 - R_v^2) \quad \textbf{58}$$

$$NRMSE = \frac{\sqrt{\frac{1}{n}\sum_{i=1}^{n}(y(i) - \tilde{y}(i))^2}}{y_{MAX} - y_{MIN}} \quad \textbf{59}$$

$$MAXE = \mathrm{MAX}(|y(i) - \tilde{y}(i)|) \quad \textbf{60}$$

$$R^2 = 1 - \frac{\sum_{i=1}^{n}(y(i) - \tilde{y}(i))^2}{\sum_{i=1}^{n}\left(y(i) - \frac{1}{n}\sum_{i=1}^{n} y(i)\right)^2} \quad \textbf{61}$$

where $y(i)$ is the target value, y_{MAX} and y_{MIN} are the maximum and minimum of the target element; $\tilde{y}(i)$ is the predicted value; n is the sample number; $NRMSE$ is the *normalized root mean square error*; $MAXE$ is the *maximum absolute error*; and R^2 is the coefficient of determination. The *v* and *tr* correspond to the *validation* and *training* dataset, respectively. The α and β coefficients need to be tuned by the user to apply the optimization algorithm.

Three performance coefficients are used to define the GA cost-function. The first is the *NRMSE*, it is a normalized coefficient defined with respect to the interval of the target element. The normalization permits the independence from the actual error's dimensions, which is a critical consideration taking into account the various robot dimensions and the diversity in the workspace volumes. Indeed, by employing the normalized coefficient two robots of different dimensions and typology can be compared. The weighted sum of the *NRMSE* coefficients for both the validation and training errors is performed with two constant coefficients α equal to 0.8 and β equal to 0.2, to induce a proportion index. The difference between the two parameters is due to the crucial importance of the validation error for the model performance evaluation with respect to the training error.

The remaining cost-function parameters, the maximum error and the coefficient of determination, are employed together to reduce the numerical value within a range similar to the NRMSE. In fact, the complement of R^2 is employed as reduction factor for the maximum Euclidean error, coefficient of error distribution. Finally, the coefficient of determination of the validation dataset is employed during the GA optimization to implement high-cost function values for non-compliant models. In fact, a threshold equal to 70% is implemented, depicted as "ANN design Rsq < 70%" in Figure 100.

The cost-function is therefore employed for the GA optimization of the ML scheme. The methodology proposes two different approaches for performance comparison and validation: a traditional *global* approach which computes all the joints simultaneously from the Cartesian coordinates; and the novel *sequential* approach derived from the single joint computation. Similar to the order matrix multiplication proposed for the FK computation, the sequential scheme divides the complex system into a set of simpler elements containing a single joint and aims to model each subsystem while retaining the interdependency between them. In fact, the deployed networks are applied to learn the IK of one joint at a time; the first network input is the Cartesian coordinates and orientation, and the output is the final joint value. The same inputs are used for the following joint, however in this case the previously computed joints values are included as extra inputs. This approach has two main advantages: (1) it increases the information provided to the ML model; (2) it allows a parallel scheme training as each joint model can be trained and optimized, separately. Finally, the sequential scheme procedure has a high degree of modularity with respect to the *global* approach as it allows the optimization of each joint model separately, which result in a set of different models for the complete robot. In fact, the evaluation of a set of simpler elements instead of a complex complete mechanism permits further studies and developments in terms of energy consumption reduction, redundancy constraints, or workspace limitations.

In summary, the GA is used to optimize each joint model for the sequential scheme. Moreover, an extra hyperparameter is incorporated to increase the method variability and allow the variation of the sequential approach computation direction. In fact, the variable can be set to compute the sequential approach starting from the base of the robot up to the TCP or the contrary path, from the TCP up to the base frame, similar

to the order matrix multiplication for the FK obtention. Despite increasing the required optimization computational time as the variables are increased, it provides a new degree of freedom in terms of model scheme which might result in an increased performance during the model deployment. A sequential approach example for a 3-DOF robot starting from the TCP towards the base frame is depicted in Figure 102.

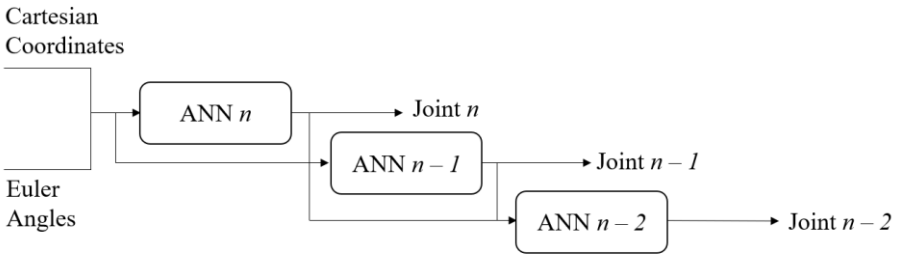

Figure 102. Sequential approach from the robot TCP towards the base.

3.4 Model Validation

The final step of the proposed methodology is the "network architecture validation". During this phase the model is evaluated and assessed based on the test dataset and the trajectories defined during the FK validation phase, presented in Figure 101a-d. Several performance parameters are employed: the mean square error (MSE), the mean absolute error (MAE), the root mean squared error (RMSE), and the maximum error (MAXE). If the model assessment proves to be non-compliant then the methodology proposed starts again from the network definition and proposes a fine-tuning phase to further improve the results obtained. Otherwise, the model is ready for its application.

Chapter 4

Simulation

This chapter introduces the simulation of the proposed methodology based on a sequential scheme based on ANN tuned with GA for an IRB140 robot. The dataset is produced with the ABB Robotstudio software, and the corresponding system is limited to the initial joints in prospect of energy consumption optimization. Furthermore, the joint limitations are presented along with the GA results and the numerical results obtained with 4 different trajectories. The results are presented both graphically and in table form.

4.1 Introduction

The proposed methodology is first assessed in simulation with a 6-DOF robotic manipulator, IRB140, depicted in Figure 103 along with the joint axes. The data accumulation for the FK dataset is obtained with the ABB Robotstudio environment which allows to simulate the motion of a given robot within a robotic cell. This preliminary evaluation for the proposed methodology permits to validate the sequential approach by comparing the optimized scheme with the numerical results obtained for the global optimized standard approach.

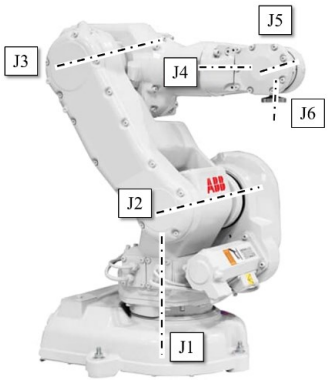

Figure 103. Simulated case study - IRB140 robot.

4.2 Dataset Generation

The initial step once the robot is chosen corresponds to the D-H parameters obtention with the automatic procedure which are afterwards employed to derive the FK model. Hence, following the description of the methodology employed to identify the parameters [171], the robot's end-effector position is acquired after sequential movements in each joint and processed to determine the motion axis. Afterwards, dual vector algebra is applied to compute the intermediate coordinate frames between consecutive joints, and finally the D-H parameters are derived.

Therefore, within the virtual environment a point p is defined, at the robot's end-effector relative to the robot's base frame. The robot is then required to execute a series of controlled-position positive movements one joint at a time, which translates to a circular (revolute joint) or linear (prismatic joint) trajectory of the tracked point. These measured paths must be defined for at least a third of the motion range and the joints must move at identical constant speeds to guarantee uniformity in the number of samples and the distribution in the consequent p positions. In fact, for the simulated case scenario, the measured paths are defined for the complete motion range of each actuator and the velocity is defined with a constant number of elements for each record trajectory, 400 elements.

The pose information is acquired during the virtual robot motion and hence the motion axis for each joint is derived. The following steps requires dual vector algebra to deal with the multiple case-definition for the X-axes depending on the consecutive identified Z-axes (intersecting lines, identical lines, parallel lines, or skewed lines). Consequently, the Y-axes are obtained with the cross product between the two already computed axes. Finally, the D-H parameters are derived as listed in Table 13.

Table 13. D-H parameters for the IRB140.

IRB140				
Joint	θ_i **[rad]**	d_i **[mm]**	a_i **[mm]**	α_i **[rad]**
1	0.0	3.52×10^{2}	7.00×10^{1}	$\pi/2$
2	$\pi/2$	2.18×10^{-8}	3.60×10^{2}	0.0
3	0.0	2.95×10^{-7}	8.94×10^{-7}	$\pi/2$
4	0.0	3.80×10^{2}	-3.51×10^{-6}	$-\pi/2$
5	0.0	-4.50×10^{-7}	2.34×10^{-6}	$\pi/2$
6	0.0	6.50×10^{1}	-4.45×10^{-7}	0.0

The found parameters are employed to obtain the homogeneous matrix for each joint and, based on matrix multiplication, obtain the transformation matrix that relates the end-effector to the base frame; from which the FK model is derived. The following step corresponds to the FK model validation for which the set of trajectories presented in the previous section are employed and the MEE performance is computed for the simulated IRB140 robot. The impact of the trajectory parameter variation based on two different levels, ±20% (*Low* and *High*), is defined in the corresponding virtual simulation.

The results for the evaluated trajectories are depicted in Table 14, where the MEE of the nominal trajectory is introduced along with the percentual variation of this coefficient when the path is perturbed. The four trajectories (circle, spiral, S-shape, and rectangle) presented small MEE coefficients validating the FK model. In particular, the MEE for evaluated paths remained below 0.002 μm with variations between ±12% for the perturbed scenarios, comparing the simulation in ABB RobotStudio and the D-H model. These numerical results are not actual achievable for real applications due to resolution issues and is justified by the software simulations. In summary, the results assess the FK model creation with the automatic D-H procedure in the simulated case scenario, therefore, the methodology proceeds to generate the dataset to be employed with the machine learning application.

Table 14. FK model error for the nominal trajectories and the perturbed scenarios.

Robot	Case	MEE [µm]	Low	High
IRB140	Circle	0.015	+9.0%	+2.0%
	Spiral	0.017	+1.0%	−8.0%
	S-Shape	0.014	−2.0%	−5.0%
	Rectangle	0.013	+7.0%	+12.0%

The procedure for the dataset generation is therefore employed based on the ranges of motion. For the evaluated case scenario the methodology is used to model the initial 3 joints of the IRB140, this choice is based on two main considerations: (i) these joints are the main sources of energy consumption and, hence, should be optimized to addressed the present industrial requirements; (ii) considering the serial kinematics and the joints location within the robot mechanism, these elements are the main source of errors as small deviations in the joint space are amplified in terms of the Cartesian positioning of the TCP. Therefore, the motion ranges considered for the evaluated case scenarios are: $[-\pi/2, \pi/2]$ for joint 1, $[0, \pi/2]$ for joint 2, and $[-\pi/2, 5\pi/18]$ for joint 3.

The 3D workspace of the IRB140 robot is shown in Figure 104, where the black pattern corresponds to the locations of the second joint (J_2) when the first joint (J_1) is moved. In a similar manner, the third joint (J_3) positions, produced with the combination of J_1 and J_2 motion, are represented with the red dots. Finally, the blue region describes the fourth joint (J_4) datapoints obtained with the motion of the previous joints. As stated before, the validation process for the considered application is carried out with a constraint workspace, resulting in a reduced representation with respect to the depicted figure.

Based on these ranges, the consequent 10,000-point dataset is produced with the pseudo-random approach presented in the previous section and divided randomly in three parts: 7,500 points for training (70%), 1,500 points for testing (15%), and 1,500 for validation (15%).

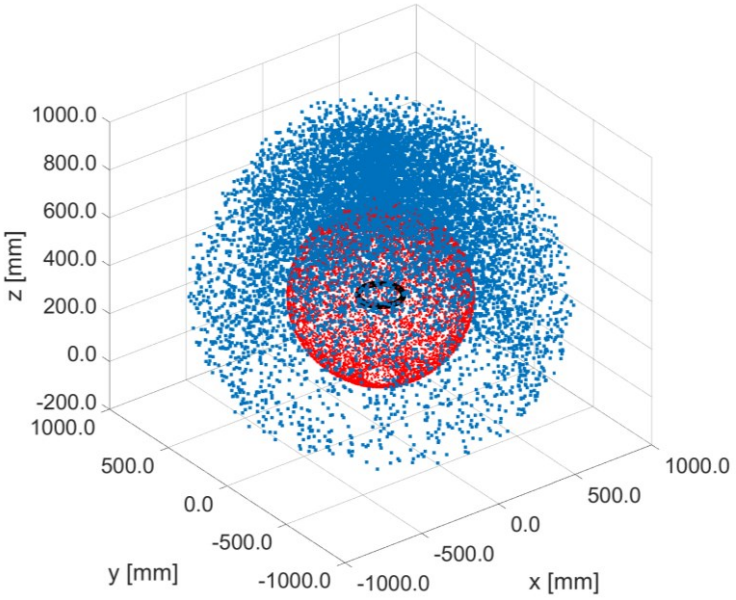

Figure 104. Real workspace for the IRB140: (blue) J4; (red) J3; (black) J2.

4.3 Network Architecture Definition

The next step in the proposed methodology corresponds to the architecture definition of the ANNs, which is obtained based on the GA optimization. This is a cumbersome optimization for which the computational time required is reduced by employing MATLAB Parallel Computation. Conceptually the aim is to employ a metaheuristic optimization scheme to minimize the cost function defined based on the normalized root mean square errors obtained during training and validation and on the maximum absolute error, which is reduced with the coefficient of determination. The cost function is defined to minimize the normalized error for the application under study whilst constraining the maximum obtainable error, or in other words, reducing the variability of the error.

The GA generates a population for the imposed variables to be tested which afterwards is modified based on mutation, crossover, and selection for the search algorithm. For each element in the population an ANN is created, and the performance coefficients derived. In fact, the training and validation datasets are employed during this step, whereas the testing dataset is kept unused. The GA will then vary the number of hidden neurons and the number of hidden layers within a pre-defined search interval. This is carried out for each joint, also considering the direction of computation (from Base or from TCP). Once the optimization finishes, the tuned parameters of the GA are obtained and are employed to train the final ANN, which in this case will be trained for a longer period, whilst maintaining the known constraints to avoid overfitting, as it is the evaluation of the minimization of the mean square error of both training and validation. In fact, the ANNs training is defined with the "scaled conjugate gradient" as the training function and the MSE as the performance coefficient.

A summary of the limitations and optimization variables is presented in Table 15. The optimization approach is employed for both the novel sequential approach and the standard global approach to avoid error inference from manual tuning and to assess the methodology performance.

Table 15. GA/ANN optimization inputs for IRB140.

Requirements	Sequential	Global
- Number of joints	J1 – J3	J1 – J3
- Algorithm limitations	Mix	<8 Layers
- Activation Functions	*tansig*	*tansig*
- Feature filtering	J4 – J6	J4 – J6
- Epochs	1,000	1,000

The chosen optimization approach, despite providing an automatic procedure for the network definition, requires an offline computational time close to 70 h for the sequential approach whereas with the global approach that requires ~30 h due to the reduced number of models the system must optimize. However, despite the high computational time required for the optimization, it can be considered of offline nature, as it does not influence the time required during the "online" application, as for example during the path definition of the given robot. Hence, taking into account this time does

not influence the execution time required, once the models are defined, it is neglected for the time-consuming considerations. Considering the sequential approach, the optimized network for the three-joint consideration with the computational direction from the robot base frame to the TCP is expressed in terms of number of layers (5 for J_1, 5 for J_2, and 6 for J_3) and hidden neurons for each hidden layer as:

$$J_1\{65 \quad 65 \quad 45 \quad 45 \quad 15\}$$
$$J_2\{65 \quad 65 \quad 60 \quad 55 \quad 15\}$$
$$J_3\{35 \quad 50 \quad 70 \quad 25 \quad 35 \quad 25\}$$

Similarly, the optimized scheme for the evaluated case scenario with the complementary computational direction, from the robot TCP to the base frame, is defined as:

$$J_1\{70 \quad 65 \quad 65 \quad 35 \quad 40 \quad 20\}$$
$$J_2\{75 \quad 75 \quad 10\}$$
$$J_3\{45 \quad 50 \quad 55 \quad 55 \quad 35 \quad 50 \quad 30\}$$

The difference between both structures shows the increment in the variability evaluation when the direction of computation is included within the optimization phase. In fact, if the modelling starts from the base frame the system shows a more complex network for the second joint (5 layers) with respect to the inverse approach for which the same joint is modelled with a three hidden layer network. This difference might be due to the parallel joint motion between the second and third joint which, when one of the two are employed as extra input for the remaining, reduces the obtainable error and simplifies the schematization. Indeed, a similar difference is observed for the third joint when the modelling starts from the last joint as the ANN has 7 hidden layers whereas for the inverse path, from base frame, the same joint is modelled with a 6 hidden layers network.

In order to assess the methodology proposed, a global standard approach is provided. In this scenario, a single ANN is employed and tuned, as before, with the GA employing the same cost-function. Consequently, the optimized structure has 7 hidden layers with the following hidden neurons for each layer: $J_{1,2,3}\{65 \quad 55 \quad 30 \quad 30 \quad 50 \quad 50 \quad 20\}$.

4.4 Model Validation

The following step in the proposed methodology corresponds to the evaluation of the IK models' performances, during which the unused test dataset and the trajectories employed for the FK model validation are used. This phase compares the results of all the optimized models obtained with respect to the sequential approach proposed. Furthermore, the locations of the validation trajectories are defined to evaluate the system in critical workspace zones, such as the extreme reaching regions of the robot, where small errors in the joint space may create significant errors in the final joint positioning. The graphical representation for the four trajectories is described with three different

schemes. First a 3D figure for the trajectory position definition inside the considered workspace within which the joints positions are differentiated with various colours: black for J_2, red for J_3, and blue for J_4. The second figure corresponds to the three-dimensional focus upon the "measured" output (proposed trajectory) and the result obtained with the ML model. Finally, to enhance the visualization of the Cartesian error for each dimensional axis, the comparison of the virtual robot data points and the ones computed with the sequential ML approach for each axis (X, Y, Z) are presented in a two-dimensional representation. The initial evaluation is carried out with a 160-datapoints Circle trajectory positioned at the extreme reaching zone in front of the robotic manipulator, depicted in Figure 105. The path is defined on the Y-Z plane, whereas the X-axis data is kept constant. The results show the promising sequential optimized model (IK-procedure) with respect to the IRB140 motion in the virtual environment.

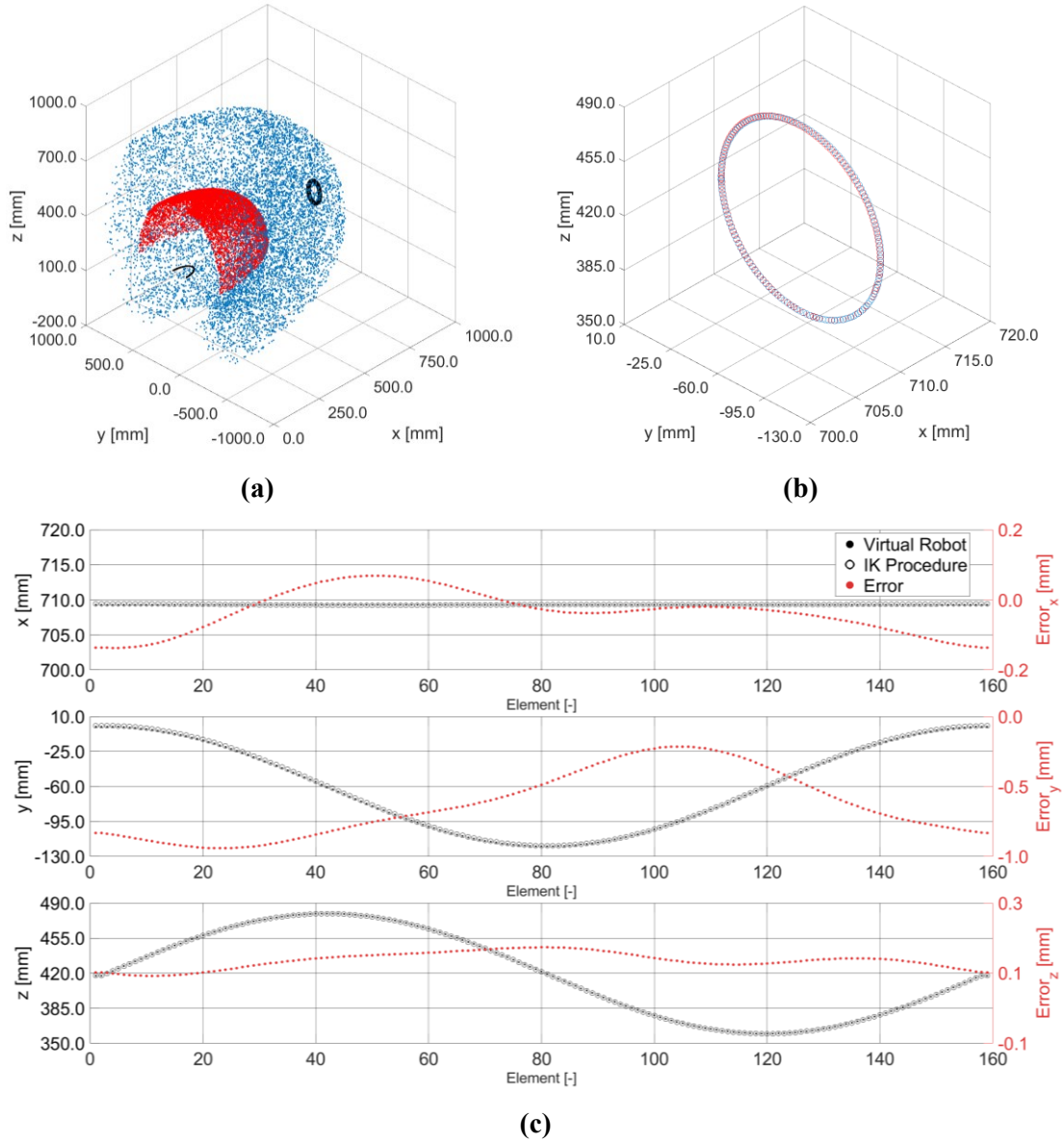

Figure 105. Circle: (a) trajectory within workspace; (b) Robot (blue) vs. IK procedure (red) 3D visualization; (c) Individual axis errors.

The circle path with the sequential model constructed from the base obtained the best results with a mean absolute error (MAE) of 0.42 mm for a 60.00 mm radius trajectory. The given model reduced the corresponding performance coefficient of the global approach of over 60% (MAE = 1.07 mm). In a similar fashion, the sequential approach proposed from the last joint presented a final MAE of 0.65 mm, which corresponds to an improvement with respect of the global approach of ~39%, assessing the sequential approach performance. Similar results are observed with the 320-datapoints Spiral path, depicted in Figure 106. As before, the trajectory is positioned in a critical location within the robot workspace in order to amplify the joint values errors in the Cartesian space. The trajectory describes a circular path upon the X-Y plane whilst reducing the Z-coordinates. As for the circle path, the best results are obtained with the novel sequential scheme from the base with a MAE of 0.45 mm, reducing of 40% the MAE of the global scheme.

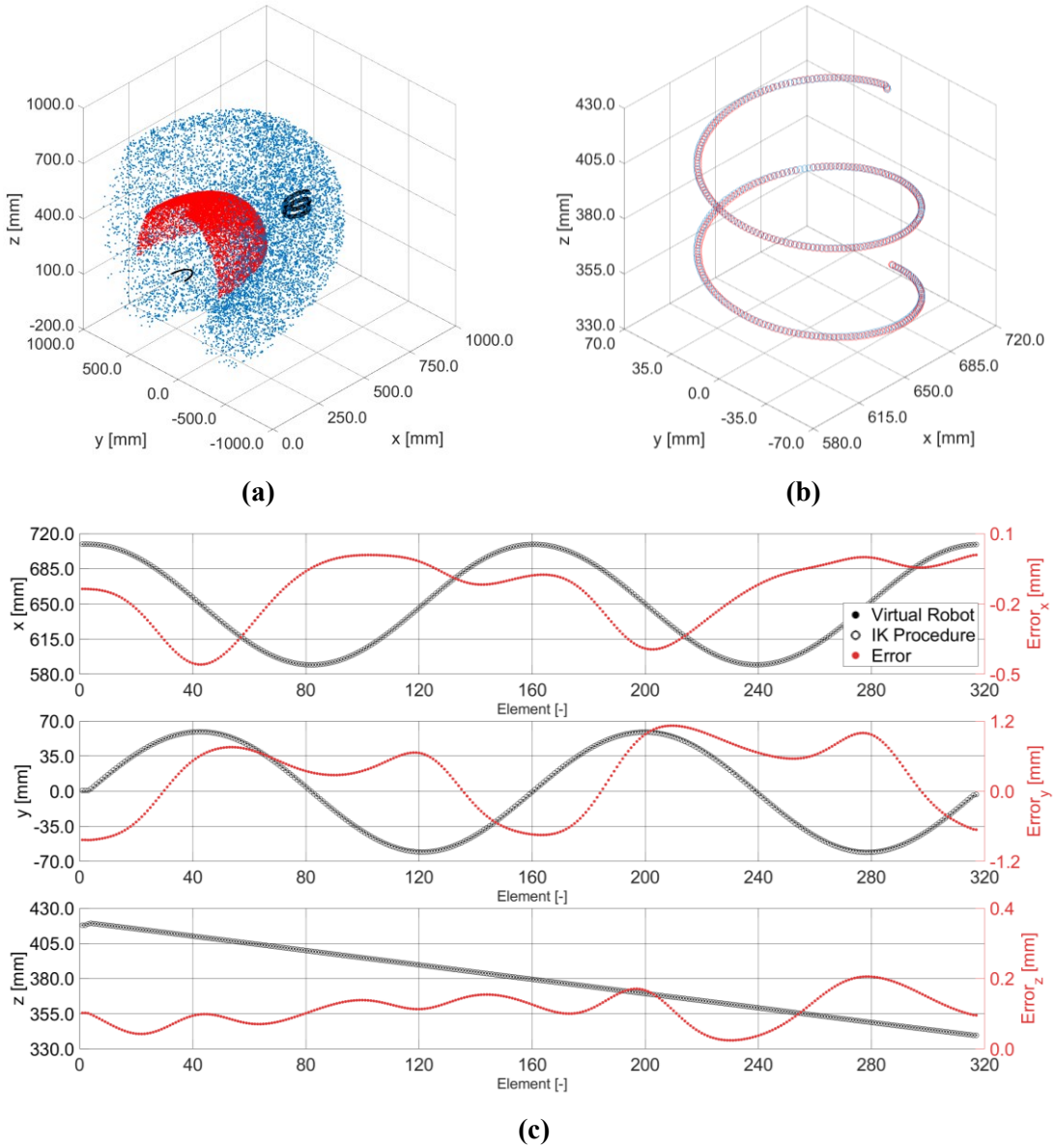

Figure 106. Spiral: (a) trajectory within workspace; (b) Robot (blue) vs. IK procedure (red) 3D visualization; (c) Individual axis errors.

In a similar fashion, a 290-datapoints rectangle trajectory is proposed on the X-Y plane, depicted in Figure 107. The sequential scheme obtained similar MAE performances with both alternatives: 0.50 mm and 0.51 mm for the scheme from base and from the last joint, respectively. Regarding the global approach the optimized model obtained a MAE of 0.79 mm, a 58% higher than the sequential approach.

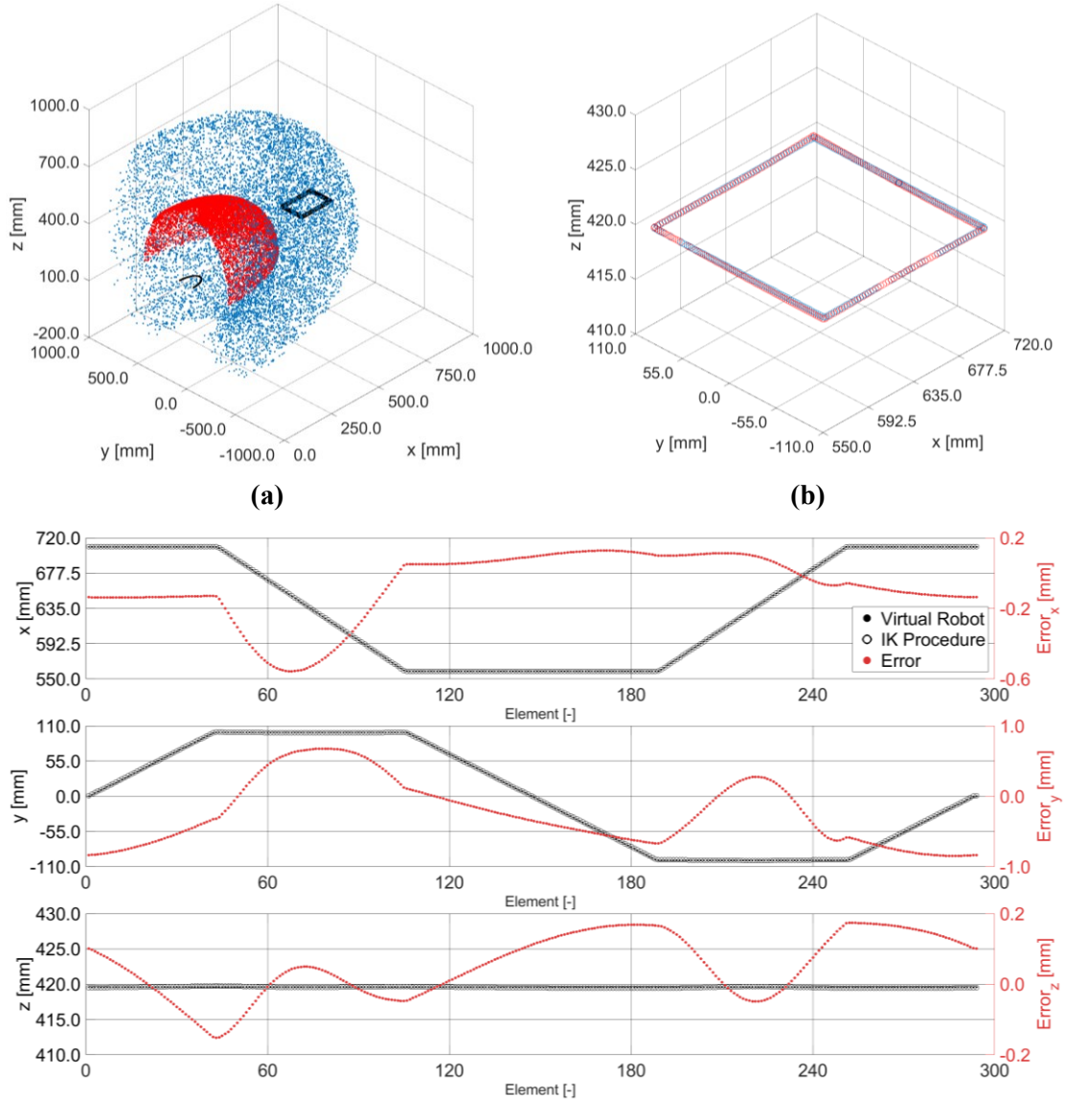

Figure 107. Rectangle: (a) trajectory within workspace; (b) Robot (blue) vs. IK procedure (red) 3D visualization; (c) Individual axis errors.

The last validation path corresponds to the S-shape trajectory with 150 datapoints disposed upon the X-Y plane, as depicted in Figure 108. This path is located within the workspace volume reaching the vicinity of both the inner and the outer limit. Nonetheless, the sequential approach from base frame obtained a MAE of 0.43 mm, a 38% smaller than the MAE of the optimized global approach. Similar to the previous trajectories, the sequential alternative from the last joint obtained similar results, with a MAE of 0.50 mm.

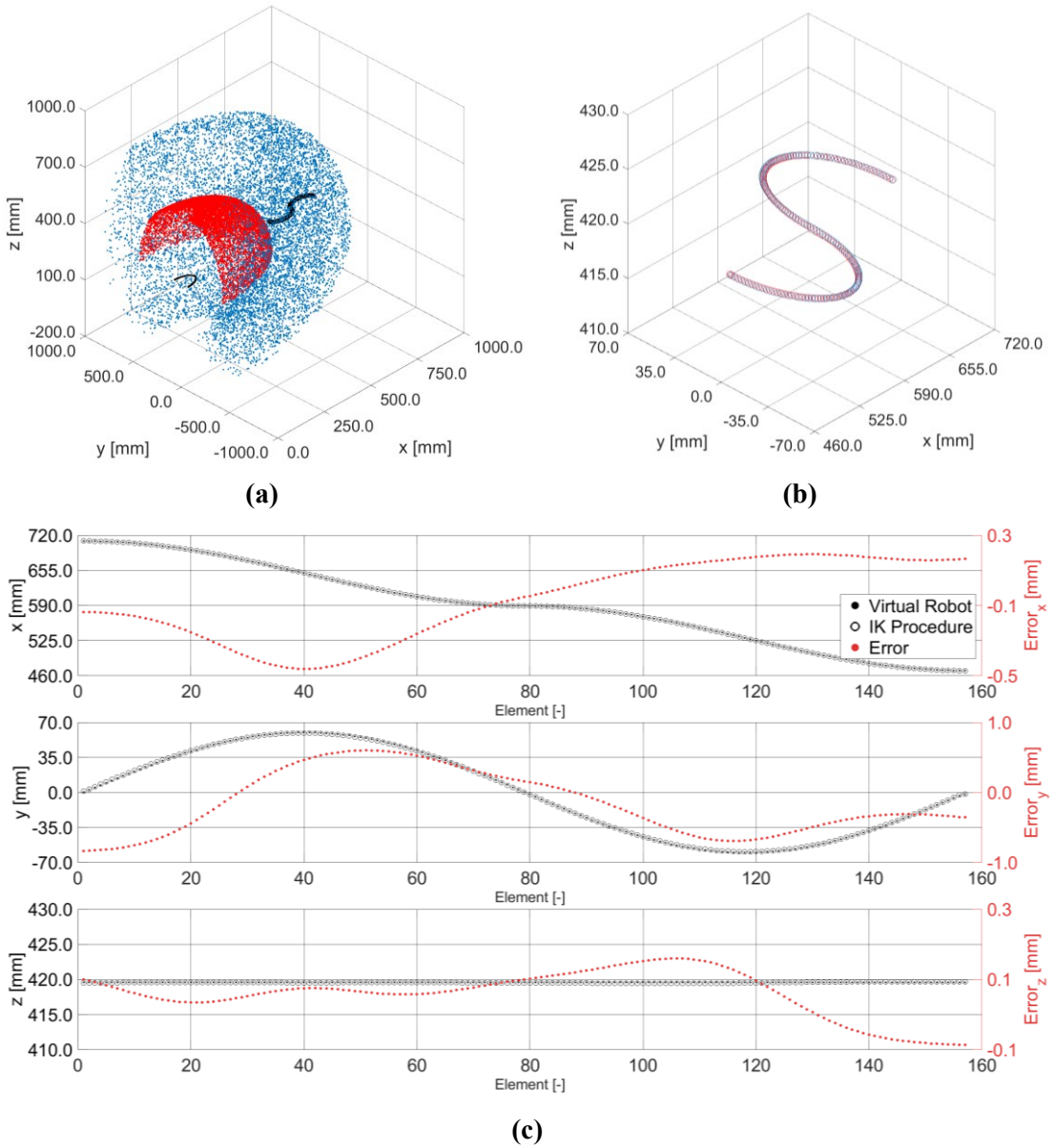

Figure 108. S-shape: (a) trajectory within workspace; (b) Robot (blue) vs. IK procedure (red) 3D visualization; (c) Individual axis errors.

The results obtained for the four trajectories with the evaluated models are summarized in Table 15 based on the following performance coefficients obtained comparing simulations and the developed models: MAE, MSE, RMSE, and MAXE. The R^2 coefficient is not presented as the results obtained values over 99.99% for all the deployed models. Comparing the adopted methods, the results highlight that the global approach (7 hidden layers) has a higher error (MAE) than the sequential method by 42.7–56.7%.

Moreover, the maximum Euclidean error is close to 1.3 mm using the global approach, while the sequential approach shows lower error (MAXE) values, reaching a minimum of 0.634 mm for the S-shape path. Considering the spiral trajectory, the sequential network starting from the base has the MAXE equal to 0.8 mm, that is lower than the global approach by 35.3%. Similar results are obtained from the rectangle

trajectory. These deviations are calculated in the extreme reaching positionings of the robot where low errors in the joint space are amplified.

Table 16. Global/Sequential IK trajectory error results in the virtual environment: MAE, MSE, MAXE.

Global 7 Layers				
Trajectory	**MAE [mm]**	**MSE [mm^2]**	**RMSE [mm]**	**MaxE [mm]**
Circle	1.07×10^{0}	1.17×10^{0}	1.08×10^{0}	1.32×10^{0}
Spiral	7.46×10^{-1}	6.42×10^{-1}	8.01×10^{-1}	1.33×10^{0}
Rectangle	7.96×10^{-1}	7.14×10^{-1}	8.45×10^{-1}	1.27×10^{0}
S-shape	6.86×10^{-1}	5.41×10^{-1}	7.36×10^{-1}	1.25×10^{0}
Sequential From TCP				
Trajectory	**MAE [mm]**	**MSE [mm^2]**	**RMSE [mm]**	**MaxE [mm]**
Circle	6.54×10^{-1}	4.78×10^{-1}	6.92×10^{-1}	9.49×10^{-1}
Spiral	6.39×10^{-1}	4.69×10^{-1}	6.85×10^{-1}	1.19×10^{0}
Rectangle	5.13×10^{-1}	3.26×10^{-1}	5.71×10^{-1}	8.66×10^{-1}
S-shape	5.02×10^{-1}	2.89×10^{-1}	5.38×10^{-1}	8.52×10^{-1}
Sequential From Base				
Trajectory	**MAE [mm]**	**MSE [mm^2]**	**RMSE [mm]**	**MaxE [mm]**
Circle	4.24×10^{-1}	2.40×10^{-1}	4.90×10^{-1}	8.77×10^{-1}
Spiral	4.48×10^{-1}	2.47×10^{-1}	4.97×10^{-1}	8.66×10^{-1}
Rectangle	5.03×10^{-1}	3.21×10^{-1}	5.67×10^{-1}	1.15×10^{0}
S-shape	4.27×10^{-1}	2.04×10^{-1}	4.51×10^{-1}	6.34×10^{-1}

In a similar manner, to provide a workspace result evaluation for the sequential approach, Table 17 lists the main error indicators in the join space related to the sequential method datasets (train, validation, test). In this case, the results are presented in [*rad*] as they are computed upon the joint errors and not the Cartesian schemes. Furthermore, considering the higher error obtained with the global approach for the validation trajectories, the dataset numerical results are not introduced for this standard method.

While the MSE value is introduced to permit the sequential approach results comparison with the other different methods in the literature, this coefficient is difficult to comprehend in terms of the error magnitude for errors smaller than the unity. In this scenario, the RMSE is proposed to obtain a unit measurement of the error coherent with the real values of the evaluated dataset. In fact, both sequential approaches show similar results, as expected from the trajectory assessment performances. Furthermore, the train-test-validation RMSE values are similar which denotes the absence of overfitting or dataset-driving models. Finally, the maximum error is similar to the results obtained for the RMSE scheme which shows limited error dispersion and hence a certain degree of uniformity in the obtained results, particularly for the sequential scheme from the base.

In order to avoid misleading performances comparisons, the results obtained in the presented literature [156–158,161] are confronted with the novel sequential schemes with the test dataset, which contains data not employed during the machine learning scheme definition and optimization.

The results presented in the literature for the MSE performance coefficient are close to 1.0×10^{-4} rad^2, while the proposed sequential methodology present a mean

squared error equal to 1.73×10^{-6} rad^2 starting from the robot Base and 1.95×10^{-6} rad^2 starting from the robot TCP. In the same way, the promising RMSE results show a maximum value lower than 1.40×10^{-3} rad.

Table 17. Train, validation, and test performance for the sequential models.

Train	**MSE [rad^2]**	**RMSE [rad]**	**MAXE [rad]**
Sequential From Base	1.23×10^{-6}	1.11×10^{-3}	9.68×10^{-3}
Sequential From TCP	9.23×10^{-7}	9.61×10^{-4}	1.07×10^{-2}
Validation	**MSE [rad^2]**	**RMSE [rad]**	**MAXE [rad]**
Sequential From Base	1.50×10^{-6}	1.22×10^{-3}	8.51×10^{-3}
Sequential From TCP	1.40×10^{-6}	1.18×10^{-3}	2.15×10^{-2}
Test	**MSE [rad^2]**	**RMSE [rad]**	**MAXE [rad]**
Sequential From Base	1.73×10^{-6}	1.32×10^{-3}	1.60×10^{-2}
Sequential From TCP	1.95×10^{-6}	1.40×10^{-3}	4.87×10^{-2}

Chapter 5

Experimental Tests

This chapter introduces the experimental campaign of the proposed methodology for a FANUC LR Mate 200iC. The dataset is produced with the internal controller through the teach pendant device, and the corresponding system is limited to the initial joints in prospect of energy consumption optimization. Furthermore, the joint limitations are presented along with the GA results and the numerical results obtained with four different trajectories. The results are presented both graphically and in table form.

5.1 Robot Experimental Campaign

An experimental campaign was executed based on the promising results obtained during the simulation assessment. The robot employed for this phase is a 6-DOF FANUC LR Mate 200iC robot, depicted in Figure 109 with the corresponding joint axes, which is similar to the one used in the simulated case scenario. For each movement, a PC-based acquisition system collects the actuators' positions and torques with a frequency of 10.0 ms, comparing the dataset quality with the robot internal information, accessible via teach-pendant.

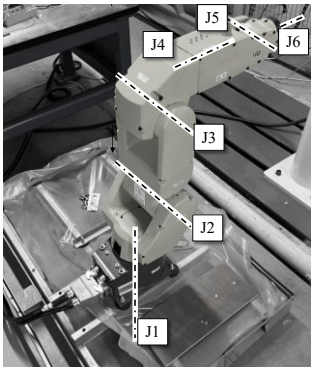

Figure 109. FANUC LRMate200-iC representation.

5.2 Dataset Generation

Similar to the simulated case scenario, the initial phase after the robot selection is the formulation of the FK model, for which the automatic D-H parameters obtention procedure is employed. The robot's end effector position is acquired through the teach-pendant after a set of sequential movements with each joint to infer the axis of the joints' motion. To avoid errors related to the internal model of the robot certain conditions have been appraised: the experimental tests are performed in laboratory conditions, assuming a constant temperature (20 °C), and the robot is calibrated before the tests. The joint-jog

path rules are defined as follows: joint motion with a range greater than 45% of total mechanical feasibility, TCP speed lower than 10 mm/s and a number of elements greater than 400. After the data is acquired for each joint, the automatic procedure is employed to derive the D-H parameters, listed in Table 18. These parameters are afterward employed to compute the transformation matrices that relates the end-effector to the base frame, from which the FK is obtained.

Table 18. D-H parameters for the FANUC LR Mate 200iC.

FANUC LRMate200-iC				
Joint	θ_i **[rad]**	d_i **[mm]**	a_i **[mm]**	α_i **[rad]**
1	0.0	3.30×10^2	7.50×10^1	$\pi/2$
2	$\pi/2$	0.00×10^0	3.00×10^2	0.0
3	0.0	0.00×10^0	7.50×10^1	$\pi/2$
4	0.0	3.20×10^2	0.00×10^0	$-\pi/2$
5	0.0	0.00×10^0	0.00×10^0	$\pi/2$
6	0.0	1.40×10^2	0.00×10^0	0.0

The following step in the proposed methodology corresponds to the dataset generation employed for the ML model derivation and validation. Hence, considering the data-driven nature of such approach, before the artificially generated dataset is produced the employed FK model must be assessed. In particular, the four trajectories proposed in Figure 101 are used and the MEE performance is computed for the LR Mate 200-iC. Furthermore, the impact of the main trajectory parameter variation in two levels defined as *High* and *Low* (±20%) is evaluated. The results show MEE coefficients under 0.06 mm assessing the FK model performance with variations under ±15% for the perturbed trajectories.

The procedure for the dataset generation is therefore employed based on the ranges of motion. Similar to the simulated case scenario, for the evaluated case scenario the methodology is used to model the initial 3 joints of the robot, this choice is based on two main considerations: (i) the robot's energy consumption; and (ii) these elements are the main source of errors as small deviations in the joint space are amplified in terms of the Cartesian positioning of the TCP.

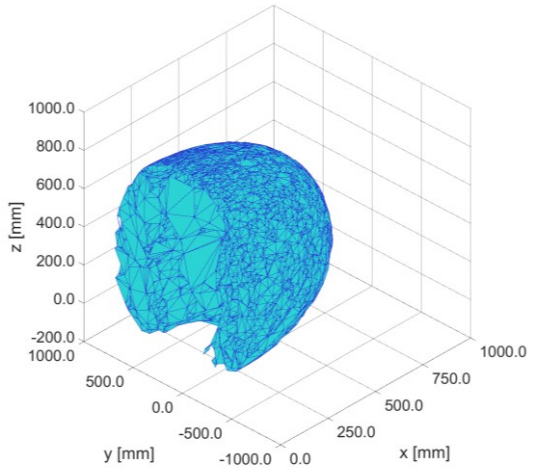

Figure 110. Constrained workspace for the FANUC LR Mate 200iC.

Furthermore, the motion ranges considered for the evaluated case scenarios are: $[-\pi/2, \pi/2]$ for J_1, $[0, \pi/2]$ for J_2, and $[-\pi/2, 5\pi/18]$ for J_3. The constrained 3D workspace of the robot is shown in Figure 110, where the blue three-sided mesh region describes the J_4 space. Finally, as the FK model is validated for the considered robotic manipulator, the pseudo-random generator creates 10,000 poses within the predefined range of motion of the robot axes. The complete dataset is afterwards randomly divided into three different parts: 7,500 points for training (70%), 1,500 points for testing (15%), and 1,500 for validation (15%).

5.3 Network Architecture Definition

The proposed methodology introduced the ANNs optimization with the GA as the following step. This is a cumbersome optimization for which the computational time required is reduced by employing MATLAB Parallel Computation. The PC used for the model computation has an Intel Core i5-8500 processor with 16GB RAM. Similar to the simulated case study, the training and validation datasets produced with the inferred FK model are employed to tune the ANN for each joint, and for the global approach for comparison. The cost function remains the same as for the simulation study, presented in Equation 58, aiming to minimize with the metaheuristic optimization the error distribution and the normalized error. The GA technique has a set of parameters that require definition to proceed with the optimization; in fact, the number of hidden layers range is limited from 3 to 7, and the neurons per layer is defined within the range from 10 to 80, with a 5 hidden neurons resolution to reduce the computational time required. Furthermore, at each scheme evaluation the ANN is generated and evaluated, which requires two main learning parameters not influenceable by the GA hyper-tuning: the "scaled conjugate gradient" is used as a training function and the loss function corresponds to the "mean squared error".

A summary of these limitations and optimization variables is presented in Table 19. In particular, the adopted technique allows the mix network optimization, providing the best configuration of the number of layers and number of neurons for each joint. Furthermore, the global approach is also optimized to validate the proposed methodology with respect to a standard model tuned with the same conditions.

Table 19. GA/ANN optimization inputs for the FANUC LR Mate 200iC.

Requirements	Sequential	Global
- Number of joints	J1 – J3	J1 – J3
- Algorithm limitations	Mix	<8 Layers
- Activation Functions	*tansig*	*tansig*
- Feature filtering	J4 – J6	J4 – J6
- Epochs	1,000	1,000

The chosen optimization approach, despite providing an automatic procedure for the network definition, requires an offline computational time close to 75 h for the sequential approach whereas with the global approach that requires ~30 h due to the reduced number of models the system must optimize. Nonetheless, the computational time can be neglected due to its offline nature, which means that the corresponding time

does not influence the real execution time once the models are trained. Considering the sequential approach, the optimized network for the three-joint consideration with the computational direction from the robot base frame to the last joint is expressed in terms of number of layers (7 for J_1, 4 for J_2, and 3 for J_3) and hidden neurons for each hidden layer as:

$$J_1\{50 \quad 45 \quad 50 \quad 30 \quad 45 \quad 40 \quad 15\}$$
$$J_2\{55 \quad 60 \quad 35 \quad 35\}$$
$$J_3\{50 \quad 40 \quad 10\}$$

Similarly, the optimized scheme for the evaluated case scenario with the complementary computational direction, from the robot last joint to the base frame, is defined as:

$$J_1\{50 \quad 45 \quad 55 \quad 15\}$$
$$J_2\{35 \quad 45 \quad 70 \quad 35 \quad 65 \quad 25 \quad 20\}$$
$$J_3\{60 \quad 60 \quad 30 \quad 15\}$$

In order to assess the methodology proposed, a global standard approach is provided. In this scenario, a single ANN is employed and tuned, as before, with the GA employing the same cost-function. Consequently, the optimized structure has 6 hidden layers with the following hidden neurons for each layer: $J_{1,2,3}\{70 \quad 60 \quad 50 \quad 75 \quad 65 \quad 25\}$.

5.4 Model Validation

The final step corresponds to the optimized model assessment for which the four FK model validation trajectories are used along with the dataset unused data. During this phase the data is employed to compare three different optimized schemes: sequential from base, sequential from TCP, and global. However, the proposed graphical representation for the IK modelling capabilities when the validation trajectories are evaluated are based on the sequential from base scheme. Nevertheless, the numerical results obtained for the three models with the four trajectories are proposed afterwards.

The following figures introduced three parts of information for the considered trajectories, firstly the path location inside the workspace is depicted to assess the problematic working area; within this figure the Cartesian representation of the joints' centres, obtained with the lines of the D-H matrix, are included. Secondly, a three-dimensional error representation between the proposed methodology results and the trajectory real datapoints is depicted. Finally, three two-dimensional representations are included to enhance the error visualization for each axis (X, Y, Z).

The initial evaluation is carried out with a 160-datapoints Circle trajectory positioned at the extreme reaching zone in front of the robotic manipulator, depicted in Figure 111. Differently from the simulated case study, in this experimental campaign the circle path is relocated to produce motion upon the three Cartesian axes. In fact, the 2D

visualization presents an oscillation upon the three axes corresponding to the tilted circle defined.

The results show the promising sequential optimized model (IK-procedure) with respect to the real robot motion. The sequential model constructed from the TCP obtained the best results for the considered trajectory, with a mean absolute error (MAE) performance coefficient of 0.41 mm. The sequential approach from the BASE presented a 26% higher MAE (0.51 mm) whereas the global approach obtained the worst results with a MAE of 0.82 mm (+100%). As previously stated, the trajectories are evaluated pointwise and, hence, the proposed error does not take into account the order of the datapoints motion.

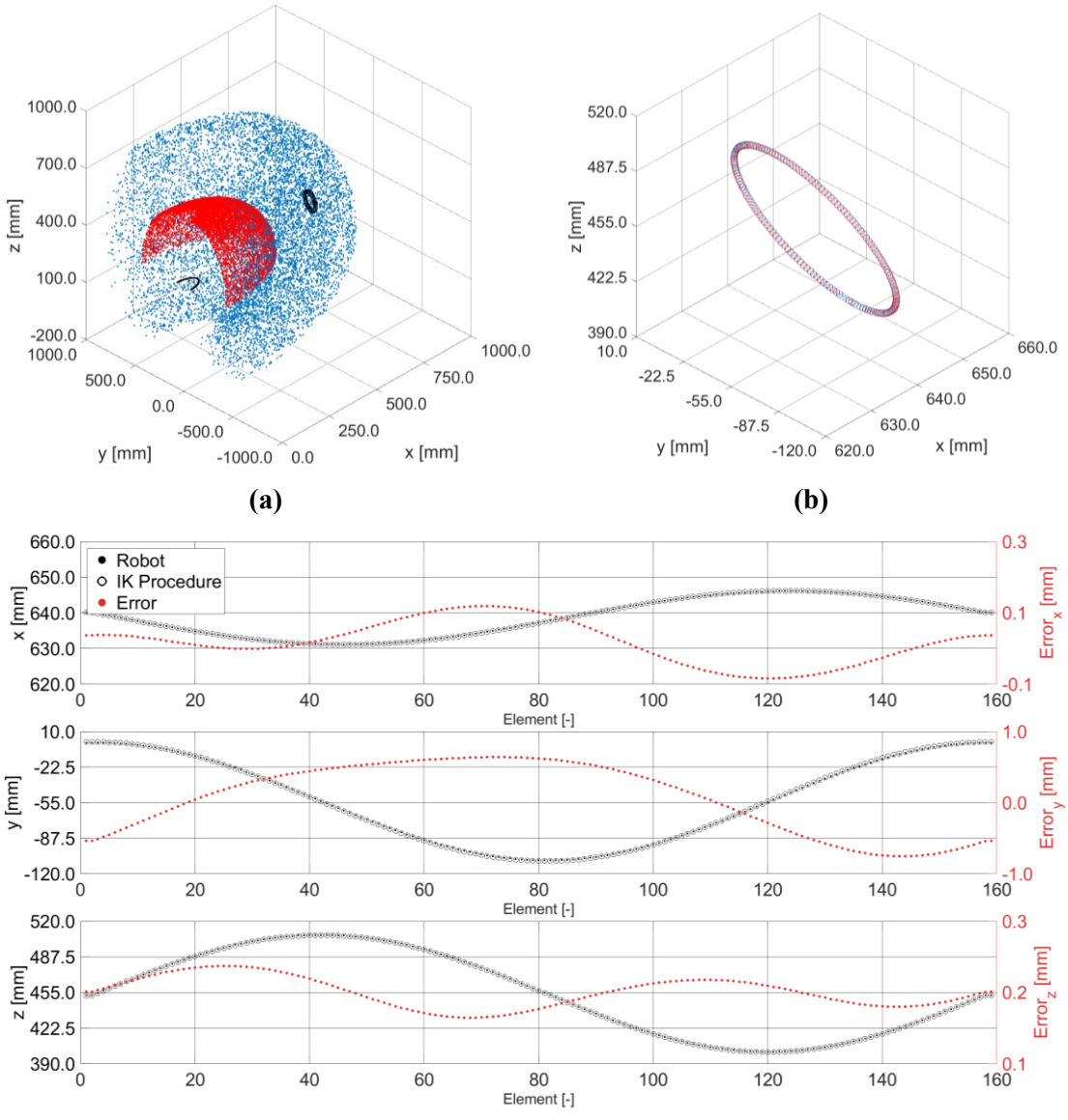

Figure 111 Circle: (a) trajectory within workspace; (b) Robot (blue) vs. IK procedure (red) 3D visualization; (c) Individual axis errors.

Similar results are observed with the 320-datapoints Spiral path, depicted in Figure 112. As before, the trajectory is positioned in a critical location within the robot workspace in order to amplify the joint values errors in the Cartesian space. However, differently from the simulated case scenario, the trajectory varies upon the three axes due to a tilt configuration of the spiral, as observed in the 2D figures.

For the evaluated trajectory the best result is obtained with the sequential approach from TCP, with a MAE equal to 0.48mm. Whilst the sequential from base obtain worse results with a MAE of 0.70 mm (~+45%), the worst results are produced with the global approach with a MAE of 0.87 mm (~+80%).

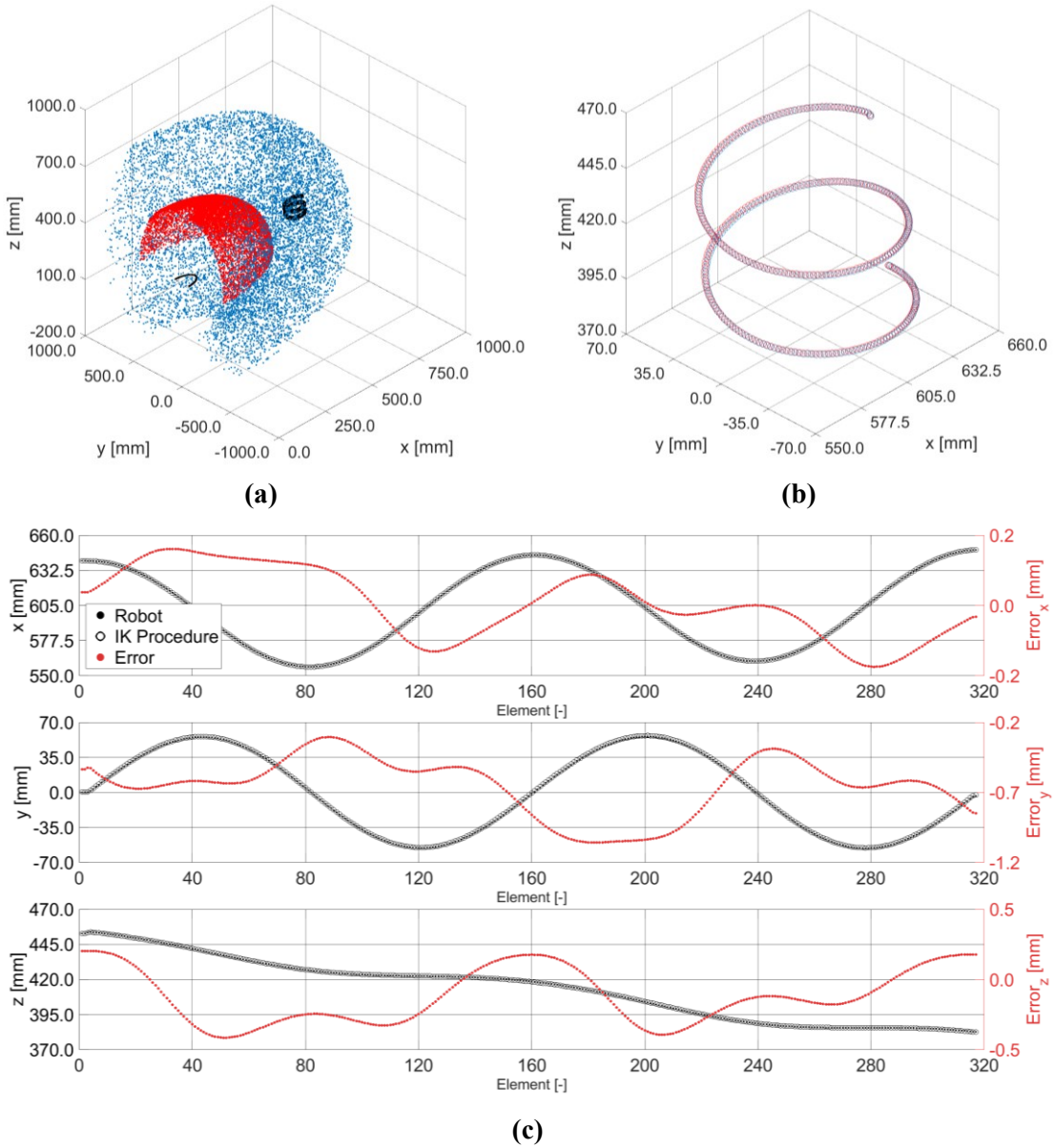

Figure 112. Spiral: (a) trajectory within workspace; (b) Robot (blue) vs. IK procedure (red) 3D visualization; (c) Individual axis errors.

In a similar fashion, a 290-datapoints rectangle trajectory is proposed as depicted in Figure 113. The path is not located on a given plane but has a certain inclination resulting in motion for the three Cartesian axes.

Conversely to the previous results, in this case scenario the sequential from base approach presented the minimum MAE with respect to the alternative sequential model and the global application. In fact, whilst the sequential from base obtained a MAE of 0.37 mm, the model from TCP presented a MAE of 0.57 mm which corresponds to an increment of ~54%. However, both approaches outperformed the global standard application with a MAE of 0.87 mm, a ~135% higher with respect to the best result and a ~+53% higher than the alternative sequential approach.

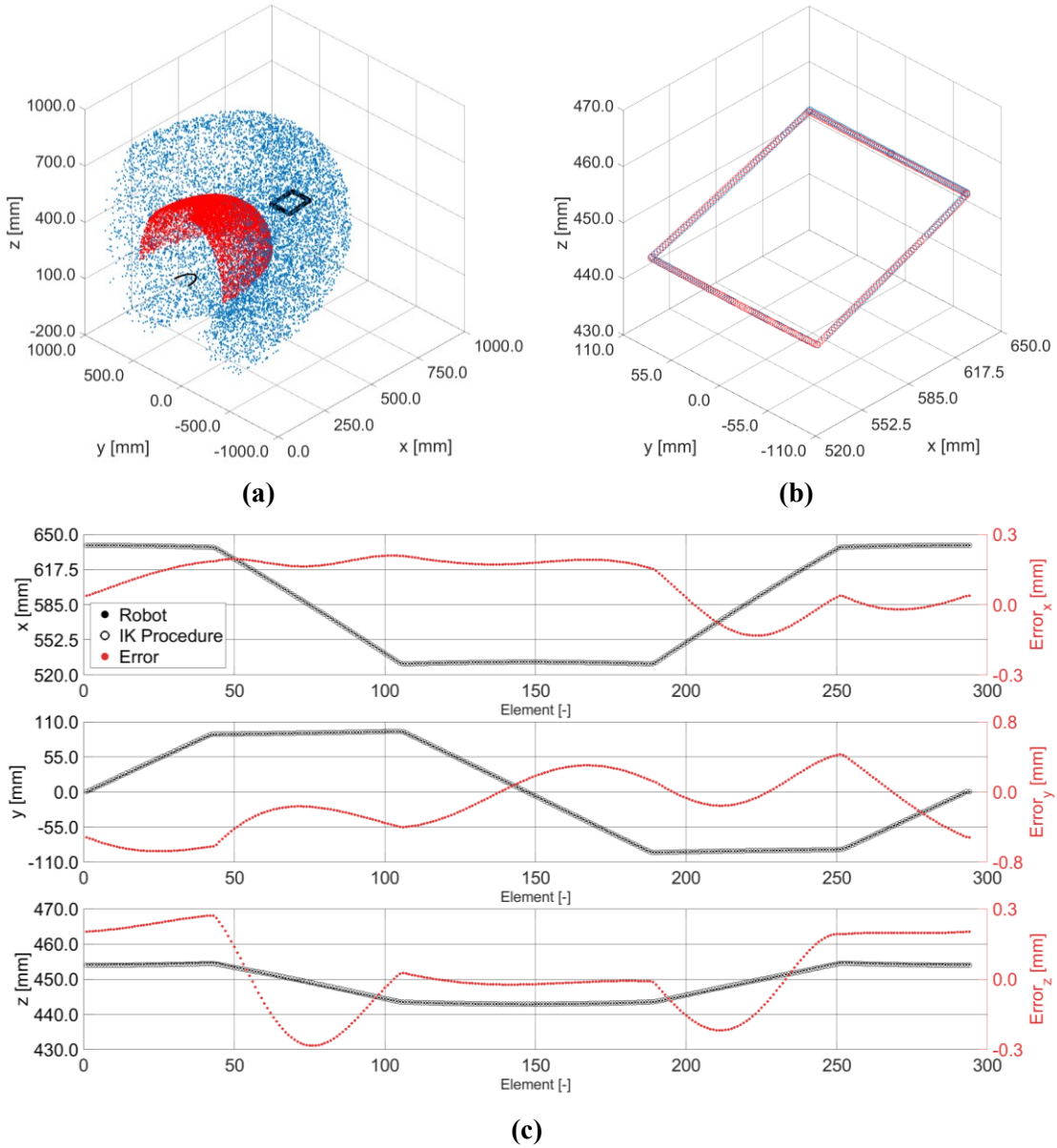

Figure 113. Rectangle: (a) trajectory within workspace; (b) Robot (blue) vs. IK procedure (red) 3D visualization; (c) Individual axis errors.

The last validation path corresponds to the S-shape trajectory with 150 datapoints as depicted in Figure 114. The path is positioned within the workspace volume reaching the vicinity of both the inner and the outer limit and, differently from the simulation case study, does not vary only upon two axes but instead all three axes are modified during the evaluated motion due to its tilted configuration. Despite the difficulties, the sequential approaches obtained the lowest MAE, 0.60 mm and 0.56 mm for the sequential from TCP and sequential from base, respectively. In fact, similar to the rectangle trajectory evaluation, the best results are obtained with the sequential from base approach. Moreover, the global approach obtained the worst results with a final MAE of 0.73 mm, which corresponds to a ~30% increment with respect to the best sequential model.

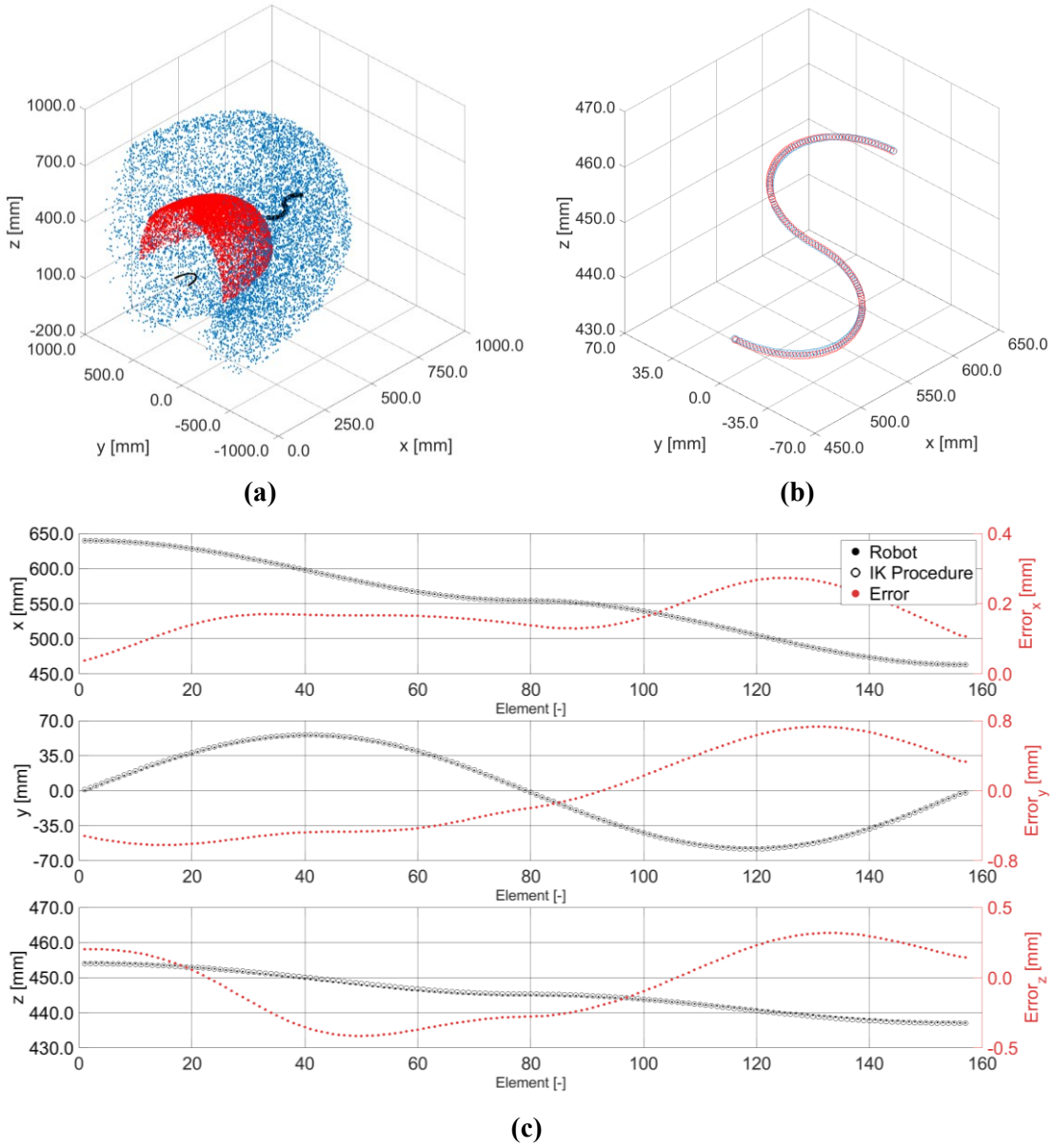

Figure 114. S-shape: (a) trajectory within workspace; (b) Robot (blue) vs. IK procedure (red) 3D visualization; (c) Individual axis errors.

The results obtained for the four trajectories with the evaluated models are summarized in Table 20, based on the following performance coefficients: MAE, MSE, RMSE, and MAXE. The R^2 coefficient is not presented as the results presented values over 99.0% for all the deployed models, confirming the goodness of the correlation.

Regarding the various deployed models, the circle trajectory presents the maximum error of 1.11 mm for the global approach, a ~65% higher than the sequential approach from TCP and a ~43% higher than the alternative sequential model from base. In a similar manner, the worst results were obtained for the rectangle trajectory, which presented an RMSE equal to 9.55×10^{-1} mm and a maximum Euclidean error of 1.77 mm for the global standard procedure. These performances are both overcome by the sequential approaches, obtaining an RMSE containment of ~31% and of ~57% for the sequential from TCP and from base, respectively. Similar results are observed for the maximum Euclidean error, with containments of ~29% for the sequential from TCP approach and of ~58% for the sequential from base method. Furthermore, the developed trajectories have a different number of elements, such as 150 in the S-shape and 320 elements in the spiral. Nevertheless, it is noted that the number of points does not influence the robustness of the final model capabilities, for example, the trajectory obtained by points has a mean absolute Euclidean error, expressed as a vector [global, sequential from TCP, sequential from base] equal to [0.73 mm, 0.60 mm, 0.56 mm] that is comparable to the results obtained by the 320-points trajectory [0.87 mm, 0.48 mm, 0.69 mm].

Table 20. Trajectory errors comparison in the laboratory environment.

Global 6 Layers				
Trajectory	**MAE [mm]**	**MSE [mm^2]**	**RMSE [mm]**	**MAXE [mm]**
Circle in Y-Z	8.19×10^{-1}	7.25×10^{-1}	8.52×10^{-1}	1.11×10^{0}
Spiral X-Y	8.67×10^{-1}	8.60×10^{-1}	9.27×10^{-1}	1.51×10^{0}
Rectangle X-Y	8.67×10^{-1}	9.13×10^{-1}	9.55×10^{-1}	1.77×10^{0}
S-shape in X-Y	7.26×10^{-1}	5.80×10^{-1}	7.62×10^{-1}	1.11×10^{0}
Sequential From TCP				
Trajectory	**MAE [mm]**	**MSE [mm^2]**	**RMSE [mm]**	**MAXE [mm]**
Circle in Y-Z	4.06×10^{-1}	2.00×10^{-1}	4.47×10^{-1}	6.75×10^{-1}
Spiral X-Y	4.82×10^{-1}	2.79×10^{-1}	5.28×10^{-1}	9.71×10^{-1}
Rectangle X-Y	5.66×10^{-1}	4.38×10^{-1}	6.62×10^{-1}	1.26×10^{0}
S-shape in X-Y	6.00×10^{-1}	4.43×10^{-1}	6.65×10^{-1}	1.06×10^{0}
Sequential From Base				
Trajectory	**MAE [mm]**	**MSE [mm^2]**	**RMSE [mm]**	**MAXE [mm]**
Circle in Y-Z	5.13×10^{-1}	2.90×10^{-1}	5.39×10^{-1}	7.77×10^{-1}
Spiral X-Y	6.99×10^{-1}	5.26×10^{-1}	7.25×10^{-1}	1.10×10^{0}
Rectangle X-Y	3.70×10^{-1}	1.64×10^{-1}	4.06×10^{-1}	7.33×10^{-1}
S-shape in X-Y	5.57×10^{-1}	3.37×10^{-1}	5.80×10^{-1}	8.38×10^{-1}

In summary, models show a residual range error of 0.370–0.699 mm of MAE for trajectory following of 120.0–200.0 mm features, as shown in Table 20. MAE (%) is close to 0.582% without any knowledge of robot kinematic. Finally, compared with the global approach, the sequential methodology presents a MAE reduction within 17% and 57% for the evaluated trajectories.

In a similar manner, to provide a workspace result evaluation for the sequential approach, Table 21 lists the main performance coefficients for the sequential methods with each dataset (train, validation, test). Hence, the results show the capability of the ANN structure to model any path or data point within the workspace. Furthermore, considering the higher error obtained with the global approach for the validation trajectories, the dataset numerical results are not introduced for this standard method.

In this scenario, the RMSE is proposed to obtain a unit measurement of the error coherent with the real values of the evaluated dataset. In fact, both sequential approaches show similar results, as expected from the trajectory assessment performances. The difference between the results obtained for the three datasets is studied to evaluate the system overfitting; for this application, similar errors confirm that the ML overfitting is not present. Finally, the maximum error can be accounted for as a measurement of the dispersion of the model predictions; the limited numerical value of this coefficient for the evaluated datasets are promising.

In order to avoid misleading performances comparisons, the results obtained in the presented literature [156–158,161] are confronted with the novel sequential schemes with the test dataset, which contains data not employed during the machine learning scheme definition and optimization. The results presented in the literature for the MSE performance coefficient are close to 1.0×10^{-4} rad^2, while the proposed sequential methodology present a mean squared error equal to 1.90×10^{-6} rad^2 and of 2.78×10^{-6} rad^2, applying the two approaches: from Base and from TCP, respectively.

Table 21. Sequential IK results for the training, validation, and testing phases.

Train	**MSE [rad^2]**	**RMSE [rad]**	**MAXE [rad]**
Sequential From Base	1.25×10^{-6}	1.12×10^{-3}	9.70×10^{-3}
Sequential From TCP	1.18×10^{-6}	1.09×10^{-3}	1.41×10^{-2}
Validation	**MSE [rad^2]**	**RMSE [rad]**	**MAXE [rad]**
Sequential From Base	1.62×10^{-6}	1.27×10^{-3}	1.33×10^{-2}
Sequential From TCP	1.83×10^{-6}	1.35×10^{-3}	3.51×10^{-2}
Test	**MSE [rad^2]**	**RMSE [rad]**	**MAXE [rad]**
Sequential From Base	1.90×10^{-6}	1.38×10^{-3}	2.56×10^{-2}
Sequential From TCP	2.78×10^{-6}	1.67×10^{-3}	6.29×10^{-2}

Conclusions

This thesis analyses and discusses problems related to unwanted vibration and positioning issues during both the micro-machining process and the interaction between the machining centre and the robotic manipulators. Particular emphasis has been given to piezoelectric modelling and nonlinear considerations along with the machine learning application for robot optimization.

With the focus on unwanted vibrations and positioning issues during machining the first section proposed two piezo-based devices, a spindle adaptive system and an active workpiece holder. The robust mechatronic design of the evaluated devices enables the piezoelectric actuators to work properly, ensuring the achievement of maximal and enduring performances.

The spindle device aims to control a 2-DOF mechanism to compensate vibration in machining. The proposed device is based on the **EP 3 587 030 A1** patent, and it has been conceptualized, prototyped, and validated in both simulation and with an experimental campaign for two different test benches during this thesis work. The system proposes a novel inertial piezo-based vibration containment compact mechatronic device for which a set of design-based flexures were constructed to act as springs decoupling elements.

Initially, the electromechanical linear model for the piezo-based system is proposed, with a similar approach to electromagnetic actuators. Afterwards, the nonlinear creep and hysteresis dynamics are modelled and simulated; in particular, the Bouc-Wen modelling scheme was chosen for the hysteresis phenomenon. Consequently, the complex nonlinear scheme was designed in Simulink, within the MATLAB environment, and validated with a set of measurements. The following step required the definition of the regulator, for which several alternatives are proposed from active resonator absorber controllers to cascade schemes; however, the best results with the highest robustness were obtained with the industrial appealing P/PD controller. The active approach reduced the displacement disturbances within the frequency interval of interest (80 Hz – 300 Hz) of more than 34% in the worst-case scenario, assessing the active device capabilities.

Finally, the active device is validated experimentally for both low-frequencies and high-frequencies scheme, achieving containments for the evaluated frequency interval from 10% up to 94% for the X-axis and from 15% up to 66% for the Y-axis. Nonetheless, the results obtained can be further improved by modifying the electronic scheme with a high-frequency dynamic amplifier. Moreover, the compactness modular characteristics of the developed device permits the mass variation to increase the maximum generable force, which is however limited by the requirement to avoid modal characteristics variations of the machining centre. Therefore, the proposed device can represent a great challenge in machine tools sector and open interesting perspectives for industrial applications of mechatronic systems within this field. Future works will address the

variation of the feedback sensor, feedforward approaches for hysteresis reduction, and machine learning schemes deployment for tool wear prediction employing the device internal acceleration sensor.

In a similar manner, a 3-DOF piezo-based compact active workpiece holder, capable of vertical motion and rotation around the remaining axes, was introduced and studied. It is based on the fixturing PKM system which was already validated for positioning without dynamic disturbances. The platform model was revisited, and the nonlinear phenomena of creep and hysteresis, with the Bouc-Wen scheme, were included along with the complete electromechanical model of the piezoelectric actuators and the mechanical system. Consequently, the complex nonlinear scheme was designed in Simulink, within the MATLAB environment, and validated with a set of available datapoints.

The three degrees of freedom permitted the vertical motion along the Z-axis and the rotation around the X- and Y-axes, by actuating the three piezoelectric actuators correspondingly, producing a workspace volume of $z = \pm 20$ μm, $\alpha_x = \pm 427.67$ μrad, and $\alpha_y = \pm 493.83$ μrad. The proposed regulator aimed to handle both the correct positioning issues related to static applications in micro-machining and the unwanted vibrations during the machining process. Therefore, a bumpless-switching PID scheme is proposed with two sets of controller parameters tuning depending on the considered application. Once the initial positioning without disturbances phase was assessed in simulation, a set of simulated case studies were proposed to address the controller switching and the dynamic disturbances containment capabilities.

Indeed, a set of single-frequency and multi-frequency tests were employed to assess the regulator. Each test had an initial set-point following phase, within which the platform was required to acquire a certain disposition for the degrees of freedom, and a final phase for which it was commanded to return to the Home position. Between the two phases the dynamic disturbance phase was evaluated. In fact, the simulation campaign presented a containment within the frequency interval of interest, 100 Hz – 1,000 Hz, from 25% and up to 56%, for the three degrees of motion. In a similar fashion, considering the disturbances measured at each actuator, the unwanted vibrations had amplitudes between 3.3 μm up to 7.9 μm and were contained to 1.5 μm and 5.8 μm, respectively. Future work will focus on disturbance disrupting schemes based on machine learning applications and improvements of the disturbance model.

Finally, the second section of this thesis presented a procedure to generate a machine learning model using a novel sequential scheme for the accurate robot's inverse kinematic formulation. The methodology proposed has three main steps: (i) IK boundary definition and pre-processing, (ii) network architecture definition based on GA, and (iii) network validation. Regarding the available literature, the proposed methodology offers several contributions. First, the machine learning model is trained and validated upon simulated data obtained with the forward kinematic equations employing an automatic procedure, based on the Denavit-Hartenberg parameters, which requires a limited amount of experimental datapoints. Second, the methodology includes the genetic algorithm

optimization to obtain the artificial neural networks hyperparameters, avoiding the manual expert-based tuning; however, the limits and discretization for the number of hidden layers and hidden neurons for each layer must be defined. Third, the sequential scheme proposed employs previously computed joints as extra inputs for the following models, increasing the available information and providing information for the future recognition and definition of redundant configurations. In fact, the novel approach permits to set and define a given joint value and, hence, allows to choose a given robot configuration, especially when the initial joints are selected. This point will be explored in future applications focused on trajectory optimization schemes, minimizing the joint movement and redundant solutions.

The proposed methodology was validated with both a simulated case scenario with an ABB IRB140 robot and an experimental campaign employing a FANUC LR Mate 200iC. The models showed promising results for the defined validation trajectories, executed in critical workspace positionings of the robot. Furthermore, the goodness of IK methodology was confirmed by evaluating the errors of the datasets in joint space and the trajectories in cartesian space. In the simulation scenario, the sequential procedure showed a reduction of the mean squared error index compared to the global scheme of 42.7–56.7%. In particular, the most effective approach was obtained by modelling the robot starting from the base to the TCP, with a final mean square error for the unused testing dataset of 1.73×10^{-6} rad^2. Similar results were obtained for the experimental campaign with the LR Mate 200iC, for which the sequential approach presented a reduction of the mean absolute error from 17% and up to 57% with respect to the global standard approach. Furthermore, the best results in terms of test dataset were obtained with the sequential approach from base with an MSE equal to 1.90×10^{-6} rad^2. Based on these promising results, the future advances of this study will focus on dealing with high-redundant schemes and non-industrial robots as non-rigid real manipulators, that are complex to model analytically. In the same way, the methodology may be improved to solve configuration limitations due to workspace constraints by external objects, reduce the motion or include power consumption optimization schemes.

In summary, this thesis focused on two main issues related to the milling complex multi-device system, the vibrations produced during the micro-milling phase and the correct workpiece positioning. The first solution was depicted in terms of two piezo-based mechatronic devices implemented within the machining centre itself to handle process induced vibrations which demonstrated their high-containment capability and high-precision workpiece positioning [13]. The complementary solution validated a machine learning approach, as implemented in other enhancements within the machining scheme [7], with a novel scheme for industrial robots [16,170] to limit the positioning issues derived from the interaction between the latter and the machining centre. Future applications will aim to employ both solutions to produce a complete solution in terms of system modelling, path optimization, and machining enhancement.

Bibliography

[1] N. Chen, H.N. Li, J. Wu, Z. Li, L. Li, G. Liu, N. He, Advances in micro milling: From tool fabrication to process outcomes, Int J Mach Tools Manuf. 160 (2021) 103670. https://doi.org/10.1016/j.ijmachtools.2020.103670.

[2] A. Aramcharoen, P.T. Mativenga, Size effect and tool geometry in micromilling of tool steel, Precis Eng. 33 (2009) 402–407. https://doi.org/10.1016/j.precisioneng.2008.11.002.

[3] T. Heitz, N. He, N. Chen, G. Zhao, L. Li, A review on dynamics in micro-milling, International Journal of Advanced Manufacturing Technology. (2022) 3467–3491. https://doi.org/10.1007/s00170-022-10014-8.

[4] M.Q. Tran, M.K. Liu, Q.V. Tran, Milling chatter detection using scalogram and deep convolutional neural network, International Journal of Advanced Manufacturing Technology. 107 (2020) 1505–1516. https://doi.org/10.1007/s00170-019-04807-7.

[5] K. Li, S. He, B. Li, H. Liu, X. Mao, C. Shi, A novel online chatter detection method in milling process based on multiscale entropy and gradient tree boosting, Mech Syst Signal Process. 135 (2020) 106385. https://doi.org/10.1016/j.ymssp.2019.106385.

[6] Y. Chen, H. Li, X. Jing, L. Hou, X. Bu, Intelligent chatter detection using image features and support vector machine, International Journal of Advanced Manufacturing Technology. 102 (2019) 1433–1442. https://doi.org/10.1007/s00170-018-3190-4.

[7] F. Aggogeri, N. Pellegrini, F.L. Tagliani, Recent Advances on Machine Learning Applications in Machining Processes, Applied Sciences. 11 (2021) 8764. https://doi.org/10.3390/app11188764.

[8] F. Shi, H. Cao, X. Zhang, X. Chen, A Reinforced k-Nearest Neighbors Method with Application to Chatter Identification in High-Speed Milling, IEEE Transactions on Industrial Electronics. 67 (2020) 10844–10855. https://doi.org/10.1109/TIE.2019.2962465.

[9] G.K. Christiand, Digital twin approach for tool wear monitoring of micro-milling, Procedia CIRP. 93 (2020) 1532–1537. https://doi.org/10.1016/j.procir.2020.03.140.

[10] A. Verl, A. Valente, S. Melkote, C. Brecher, E. Ozturk, L.T. Tunc, Robots in machining, CIRP Annals. 68 (2019) 799–822. https://doi.org/10.1016/j.cirp.2019.05.009.

[11] S. Wan, X. Li, W. Su, J. Yuan, J. Hong, X. Jin, Active damping of milling chatter vibration via a novel spindle system with an integrated electromagnetic actuator,

Precis Eng. 57 (2019) 203–210. https://doi.org/10.1016/j.precisioneng.2019.04.007.

[12] E. Abele, H. Hanselka, F. Haase, D. Schlote, A. Schiffler, Development and design of an active work piece holder driven by piezo actuators, Production Engineering. 2 (2008) 437–442. https://doi.org/10.1007/s11740-008-0123-3.

[13] F. Aggogeri, N. Pellegrini, F.L. Tagliani, Extended pkm fixturing system for micro-positioning and vibration rejection in machining application, Sensors. 21 (2021). https://doi.org/10.3390/s21227739.

[14] X. Zhang, C. Wang, J. Liu, R. Yan, H. Cao, X. Chen, Robust active control based milling chatter suppression with perturbation model via piezoelectric stack actuators, Mech Syst Signal Process. 120 (2019) 808–835. https://doi.org/10.1016/j.ymssp.2018.10.043.

[15] D. Li, H. Cao, X. Zhang, X. Chen, R. Yan, Model predictive control based active chatter control in milling process, Mech Syst Signal Process. 128 (2019) 266–281. https://doi.org/10.1016/j.ymssp.2019.03.047.

[16] F.L. Tagliani, N. Pellegrini, F. Aggogeri, Machine Learning Sequential Methodology for Robot Inverse Kinematic Modelling, Applied Sciences. 12 (2022) 9417. https://doi.org/10.3390/app12199417.

[17] T. Segreto, R. Teti, Machine learning for in-process end-point detection in robot-assisted polishing using multiple sensor monitoring, International Journal of Advanced Manufacturing Technology. 103 (2019) 4173–4187. https://doi.org/10.1007/s00170-019-03851-7.

[18] Q. An, Z. Tao, X. Xu, M. el Mansori, M. Chen, A data-driven model for milling tool remaining useful life prediction with convolutional and stacked LSTM network, Measurement (Lond). 154 (2020) 107461. https://doi.org/10.1016/j.measurement.2019.107461.

[19] M. Postel, B. Bugdayci, K. Wegener, Ensemble transfer learning for refining stability predictions in milling using experimental stability states, International Journal of Advanced Manufacturing Technology. 107 (2020) 4123–4139. https://doi.org/10.1007/s00170-020-05322-w.

[20] F. Aggogeri, A. Borboni, A. Merlo, N. Pellegrini, R. Ricatto, Real-time performance of mechatronic PZT module using active vibration feedback control, Sensors (Switzerland). 16 (2016). https://doi.org/10.3390/s16101577.

[21] C. YUE, H. GAO, X. LIU, S.Y. LIANG, L. WANG, A review of chatter vibration research in milling, Chinese Journal of Aeronautics. 32 (2019) 215–242. https://doi.org/10.1016/j.cja.2018.11.007.

[22] G. Quintana, J. Ciurana, Chatter in machining processes: A review, Int J Mach Tools Manuf. 51 (2011) 363–376. https://doi.org/10.1016/j.ijmachtools.2011.01.001.

[23] F. Aggogeri, F. Al-Bender, B. Brunner, M. Elsaid, M. Mazzola, A. Merlo, D. Ricciardi, M. de La O Rodriguez, E. Salvi, Design of piezo-based AVC system for machine tool applications, Mech Syst Signal Process. 36 (2013) 53–65. https://doi.org/10.1016/j.ymssp.2011.06.012.

[24] A. Rashid, C. Mihai Nicolescu, Active vibration control in palletised workholding system for milling, Int J Mach Tools Manuf. 46 (2006) 1626–1636. https://doi.org/10.1016/j.ijmachtools.2005.08.020.

[25] D. Li, H. Cao, J. Liu, X. Zhang, X. Chen, Milling chatter control based on asymmetric stiffness, Int J Mach Tools Manuf. 147 (2019) 103458. https://doi.org/10.1016/j.ijmachtools.2019.103458.

[26] C. Wang, X. Zhang, J. Liu, R. Yan, H. Cao, X. Chen, Multi harmonic and random stiffness excitation for milling chatter suppression, Mech Syst Signal Process. 120 (2019) 777–792. https://doi.org/10.1016/j.ymssp.2018.11.019.

[27] A. Parus, B. Powałka, K. Marchelek, S. Domek, M. Hoffmann, Active vibration control in milling flexible workpieces, Journal of Vibration and Control. 19 (2013) 1103–1120. https://doi.org/10.1177/1077546312442097.

[28] L. Zhu, C. Liu, Recent progress of chatter prediction, detection and suppression in milling, Mech Syst Signal Process. 143 (2020) 106840. https://doi.org/10.1016/j.ymssp.2020.106840.

[29] W. Ma, Y. Yang, X. Jin, Chatter suppression in micro-milling using shank-mounted Two-DOF tuned mass damper, Precis Eng. 72 (2021) 144–157. https://doi.org/10.1016/J.PRECISIONENG.2021.04.017.

[30] Y. Yang, W. Dai, Q. Liu, Design and implementation of two-degree-of-freedom tuned mass damper in milling vibration mitigation, J Sound Vib. 335 (2015) 78–88. https://doi.org/10.1016/j.jsv.2014.09.032.

[31] M. Wan, X. bin Dang, W.H. Zhang, Y. Yang, Optimization and improvement of stable processing condition by attaching additional masses for milling of thin-walled workpiece, Mech Syst Signal Process. 103 (2018) 196–215. https://doi.org/10.1016/j.ymssp.2017.10.008.

[32] J. Munoa, X. Beudaert, Z. Dombovari, Y. Altintas, E. Budak, C. Brecher, G. Stepan, Chatter suppression techniques in metal cutting, CIRP Ann Manuf Technol. 65 (2016) 785–808. https://doi.org/10.1016/j.cirp.2016.06.004.

[33] T. Huang, Z. Chen, H.T. Zhang, H. Ding, Active control of an active magnetic bearings supported spindle for chatter suppression in milling process, Journal of Dynamic Systems, Measurement and Control, Transactions of the ASME. 137 (2015) 1–11. https://doi.org/10.1115/1.4030841.

[34] M. Chen, C.R. Knospe, Chatter Using Active Magnetic Bearings, 15 (2007) 220–232.

[35] N.J.M. van Dijk, N. van de Wouw, E.J.J. Doppenberg, H.A.J. Oosterling, H. Nijmeijer, Robust active chatter control in the high-speed milling process, IEEE Transactions on Control Systems Technology. 20 (2012) 901–917. https://doi.org/10.1109/TCST.2011.2157160.

[36] C.R. Knospe, Active magnetic bearings for machining applications, Control Eng Pract. 15 (2007) 307–313. https://doi.org/10.1016/j.conengprac.2005.12.002.

[37] G.P. Ren, Z. Chen, H.T. Zhang, Y. Wu, H. Meng, D. Wu, H. Ding, Design of Interval Type-2 Fuzzy Controllers for Active Magnetic Bearing Systems, IEEE/ASME Transactions on Mechatronics. 25 (2020) 2449–2459. https://doi.org/10.1109/TMECH.2020.2978018.

[38] X. Li, S. Wan, J. Yuan, Y. Yin, J. Hong, Active suppression of milling chatter with LMI-based robust controller and electromagnetic actuator, J Mater Process Technol. 297 (2021) 117238. https://doi.org/10.1016/j.jmatprotec.2021.117238.

[39] S. Wan, X. Li, W. Su, J. Yuan, J. Hong, Active chatter suppression for milling process with sliding mode control and electromagnetic actuator, Mech Syst Signal Process. 136 (2020) 106528. https://doi.org/10.1016/j.ymssp.2019.106528.

[40] E. Diez, E. Leal-Muñoz, H. Perez, A. Vizan, Dynamic analysis of a piezoelectric system to compensate for workpiece deformations in flexible milling, Mech Syst Signal Process. 91 (2017) 278–294. https://doi.org/10.1016/j.ymssp.2017.01.014.

[41] C. Brecher, D. Manoharan, U. Ladra, H.-G. Köpken, Chatter suppression with an active workpiece holder, Production Engineering. 4 (2010) 239–245. https://doi.org/10.1007/s11740-009-0204-y.

[42] D.G. Ford, A. Myers, F. Haase, S. Lockwood, A. Longstaff, Active vibration control for a CNC milling machine, Proc Inst Mech Eng C J Mech Eng Sci. 228 (2014) 230–245. https://doi.org/10.1177/0954406213484224.

[43] L. Sallese, N. Grossi, A. Scippa, G. Campatelli, Numerical investigation of chatter suppression in milling using active fixtures in open-loop control, JVC/Journal of Vibration and Control. 24 (2018) 1757–1773. https://doi.org/10.1177/1077546316668686.

[44] C. Wang, X. Zhang, Y. Liu, H. Cao, X. Chen, Stiffness variation method for milling chatter suppression via piezoelectric stack actuators, Int J Mach Tools Manuf. 124 (2018) 53–66. https://doi.org/10.1016/j.ijmachtools.2017.10.002.

[45] B. Denkena, O. Gümmer, Process stabilization with an adaptronic spindle system, Production Engineering. 6 (2012) 485–492. https://doi.org/10.1007/s11740-012-0397-3.

[46] W.G. Drossel, V. Wittstock, Adaptive spindle support for improving machining operations, CIRP Ann Manuf Technol. 57 (2008) 395–398. https://doi.org/10.1016/j.cirp.2008.03.051.

[47] D. Li, H. Cao, F. Shi, X. Zhang, X. Chen, Model Predictive Control Based Chatter Suppression in Milling Process via Piezoelectric Stack Actuators, Procedia CIRP. 78 (2018) 31–36. https://doi.org/10.1016/j.procir.2018.08.308.

[48] D. Li, H. Cao, X. Chen, Fuzzy control of milling chatter with piezoelectric actuators embedded to the tool holder, Mech Syst Signal Process. 148 (2021) 107190. https://doi.org/10.1016/j.ymssp.2020.107190.

[49] J.L. Dohner, J.P. Lauffer, T.D. Hinnerichs, N. Shankar, M. Regelbrugge, C.-M. Kwan, R. Xu, B. Winterbauer, K. Bridger, Mitigation of chatter instabilities in milling by active structural control, J Sound Vib. 269 (2004) 197–211. https://doi.org/10.1016/S0022-460X(03)00069-5.

[50] F. Aggogeri, A. Merlo, N. Pellegrini, Active vibration control development in ultra-precision machining, Journal of Vibration and Control. 27 (2021) 790–801. https://doi.org/10.1177/1077546320933477.

[51] F. Shi, H. Cao, D. Li, X. Chen, X. Zhang, Active chatter control in high speed milling processes based on H ∞ almost disturbance decoupling problem, Procedia CIRP. 78 (2018) 37–42. https://doi.org/10.1016/j.procir.2018.09.050.

[52] F. Shi, H. Cao, X. Zhang, X. Chen, A chatter mitigation technique in milling based on H∞-ADDPMS and piezoelectric stack actuators, The International Journal of Advanced Manufacturing Technology. 101 (2019) 2233–2248. https://doi.org/10.1007/s00170-018-2913-x.

[53] J. Monnin, F. Kuster, K. Wegener, Optimal control for chatter mitigation in milling-Part 1: Modeling and control design, Control Eng Pract. 24 (2014) 156–166. https://doi.org/10.1016/j.conengprac.2013.11.010.

[54] J. Monnin, F. Kuster, K. Wegener, Optimal control for chatter mitigation in milling-Part 2: Experimental validation, Control Eng Pract. 24 (2014) 167–175. https://doi.org/10.1016/j.conengprac.2013.11.011.

[55] C. Wang, X. Zhang, J. Liu, H. Cao, X. Chen, Adaptive vibration reshaping based milling chatter suppression, Int J Mach Tools Manuf. 141 (2019) 30–35. https://doi.org/10.1016/j.ijmachtools.2019.04.001.

[56] D. Li, H. Cao, X. Chen, Active control of milling chatter considering the coupling effect of spindle-tool and workpiece systems, Mech Syst Signal Process. 169 (2022) 108769. https://doi.org/10.1016/j.ymssp.2021.108769.

[57] I. Mancisidor, J. Munoa, R. Barcena, X. Beudaert, M. Zatarain, Coupled model for simulating active inertial actuators in milling processes, International Journal of Advanced Manufacturing Technology. 77 (2015) 581–595. https://doi.org/10.1007/s00170-014-6469-0.

[58] S. Huyanan, N.D. Sims, Vibration control strategies for proof-mass actuators, JVC/Journal of Vibration and Control. 13 (2007) 1785–1806. https://doi.org/10.1177/1077546307080031.

[59] M.F. Zaeh, R. Kleinwort, P. Fagerer, Y. Altintas, Automatic tuning of active vibration control systems using inertial actuators, CIRP Ann Manuf Technol. 66 (2017) 365–368. https://doi.org/10.1016/j.cirp.2017.04.051.

[60] E. Abele, G. Pfeiffer, B. Jalizi, A. Bretz, Simulation and development of an active damper with robust μ-control for a machine tool with a gantry portal, Production Engineering. 10 (2016) 519–528. https://doi.org/10.1007/s11740-016-0691-6.

[61] M. Ozsoy, N.D. Sims, E. Ozturk, Robotically assisted active vibration control in milling: A feasibility study, Mech Syst Signal Process. 177 (2022) 109152. https://doi.org/10.1016/j.ymssp.2022.109152.

[62] F. Aggogeri, A. Borboni, A. Merlo, N. Pellegrini, M. Tiboni, Design of a 3-DOFs parallel robotic device for miniaturized object machining, Springer International Publishing, 2019. https://doi.org/10.1007/978-3-030-00232-9_34.

[63] J. Munoa, I. Mancisidor, N. Loix, L.G. Uriarte, R. Barcena, M. Zatarain, Chatter suppression in ram type travelling column milling machines using a biaxial inertial actuator, CIRP Ann Manuf Technol. 62 (2013) 407–410. https://doi.org/10.1016/j.cirp.2013.03.143.

[64] M.M. Uddin, J. Saak, B. Kranz, P. Benner, Computation of a compact state space model for an adaptive spindle head configuration with piezo actuators using balanced truncation, Production Engineering. 6 (2012) 577–586. https://doi.org/10.1007/s11740-012-0410-x.

[65] J. Munoa, X. Beudaert, K. Erkorkmaz, A. Iglesias, A. Barrios, M. Zatarain, Active suppression of structural chatter vibrations using machine drives and accelerometers, CIRP Ann Manuf Technol. 64 (2015) 385–388. https://doi.org/10.1016/j.cirp.2015.04.106.

[66] S. Wang, Q. Song, Z. Liu, Vibration suppression of thin-walled workpiece milling using a time-space varying PD control method via piezoelectric actuator, International Journal of Advanced Manufacturing Technology. 105 (2019) 2843–2856. https://doi.org/10.1007/s00170-019-04493-5.

[67] A. Parus, A. Bodnar, K. Marchelek, M. Chodzko, Using of active clamping device for workpiece vibration suppression, Journal of Vibration Engineering and Technologies. 3 (2015) 161–167.

[68] D. Zhang, D.G. Chetwynd, X. Liu, Y. Tian, Investigation of a 3-DOF micro-positioning table for surface grinding, Int J Mech Sci. 48 (2006) 1401–1408. https://doi.org/10.1016/j.ijmecsci.2006.07.006.

[69] N. Chen, C. Tian, Design, modeling and testing of a 3-DOF flexible piezoelectric thin sheet nanopositioner, Sens Actuators A Phys. 323 (2021) 112660. https://doi.org/10.1016/j.sna.2021.112660.

[70] Z. Guo, Y. Tian, X. Liu, B. Shirinzadeh, F. Wang, D. Zhang, An inverse Prandtl-Ishlinskii model based decoupling control methodology for a 3-DOF flexure-

based mechanism, Sens Actuators A Phys. 230 (2015) 52–62. https://doi.org/10.1016/j.sna.2015.04.018.

[71] J. Yang, Z. Xu, Q. Wu, M. Zhu, S. He, C. Qin, Dynamic modeling and control of a 6-DOF micro-vibration simulator, Mech Mach Theory. 104 (2016) 350–369. https://doi.org/10.1016/j.mechmachtheory.2016.06.011.

[72] C. Wang, X. Xie, Y. Chen, Z. Zhang, Investigation on active vibration isolation of a Stewart platform with piezoelectric actuators, J Sound Vib. 383 (2016) 1–19. https://doi.org/10.1016/j.jsv.2016.07.021.

[73] I.A. Abu Hanieh, A. Preumont, N. Loix, Piezoelectric Stewart platform for general purpose active damping interface and precision control, European Space Agency, (Special Publication) ESA SP. (2001) 331–334.

[74] L. Lin, M. Tsay, Modeling and control of micropositioning systems using Stewart platforms, J Robot Syst. 17 (2000) 17–52. https://doi.org/10.1002/(SICI)1097-4563(200001)17:1<17::AID-ROB2>3.0.CO;2-Q.

[75] M. Goldfarb, N. Celanovic, Modeling piezoelectric stack actuators for control of micromanipulation, IEEE Control Syst. 17 (1997) 69–79. https://doi.org/10.1109/37.588158.

[76] H.J.M.T.S. Adriaens, W.L. de Koning, R. Banning, Modeling piezoelectric actuators, IEEE/ASME Transactions on Mechatronics. 5 (2000) 331–341. https://doi.org/10.1109/3516.891044.

[77] M. Goldfarb, N. Celanovic, A Lumped Parameter Electromechanical Model for Describing the Nonlinear Behavior of Piezoelectric Actuators, J Dyn Syst Meas Control. 119 (1997) 478–485. https://doi.org/10.1115/1.2801282.

[78] IEEE Standard on Piezoelectricity, ANSI/IEEE Std. (1988). https://doi.org/10.1109/IEEESTD.1988.79638.

[79] M. Pozzi, T. King, Piezoelectric modelling for an impact actuator, Mechatronics. 13 (2003) 553–570. https://doi.org/10.1016/S0957-4158(02)00004-1.

[80] T.G. Zsurzsan, C. Mangeot, M.A.E. Andersen, Z. Zhang, N.A. Andersen, Piezoelectric stack actuator parameter extraction with hysteresis compensation, 2014 16th European Conference on Power Electronics and Applications, EPE-ECCE Europe 2014. (2014). https://doi.org/10.1109/EPE.2014.6910969.

[81] Y. He, X. Chen, Z. Liu, Y. Chen, Active vibration control of motorized spindle based on mixed H ∞ /Kalman filter robust state feedback control, JVC/Journal of Vibration and Control. 25 (2019) 1279–1293. https://doi.org/10.1177/1077546318820935.

[82] G.Y. Gu, L.M. Zhu, C.Y. Su, H. DIng, S. Fatikow, Modeling and control of piezo-actuated nanopositioning stages: A survey, IEEE Transactions on Automation Science and Engineering. 13 (2016) 313–332. https://doi.org/10.1109/TASE.2014.2352364.

[83] M. al Janaideh, S. Rakheja, C.Y. Su, An analytical generalized Prandtl-Ishlinskii model inversion for hysteresis compensation in micropositioning control, IEEE/ASME Transactions on Mechatronics. 16 (2011) 734–744. https://doi.org/10.1109/TMECH.2010.2052366.

[84] G.-Y. Gu, L.-M. Zhu, C.-Y. Su, H. Ding, Motion Control of Piezoelectric Positioning Stages: Modeling, Controller Design, and Experimental Evaluation, IEEE/ASME Transactions on Mechatronics. 18 (2013) 1459–1471. https://doi.org/10.1109/TMECH.2012.2203315.

[85] H.M.S. Georgiou, R. ben Mrad, Electromechanical modeling of piezoceramic actuators for dynamic loading applications, Journal of Dynamic Systems, Measurement and Control, Transactions of the ASME. 128 (2006) 558–567. https://doi.org/10.1115/1.2234486.

[86] L. Juhász, J. Maas, B. Borovac, Parameter identification and hysteresis compensation of embedded piezoelectric stack actuators, Mechatronics. 21 (2011) 329–338. https://doi.org/10.1016/j.mechatronics.2010.12.006.

[87] M. Quant, H. Elizalde, A. Flores, R. Ramírez, P. Orta, G. Song, A comprehensive model for piezoceramic actuators: Modelling, validation and application, Smart Mater Struct. 18 (2009). https://doi.org/10.1088/0964-1726/18/12/125011.

[88] M. al Janaideh, M. al Saaideh, M. Rakotondrabe, On hysteresis modeling of a piezoelectric precise positioning system under variable temperature, Mech Syst Signal Process. 145 (2020) 106880. https://doi.org/10.1016/j.ymssp.2020.106880.

[89] G.H. Choi, J.H. Oh, G.S. Choi, Repetitive tracking control of a coarse-fine actuator, IEEE/ASME International Conference on Advanced Intelligent Mechatronics, AIM. (1999) 335–340. https://doi.org/10.1109/AIM.1999.803188.

[90] V. Lampaert, F. Al-Bender, J. Swevers, A generalized Maxwell-slip friction model appropriate for control purposes, 2003 International Conference Physics and Control, PhysCon 2003 - Proceedings. 4 (2003) 1170–1177. https://doi.org/10.1109/PHYCON.2003.1237071.

[91] R.J. Wood, E. Steltz, R.S. Fearing, Nonlinear performance limits for high energy density piezoelectric bending actuators, Proc IEEE Int Conf Robot Autom. 2005 (2005) 3633–3640. https://doi.org/10.1109/ROBOT.2005.1570673.

[92] Y.C. Huang, D.Y. Lin, Tracking control of a piezoelectric actuator based on experiment hysteretic modeling, IEEE/ASME International Conference on Advanced Intelligent Mechatronics, AIM. 1 (2003) 308–313. https://doi.org/10.1109/AIM.2003.1225113.

[93] Z. Li, J. Shan, U. Gabbert, A Direct Inverse Model for Hysteresis Compensation, IEEE Transactions on Industrial Electronics. 68 (2020) 4173–4181. https://doi.org/10.1109/tie.2020.2984452.

[94] Shunli Xiao, Yangmin Li, Modeling and High Dynamic Compensating the Rate-Dependent Hysteresis of Piezoelectric Actuators via a Novel Modified Inverse Preisach Model, IEEE Transactions on Control Systems Technology. 21 (2013) 1549–1557. https://doi.org/10.1109/TCST.2012.2206029.

[95] S.R. Viswamurthy, R. Ganguli, Modeling and compensation of piezoceramic actuator hysteresis for helicopter vibration control, Sens Actuators A Phys. 135 (2007) 801–810. https://doi.org/10.1016/j.sna.2006.09.020.

[96] P. Ge, M. Jouaneh, Generalized preisach model for hysteresis nonlinearity of piezoceramic actuators, Precis Eng. 20 (1997) 99–111. https://doi.org/10.1016/s0141-6359(97)00014-7.

[97] D. Song, C.J. Li, Modeling of piezo actuator's nonlinear and frequency dependent dynamics, Mechatronics. 9 (1999) 391–410. https://doi.org/10.1016/S0957-4158(99)00005-7.

[98] H. Hu, R. ben Mrad, A discrete-time compensation algorithm for hysteresis in piezoceramic actuators, Mech Syst Signal Process. 18 (2004) 169–185. https://doi.org/10.1016/S0888-3270(03)00021-9.

[99] H. Hu, R. ben Mrad, On the classical Preisach model for hysteresis in piezoceramic actuators, Mechatronics. 13 (2003) 85–94. https://doi.org/10.1016/S0957-4158(01)00043-5.

[100] H. Jiang, H. Ji, J. Qiu, Y. Chen, A modified prandtl-ishlinskii model for modeling asymmetric hysteresis of piezoelectric actuators, IEEE Trans Ultrason Ferroelectr Freq Control. 57 (2010) 1200–1210. https://doi.org/10.1109/TUFFC.2010.1533.

[101] A. Esbrook, X. Tan, H.K. Khalil, Control of systems with hysteresis via servocompensation and its application to nanopositioning, IEEE Transactions on Control Systems Technology. 21 (2013) 725–738. https://doi.org/10.1109/TCST.2012.2192734.

[102] G.Y. Gu, M.J. Yang, L.M. Zhu, Real-time inverse hysteresis compensation of piezoelectric actuators with a modified Prandtl-Ishlinskii model, Review of Scientific Instruments. 83 (2012). https://doi.org/10.1063/1.4728575.

[103] Y. Shan, K.K. Leang, Accounting for hysteresis in repetitive control design: Nanopositioning example, Automatica. 48 (2012) 1751–1758. https://doi.org/10.1016/j.automatica.2012.05.055.

[104] M. al Janaideh, S. Rakheja, C.Y. Su, Experimental characterization and modeling of rate-dependent hysteresis of a piezoceramic actuator, Mechatronics. 19 (2009) 656–670. https://doi.org/10.1016/j.mechatronics.2009.02.008.

[105] M. Rakotondrabe, Classical Prandtl-Ishlinskii modeling and inverse multiplicative structure to compensate hysteresis in piezoactuators, Proceedings of the American Control Conference. (2012) 1646–1651. https://doi.org/10.1109/acc.2012.6314620.

[106] M. al Janaideh, J. Mao, S. Rakheja, W. Xie, C.Y. Su, Generalized Prandtl-Ishlinskii hysteresis model: Hysteresis modeling and its inverse for compensation in smart actuators, Proceedings of the IEEE Conference on Decision and Control. (2008) 5182–5187. https://doi.org/10.1109/CDC.2008.4739202.

[107] W. Wang, R. Wang, Z. Chen, Z. Sang, K. Lu, F. Han, J. Wang, B. Ju, A new hysteresis modeling and optimization for piezoelectric actuators based on asymmetric Prandtl-Ishlinskii model, Sens Actuators A Phys. 316 (2020) 112431. https://doi.org/10.1016/j.sna.2020.112431.

[108] J. Xu, J. Lou, Y. Yang, T. Chen, H. Chen, Y. Cui, Hysteresis modeling and feedforward compensation of a flexible structure actuated by macro fiber composites using bias bipolar Prandtl-Ishlinskii model, J Intell Mater Syst Struct. (2021) 1045389X2199588. https://doi.org/10.1177/1045389X21995881.

[109] W. Wang, F. Han, Z. Chen, R. Wang, C. Wang, K. Lu, J. Wang, B. Ju, Modeling and Compensation for Asymmetrical and Dynamic Hysteresis of Piezoelectric Actuators Using a Dynamic Delay Prandtl–Ishlinskii Model, Micromachines (Basel). 12 (2021) 92. https://doi.org/10.3390/mi12010092.

[110] X. Shan, H. Song, H. Cao, L. Zhang, X. Zhao, J. Fan, A Dynamic Hysteresis Model and Nonlinear Control System for a Structure-Integrated Piezoelectric Sensor-Actuator, Sensors. 21 (2021) 269. https://doi.org/10.3390/s21010269.

[111] S. Kang, H. Wu, Y. Li, S. Yu, X. Yang, J. Yao, A fractional-order normalized Bouc-Wen model for piezoelectric hysteresis nonlinearity, ArXiv. (2020). https://doi.org/10.1109/tmech.2021.3058851.

[112] T.V. Minh, T.T. Tung, X. Chen, Precision Control of Piezoelectric Actuator Using Modified Bouc-Wen Model, International Conference on Advanced Mechatronic Systems, ICAMechS. 2020-Decem (2020) 162–167. https://doi.org/10.1109/ICAMechS49982.2020.9310116.

[113] M. Rakotondrabe, Bouc – Wen Modeling and Inverse Multiplicative Structure Actuators, IEEE Transactions on Automation Science and Engineering. 8 (2011) 428–431.

[114] R.-F. Fung, M.-H. Weng, Y.-S. Kung, FPGA-based adaptive backstepping fuzzy control for a micro-positioning Scott-Russell mechanism, Mech Syst Signal Process. 23 (2009) 2671–2686. https://doi.org/10.1016/j.ymssp.2009.01.005.

[115] Y. ling Yang, J. qiang Lou, G. hua Wu, Y. ding Wei, L. Fu, Design and position/force control of an S-shaped MFC microgripper, Sens Actuators A Phys. 282 (2018) 63–78. https://doi.org/10.1016/J.SNA.2018.09.021.

[116] W. Zhu, D.H. Wang, Non-symmetrical Bouc-Wen model for piezoelectric ceramic actuators, Sens Actuators A Phys. 181 (2012) 51–60. https://doi.org/10.1016/j.sna.2012.03.048.

[117] J. Yi, S. Chang, Y. Shen, Disturbance-observer-based hysteresis compensation for piezoelectric actuators, IEEE/ASME Transactions on Mechatronics. 14 (2009) 456–464. https://doi.org/10.1109/TMECH.2009.2023986.

[118] K. Ahmed, P. Yan, S. Li, Duhem Model-Based Hysteresis Identification in Piezo-Actuated Nano-Stage Using Modified Particle Swarm Optimization, Micromachines (Basel). 12 (2021) 315. https://doi.org/10.3390/mi12030315.

[119] L. Liu, Q. Li, H. Yun, J. Liang, X. Ma, Composite modeling and parameter identification of broad bandwidth hysteretic dynamics in piezoelectric fast steering platform, Mech Syst Signal Process. 121 (2019) 97–111. https://doi.org/10.1016/j.ymssp.2018.11.007.

[120] J. Cai, F. Chen, Y. Gao, W. Dong, Hybrid controller of a linear piezoelectric walking stage relying on stack/shear piezoelectric actuators, Precis Eng. 72 (2021) 272–281. https://doi.org/10.1016/j.precisioneng.2021.05.005.

[121] M. S, M. Rao, N. Karanth P, S.M. Kulkarni, A.R. Upadhya, Development and assessment of large stroke piezo-hydraulic actuator for micro positioning applications, Precis Eng. 67 (2021) 324–338. https://doi.org/10.1016/j.precisioneng.2020.10.012.

[122] S. Kang, H. Wu, Y. Li, X. Yang, J. Yao, A Fractional-Order Normalized Bouc-Wen Model for Piezoelectric Hysteresis Nonlinearity, IEEE/ASME Transactions on Mechatronics. 27 (2022) 126–136. https://doi.org/10.1109/TMECH.2021.3058851.

[123] W. Zhu, F. Yang, X. Rui, Robust independent modal space control of a coupled nano-positioning piezo-stage, Mech Syst Signal Process. 106 (2018) 466–478. https://doi.org/10.1016/j.ymssp.2018.01.016.

[124] G. Wang, G. Chen, F. Bai, Modeling and identification of asymmetric Bouc–Wen hysteresis for piezoelectric actuator via a novel differential evolution algorithm, Sens Actuators A Phys. 235 (2015) 105–118. https://doi.org/10.1016/j.sna.2015.09.043.

[125] W. Zhu, X.T. Rui, Hysteresis modeling and displacement control of piezoelectric actuators with the frequency-dependent behavior using a generalized Bouc-Wen model, Precis Eng. 43 (2016) 299–307. https://doi.org/10.1016/j.precisioneng.2015.08.010.

[126] S. Kang, H. Wu, X. Yang, Y. Li, L. Pan, B. Chen, Fractional robust adaptive decoupled control for attenuating creep, hysteresis and cross coupling in a parallel piezostage, Mech Syst Signal Process. 159 (2021) 107764. https://doi.org/10.1016/j.ymssp.2021.107764.

[127] Z. Wei, B.L. Xiang, R.X. Ting, Online parameter identification of the asymmetrical Bouc-Wen model for piezoelectric actuators, Precis Eng. 38 (2014) 921–927. https://doi.org/10.1016/j.precisioneng.2014.06.002.

[128] P.-B. Nguyen, S.-B. Choi, B.-K. Song, A new approach to hysteresis modelling for a piezoelectric actuator using Preisach model and recursive method with an application to open-loop position tracking control, Sens Actuators A Phys. 270 (2018) 136–152. https://doi.org/10.1016/j.sna.2017.12.034.

[129] C.-C. Kao, R.-F. Fung, Using the modified PSO method to identify a Scott-Russell mechanism actuated by a piezoelectric element, Mech Syst Signal Process. 23 (2009) 1652–1661. https://doi.org/10.1016/j.ymssp.2008.12.003.

[130] R.-F. Fung, Y.-L. Hsu, M.-S. Huang, System identification of a dual-stage XY precision positioning table, Precis Eng. 33 (2009) 71–80. https://doi.org/10.1016/j.precisioneng.2008.04.002.

[131] Y. Yang, Y. Wei, J. Lou, L. Fu, G. Tian, M. Wu, Hysteresis modeling and precision trajectory control for a new MFC micromanipulator, Sens Actuators A Phys. 247 (2016) 37–52. https://doi.org/10.1016/j.sna.2016.05.027.

[132] J.-L. Ha, Y.-S. Kung, R.-F. Fung, S.-C. Hsien, A comparison of fitness functions for the identification of a piezoelectric hysteretic actuator based on the real-coded genetic algorithm, Sens Actuators A Phys. 132 (2006) 643–650. https://doi.org/10.1016/j.sna.2006.02.022.

[133] R.F. Fung, W.C. Lin, System identification of a novel 6-DOF precision positioning table, Sens Actuators A Phys. 150 (2009) 286–295. https://doi.org/10.1016/j.sna.2009.01.007.

[134] V. Kučera, D. Pilbauer, T. Vyhlídal, N. Olgac, Extended delayed resonators – Design and experimental verification, Mechatronics. 41 (2017) 29–44. https://doi.org/10.1016/j.mechatronics.2016.10.019.

[135] T. Vyhlídal, D. Pilbauer, B. Alikoç, W. Michiels, Analysis and design aspects of delayed resonator absorber with position, velocity or acceleration feedback, J Sound Vib. 459 (2019) 114831. https://doi.org/10.1016/j.jsv.2019.06.038.

[136] S. Chesné, G. Inquieté, P. Cranga, F. Legrand, B. Petitjean, Innovative Hybrid Mass Damper for Dual-Loop Controller, Mech Syst Signal Process. 115 (2019) 514–523. https://doi.org/10.1016/j.ymssp.2018.06.023.

[137] D. Pilbauer, T. Vyhlídal, W. Michiels, Optimized design of robust resonator with distributed time-delay, J Sound Vib. 443 (2019) 576–590. https://doi.org/10.1016/j.jsv.2018.12.002.

[138] Z. Šika, T. Vyhlídal, Z. Neusser, Two-dimensional delayed resonator for entire vibration absorption, J Sound Vib. 500 (2021). https://doi.org/10.1016/j.jsv.2021.116010.

[139] R. Jenkins, N. Olgac, Real-Time Tuning of Delayed Resonator-Based Absorbers for Spectral and Spatial Variations, Journal of Vibration and Acoustics, Transactions of the ASME. 141 (2019) 1–9. https://doi.org/10.1115/1.4041592.

[140] N. Jalili, Piezoelectric-based vibration control: From macro to micro/nano scale systems, Springer US, Boston, MA, 2010. https://doi.org/10.1007/978-1-4419-0070-8.

[141] D. Pilbauer, T. Vyhlidal, N. Olgac, Delayed resonator with distributed delay in acceleration feedback - Design and experimental verification, IEEE/ASME Transactions on Mechatronics. 21 (2016) 2120–2131. https://doi.org/10.1109/TMECH.2016.2516763.

[142] T. Vyhlídal, N. Olgac, V. Kučera, Delayed resonator with acceleration feedback – Complete stability analysis by spectral methods and vibration absorber design, J Sound Vib. 333 (2014) 6781–6795. https://doi.org/10.1016/j.jsv.2014.08.002.

[143] D. Manocha, J.F. Canny, Efficient Inverse Kinematics for General 6R Manipulators, IEEE Transactions on Robotics and Automation. 10 (1994) 648–657. https://doi.org/10.1109/70.326569.

[144] I. Zaplana, L. Basanez, A novel closed-form solution for the inverse kinematics of redundant manipulators through workspace analysis, Mech Mach Theory. 121 (2018) 829–843. https://doi.org/10.1016/j.mechmachtheory.2017.12.005.

[145] S. Chiaverini, G. Oriolo, A.A. Maciejewski, Redundant Robots, in: Springer Handbook of Robotics, Spring, 2016: pp. 221–242. https://doi.org/10.1007/978-3-319-32552-1_10.

[146] R. Dou, S. Yu, W. Li, P. Chen, P. Xia, F. Zhai, H. Yokoi, Y. Jiang, Inverse kinematics for a 7-DOF humanoid robotic arm with joint limit and end pose coupling, Mech Mach Theory. 169 (2022) 104637. https://doi.org/10.1016/j.mechmachtheory.2021.104637.

[147] M. Shimizu, H. Kakuya, W.K. Yoon, K. Kitagaki, K. Kosuge, Analytical inverse kinematic computation for 7-DOF redundant manipulators with joint limits and its application to redundancy resolution, IEEE Transactions on Robotics. 24 (2008) 1131–1142. https://doi.org/10.1109/TRO.2008.2003266.

[148] M. Gong, X. Li, L. Zhang, Analytical Inverse Kinematics and Self-Motion Application for 7-DOF Redundant Manipulator, IEEE Access. 7 (2019) 18662–18674. https://doi.org/10.1109/ACCESS.2019.2895741.

[149] R. Featherstone, Position and Velocity Transformations Between Robot End-Effector Coordinates and Joint Angles, Int J Rob Res. 2 (1983) 35–45. https://doi.org/10.1177/027836498300200203.

[150] H. Deng, C. Xie, An improved particle swarm optimization algorithm for inverse kinematics solution of multi-DOF serial robotic manipulators, Soft Comput. 25 (2021) 13695–13708. https://doi.org/10.1007/s00500-021-06007-6.

[151] N. Rokbani, M. Slim, A.M. Alimi, The Beta distributed PSO, β-PSO, with application to Inverse Kinematics, in: 2021 National Computing Colleges

Conference (NCCC), IEEE, 2021: pp. 1–6. https://doi.org/10.1109/NCCC49330.2021.9428811.

[152] L. Yiyang, J. Xi, B. Hongfei, W. Zhining, S. Liangliang, A General Robot Inverse Kinematics Solution Method Based on Improved PSO Algorithm, IEEE Access. 9 (2021) 32341–32350. https://doi.org/10.1109/ACCESS.2021.3059714.

[153] C.T. Lee, J.Y. Chang, A workspace-analysis-based genetic algorithm for solving inverse kinematics of a multi-fingered anthropomorphic hand, Applied Sciences (Switzerland). 11 (2021) 2668. https://doi.org/10.3390/app11062668.

[154] Z. Zeng, Z. Chen, G. Shu, Q. Chen, Optimization of analytical inverse kinematic solution for redundant manipulators using GA-PSO algorithm, in: 2018 IEEE Industrial Cyber-Physical Systems (ICPS), IEEE, 2018: pp. 446–451. https://doi.org/10.1109/ICPHYS.2018.8390746.

[155] S.S. Chiddarwar, N. Ramesh Babu, Comparison of RBF and MLP neural networks to solve inverse kinematic problem for 6R serial robot by a fusion approach, Eng Appl Artif Intell. 23 (2010) 1083–1092. https://doi.org/10.1016/j.engappai.2010.01.028.

[156] A.-V. Duka, Neural Network based Inverse Kinematics Solution for Trajectory Tracking of a Robotic Arm, Procedia Technology. 12 (2014) 20–27. https://doi.org/10.1016/j.protcy.2013.12.451.

[157] S. Habibkhah, R. v. Mayorga, The computation of the inverse kinematics of a 3 DOF redundant manipulator via an ann approach and a virtual function, ICINCO 2020 - Proceedings of the 17th International Conference on Informatics in Control, Automation and Robotics. (2020) 471–477. https://doi.org/10.5220/0009834904710477.

[158] S.M. Varedi-Koulaei, M. Mokhtari, Trajectory Tracking Solution of a Robotic Arm Based on Optimized ANN, Proceedings of the 6th RSI International Conference on Robotics and Mechatronics, IcRoM 2018. (2019) 76–81. https://doi.org/10.1109/ICRoM.2018.8657567.

[159] H. Li, Z. Song, Z. Jiang, Y. Mo, W. Ni, Solving Inverse Kinematics of Industrial Robot Based on BP Neural Network, 2017 IEEE 7th Annual International Conference on CYBER Technology in Automation, Control, and Intelligent Systems, CYBER 2017. (2018) 1167–1171. https://doi.org/10.1109/CYBER.2017.8446102.

[160] J. Narayan, A. Singla, ANFIS based kinematic analysis of a 4-DOFs SCARA robot, 4th IEEE International Conference on Signal Processing, Computing and Control, ISPCC 2017. 2017-Janua (2017) 205–211. https://doi.org/10.1109/ISPCC.2017.8269676.

[161] S.K. Shah, R. Mishra, L.S. Ray, Solution and validation of inverse kinematics using Deep artificial neural network, Mater Today Proc. 26 (2020) 1250–1254. https://doi.org/10.1016/j.matpr.2020.02.250.

[162] A.R.J. Almusawi, L.C. Dülger, S. Kapucu, A New Artificial Neural Network Approach in Solving Inverse Kinematics of Robotic Arm (Denso VP6242), Comput Intell Neurosci. 2016 (2016). https://doi.org/10.1155/2016/5720163.

[163] A. Singh, P. Pandey, G.C. Nandi, Effectiveness of multi-gated sequence model for the learning of kinematics and dynamics of an industrial robot, Industrial Robot. 48 (2021) 62–70. https://doi.org/10.1108/IR-01-2020-0010.

[164] M.J. Thomas, M.M. Sanjeev, A.P. Sudheer, J. M.L, Comparative study of various machine learning algorithms and Denavit–Hartenberg approach for the inverse kinematic solutions in a 3-PPSS parallel manipulator, Industrial Robot. 47 (2020) 683–695. https://doi.org/10.1108/IR-11-2019-0233.

[165] R. Köker, T. Çakar, Y. Sari, A neural-network committee machine approach to the inverse kinematics problem solution of robotic manipulators, Eng Comput. 30 (2014) 641–649. https://doi.org/10.1007/s00366-013-0313-2.

[166] R. Köker, T. Çakar, A neuro-genetic-simulated annealing approach to the inverse kinematics solution of robots: a simulation based study, Eng Comput. 32 (2016) 553–565. https://doi.org/10.1007/s00366-015-0432-z.

[167] R. Köker, A neuro-simulated annealing approach to the inverse kinematics solution of redundant robotic manipulators, Eng Comput. 29 (2013) 507–515. https://doi.org/10.1007/s00366-012-0277-7.

[168] Z. Zhou, H. Guo, Y. Wang, Z. Zhu, J. Wu, X. Liu, Inverse kinematics solution for robotic manipulator based on extreme learning machine and sequential mutation genetic algorithm, Int J Adv Robot Syst. 15 (2018) 1–15. https://doi.org/10.1177/1729881418792992.

[169] J. Demby'S, Y. Gao, G.N. Desouza, A Study on Solving the Inverse Kinematics of Serial Robots using Artificial Neural Network and Fuzzy Neural Network, IEEE International Conference on Fuzzy Systems. 2019-June (2019). https://doi.org/10.1109/FUZZ-IEEE.2019.8858872.

[170] F. Aggogeri, N. Pellegrini, C. Taesi, F.L. Tagliani, Inverse kinematic solver based on machine learning sequential procedure for robotic applications, J Phys Conf Ser. 2234 (2022). https://doi.org/10.1088/1742-6596/2234/1/012007.

[171] C. Faria, J.L. Vilaca, S. Monteiro, W. Erlhagen, E. Bicho, Automatic Denavit-Hartenberg Parameter Identification for Serial Manipulators, in: IECON 2019 - 45th Annual Conference of the IEEE Industrial Electronics Society, IEEE, 2019: pp. 610–617. https://doi.org/10.1109/IECON.2019.8927455.

[172] S.B. Šegota, N. Anđelić, V. Mrzljak, I. Lorencin, I. Kuric, Z. Car, Utilization of multilayer perceptron for determining the inverse kinematics of an industrial robotic manipulator, Int J Adv Robot Syst. 18 (2021) 172988142092528. https://doi.org/10.1177/1729881420925283.

[173] T. Zhang, Y. Song, H. Wu, Q. Wang, A novel method to identify DH parameters of the rigid serial-link robot based on a geometry model, Industrial Robot. 48 (2021) 157–167. https://doi.org/10.1108/IR-05-2020-0103.

[174] R. Reinhart, Z. Shareef, J. Steil, Hybrid Analytical and Data-Driven Modeling for Feed-Forward Robot Control, Sensors. 17 (2017) 311. https://doi.org/10.3390/s17020311.

[175] F. Cursi, G.P. Mylonas, P. Kormushev, Adaptive Kinematic Modelling for Multiobjective Control of a Redundant Surgical Robotic Tool, Robotics. 9 (2020) 68. https://doi.org/10.3390/robotics9030068.

[176] A. Csiszar, J. Eilers, A. Verl, On solving the inverse kinematics problem using neural networks, 2017 24th International Conference on Mechatronics and Machine Vision in Practice, M2VIP 2017. 2017-Decem (2017) 1–6. https://doi.org/10.1109/M2VIP.2017.8211457.

[177] F. Alonso-Martín, J. Gamboa-Montero, J. Castillo, Á. Castro-González, M. Salichs, Detecting and Classifying Human Touches in a Social Robot Through Acoustic Sensing and Machine Learning, Sensors. 17 (2017) 1138. https://doi.org/10.3390/s17051138.

[178] S. Baressi Šegota, N. Anđelić, M. Šercer, H. Meštrić, Dynamics Modeling of Industrial Robotic Manipulators: A Machine Learning Approach Based on Synthetic Data, Mathematics 2022, Vol. 10, Page 1174. 10 (2022) 1174. https://doi.org/10.3390/MATH10071174.